

# **The Production and Investigation of Cold Antihydrogen Atoms**

Dissertation  
der Fakultät für Physik  
der Ludwig-Maximilians-Universität München



vorgelegt von  
Heiko Pittner  
aus Schwäbisch Gmünd

München, im April 2005

1. Gutachter: Prof. Dr. Theodor W. Hänsch<sup>1</sup>
2. Gutachter: Prof. Dr. Walter Oelert<sup>2</sup>

Tag der mündlichen Prüfung: 27. 4. 2005

---

<sup>1</sup>Ludwig-Maximilians-Universität München und Max-Planck-Institut für Quantenoptik

<sup>2</sup>IKP, Forschungszentrum Jülich und Ruhr-Universität Bochum

*Dedicated to my parents and to Murielle, and for the  
memory of my brother Markus.*



# Abstract

This work reports on experiments in which antihydrogen atoms have been produced in cryogenic Penning traps from antiproton and positron plasmas by two different methods and on experiments that have been carried out subsequently in order to investigate the antihydrogen atoms.

By the first method antihydrogen atoms have been formed during the process of positron cooling of antiprotons in so called nested Penning traps and detected via a field ionization method. A linear dependence of the number of detected antihydrogen atoms on the number of positrons has been found. A measurement of the state distribution has revealed that the antihydrogen atoms are formed in highly excited states. This suggests along with the high production rate that the antihydrogen atoms are formed by three–body recombination processes and subsequent collisional deexcitations. However current theory cannot yet account for the measured state distribution. Typical radii of the detected antihydrogen atoms lie in the range between  $0.4\text{ }\mu\text{m}$  and  $0.15\text{ }\mu\text{m}$ . The deepest bound antihydrogen atoms have radii below  $0.1\text{ }\mu\text{m}$ . Antihydrogen atoms with that size have chaotic positron orbits so that for the first time antihydrogen atoms have been detected that cannot be described by the GCA–model. The kinetic energy of the weakest bound antihydrogen atoms has been measured to about 200 meV, which corresponds to an antihydrogen velocity of approximately 6 200 m/s. A simple model suggests that these atoms are formed from only one deexcitation collision and methods that might lead to a decrease of the antihydrogen velocity are presented.

By the second method antihydrogen atoms have been synthesized in charge–exchange processes. Lasers are used to produce a Rydberg cesium beam within the cryogenic Penning trap that collides with trapped positrons so that Rydberg positronium atoms are formed via charge–exchange reactions. Due to their charge neutrality the Rydberg positronium atoms are free to leave the positron trapping region. The Rydberg positronium atoms that collide with nearby stored antiprotons form antihydrogen atoms in charge–exchange reactions. So far,  $14 \pm 4$  antihydrogen atoms have been detected background–free via a field–ionization method.

The antihydrogen atoms produced via the two–step charge–exchange mechanism are expected to have a temperature of 4.2 K, the temperature of the antiprotons from which they are formed. A method is proposed by which the antihydrogen temperature can be determined with an accuracy of better than 1 K from a measurement of the time delay between antihydrogen annihilation events and the laser pulse that initiates the antihydrogen production via the production of Rydberg cesium atoms. First experiments have been carried out during the last days of the 2004 beam time, but the number of detected antihydrogen annihilations has been too low for a determination of the antihydrogen temperature.

Trapped antiprotons have been directly exposed to laser light delivered by a Titanium:Sapphire laser in order to investigate if the laser light causes any loss on the

trapped antiprotons. Experiments have shown that no extra loss occurs for laser powers of less than 590 mW. This is an important result against the background of the future plan to confine antihydrogen atoms in a combined Penning–Ioffe trap and then to carry out laser spectroscopy on these atoms, since it reveals that laser light does not cause an increase of the pressure in the trapping region to the extend that annihilations with the background gas become noticeable.

The ATRAP Collaboration plans to precisely investigate antihydrogen atoms. The ultimate goal is to test the CPT–theorem by a high precision measurement of the 1S–2S transition of antihydrogen and a comparison with the precisely known value of the corresponding transition in hydrogen. This thesis presents the achievement of the first step towards this challenging goal: the production of cold antihydrogen itself.

# Zusammenfassung

In dieser Arbeit werden Experimente beschrieben, in denen die Erzeugung von Antiwasserstoffatomen aus in Penning–Fallen gespeicherten Antiproton- und Positronplasmen mittels zweier unterschiedlicher Erzeugungsmethoden gelungen ist. Darüberhinaus werden Experimente vorgestellt, durch die die Eigenschaften der Antiwasserstoffatome untersucht wurden.

In der ersten Methode werden Antiwasserstoffatome beim Kühlen von Antiprotonen durch Positronen in einer sogenannten verschachtelten Penning–Falle hergestellt und durch Feldionisation nachgewiesen. Ein linearer Zusammenhang zwischen der Anzahl der detektierten Antiwasserstoffatome und der zur Erzeugung verwendeten Anzahl der Positronen konnte gemessen werden. Eine Messung der Zustandsverteilung ergab, dass die Antiwasserstoffatome in hochangeregten Zuständen erzeugt werden. Zusammen mit der hohen Erzeugungsrate lässt dies den Schluss zu, dass Dreikörperrekombination mit anschliessenden Positron–Positron Kollisionen, die zu einer weiteren Abregung der Zustände führen, der verantwortliche Erzeugungsmechanismus ist. Die gegenwärtige Theorie der Dreikörperrekombination kann allerdings noch nicht die detektierte Zustandsverteilung erklären. Typische Radien der hergestellten Antiwasserstoffatome liegen zwischen  $0.15\text{ }\mu\text{m}$  und  $0.4\text{ }\mu\text{m}$ . Die am stärksten gebundenen Antiwasserstoffatome besitzen Radien, die kleiner sind als  $0.1\text{ }\mu\text{m}$ . Die Positronenorbits von Atomen dieser Grösse sind chaotisch. Es wurden also zum ersten Mal Antiwasserstoffatome nachgewiesen, die nicht mehr durch das in der Theorie der Dreikörperstossprozesse oft verwendete GCA–Modell beschrieben werden können. Die kinetische Energie der am schwächsten gebundenen Atome ist zu etwa 200 meV gemessen werden. Dies entspricht einer Geschwindigkeit von circa 6 200 m/s. Mittels eines einfachen Modells lässt sich schlussfolgern, dass diese Atome jeweils nur durch eine einzige abregende Positron–Positron Kollision geformt wurden. Daraus lassen sich Möglichkeiten ableiten, mit denen die Antiwasserstoffgeschwindigkeit eventuell verringert werden könnte.

In der zweiten Methode werden Antiwasserstoffatome mittels Ladungsaustauschreaktionen synthetisiert. Laser werden verwendet, um einen Strahl von Rydberg–Cäsiumatomen zu erzeugen, der auf die in der Penning–Falle gespeicherten Positronen gerichtet ist. In Kollisionen zwischen den Positronen und den Rydberg–Cäsiumatomen entsteht Rydberg–Positronium. Aufgrund ihrer Ladungsneutralität können diese die Positronenfalle verlassen. Der Teil der Rydberg–Positroniumatome, der mit der in der Nähe gespeicherten Antiprotonenwolke kollidiert, kann in einem zweiten Ladungsaustausch Antiwasserstoff bilden. Dieser Antiwasserstoff wird ebenso wie in der ersten Methode durch Feldionisation nachgewiesen. Bisher wurden  $14 \pm 4$  Antiwasserstoffatome detektiert.

Wir vermuten, dass der durch Ladungsaustausch erzeugte Antiwasserstoff eine Temperatur von 4.2 K besitzt, weil dies die Temperatur der zu seiner Herstellung verwendeten Antiprotonen ist. Eine Methode, die auf einer Messung der Zeitverzögerung zwischen dem Laserpuls, der den Antiwasserstoff–Herstellungsprozess durch die Erzeugung von

Rydberg-Cäsiumatomen in Gang setzt und den darauffolgenden Antiwasserstoffannihilation beruht, wird in dieser Arbeit vorgeschlagen und analytisch untersucht. Es zeigt sich, dass damit die Antiwasserstofftemperatur mit einer Genauigkeit, die besser ist als 1 K, bestimmt werden kann. Erste Experimente wurden dazu am Ende der Strahlzeit des Jahres 2004 durchgeführt, aber die Anzahl der gemessenen Antiwasserstoffannihilations war zu gering, um damit die Antiwasserstofftemperatur bestimmen zu können.

Um herauszufinden, ob Laserlicht innerhalb der Penning-Falle zu einem erhöhten Antiprotonenverlust führt, wurden gespeicherte Antiprotonen mit Laserlicht, das von einem Titan:Saphir Laser erzeugt wurde, bestrahlt. Dabei zeigte sich, dass eine Laserleistung unter 590 mW nicht zu einem erhöhten Antiprotonenverlust führt. Dies ist ein wichtiges Resultat vor dem Hintergrund, dass die ATRAP Kollaboration plant, Antiwasserstoff in einer kombinierten Penning-Ioffe Falle zu speichern, um diesen dann mit Methoden der hochauflösenden Laserspektroskopie zu untersuchen, denn dies zeigt, dass durch das Laserlicht das Vakuum in der Penningfalle nicht soweit steigt, dass es zu einen zusätzlichen Verlust durch Annihilationen mit Hintergrundgas kommt.

Die ATRAP Kollaboration plant Antiwasserstoff genau zu untersuchen. Das ultimative Ziel ist ein Test des CPT-Theorems durch eine hochpräzise Messung des 1S–2S Überganges in Antiwasserstoff, der dann mit dem bekannten Wert des entsprechenden Überganges in Wasserstoff verglichen wird. Diese Arbeit beschreibt und diskutiert das Erreichen des ersten Meilensteins hin zu diesem anspruchsvollen Ziel, die Erzeugung von Antiwasserstoff.

# Table of Contents

<b>Table of Contents</b>	<b>ix</b>
<b>1 Introduction</b>	<b>1</b>
<b>2 The ATRAP Experiment</b>	<b>7</b>
2.1 Overview . . . . .	7
2.2 The Antiproton Decelerator (AD) . . . . .	8
2.3 The Positron Source . . . . .	8
2.4 The Penning Trap . . . . .	10
2.4.1 Penning Trap Theory . . . . .	10
2.4.2 The Penning Traps at ATRAP . . . . .	14
2.4.3 Integration of Optical Fibers in the Hbar2 Penning Trap Apparatus	19
2.5 Particle Detection . . . . .	22
2.5.1 Non-Destructive Particle Detection . . . . .	22
2.5.2 Destructive Particle Detection and the Detector System . . . . .	24
<b>3 Loading Particles</b>	<b>29</b>
3.1 Positron Loading . . . . .	29
3.2 Loading Electrons . . . . .	32
3.2.1 Loading Electrons from the Radioactive Source . . . . .	32
3.2.2 Electron loading with the FEP . . . . .	34
3.3 Accumulating Antiprotons from the AD into the Penning Trap . . . . .	35
3.3.1 Monitoring and Steering the Antiproton Beam by the PPAC . .	35
3.3.2 Slowing Antiprotons . . . . .	36
3.3.3 Antiproton Trapping . . . . .	37

3.3.4	Electron Cooling of Antiprotons . . . . .	40
3.4	Stacking of Antiprotons . . . . .	42
<b>4</b>	<b>Antihydrogen Production in a Nested Penning Trap</b>	<b>45</b>
4.1	Introduction . . . . .	45
4.1.1	Antihydrogen Production by Radiative Recombination . . . . .	45
4.1.2	Stimulated Radiative Recombination . . . . .	46
4.1.3	The Three–Body Recombination Process . . . . .	47
4.2	First Observation of Antihydrogen Atoms . . . . .	48
4.2.1	The Experimental Setup . . . . .	48
4.2.2	Experimental Results . . . . .	51
4.3	State Distribution of Antihydrogen . . . . .	51
4.3.1	The Experimental Setup . . . . .	52
4.3.2	More Antihydrogen Atoms by Driving Antiprotons . . . . .	52
4.3.3	Dependence of Antihydrogen Production on the Number of Positrons	55
4.3.4	The State Distribution of the Formed Antihydrogen . . . . .	56
4.4	Measuring the Velocity of Antihydrogen Atoms . . . . .	59
4.4.1	Experimental Setup . . . . .	60
4.4.2	The Experimental Results . . . . .	60
4.4.3	Discussion of the Experimental Results . . . . .	62
4.5	Summary and Conclusion . . . . .	65
<b>5</b>	<b>Trapped Antiprotons exposed to Laser Light</b>	<b>67</b>
5.1	Introduction . . . . .	67
5.2	The Titanium:Sapphire Laser System . . . . .	67
5.3	Laser Electrodes . . . . .	71
5.4	Experiments on Trapped Antiprotons . . . . .	73
5.4.1	Introduction . . . . .	73
5.4.2	Experimental Setup . . . . .	74
5.4.3	Experimental Results . . . . .	74
5.5	Summary and Conclusion . . . . .	76
<b>6</b>	<b>Antihydrogen via a Two–Stage Rydberg Charge–Exchange Process</b>	<b>77</b>
6.1	Introduction . . . . .	77

6.2	Theoretical Overview . . . . .	80
6.2.1	The Excitation Scheme . . . . .	80
6.2.2	The Two-Stage Charge-Exchange Process . . . . .	86
6.3	The Experimental Setup . . . . .	89
6.3.1	The Penning Trap Apparatus . . . . .	89
6.3.2	Lasers . . . . .	92
6.4	The Experiments . . . . .	93
6.4.1	Excitation from the $6S_{1/2}$ Ground State to the $6P_{3/2}$ State . . . . .	94
6.4.2	Excitation from the $6P_{3/2}$ State to a Rydberg State . . . . .	106
6.4.3	The Production of Antihydrogen . . . . .	110
6.5	Summary and Conclusion of this Chapter . . . . .	114
<b>7</b>	<b>Towards a Temperature Measurement of the Antihydrogen Atoms Produced in the Two-Step Charge-Exchange Process</b>	<b>117</b>
7.1	Introduction . . . . .	117
7.2	Numerical Analysis . . . . .	118
7.2.1	Description of the Algorithm . . . . .	118
7.2.2	Numerical Results . . . . .	122
7.3	Experimental Setup . . . . .	125
7.3.1	The Laser System and the Data Acquisition . . . . .	125
7.3.2	Experimental Setup in the Penning Trap Apparatus . . . . .	126
7.4	Experimental Results . . . . .	127
7.5	Summary and Conclusion . . . . .	130
<b>8</b>	<b>Outlook</b>	<b>131</b>
<b>A</b>	<b>Author's List of Publications</b>	<b>133</b>
	<b>Bibliography</b>	<b>135</b>
	<b>Acknowledgements</b>	<b>148</b>



# Chapter 1

## Introduction

Antimatter has fascinated scientists and non-scientists since its existence was predicted by Dirac [Dir28] in 1928. This prediction and the discoveries of the positron ( $e^+$ ) by Anderson [And32] and of the antiproton ( $\bar{p}$ ) by Chamberlain, Segrè, Wiegand, and Ypsilantis [CSWY55] were one of the greatest successes of relativistic quantum theory and of 20th century physics. A new milestone in the field of antimatter physics was achieved in 1995, when the first eleven anti-atoms in form of antihydrogen ( $\bar{H}$ ), the bound state of an antiproton and a positron, were produced at CERN's Low Energy Antiproton Ring (LEAR) shortly before its de-commissioning [BBB<sup>+</sup>96]. In a similar experiment carried out at Fermilab in 1998, 57 antihydrogen atoms were detected [BCG<sup>+</sup>98]. A few experiments to investigate the produced antihydrogen atoms have been proposed and put forward. For an overview, see [EH99] and references therein. However, because of the low numbers of produced antihydrogen atoms and because these atoms are at a velocity of about 90% of the speed of light, they are not suited for any further high precision measurements.

In contrast, the progress made in trapping of antiprotons and positrons (for an overview see for example [Gab01]) and in trapping and cooling of hydrogen atoms [HKD<sup>+</sup>87, vRBJW88, MDS<sup>+</sup>88, DSY<sup>+</sup>91, LWS<sup>+</sup>93, SWL<sup>+</sup>93], as well as in the theory of production mechanisms [GO91, Fed97, NPWW83, HCJD87, Cha90, HHC98] made it possible to consider the production of cold antihydrogen atoms that can be confined in a neutral particle trap. Furthermore, the high precision achieved in laser spectroscopy of cold hydrogen atoms [NHR<sup>+</sup>00, CFK<sup>+</sup>96] suggests that such techniques could be applied to antihydrogen to precisely investigate antimatter and to yield new tests for such fundamental theorems as the CPT-theorem and the weak equivalence principle (WEP).

The CPT-theorem was developed by Lüders [Lüd57], Pauli [Pau55], Bell [Bel55], and Jost [Jos65]. CPT means **C**harge conjugation, **P**arity conjugation, and **T**ime reversal. After P-violation has been found in the  $\beta$ -decay of polarized nuclei by Wu et al. [WAH<sup>+</sup>57] in 1957 and CP-violation has been found in the decay of K-mesons by Christenson et al. [CCFT64] in 1964, the CPT transformation is considered to be a

fundamental invariant of nature. However, the CPT–theorem is not on such unshakeable grounds as, for instance, conservation of energy. Todorov et al. [OT68, ST68] have shown that the CPT theorem can be violated when non–finite representations of the Lorentz group are allowed. Wald [Wal80] pointed out that the curved space–time required by gravitation could provide an obstacle to the proof of CPT, which required flat space–time. Additionally, John Bell developed a model field theory in which CPT–violation occurred through non–locality. Yet another reason to test the CPT–theorem is that it provides a link between the experimentally observed CP–violation, and the as yet unobserved T–violation [Kab70]. Moreover, more fundamental theories, such as string theory, may include spontaneous breaking of the CPT–symmetry [BKR99].

The CPT–theorem requires that particles and their anti-particles have equal masses and lifetimes, and equal and opposite electric charges and magnetic moments. It also predicts equal atomic structure and spectra for matter and antimatter atomic systems. In general, a test of the CPT–theorem would be based on a comparison between a quantity measured with high precision on a particle and on the corresponding antiparticle. A detailed overview of experimental tests of the CPT–theorem carried out in various systems can be found in [PDG00]. The charge to mass ratio of an antiproton and a proton has been measured to 90 ppt [GKH<sup>+</sup>99]. This result was combined with spectroscopic studies of antiprotonic helium atoms to establish a limit of 5 parts in  $10^7$  for a difference in the inertial masses of protons and antiprotons [YMH<sup>+</sup>02]. The equality of the positron and electron magnetic moment was established with an accuracy of  $10^{-12}$  [DSD87], and the difference between the Kaon and Anti–kaon mass was measured with a relative accuracy of  $5 \times 10^{-18}$  [CCC<sup>+</sup>90, GBB<sup>+</sup>93].

A very stringent test of the CPT–theorem on antihydrogen would be based on a measurement of the absolute frequency of the transition from the 1S ground state to the metastable 2S state with a similar precision which has already been achieved for hydrogen [BKR99]. The absolute frequency of the transition from the 1S ground state to the metastable 2S state has already been measured in a cold atomic hydrogen beam by Niering et al. [NHR<sup>+</sup>00] with an accuracy of 1.8 parts in  $10^{14}$  and by Cesar et al. [CFK<sup>+</sup>96] in a trapped hydrogen cloud with an accuracy of  $1.7 \times 10^{-12}$ . The 1.3 Hz natural linewidth of this transition could yield an ultimate precision to  $10^{-15}$  to  $10^{-18}$  [MH88]. Another test of the CPT–theorem would rely upon a high–precision measurement of the anti–hydrogen ground state hyperfine splitting [WEH<sup>+</sup>03], since the hyperfine splitting of the hydrogen ground states has also been measured with high precision. For a detailed overview of these experiments, see [Ram90].

The CPT–theorem predicts the equality of the inertial masses of matter and antimatter. It therefore only predicts how antimatter falls in the gravitational field of an anti–earth, that is in the same way as matter falls in the gravitational field of the earth. The WEP is the cornerstone of the General Theory of Relativity and it claims the equality of gravitational and inertial mass. The gravitational accelerations of a variety of composite objects of ordinary matter have been shown to be equal with a precision of one part in  $10^{12}$  in the Eötvös–Dicke experiments [Wil81]. Arguments against a

difference in gravitational acceleration of matter and antimatter have been summarized and discussed by Nieto and Goldman [NG91] but no quantitative measurement of the gravitational acceleration has been carried out so far. An experiment to measure the gravitational acceleration of antiprotons has been proposed and put forward. The experiment was affected by difficulties of shielding the charged antiprotons against electromagnetic fields and stopped due to the shutdown of LEAR without results on antimatter gravity [GN82, DROM92]. Antihydrogen since it is stable and neutral is much better suited for an antigravity experiment and it would allow direct tests of the gravitational acceleration of antimatter in the gravitational field of the earth without any problems associated with electromagnetic interactions [WFH<sup>+</sup>03, WH04].

CERN commissioned the Antiproton Decelerator (AD) in 1998 [BEM04]. The ATRAP Collaboration<sup>1</sup> [ATR97] started at the AD in the year 2000 with the ultimate goal to test the CPT-theorem by a high-precision measurement of the 1S–2S transition frequency in antihydrogen. In order to arrive at that challenging goal, it was then planned to produce cold antihydrogen atoms, preferentially in the ground state, in a Penning trap from trapped antiproton and positron plasmas in a first step and in a second step to confine the cold antihydrogen in an Ioffe trap [Pri83].

The simplest way to load antihydrogen into an Ioffe trap would be to synthesize it from its constituents and thus to superpose the Ioffe trap to the Penning trap. A consequence of the cylinder symmetry of Penning traps is the confinement theorem [O’N80] which prevents the radial diffusion of charged particles from a Penning trap. The magnetic gradient of the Ioffe trap destroys the cylinder symmetry of the Penning trap and therefore violates the confinement theorem. Despite this, such a combined Ioffe–Penning trap was predicted to be able to confine antiprotons and positrons, at least in the low particle limit [SYG01]. Such a combined Penning–Ioffe trap is currently (Dec. 2004) under construction at the ATRAP Collaboration so that probably the first attempts to trap antihydrogen atoms will take place in the year 2006<sup>2</sup>. Technically realizable Ioffe traps tend to have a trap depth of less than 1 K [Wal93], which quantifies the word “cold antihydrogen” to antihydrogen atoms at a temperature below 1 K.

In a third step, the ATRAP Collaborations plans then to work towards a high precision measurement of the 1S–2S transition. The inhomogeneous magnetic field of the Ioffe trap broadens and shifts the antihydrogen spectral lines [HZ93]. It will therefore be necessary to cool the trapped antihydrogen as much as possible in order to reduce the spatial extent of the trapped antihydrogen cloud. Antihydrogen can be laser-cooled with Lyman- $\alpha$  laser light at 121.6 nm to the recoil limit which corresponds to a temperature of about 1 mK [MvdS99]. Laser cooling of trapped hydrogen has already been demonstrated with a pulsed Lyman- $\alpha$  source [SWL<sup>+</sup>93]. Cooling should be even more efficient with a CW–Lyman- $\alpha$  source. This source is available since 1999 [EJW99] but laser cooling of hydrogen has not yet been demonstrated with it.

---

<sup>1</sup>A list of the current and former members of the ATRAP Collaboration is given along with their home institutes in Tab. 1.1 at the end of this chapter.

<sup>2</sup>The AD shut down in Nov. 2004 and will probably not deliver antiprotons before May 2006.

For a measurement of the 1S-2S two-photon transition the approaches used in the hydrogen measurements can probably not be applied because they were carried out with a large number of atoms ( $10^{15} - 10^{17}$  atoms per second in a beam [NHR<sup>+00</sup>],  $10^{10} - 10^{13}$  atoms in a trap [CFK<sup>+96</sup>, CK99]). For the case of antihydrogen the available number of trapped antihydrogen atoms will probably not exceed a few thousands. A shelving scheme has been proposed for spectroscopy on antihydrogen where in principle one trapped antihydrogen atom would be sufficient [HZ93]. This scheme suggests to excite and observe resonance fluorescence on the Lyman- $\alpha$  transition, while the incident Lyman- $\alpha$  laser light could simultaneously laser cool the trapped atoms. A 1S-2S two-photon transition induced with the 243 nm radiation would “shelve” the positron in the 2S state and disrupt the fluorescence radiation for the lifetime of the metastable 2S state. A serious problem of this scheme might arise from photoionization of the excited  $n = 2$  antihydrogen atoms by the VUV laser light. It is thus still an open question if the suggested scheme can be employed on trapped antihydrogen atoms.

In the year 2002, the ATRAP Collaboration could announce the detection of antihydrogen [GBO<sup>+02a</sup>, GBO<sup>+02b</sup>] during positron cooling of antiprotons [GET<sup>+01</sup>] in a nested Penning trap [GRHK88] only a few weeks after the competing ATHENA Collaboration [ATH96, AAB<sup>+02</sup>]. In order to clarify if the first step, namely the production of cold and trapable antihydrogen has been realized, we focused subsequently on the investigation of the production mechanism and have been able to measure the state distribution [GBO<sup>+02b</sup>, GSS<sup>+05</sup>] and the velocity of antihydrogen atoms [GBO<sup>+02b</sup>]. These measurements reveal that the antihydrogen atoms are formed in highly excited states and at a velocity too high to be trapped. In 2003, the ATRAP Collaboration demonstrated the production of antihydrogen by an alternative production method [SSS<sup>+04</sup>] based on a Rydberg charge-exchange process [HHC98]. The antihydrogen atoms produced by this method are expected to have a temperature of about 4.2 K. About 4% of the atoms, the ones at the lower end of the Maxwell-Boltzmann distribution, have then kinetic energies which corresponds to temperatures below 1 K. These atoms should then be trapable in a 1 K deep trap.

This thesis grew out of my participation in the ATRAP experiments from September 2001 to November 2004. It reports on the progress made towards the realization of the first major step, namely the production and investigation of cold antihydrogen atoms and additionally on first laser experiments on trapped antiprotons. Most of the work presented here is the result of the efforts of many people. As a PhD student coming from the Max-Planck-Institute of Quantum Optics, I was mainly responsible for the construction and the maintenance of the various laser systems used so far at the ATRAP experiment. Additionally, with the “post-doc” Cody Storry and the PhD student Daniel Comeau, I was building the so called hbar2 Penning trap apparatus. Hbar2 is the second Penning trap next to hbar1 and both traps will be described in detail in section 2.4.2. Hbar2 is the apparatus in which all experiments with lasers are carried out. Last but not least, I became responsible for the vacuum system of the lower beam pipe through which the antiprotons pass before they enter the Penning traps.

## Overview of the Thesis

- Chapter 2 gives a general overview of the experimental setup of the ATRAP experiment.
- Chapter 3 describes how antiprotons are loaded from the AD and how positrons are loaded from the radioactive source into the Penning trap apparatus.
- Chapter 4 presents the experiments which lead to the production of antihydrogen atoms by merging antiprotons and positrons in so called nested Penning traps. It additionally describes the experiments by which the state distribution and the velocity of the atoms have been measured.
- Chapter 5 describes a Titanium:Sapphire laser system and the so called laser electrodes which were designed in order to guide laser light from the Titanium:Sapphire laser into the inside of the electrode stack. Trapped antiprotons have been exposed to laser light in order to investigate if laser light induces antiproton losses.
- Chapter 6 describes the experiments by which antihydrogen atoms could be produced by an alternative production scheme, namely via a two-step Rydberg charge-exchange mechanism.
- Chapter 7 presents an experiment by which an attempt has been made to determine the velocity of the antihydrogen atoms produced via a two-step charge-exchange mechanism as presented in chapter 6.
- An outlook is given in Chapter 8.

**Harvard University, Cambridge Massachusetts, USA:**

Gerald Gabrielse, Nathaniel Bowden, John Estrada, David Le Sage, Paul Oxley, Cody Storry, Andrew Speck, Joseph Tan, Melissa Wessels, and Peter Yesley

**IKP, Forschungszentrum Jülich, Germany:**

Walter Oelert, Frank Goldenbaum, Dieter Grzonka, Georg Schepers, and Thomas Sefzick

**Max–Planck–Institut für Quantenoptik, Garching, Germany:**

Theodor W. Hänsch, Peter Fendel, Birgit Henrich, Maximilian Herrmann, Anette Pahl, Heiko Pittner, and Jochen Walz

**Vrije Universiteit, Amsterdam, NL:**

Kjeld S. E. Eikema

**York University:**

Eric Hessels and Daniel Comeau

**Early contributions came from:**

**Institute for Medium Energy Physics, Vienna, Austria:**

W. Breunlich, M. Cargnelli, H. Fuhrmann, R. King, R. Ursin, and J. Zmeskal

**Institut für Strahlen- und Kernphysik, University of Bonn, Bonn, Germany:**

H. Kalinowsky

**FOM Institute for Atomic and Molecular Physics, Amsterdam, NL:**

C. Wesdorp

Table 1.1: List of former and present members of the ATRAP Collaboration along with their home institutes.

# Chapter 2

## The ATRAP Experiment

This chapter gives a brief description of the ATRAP experiment: A general overview is given in section 2.1 followed by descriptions of the antiproton decelerator (AD) in section 2.2 and the positrons source in section 2.3. The basic theory of Penning traps is described in section 2.4.1 and the basic properties of the actual Penning trap apparatuses used at the ATRAP experiment are summarized in section 2.4.2. The non-destructive particle counting techniques are given in section 2.5.1 followed by an overview of the ATRAP fiber (section 2.5.2.1) and scintillator paddle detectors (section 2.5.2.2).

### 2.1 Overview

ATRAP is one of four experiments located inside the Antiproton Decelerator (AD) at CERN. The three other experiments are ATHENA [ATH96], ASACUSA [ASA97] and pbar medical (ACE) [MH03]. A drawing of the AD-ring along with the location of the four experiments is depicted in Fig. 2.1. As indicated, the ATRAP experiment is located on a platform three meters above the ground of the AD hall. The ATRAP experiment has two experimental zones, however only zone I is in usage up to now. The zone is well shielded by concrete walls to provide sufficient radiation protection, and it is not accessible when an experiment is carried out. The electronic devices used to steer and control the experiment are installed in the left Faraday cage, whereas all the laser and optical equipment are housed in the laser cabin.

A side view of zone I is given in Fig. 2.2. Central to the experimental zone is the superconducting magnet which houses the Penning trap apparatus and provides a homogeneous magnetic field of about 5.3 T inside its bore at the location of the actual Penning trap electrodes. This magnet houses the fiber detector, and the BGO detector and in addition, outer scintillator paddles are mounted to its outside as shown in Fig. 2.2.

The figure also indicates that antiprotons delivered by the AD pass several bending magnets and enter the zone from below in a vertical direction. A **P**arallel **P**late **A**valanche **C**ounter (PPAC) and an energy tuning cell are situated in the antiproton beam line in front of the actual Penning trap which allow to control and steer and energy tune the antiproton beam. This will be described further in sections 3.3.1 and 3.3.2.

## 2.2 The Antiproton Decelerator (AD)

In this section, a brief overview of the AD is presented. More details can be found in [EH99, BEM04]. The AD is the successor of CERN’s **L**ow **E**nergy **A**ntiproton **R**ing (LEAR) and is currently the only low-energy antiproton source worldwide. Commissioning of the AD started in Fall 1998 and the experiments started taking antiproton beam in July 2000. Since then, it has delivered antiprotons to the four experiments non-stop from Mondays to Fridays in the period from the end of May until the beginning of November. The ATHENA, ATRAP, ASACUSA Collaborations share the beam in eight hour shifts, while pbar medical has taken a few days of beam during the 2003 and 2004 beam run.

The AD is a synchrotron operating in the reversed mode. It delivers 80 ns long bunches of about  $3 \times 10^7$  antiprotons with an energy of 5.3 MeV every 86 s [BEM04]. For the production of antiprotons, a proton beam with a momentum of 26 GeV/c and an intensity of  $10^{13} \text{ s}^{-1}$  delivered from CERN’s proton synchrotron (PS) is extracted onto an iridium target located underground just outside the AD hall from which antiprotons at a momentum of 3.5 GeV/c are separated. These antiprotons are injected into the AD via the beam line as depicted in Fig. 2.1. Stochastic cooling [MPTvdM80] is used to reduce the spatial emittance and the momentum spread of the bunches at the 3.5 GeV/c stage. The bunches are then decelerated to 2 GeV/c, where stochastic cooling is employed again. Electron cooling [EH99] is used after subsequent deceleration steps to 300 MeV/c and 100 MeV/c, which corresponds to an energy of 5.3 MeV.

## 2.3 The Positron Source

The radioactive isotope which we use as a source of positrons is  $^{22}\text{Na}$ . This isotope has a half life of 2.6 years and 90 % of all decays produce positrons. The positrons are emitted with an energy ranging from zero to 546 keV. In August 2002, the source had an activity of 70 mCi [Bow]. The actual radioactive source is contained inside a tungsten capsule mounted on the bottom of a rod which is 19 cm long and 1.54 cm in diameter. The rod is made out of Elkonite (90 % tungsten, 10 % copper) that absorbs radiation. Due to the strength of the source, it must be stored in the so called block house, a lead enclosure that is located above the Penning trap as depicted in Fig. 2.2. The rod is fixed

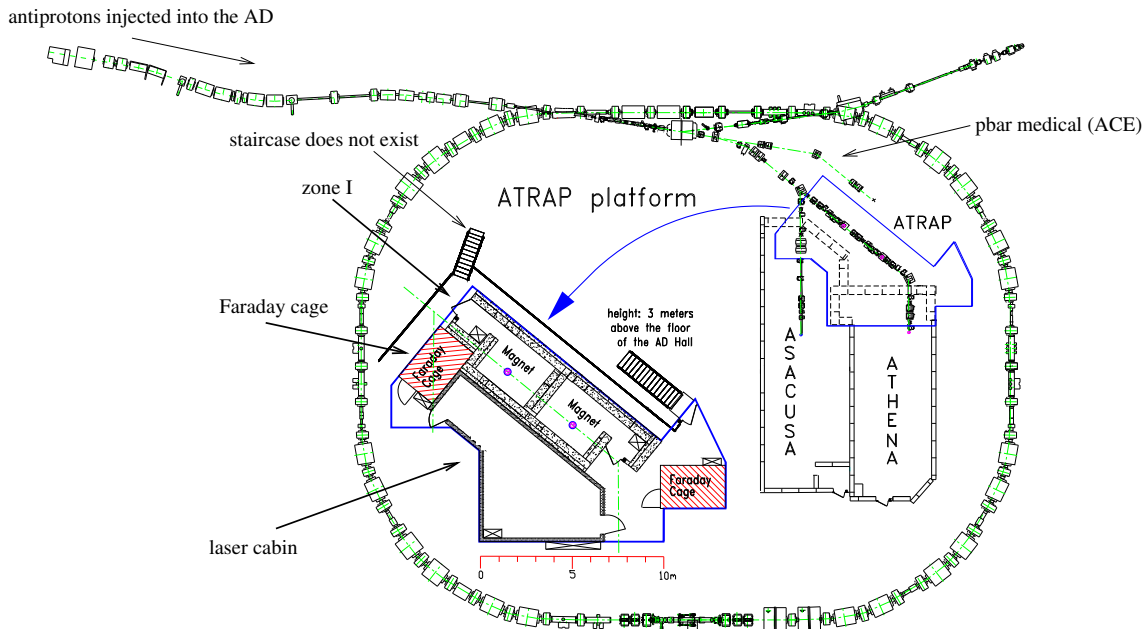


Figure 2.1: The AD ring is depicted along with the locations of the ATHENA, pbar medical, ASACUSA, and ATRAP experiment. The ATRAP experiment is located on a platform three meters above the floor of the AD hall. ATRAP has two experimental zones, however only zone I is used up to now. The Faraday cage houses all the electronic devices required for the steering and control of the experiments. All lasers and other optical equipment are placed inside the laser cabin from which an optical path to zone I exists. The laser cabin is also a Faraday cage. The antiprotons enter the AD ring via the left beam line with a momentum of  $3.5 \text{ GeV}/c$  and after completion of several deceleration stages about  $3 \times 10^7$  antiprotons are delivered in a 80 ns long bunch every 86 s to the experiments with a momentum of  $100 \text{ MeV}/c$ , corresponding to an energy of  $5.3 \text{ MeV}$ .

by a polypropylene line and can be lowered down remotely into the superconducting solenoid so that the positron emitter sits directly in front of the Penning trap.

## 2.4 The Penning Trap

Penning traps are devices for trapping charged particles. They have been invented by Hans Dehmelt and have found many applications in various fields of physics, for example for high precision measurements of the charge to mass ratio of charged particles [GKH<sup>+</sup>99] or in plasma physics [BW84, KD01, DAD<sup>+</sup>01, HAD00]. They are also used by the ATRAP Collaboration for the confinement of antiprotons and positrons and will therefore be described in the following. In section 2.4.1 an overview of the general properties of Penning traps is given whereas in section 2.4.2, the Penning traps used by the ATRAP Collaboration are described.

### 2.4.1 Penning Trap Theory

In this section, a brief summary of the most relevant properties of Penning traps is presented. A thorough review of Penning trap theory can be found in [BG86].

In a theoretical treatment, usually the case of an ideal Penning trap is discussed. For an ideal Penning trap, the field configuration consists of a static electric field  $\mathbf{E} = -\nabla V$  which is derived from a quadrupole potential of the form

$$V = V_0 \frac{z^2 - \frac{\rho^2}{2}}{2d^2}, \quad (2.1)$$

where  $V_0$  is an electric potential,  $d$  is a characteristic dimension of the trap,  $z$  is the axial coordinate, and  $\rho = \sqrt{x^2 + y^2}$  is the radial coordinate perpendicular to  $z$ . The electric potential is superimposed to a static homogeneous magnetic field  $\mathbf{B}$  given by

$$\mathbf{B} = B_0 \hat{\mathbf{z}}, \quad (2.2)$$

where  $B_0$  is the magnitude and  $\hat{\mathbf{z}}$  is the unit vector along the  $z$ -axis.

A way to generate the quadrupole potential given in Eq. 2.1 is by placing (ideal) electrodes along equipotentials of  $V$ . Three electrodes are required as shown in Fig. 2.3a. Two endcap electrodes along the two branches of the hyperboles of revolution  $z^2 = z_0^2 + \rho^2$  and one ring electrode along the hyperbola of revolution  $z^2 = (\rho^2 - \rho_0^2)/2$ . The constants  $z_0$  and  $\rho_0$  are the minimal axial and radial distances to the electrodes and  $d$  is given by  $d^2 = (z_0^2 + \rho_0^2)/2$  so that  $V_0$  is the potential difference between the endcap and the ring electrode. Another way to produce the quadrupole potential given in Eq. 2.1 is the so-called open-access [GHR89] or Malmberg–Penning trap [Dub99], a trap configuration which is also employed by ATRAP. This type of trap consists as depicted

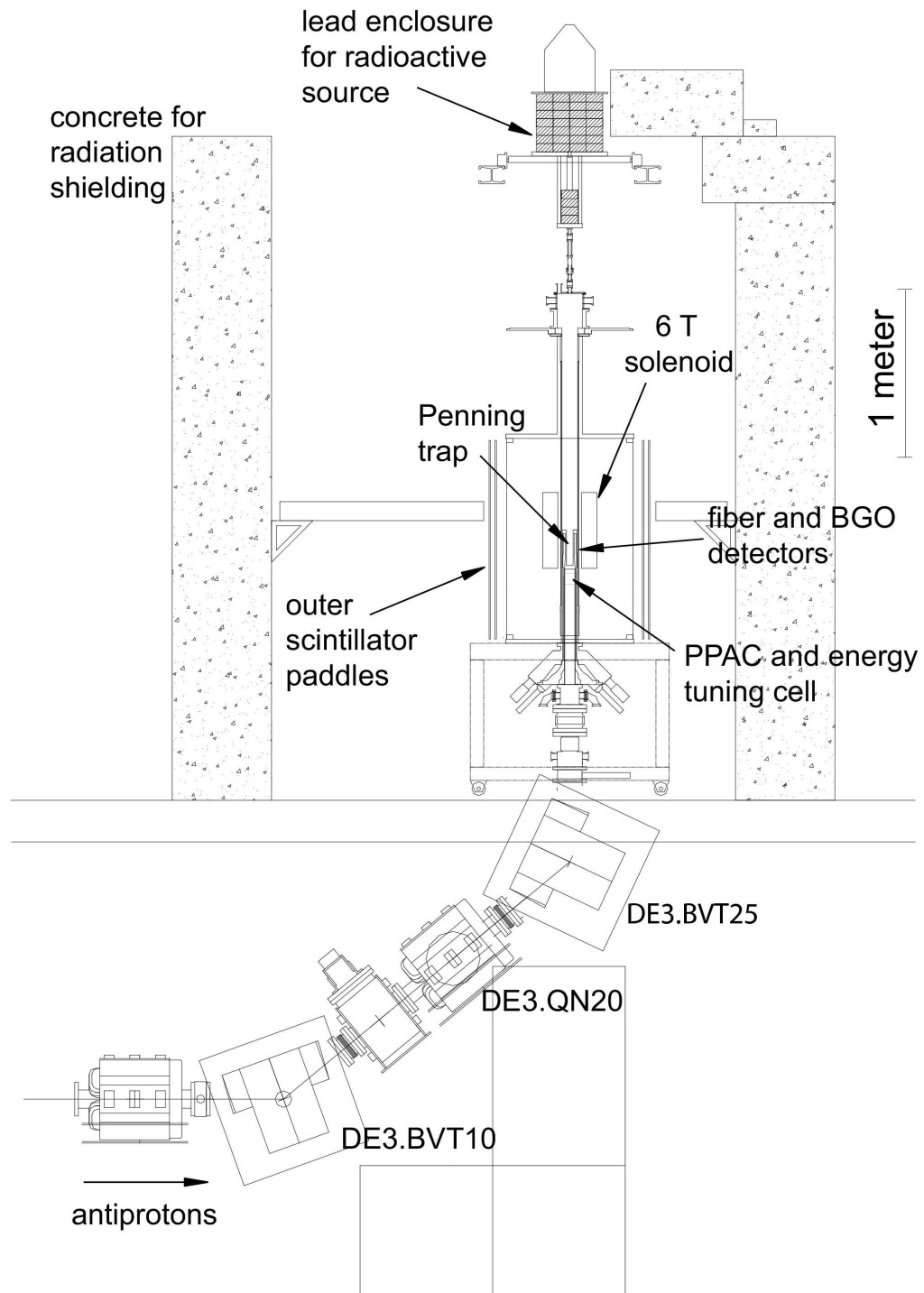


Figure 2.2: This graphic shows a side view of zone I.

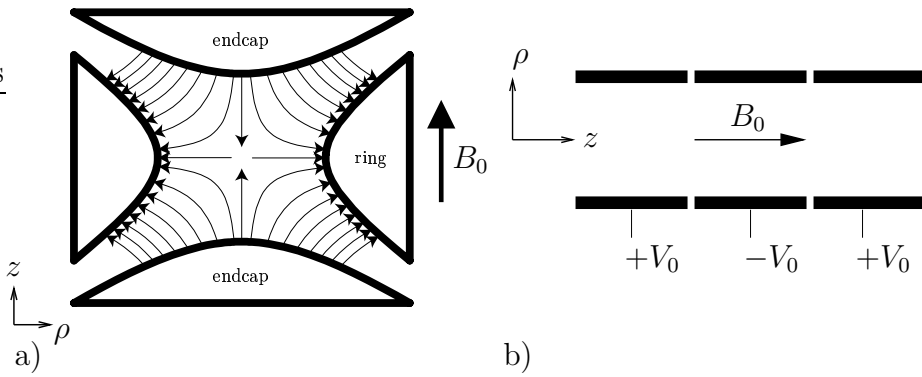


Figure 2.3: Two configurations of the Penning trap electrodes are depicted. In part a), the electrodes are hyperboles of revolution. In part b), the electrodes consist of cylindrical rings.

schematically in Fig. 2.3 of cylindrical electrodes with a symmetry axis which is aligned along the direction of the magnetic field. In order to obtain a quadrupole potential inside the electrodes, the geometry and the potentials applied to the individual electrodes have to be chosen carefully and a concrete example will be given in the next section. A detailed theoretical treatment how to design the electrodes and the potentials can be found in [Est02, Yes01].

The motion of a particle of charge  $e$  and mass  $m$  in the electric and magnetic field of an ideal Penning trap is described by [Jac98]

$$m\ddot{\mathbf{x}} = -e\nabla V + e\dot{\mathbf{x}} \times \mathbf{B}. \quad (2.3)$$

which yields for  $\mathbf{x} = (x, y, z)$  and  $\mathbf{B} = (0, 0, B_0)$  the following set of differential equations

$$\ddot{x} = \frac{eV_0}{2md^2}x + \omega_c \dot{y} \quad (2.4)$$

$$\ddot{y} = \frac{eV_0}{2md^2}y - \omega_c \dot{x} \quad (2.5)$$

$$\ddot{z} = -\frac{eV_0}{md^2}z. \quad (2.6)$$

Here,  $\omega_c = \frac{eB_0}{m}$  has been employed.  $\omega_c$  is the cyclotron frequency of a charged particle orbiting in a circular orbit in the plane perpendicular to the magnetic field.

As can be seen from Eq. 2.4–Eq. 2.6, the motion along the  $z$ -axis decouples from the motion in the  $xy$ -plane. The motion along the  $z$ -axis is according to Eq. 2.6 independent of the magnetic field and is a harmonic motion with an axial angular frequency given by [BG86]

$$\omega_z = \sqrt{\frac{eV_0}{md^2}}. \quad (2.7)$$

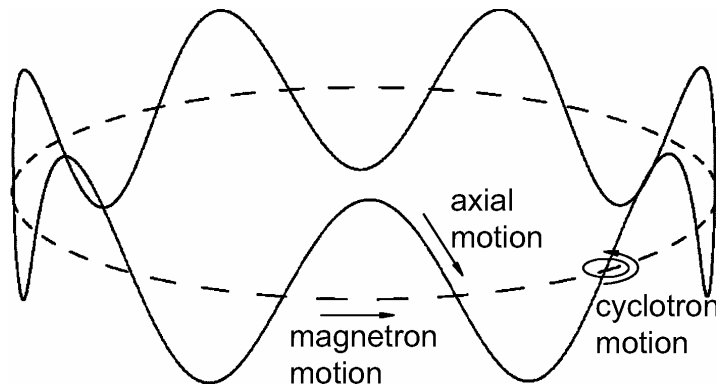


Figure 2.4: The orbit of a charged particle in a Penning trap. The motion is a superposition of the axial motion, the cyclotron motion, and the magnetron motion.

Confinement of a charged particles requires therefore  $eV_0 > 0$  and thus a quadrupole potential which is confining for protons and positrons is anti-confining for antiprotons and electrons.

The two coupled differential equations given in Eq. 2.4 and in Eq. 2.5 can be solved with the Ansatz  $x + iy = a \exp(i\omega_+ t) + b \exp i(\omega_- t)$  yielding the modified cyclotron frequency [BG86]

$$\omega_+ = \frac{1}{2} \left( \omega_c + \sqrt{\omega_c^2 - 2\omega_z^2} \right), \quad (2.8)$$

and the magnetron frequency [BG86]

$$\omega_- = \frac{1}{2} \left( \omega_c - \sqrt{\omega_c^2 - 2\omega_z^2} \right). \quad (2.9)$$

For  $\omega_\pm$  to be real,  $\omega_c \geq \sqrt{2}\omega_z$  has to hold. Under the usual operating conditions [BG86],  $\omega_c \gg \omega_z$  and thus

$$\omega_c \approx \omega_+ \gg \omega_z \gg \omega_-. \quad (2.10)$$

The motion in the xy-plane can be understood as a superposition of the fast cyclotron motion and a slow  $\mathbf{E} \times \mathbf{B}$  drift (magnetron) motion caused by the crossed electric and magnetic fields. Superposed to the motion in the xy-plane is the axial motion. The three particle motions are illustrated in Fig. 2.4. Typical frequencies are given in Tab. 2.1. All motions are well separated in frequency, and both the cyclotron and axial frequencies are because of the different masses quite different for electrons/positrons and protons/antiprotons.

The presented results are only strictly valid for the case of an ideal Penning trap, that is for the case of an electric potential of the form given by Eq. 2.1. It has however to be pointed out that the confining potential needs not to be strictly a quadrupole potential.

frequency	electrons/positrons	protons/antiprotons
$\omega_+$	$2\pi \times 150 \text{ GHz}$	$2\pi \times 82 \text{ MHz}$
$\omega_z$	$2\pi \times 30 \text{ MHz}$	$2\pi \times 1.6 \text{ MHz}$
$\omega_-$	$2\pi \times 3 \text{ kHz}$	$2\pi \times 15.4 \text{ kHz}$

Table 2.1: Typical frequencies of an electron or proton in a Penning trap with  $B = 5.3 \text{ T}$  and  $V_0 = 15 \text{ V}$ .

A potential well which provides an axially restoring force is sufficient for confinement of particles. In practice, we usually verify experimentally, if a chosen potential structure yields to a stable confinement of particles.

The difference in the cyclotron frequency between protons/antiprotons and electrons/positrons is of particular interest. The electric and magnetic fields cause an acceleration and as a response the charge radiates electromagnetic waves so that the motion of the charged particle is damped. The power radiated is proportional to the square of the frequency [Jac98]. The frequencies of all proton/antiproton motions are in the radio frequency range, therefore radiative damping is negligible. This is also the case for the axial and the magnetron motion of an electron or positron. However radiative decay is the dominant decay mechanism for the electron or positron cyclotron motion and the cyclotron damping constant is given by

$$\gamma_c = \frac{\epsilon_0^{1/2} \mu_0^{3/2} e^2 \omega_c^2}{3\pi m}. \quad (2.11)$$

The equation has been taken from [BG86] and converted to the SI-system.  $\epsilon_0$  denotes the permittivity of the vacuum and  $\mu_0$  denotes the permeability of the vacuum.  $\gamma_c$  is about  $0.3 \text{ s}^{-1}$  for an electron or positron at a cyclotron frequency of  $\omega_c/2\pi = 150 \text{ GHz}$ . Since the electrodes are cooled to liquid helium temperature, electrons and positrons inside the trap thermalize by radiative decay of the cyclotron motion to the environment. Due to trap imperfections caused for example by a non-quadrupole electric potential the cyclotron motion also couples to the other motions. Therefore, the radiative decay of the cyclotron motion provides an effective cooling mechanism that keeps the electrons and positrons at an average energy of about  $4.2 \text{ K}$ . This property is especially important for loading antiprotons from the AD into the Penning trap as described in section 3.3 and in [GBO<sup>+</sup>02c] and also for positron cooling of antiprotons which is described in [GET<sup>+</sup>01].

## 2.4.2 The Penning Traps at ATRAP

At ATRAP, two similar Penning trap apparatuses referred to as hbar1 and hbar2 are currently in operation. Hbar1 is in operation since summer 2000 and hbar2 was assembled during spring 2002 and it is in operation since September 2002. In this section,

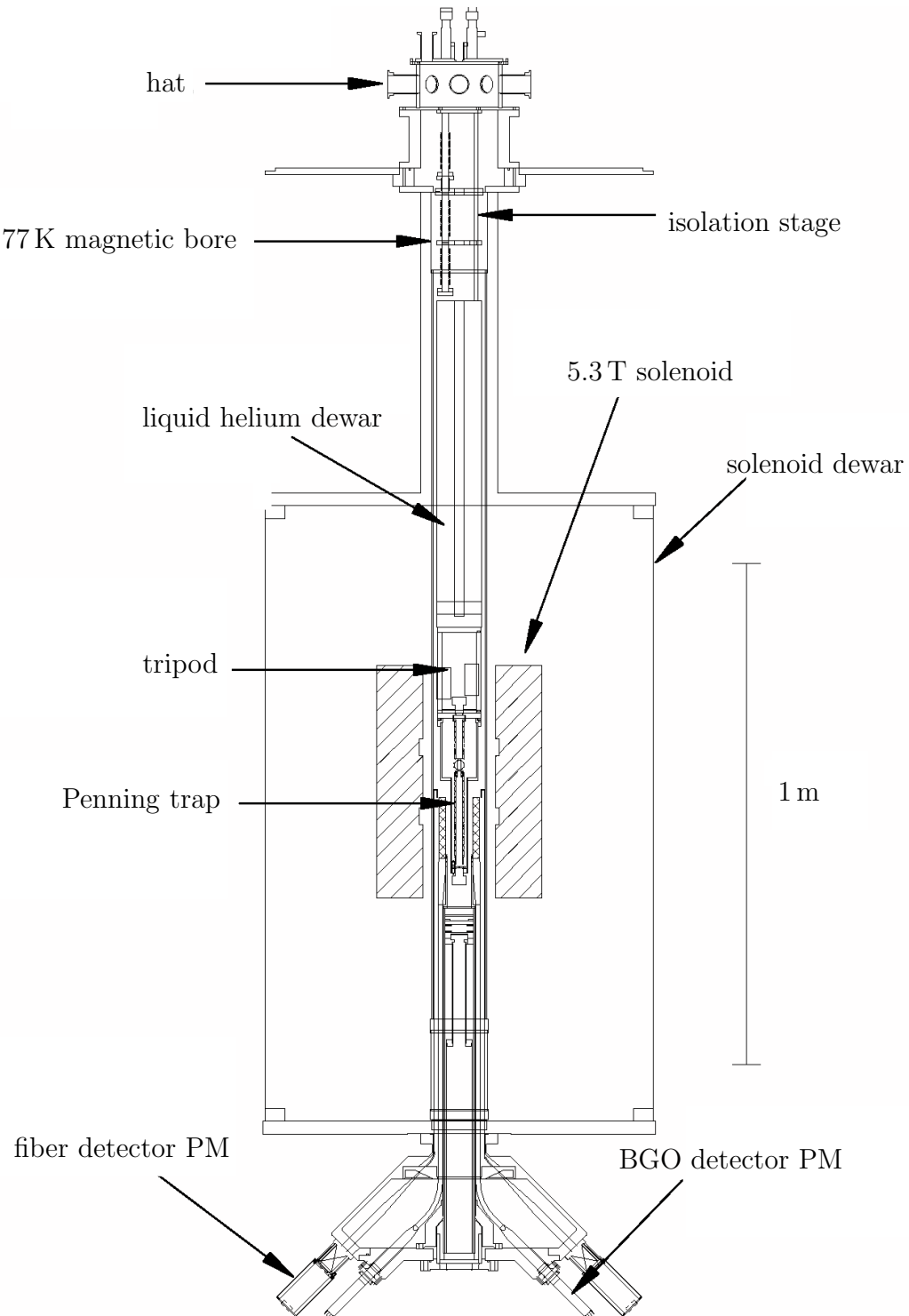


Figure 2.5: Side view of the cryogenic Penning trap apparatus sitting in the superconduction solenoid. The apparatus is lowered into and pulled out of the bore from above. The fiber detector and the BGO detector are inserted from below and the photo multipliers (PM) are attached to the detectors at the outside.

both Penning trap apparatuses will be described briefly. Other, more detailed descriptions of the hbar1 apparatus can be found in [Yes01, Est02, Oxl03]. Both devices are very similar in the design, except some extra features have been implemented in hbar2. It has been built not only as a replacement of hbar1 but also in order to carry out initial laser experiments on antiprotons and antihydrogen which are described in detail in section 5 and in order to produce and investigate antihydrogen from a two-step charge-exchange process as described in chapters 6 and 7.

A sectional view of the Penning trap apparatus as it resides in the 10 cm bore of the superconducting solenoid which provides a homogeneous magnetic field of about 5.3 T is depicted in Fig. 2.5. The very top part of the Penning trap apparatus is referred to as the hat. It is a stainless steel structure with a pump port by which the magnetic bore can be evacuated and which contains more than 100 room temperature vacuum feedthroughs for the electronic lines used to control the Penning trap. The components below are mounted to the hat so that the whole Penning trap apparatus can be lowered into and pulled out of the magnet's bore from above. Once installed in the bore, the hat resides on the top plate of the solenoid and an o-ring seal between the hat and the top plate isolates the magnetic bore from the surrounding. The magnetic bore is evacuated to a pressure of less than  $10^{-6}$  bar via a pump port at the hat.

The four liter liquid helium dewar is made out of OFHC-copper and is mounted to the hat from below via a G-10 support structure, which is called isolation stage. This structure provides a good thermal isolation between the dewar and the hat because the thermal conductivity of G-10 is very low. Due to this low thermal conductivity, the low pressure in the bore and because the wall of the bore resides at 77 K, the dewar and the parts below are thermally well shielded. The liquid helium dewar is thermally well connected by a 13 cm long three-legged structure made out of OFHC-copper called tripod to the pinbase, which is also machined out of OFHC-copper.

As depicted in Fig. 2.6, the pinbase and the adjacent titanium trap can form a separate vacuum container which houses the actual Penning trap electrodes. The pinbase contains cryogenic electric feedthroughs which are connected by constantan wires with the feedthroughs at the hat. On the opposite side, each feedthrough is connected via gold plated copper straps to an electrode. Before installing the apparatus into the magnet's bore, this vacuum container is evacuated to a pressure of about  $10^{-6}$  mbar and then hermetically sealed by a pinch-off. Once installed and cooled by the liquid helium reservoir to 4.2 K, cryopumping takes place and the vacuum inside the trap can drops below  $5 \times 10^{-17}$  torr. This pressure has been derived from a measurement of the lifetime of trapped antiprotons ( $> 3.2$  months) in a similar Penning trap apparatus [GFO<sup>+</sup>90]. The antiprotons enter the trapping region by a  $10 \mu\text{m}$  titanium window from below while the positrons enter also through a  $10 \mu\text{m}$  titanium window located at the center of the pinbase from above. The block house is connected to the hat by a vacuum tubing and the positron source is lowered during positron loading through the hat, the isolation stage and the dewar directly in front of this window. The actual electrode structures of hbar1 and hbar2 are depicted in Fig. 2.7a and b, respectively. The hbar1

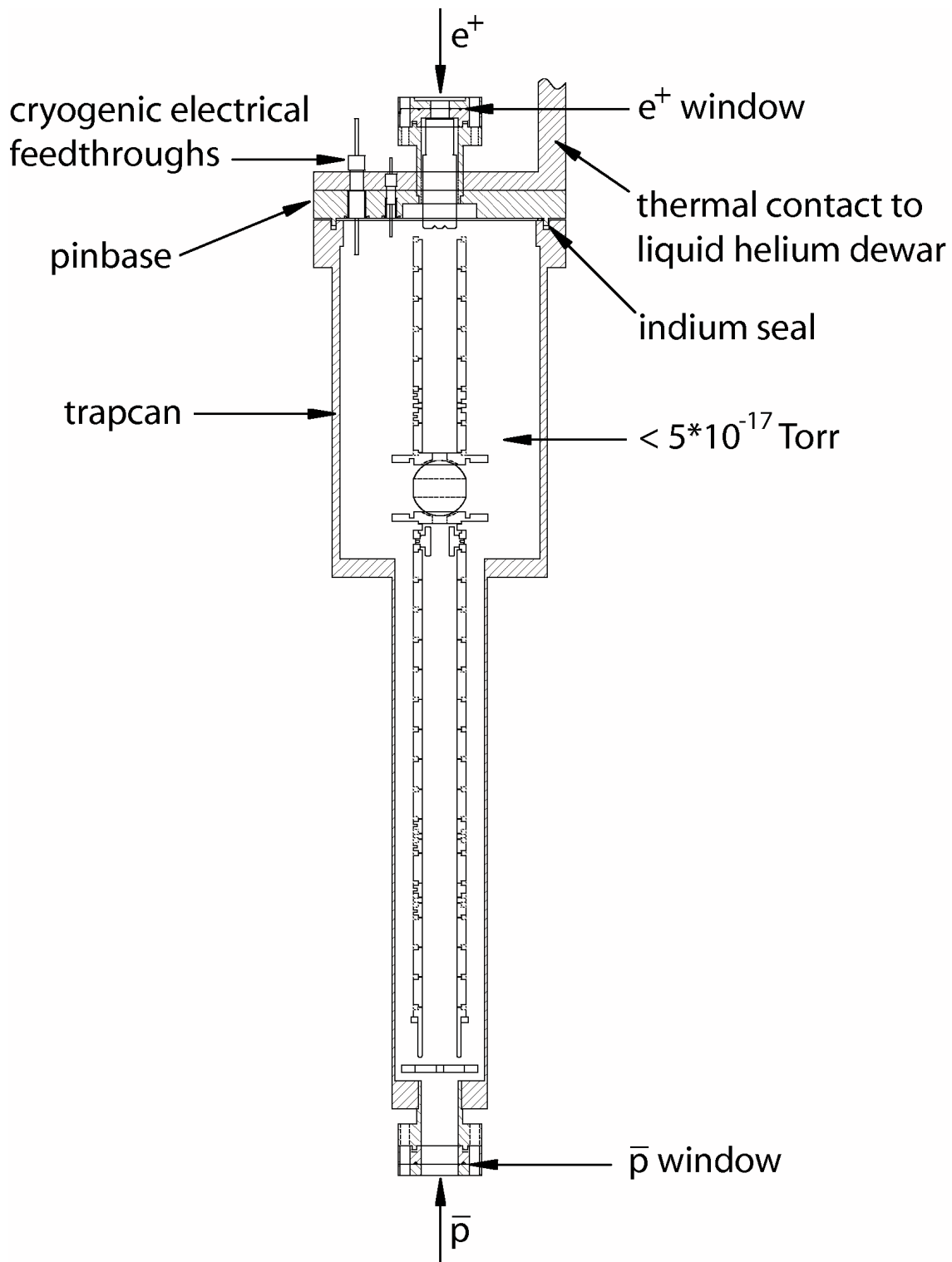


Figure 2.6: The hermetically sealed trap can which houses the actual Penning trap is depicted. Here the electrode stack of hbar1 is shown. For clarity, the electrode support structure is not shown.

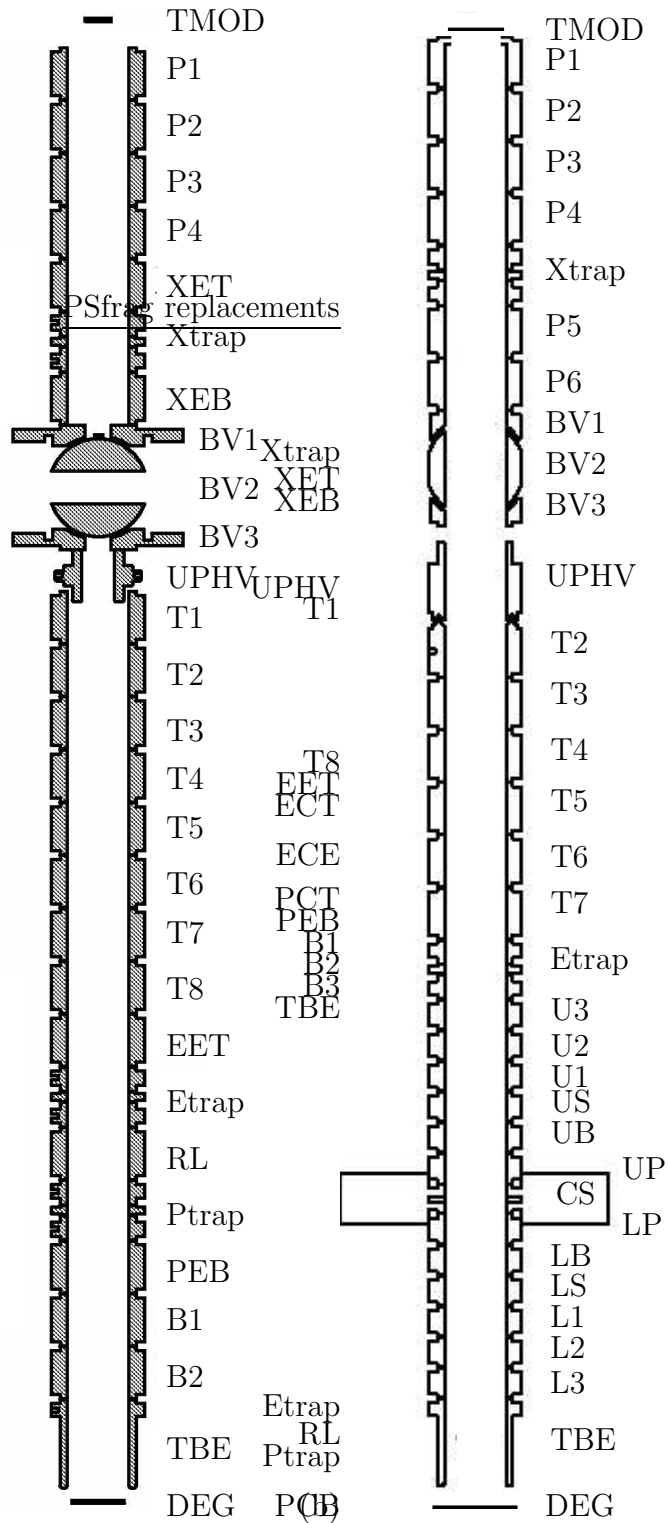


Figure 2.7: a) Electrode stack of hbar1 and b) electrode stack of hbar2. The inner diameter the electrodes is 12 mm which can be used as a scale for the two graphs.

Penning trap consists of 33 cylindrical electrodes and the hbar2 Penning trap consists of 36 cylindrical electrodes. All electrodes are machined out of OFHC copper and their surfaces are gold plated. Macor spacer rings with a height of 0.18 mm electrically isolate the electrodes from each other. The inner diameter of most electrodes is 12 mm. Only in the hbar1 Penning trap BV1 and BV3 have an inner diameter of 8 mm and BV2 of 6 mm. The height of the electrodes P1–P6, XET, XEB, T1–T8, EET, RL, PEB, B1 and B2 is 10 mm while the height of the electrodes U3–L3 is 5 mm. The electrodes P1–XEB in the hbar1 Penning trap and P1–P6 in the hbar2 Penning trap are referred to as upper electrode stack. These electrodes are used for positron loading. The Xtrap electrode is an especially designed electrode in which the number of positrons can be determined as described in section 2.5.1. The electrodes UPHV–TBE in the hbar1 and hbar2 Penning trap apparatus are referred to as lower electrode stack and these electrodes are used for antiproton accumulation and for the production of antihydrogen. The electrodes Etrap and Ptrap are designed in the same way as Xtrap and are used for counting positrons and electrons. The electrodes U3–L3 of the hbar2 electrode stack are especially designed for the experiment described in chapter 6 in which antihydrogen is produced via a charge exchange process. Around the CS electrode, as indicated by the two rectangles, a setup for the production and detection of a Rydberg cesium beam is mounted which is further described in chapter 6. The UPHV electrode and the Degrader (DEG) can accommodate high voltages of about 3 kV which are used for antiproton trapping as will be discussed in detail in section 3.3.3.

The inner electrode (BV2) of the ball valve is a rotatable ball which allows to open and close a path between the upper and the lower electrode stacks. Many turns of copper wire are wound around and glued onto the ball. A current through the wire causes a torque on the ball due to the presence of the homogenous magnetic field. Depending on the direction of the current flow, the ball valve opens or shuts. The ball valve is always in the closed position except when positrons which are accumulated in the upper electrode stack are transferred to the bottom electrode stack. A closed ball valve prevents that high energy antiprotons coming from the AD strike the TMOD crystal, which is mounted to the very top of the electrode stack. The TMOD crystal and the RMOD crystal (mounted to the ball valve pointing into the upper electrode stack when it is shut) consist of tungsten and both are required for positron loading. The fast antiprotons can remove adsorbed gas cryopumped onto the crystal surface and therefore stop the positron loading technique to work [GHR<sup>+</sup>99]. The positron loading technique employed at ATRAP will be described in section 3.1.

### 2.4.3 Integration of Optical Fibers in the Hbar2 Penning Trap Apparatus

As mentioned in the previous section, some extra features have been implemented in hbar2 in order to carry out the experiments described in the chapters 5, 6, and 7.

The experiments require the availability of laser light in the range between 511 nm and 850 nm in the Penning trap region. In both cases, the laser light is delivered via optical fibers with specifications given below to the Penning trap region. In order to integrate the optical fibers into the Penning trap apparatus, vacuum feedthroughs at the hat of the Penning trap and cryogenic feedthroughs at the pinbase had to be developed and their design is described in this section.

For the experiments described in chapter 6 and 7, we have used an OFS [OFS] all silica low OH multimode fiber with product number CFO1493-54, with a numerical aperture of 0.22, and a loss of 10-20 dB/km for wavelengths between 500 and 900 nm. The core diameter is  $940 \pm 15\mu\text{m}$ , the cladding diameter is  $1000 \pm 15\mu\text{m}$ , the coating diameter is  $1035 \pm 15\mu\text{m}$ , and the buffer diameter is  $1400 \pm 50\mu\text{m}$  [OFS]. This type of fiber is referred to in the following as type I. For the experiment described in section 5, basically the same type of fiber is used but with a smaller core. The product number of the fiber is CFO1493-42. It has a numerical aperture of 0.22, a loss of 10-20 dB/km for wavelengths between 500 nm and 900 nm. The core diameter is  $365 \pm 10\mu\text{m}$ , the cladding diameter is  $400 \pm 10\mu\text{m}$ , the coating diameter is  $430 + 5 - 10\mu\text{m}$ , and the buffer diameter is  $1400 \pm 50\mu\text{m}$  [OFS]. This type of fiber is referred to in the following as type II. For each, type I and type II, one fiber runs from the laser cabin to the experimental zone I. Two fibers of type I and two fibers of type II are installed in the Penning trap apparatus. An installed fiber is connected to a fiber of the same type coming from the laser cabin by use of a fiber to fiber coupler.

Four fiber feedthroughs are therefore installed at the hat of the Penning trap apparatus. The design is identical for type I and type II fibers. A fiber feedthrough is shown in Fig. 2.8. It consists of an aluminum cylinder with a height of 25 mm and a diameter of 9.5 mm. An o-ring with an inner diameter of 1.5 mm and a brass screw ( $M4 \times 20$ ) is bolted into the cylinder from one side. The fibers are strung through a hole with a diameter of 1.5 mm which is drilled through the center axis of the screw and the cylinder. When the brass screw is tightened the o-ring is pressed against the cylinder and the fiber and thus forms a vacuum seal. The cylinder fits gently into a commercial quick-flange which is welded into the hat.

The fibers run from the hat through the isolation stage and the liquid helium dewar to the pinbase where the four fibers are feed through two cryogenic feedthroughs into the trap can. A cryogenic feedthrough for two fibers is depicted in Fig. 2.9. It is machined out of OFHC copper and consists of a copper flange with two conically shaped tubes (inner diameter 1.1 mm) through each of which a fiber is strung. The fibers are glued (Emerson Cumming, Styccast 2850FT, Catalyst 24LV) to the top of the tubing and the glue acts as a vacuum seal. Before the fibers were installed, the buffer layer has been removed in the part below the vacuum seal because otherwise a small leak between the coating and the buffer would destroy the UHV of the trap can. The flange of the feedthrough fits into a home-made flange which is welded into the pinbase. An indium seal is placed between the feedthrough and the flange in order to preserve the good vacuum of the trap can.

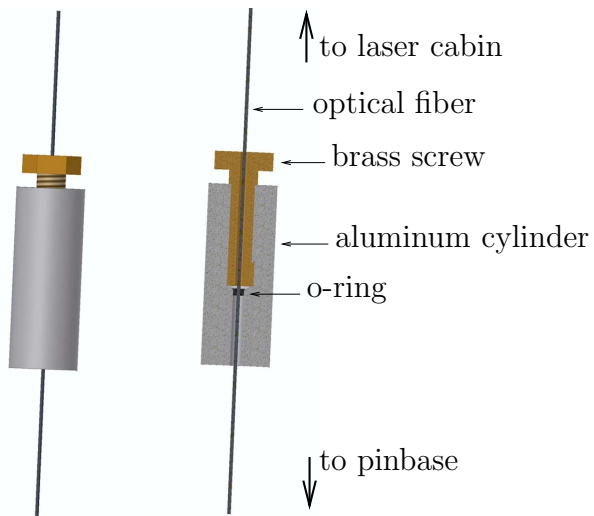


Figure 2.8: The fiber feedthrough which is employed at the hat of the Penning trap. The aluminum screw squeezes the o-ring so that it is pressed against the aluminum cylinder and the fiber and thus forms a vacuum seal.

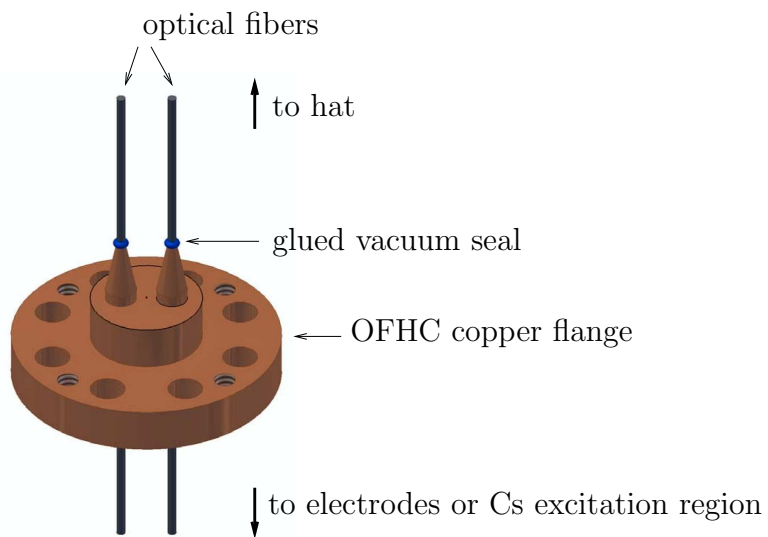


Figure 2.9: Fiber feedthrough used at the pinbase.

The type I fiber is then connected with the cesium excitation region which will be further described in chapter 6, while the end of the type II is connected with holes in electrodes T4 and T7 so that the particles can be exposed directly to laser light which is further described in chapter 5.

## 2.5 Particle Detection

The question now arises how trapped particles are detected. At ATRAP, positrons and electrons are detected non-destructively by a radio frequency detection technique, which is described in section 2.5.1. In contrast antiprotons are detected destructively by releasing them from the Penning trap and by counting the annihilations monitored by the detector system. The detector system and detection method is described in section 2.5.2.

### 2.5.1 Non-Destructive Particle Detection

At the ATRAP experiment, electrons and positrons are detected non-destructively by a radio frequency detection technique, which is described in this section. Additional information on non-destructive detection of charged particles can also be found in [BG86, Hal99, Yes01, Est02, Bow03, Oxl03].

It has been derived in section 2.4.1, that the axial motion of a particle in an ideal Penning trap is a harmonic oscillation, which is as given in Tab. 2.1 for the case of electrons and positrons in the radio frequency range. The hbar1 and hbar2 apparatuses contain several sets of electrodes, e.g. Etrap in hbar1 and XTrap in hbar2, which are used to produce a quadratic potential variation along the z-axis. Such sets consist of a ring electrode (1.75 mm long) in between two compensation electrodes (4.75 mm long). An endcap electrode (10.08 mm long) next to each compensation electrode completes the set. XET and XEB are for example the endcap electrodes to Xtrap in the upper electrode stack of hbar1. The electrode sets have been designed so that if  $V_0$  is applied to the ring electrode and  $0.881V_0$  to the two compensation electrodes, and zero volts to the endcaps, then the electric potential along the z-axis is harmonic and the particles oscillate in the axial direction with an angular frequency [Oxl03]

$$\omega' = \sqrt{\frac{CeV_0}{md^2}}. \quad (2.12)$$

Here  $C$  is a geometry-dependent factor, which is  $C = 0.545$  in the case of hbar1 and hbar2,  $d$  is a characteristic trap dimension that is  $d = 5.1$  mm for both traps, and  $e$  and  $m$  are the particle's charge and mass.

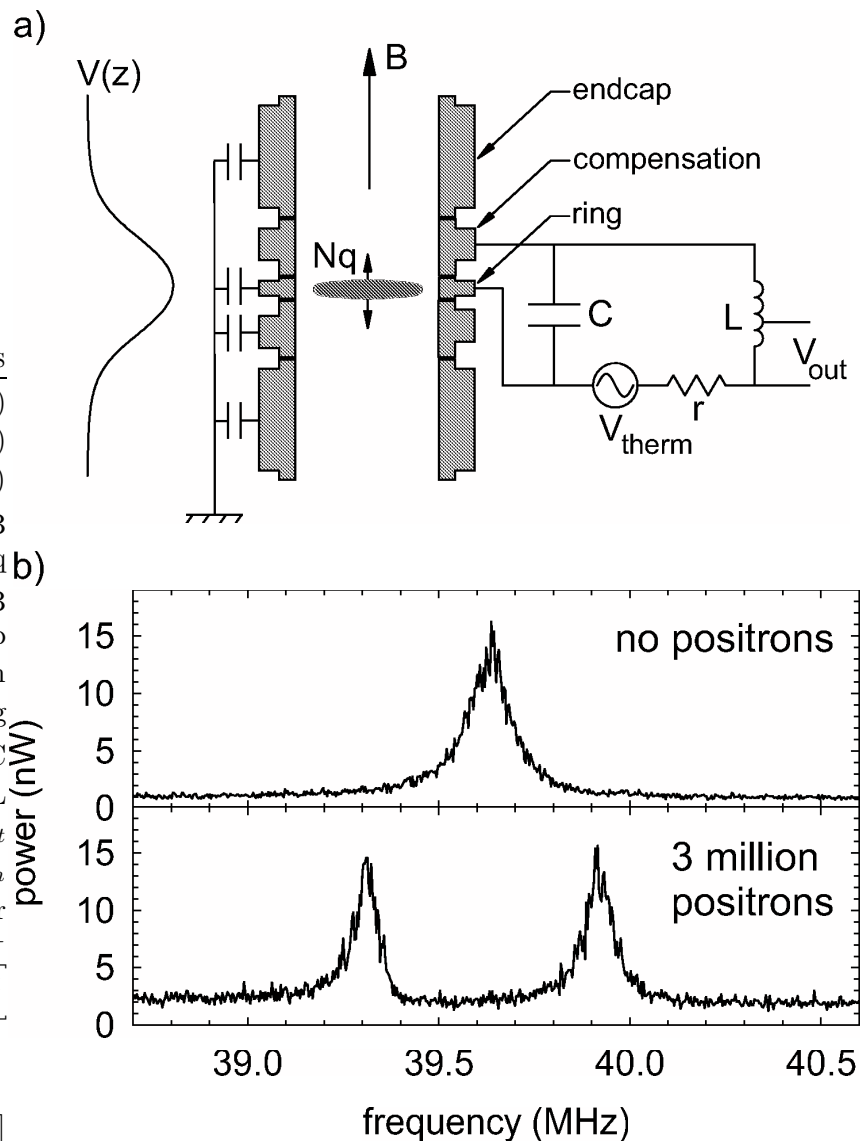


Figure 2.10: a) The electrodes and electric circuit used for the measurement of the frequency response of  $N$  oscillating charges in a quadratic potential. b) The frequency response measured with zero and with 3 million positrons.

A cross sectional view of such a set of electrodes is given in Fig. 2.10a. As depicted schematically, a RLC-circuit connects the ring electrode with one compensation electrode. The signal voltage,  $V_{out}$  modulates the gate of a cryogenic FET, located above the pinbase. The gate signal of the FET is amplified and measured with a spectrum analyzer. Without any particles present in the trap, the frequency spectrum is simply given by the spectral response of the circuit that is driven by the thermal noise  $V_{therm}$  in the resistor  $r$  (the resistor is at 4.2 K). The power distribution  $P(\omega)$  of the resulting noise driven signal is given in the top part of Fig 2.10b. It is a Lorentzian with a peak at the resonance frequency  $\omega_{LC}$  of the circuit.

An axially oscillating positron or electron plasma induces alternating image charges in the electrodes which in turn cause an oscillating current  $I$  to flow through the resistor  $r$ . The image charges due to oscillating particles couple the particle oscillation to the tuned circuit oscillator. The result is a pair of coupled oscillators with two different mode frequencies  $\omega_{1,2}$  which are given in the limit of large clouds ( $> 500\,000$  particles) by [Hal99]

$$\omega_{1,2} = \omega_{LC} \pm \frac{1}{2} \sqrt{\gamma N}, \quad (2.13)$$

where  $\gamma$  is a characteristic constant of the trap and  $N$  is the number of particles in the plasma. In the bottom part of Fig. 2.10b the spectral response of three million positrons measured by a spectrum analyzer is depicted. The frequency spacing  $\Delta\omega$  of the two peaks is according to Eq. 2.13 given by  $\Delta\omega = \omega_1 - \omega_2 = \sqrt{\gamma N}$  and thus from  $\Delta\omega$  the number of particles can be determined, if  $\gamma$  is known. This constant is calibrated from time to time by a measurement of the particle number  $N$  via a destructive detection technique which is as follows. Trapped positrons or electrons are dumped onto the degrader (DEG), where the current due to the particles is measured with a charge sensitive amplifier. Integration of the voltage trace and knowledge of the amplifier sensitivity yields the total charge and thus, particle number, so that by a comparison with the measured spectrum  $\gamma$  can be determined.

Generally, all numbers of positrons and electrons given in this thesis have been measured by this non-destructive detection method. The error in the determination of the number of particles is because of uncertainties in the calibration about 20 %.

### 2.5.2 Destructive Particle Detection and the Detector System

In contrast to positrons and electrons, antiprotons are detected destructively. The electric trapping potential is ramped down quickly so that the antiprotons leave the trap and finally annihilate at the surface of an electrode or at the degrader. In antiproton-proton annihilation events,  $3.0 \pm 0.2$  charged pions are produced on average [Ams98]. Two detectors, the fiber detector described in section 2.5.2.1 and the outer scintillator paddles described in section 2.5.2.2, are available to detect the charged pions. The

signals of both detectors is used to trigger the data acquisition, which is described in section 2.5.2.3. The detectors have been designed and built and are maintained by the Jülich group and very detailed information can be found in [Yes01, Est02, Bow03, Oxl03], so that the overview presented here will be rather short.

### 2.5.2.1 The Fiber Detector

The fiber detector consists of three layers of 128 scintillating fibers, with one layer of straight fibers (fiber diameter 1.9 mm) and two layers bent in a helix by 150° around the axis (fiber diameter 1.5 mm). The location of the fiber detector in the superconducting magnet is depicted schematically in Fig. 2.2. It resides in the magnet's bore and surrounds the bottom part of the electrode stack. A more detailed top view and a side view of the location of the detector is depicted in Fig. 2.11a and b. In this figure, the location of the BGO detector is also shown. This detector has not been used for the work presented in this thesis and is therefore not described here. Each fiber is connected with a photomultiplier which is located below the superconducting magnet as shown in Fig. 2.5. A charged pion which passes through a fiber causes a light pulse and the electric signal from the photomultiplier is converted to a digital signal by an ADC unit and analyzed by the data acquisition system. Because of the high average number of events from a single antiproton annihilation, this detector operates with a 94 % detection efficiency [Grz]. Cosmic events and photomultiplier noise yield a background count rate of  $75\text{ s}^{-1}$  for an individual fiber layer. We therefore generally register in the data acquisition the so called fiber counts, which are two coincident signals (within a 50 ns time window) from two separate layers. The background count rate of fiber counts is reduced to  $10\text{ s}^{-1}$  [Grz].

### 2.5.2.2 The Outer Scintillator Paddles

The outer scintillator paddles consist of 18 rectangular paddles which surround the magnet in two layers as shown in Fig. 2.12. They have basically the same height as the magnet as shown in Fig. 2.5. A charged pion passing through a paddle produces scintillator light which is guided by a plexiglass light guide to an attached photomultiplier. The electrical signal from the photomultiplier is converted to a digital signal by an ADC unit. The two layers are operated in coincidence within a 50 ns time window to suppress noise and background events. Antiproton annihilation events resulting in a scintillator paddle coincidence are called single events and are detected with an efficiency of about 50 % [Grz]. Background events occur at a rate of  $60\text{ s}^{-1}$  mainly due to cosmic rays [Grz].

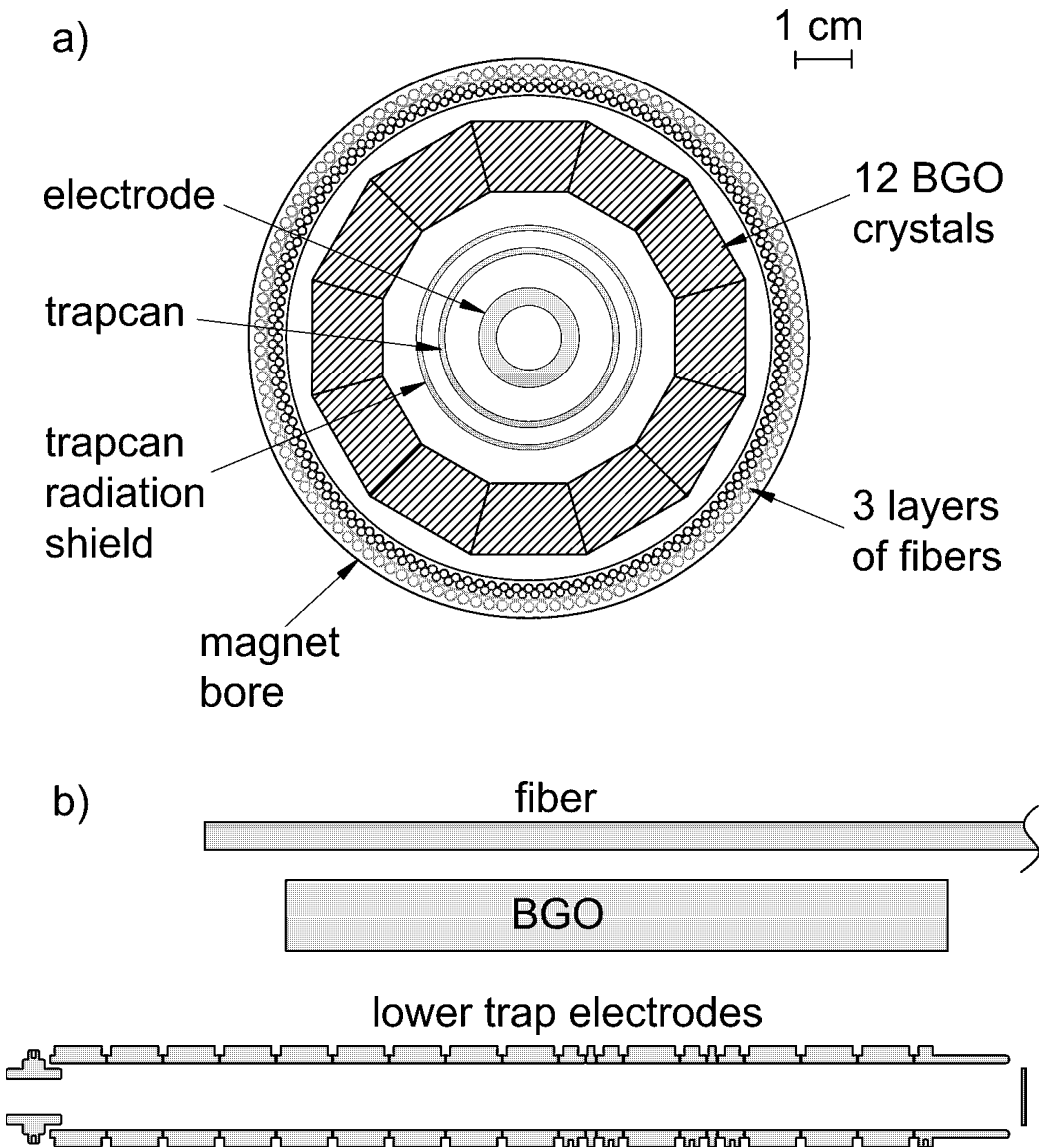


Figure 2.11: a) Top and b) side view of the fiber and BGO detectors which surround the lower electrode stack. The BGO detector was used for the detection of  $\gamma$ -rays produced in positron-electron annihilations but was removed from the experiment after the background-free detection technique was established. The graph is taken from [Oxl03].

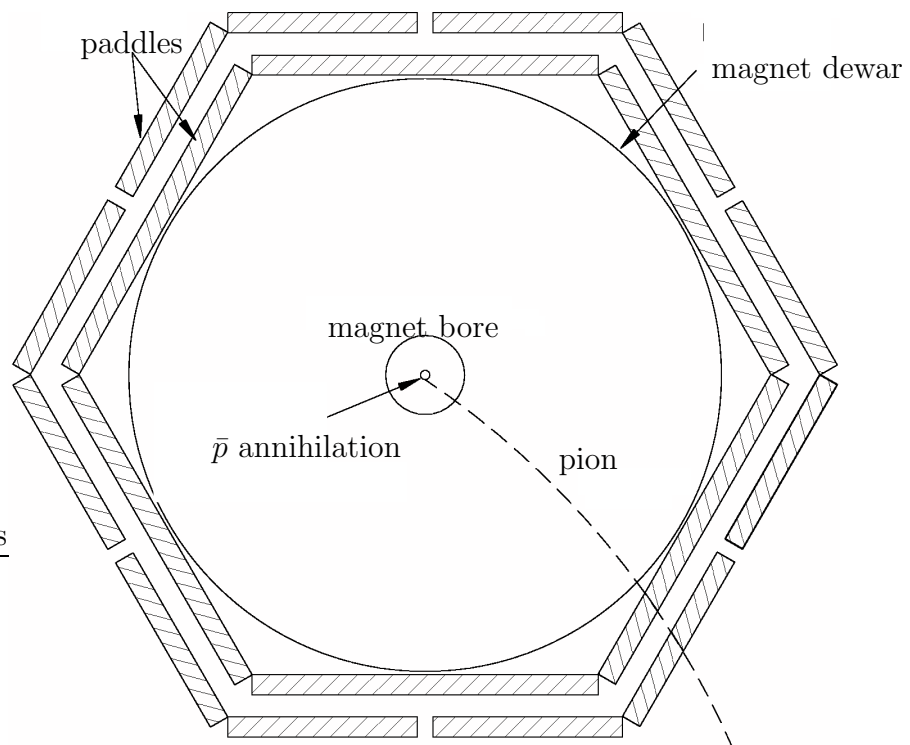


Figure 2.12: Cut view of the scintillator paddles. The paddle surround the magnet and is as tall as the magnet resulting in an effective antiproton detection efficiency of 50 %.

### 2.5.2.3 Trigger Counts and the Data Acquisition System

A fiber count and a single count which are registered within a 50 ns time window is referred to as a trigger count. The antiproton detection efficiency is reduced to 48 % but the background rate is reduced to about  $1.2 \text{ s}^{-1}$  [Grz], which makes trigger counts very useful for the recording of rare events. A trigger count triggers the data acquisition, which means that the status of all detector elements is read out and stored. This process takes about 1 ms to complete so that the data acquisition system is limited to operating at trigger count rates of 1 kHz or less.

# Chapter 3

## Loading Particles

In the previous chapter, the devices and techniques for the trapping and the detection of antiprotons, positrons and electrons have been presented. In this chapter, the methods to accumulate the particles in the Penning trap are presented. The method used by ATRAP for the accumulation of positrons is presented in section 3.1 and the method employed for loading electrons is discussed in section 3.2. In section 3.3 the method of antiprotons loading from the AD into the Penning trap is presented.

### 3.1 Positron Loading

In this section, the method employed by the ATRAP experiment for the loading of positrons is described briefly. More detailed descriptions can be found in [ERTG00, Est02, Bow03]. For alternative methods not employed by ATRAP to load positrons in a Penning trap, see [Gab04] and references therein. The positrons are loaded from the positron source which is lowered during positron loading to the tripod region. The positron source emits positrons within a continuous energy range between zero and 545 keV. Due to the 5.3 T homogeneous magnetic field of the superconducting solenoid, the emitted positrons are guided axially in the direction of the trapping region. The fast positrons enter the trap can from the top through a  $10\ \mu\text{m}$  thick titanium foil as depicted schematically in Fig. 2.6 and pass then through the transmission moderator (TMOD), a  $2\ \mu\text{m}$  tungsten crystal whose surface is cut at the W(100) crystal plane. The upper electrode stack is shown along with TMOD in Fig. 3.1a. About 0.05 % of the incident positrons emerge from the transmission moderator (TMOD) with an energy of about 2 eV [ERTG00]. Such a low energy positron can form a Rydberg positronium atom with a secondary electron while exiting the moderator. The positron and the electron are tightly confined in the radial direction by the magnetic field, while their axial position can be influenced through an electric field which is applied to the moderator. Biasing the transmission moderator with a potential  $V_t$  with respect to the neighboring

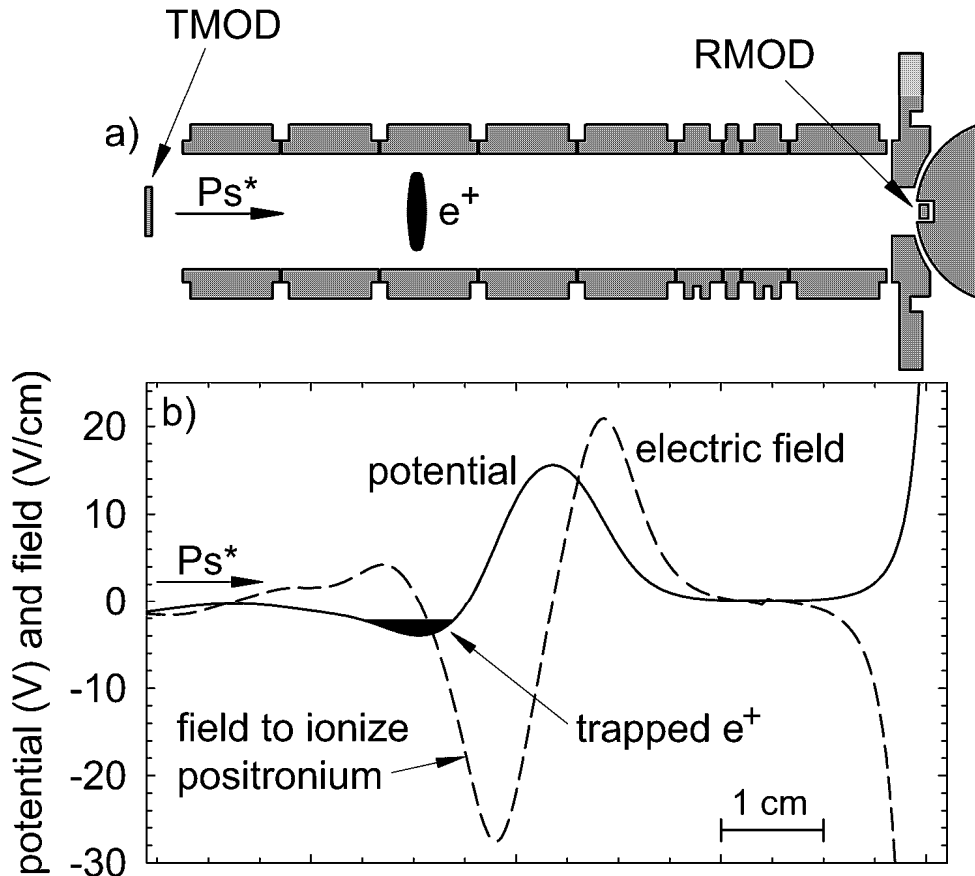


Figure 3.1: a) A side view of upper electrode stack along with TMOD and RMOD. RMOD is located at the ball valve viewing the upper electrode stack when it is closed. b) Potentials used to trap positrons from positronium created at TMOD.

electrodes adds energy  $eV_t$  to one species and removes  $eV_t$  from the other. The electric potential on axis and the corresponding electric field present in the upper electrode stack are shown in Fig. 3.1b. It is well known from experiments with Rydberg atoms that highly excited atoms can be ionized by electric fields [Gal93]. The potential well structure is constructed so that an electric field with a maximum magnitude of about 27 V/cm is formed on the fourth electrode. This empirically determined field strength is more than enough to ionize the Rydberg positronium atoms passing that field. The freed positrons are then stored in the potential well formed at the third electrode from the left. By reversing the potentials in the trapping region electrons at the same rate can be trapped confirming the role of positronium.

Most of the positrons pass the trap and impinge upon the reflection moderator (RMOD), which is located at the ball valve viewing the upper electrode stack when the ball valve

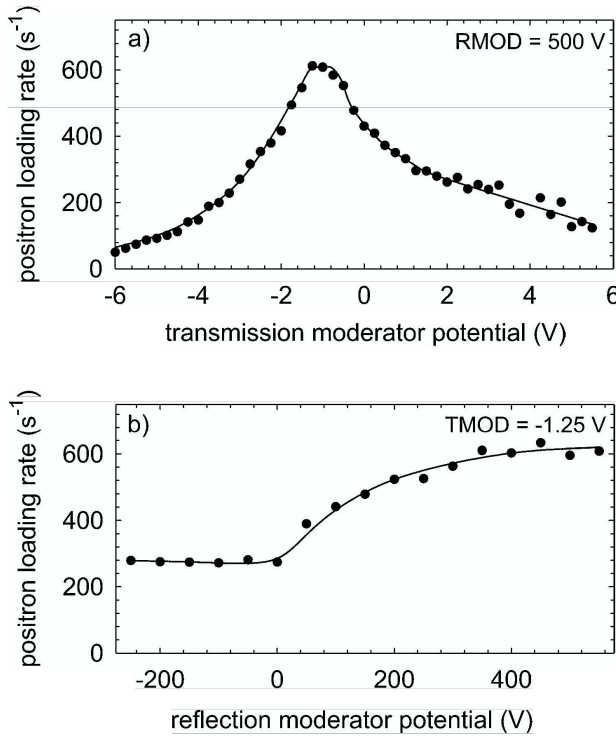


Figure 3.2: a) The loading rate is given as a function of the potential  $V_t$  which is applied to the transmission moderator.

b) The loading rate is given as a function of the potential  $V_r$  which is applied to the reflection moderator. The graph is taken from [Oxl03].

is closed. RMOD is a 2 mm tungsten crystal whose surface is cut at the W(110) crystal plane. A fraction  $\eta \approx 10^{-3}$  [ERTG00] of impinging positrons slow and diffuse near the entrance surface of RMOD, and re-emerge with low energies [SL88]. RMOD is biased by the potential  $V_r$ , which is typically about 500 V and thus the re-emerged positrons travel back to the transmission moderator where a fraction of the backward traveling positrons emerge accompanied by a secondary electron and form Rydberg positronium just as described above. Fig. 3.2a shows how the positron loading rate depends upon the voltage  $V_t$  applied to TMOD and Fig. 3.2b shows how the positron formation rate depends upon the voltage  $V_r$  applied to RMOD. The maximum loading rate occurs at  $V_t = -1.25$  V and  $V_r = 500$  V and it is strongly dependent on the voltages applied to the moderator TMOD. It can be deduced from Fig. 3.2b, that the proper use of RMOD increases the loading rate by a factor of about 2, since it is about 300 for  $V_r = -200$  V and about 600 for  $V_r = +400$  V.

The formation rate for Rydberg positronium depends also upon the gas adsorbed on the surface of the transmission moderator, however this is not very well understood [Est02]. The positron loading rate diminishes over time as frozen gas atoms are removed from TMOD by the impact of the positrons. Therefore, the trap has to be warmed up and

re-cooled to liquid helium temperature nearly every weekend during beam time. This is also the raison d'être for the ball valve since without it incoming antiprotons which are not slowed by the degrader would very quickly remove the gas layer from the TMOD.

During normal operation, we load about 300 positrons per second. This yields about 720 000 positrons after a typical loading time of 40 minutes. The maximum number which can be loaded into the Penning trap apparatus is about five million. Higher numbers tend to have unstable clouds and can therefore not be manipulated any further.

## 3.2 Loading Electrons

The ability to load electrons is also crucial for several reasons. At first, electrons are much easier and faster to load than positrons and antiprotons. They are therefore frequently used to test the proper functioning of the Penning trap apparatus. Trapped electrons also behave similar to trapped positrons, so that many positron manipulation techniques can be developed with electrons. Secondly, electrons are needed for antiproton loading, as will be described in section 3.3. In this section, the two electron loading techniques employed by ATRAP are described. In section 3.2.1, the electron loading technique which uses the radioactive source is described and in section 3.2.2, the method which uses a field emission point is presented.

### 3.2.1 Loading Electrons from the Radioactive Source

Electrons can in principle be loaded in the same way positrons are loaded just by reversing the potential depicted in Fig. 3.1b. However, the loading rate equals the positron loading rate and is therefore very low.

For the case of electrons, higher loading rates can be obtained by the following method. The top part of Fig. 3.3 shows the lower part of the electrode stack of the hbar1 Penning trap apparatus (The method is employed in the same way in the hbar2 Penning trap apparatus), and solid curve in the lower part of Fig. 3.3 depicts the initial potential structure present on axis in the trap. The high energy positrons delivered by the radioactive source are confined axially by the strong magnetic field and pass through the electrode stack and impinge on the degrader (DEG), where secondary electrons are created. The secondary electrons are collected at the electrode TBE. The collected electrons are then split into several potential wells depicted by the dashed curve in the bottom part of Fig. 3.3. Due to the presence of such seed electrons, secondary electrons created at DEG can be loaded into these wells as well. The electron accumulation rate as a function of the number of wells is given in Fig. 3.4. The accumulation rate increases with the number of wells but saturates for more than six potential wells. The average loading rate into six or more wells is about 4 500 electrons per second and therefore about 2.7 million electrons can be loaded during 10 minutes.

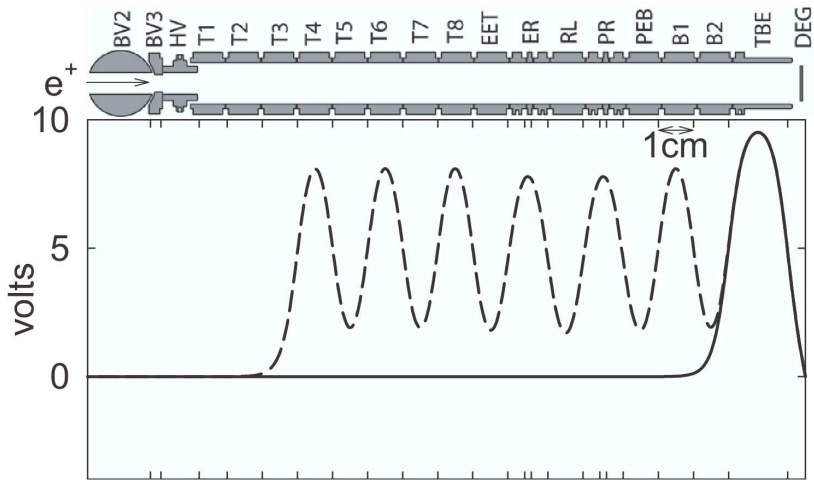


Figure 3.3: The top part of the graph shows the bottom part of the hbar1 electrode stack. The bottom part shows the initial potential (solid) curve to load secondary electrons from the degrader onto TBE. The loading rate is improved by the use of more potential wells (dashed lines). However in order to accumulate secondary electrons, electrons accumulated at TBE have to be stored there. The graph is taken from [Bow03].

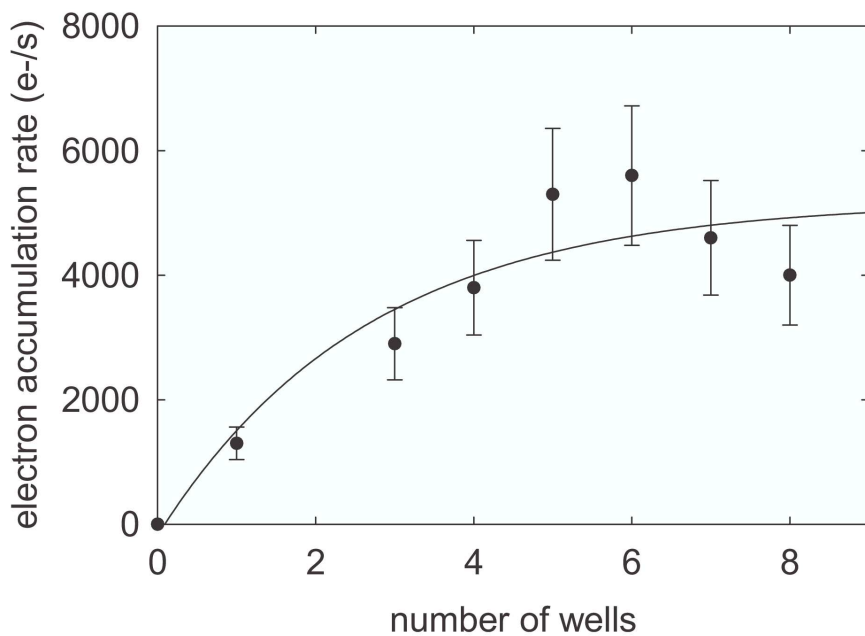


Figure 3.4: Electron accumulation rate as a function of the number of potential wells. The graph is taken from [Bow03].

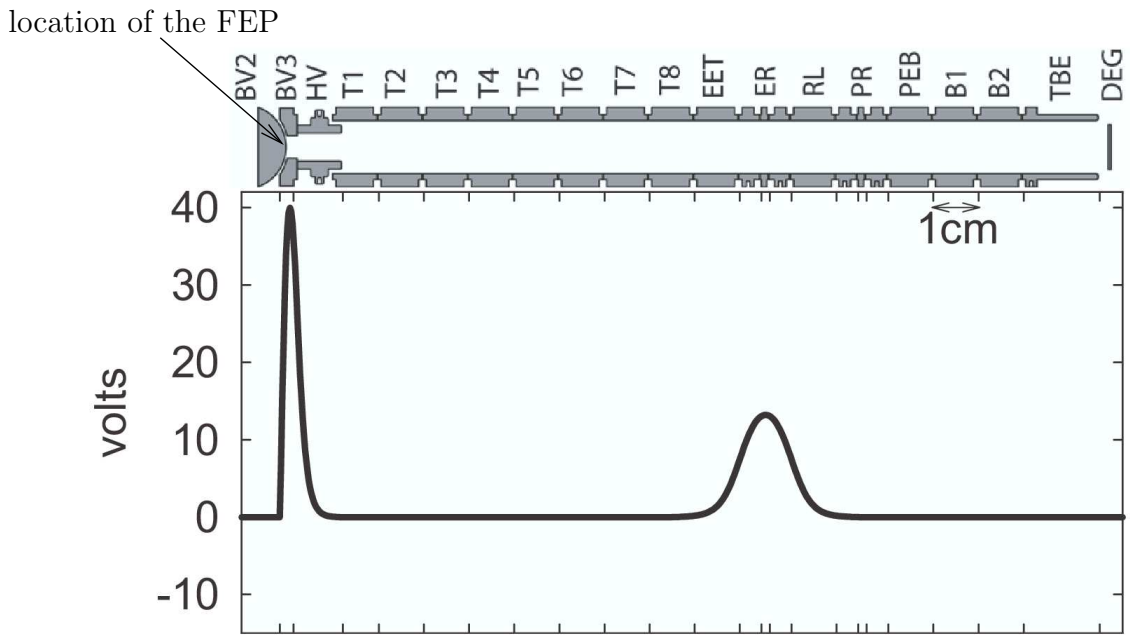


Figure 3.5: The top part of the graph shows a side view of the lower part of the hbar1 Penning trap apparatus. The bottom part depicts the potential structure applied during electron loading from the FEP. The graph is taken from [Bow03]

### 3.2.2 Electron loading with the FEP

An alternative way to load electrons is by use of a field emission point (FEP). The FEP is a 0.5 mm tungsten wire with a very sharp tip at one end. It is mounted as shown schematically in Fig. 3.5 on the ball valve on the opposite side of the RMOD. It is electrically isolated from the valve and when the ball valve is closed, it points into the bottom trap. The potential structure used to load electrons into the trap is shown in the bottom part of Fig. 3.5. If a few hundred volts are applied to the tip relative to the ball, a beam of electrons is extracted from it by the very high electric field that is generated. A typical value for the electron beam current is 20 nA. Due to the magnetic field these electrons travel to the degrader, where they can liberate atoms that are frozen to it. Collisions between electrons and atoms can produce secondary electrons which can be trapped in the potential wells, as is shown in Fig. 3.5. Typically 5 million electrons are loaded within 10 seconds and therefore this is the preferred loading technique for electrons. However, since it depends on a proper functioning of the FEP, the method described in the previous section is also frequently employed.

### 3.3 Accumulating Antiprotons from the AD into the Penning Trap

In this section, the methods to trap antiprotons delivered in bunches by the Antiproton Decelerator at an energy of 5.3 MeV within the Penning trap are presented. Before the antiprotons enter the Penning trap, they pass a parallel plate avalanche counter (PPAC) [Ste76], which is used to monitor the antiprotons and to steer them into the trap. The PPAC and its use is described in section 3.3.1. The antiprotons are delivered at an energy too high to be trapped and thus they are slowed by passing through an energy tuning cell and a degrader, which is described in section 3.3.2. The slowed antiprotons are trapped by methods described in section 3.3.3 and large numbers of antiprotons are accumulated by a method which is called stacking of antiprotons. This method is described in section 3.4.

#### 3.3.1 Monitoring and Steering the Antiproton Beam by the PPAC

The antiprotons delivered from the AD are bent from their horizontal trajectory into a vertical trajectory as shown in Fig. 2.2 on page 11 by the magnets DE3.BVT10, DE3.QN20, and DE3.BVT25 and then pass through the PPAC which is situated in the bore of the magnet just before the Penning trap.

The PPAC consists of two large area anode-cathode pairs oriented in the xy-plane perpendicular to the beam. The cathodes consist of thin sheets of aluminized mylar, whereas each anode consists of five parallel strips of mylar. The strips are 2 mm wide with a gap of 0.5 mm between adjacent strips. The strips of one anode are oriented along the x-direction, and the strips of the other anode are oriented along the y-direction. Argon gas flows between an anode-cathode pair and an electric potential of 200 V is maintained across each pair. An antiproton passing through the PPAC can ionize an argon atom and therefore produce an electron which is accelerated towards the anode. The electron current on each strip flows through a resistor and the voltage across the resistor is measured by an oscilloscope. The applied voltage between the strips is so low that the PPAC is operated in a linear mode, so that an electron does not ionize any further argon atoms. The voltage measured per strip is thus a measurement of the number of antiprotons passing through the strip and due to the orientation of the 10 strips with respect to each other, the position and spot size of the antiproton beam can be monitored.

The PPAC is used as a diagnostic tool for positioning and focusing the beam. The beam is steered in the y-direction by changing the currents in the magnets DE3.BVT10 and DE3.BVT25, and in the x-direction by tuning the current in the magnet DE0.DHZ45 which is located further upstream. Focusing in the y-direction is performed by changing

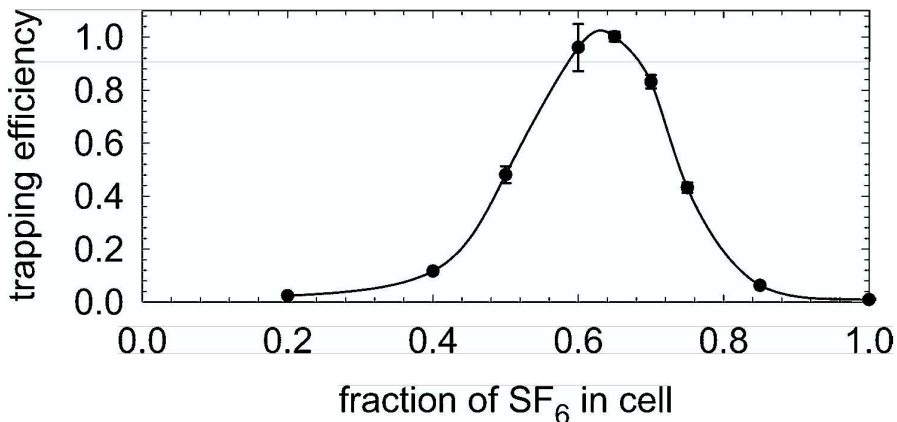


Figure 3.6: The trapping efficiency is depicted as a function of the fraction of SF<sub>6</sub> gas in the energy tuning cell. The graph is taken from [Oxl03].

the current in DE3.QN20 and in the x-direction by changing the current in DE0.QN50 which is also located further upstream. In this way the beam can be positioned and focused entirely onto the central 2 mm wide anode strip in each direction so that it enters the Penning trap on its central axis.

### 3.3.2 Slowing Antiprotons

The energy loss of the 5.3 MeV antiprotons passing through the PPAC is about 0.5 MeV [Oxl03]. In order to trap them, their kinetic energy has to be smaller than 3 keV since only voltages up to 3 kV can be applied to the high voltage electrodes (UPHV and DEG) of the Penning trap apparatus. The degrader electrode (DEG) is a 125  $\mu\text{m}$  thick beryllium degrader foil (DEG) which resides directly in front of the lower electrode stack as shown in Fig. 2.7. The antiprotons which pass through the degrader emerge at the opposite side at energies less than 3 keV so that they can be trapped by a method described in the next section.

In order to optimize the number of trapped antiprotons, an energy tuning cell has been placed above the PPAC. This cell is 15 mm long and filled with a mixture of SF<sub>6</sub> gas and helium. The relative amount of the two gases can be controlled. More SF<sub>6</sub> gas in the cell leads to a higher energy loss of the antiproton which pass through. The total tuning range of the cell is 0.6 MeV [Oxl03] and the optimum mixture varies from one cool down to the next since residual gas in the magnet bore can freeze and built up a layer onto the cold surfaces through which the antiprotons pass. The optimum mixture is chosen so that the number of trapped antiprotons from a single AD pulse (the trapping method is described in the next section) is at a maximum. A typical measurement of the trapping efficiency, which is the number of trapped antiprotons

normalized to the maximum value, is depicted in Fig. 3.6 as a function of the relative amount of SF<sub>6</sub> gas in the tuning cell. As can be seen, the trapping efficiency depends strongly on the appropriate choice of the relative amount of SF<sub>6</sub> gas in the tuning cell. Such a tuning curve is measured weekly or even more often to ensure that antiproton trapping is as efficient as possible.

### 3.3.3 Antiproton Trapping

The lower part of the hbar1 electrode stack is depicted in Fig. 3.7a (The trapping method is used in the same way in the hbar2 apparatus). The antiprotons which pass through the degrader (DEG) are indicated by the arrow to the right. For the initial studies presented in the following, no electrons have been loaded. The potential structure at the time when a 80 ns long antiproton bunch arrives is shown in Fig. 3.7b. A static -3 kV potential is applied to the upper high voltage electrode (HV) and all other electrodes are kept at ground. The antiprotons which pass through the degrader with an energy of less than 3 keV are confined radially by the 5.3 T magnetic field and are reflected back in the axial direction by the potential at HV. The 80 ns duration of the entering pulse is short in comparison with the time that it takes for antiprotons at an energy of 3 keV to travel from DEG to HV and back. Thus the degrader voltage can be changed from 0 V to -3 keV before the antiprotons arrive again. The resulting potential structure is depicted in Fig. 3.7c. The antiprotons with an axial energy of less than 3 keV are trapped and bounce back and forth in the long well between HV and DEG.

In order to understand antiproton trapping of a single AD pulse into a long well in more detail, we have performed several experiments. At first, we have monitored the number of antiproton annihilations (trigger counts) as a function of time after the potential well at the degrader has been set to -3 kV. In Fig. 3.8a, the corresponding number of antiprotons normalized to 1 000 captured from an AD pulse is shown as a function of time. The loss of captured antiprotons is initially very high and the number decreases exponentially with a 1/e value of 20 s. Within the first 50 s the number of trapped antiprotons decreases from about 22 000 to 14 000, but then there is essentially no further loss. This absolute numbers depend on the intensity of the antiproton beam delivered by the AD and 14 000 to 16 000 captured antiprotons are more typical.

In a second experiment, the electric potential applied to HV and to DEG is changed and the number of antiprotons that are captured after 300 s is measured by releasing them from the trapping well and counting them destructively. The result is shown in Fig. 3.8b, where the number of trapped antiprotons normalized to 1 000 is depicted as a function of the potential applied to HV and DEG. Surprisingly, the number saturates with a 1/e value of 830 V presumably because antiprotons with more axial energy have also more radial energy which causes them to hit the trap electrodes. In conclusion, a trapping potential of 3 kV which is a save value in view of sparks is the right choice for trapping antiprotons into the ATRAP Penning traps, since any higher potential will not yield to a substantial increase in the number of trapped antiprotons.

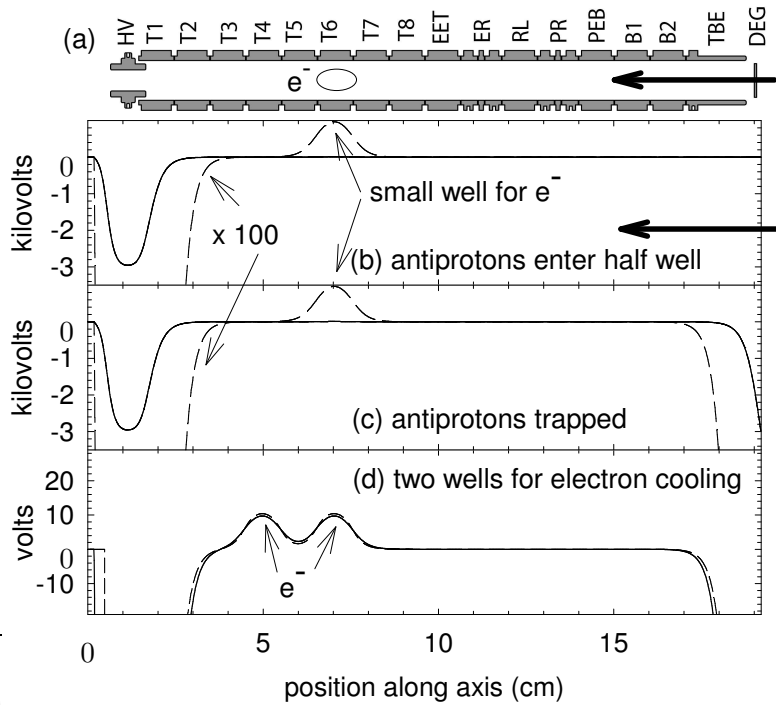


Figure 3.7: (a) Drawing of the lower electrode stack. HV is the high voltage electrode to which -3 kV is applied. In order to close the trap the same voltage is also applied to the degrader DEG. (b) Potential structure when the antiprotons enter the trap. (c) Potential structure when the trap is closed. The antiprotons bounce back and forth the big well and are slowed by electrons loaded into the small well. The last two configurations are for initially loading electrons using a positron beam (d) and for electron-cooling in two wells (e). The graph is taken from [GBO<sup>+</sup>02c].

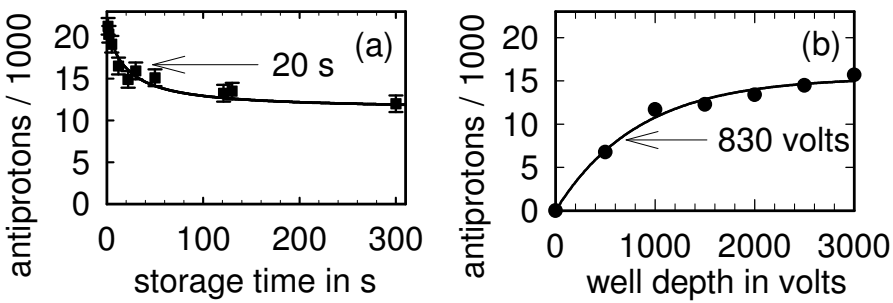


Figure 3.8: The number of antiprotons captured from an AD pulse has approximately an exponential dependence upon storage time (a) and well depth (b) with the 1/e values indicated. The graph is taken from [GBO<sup>+</sup>02c].

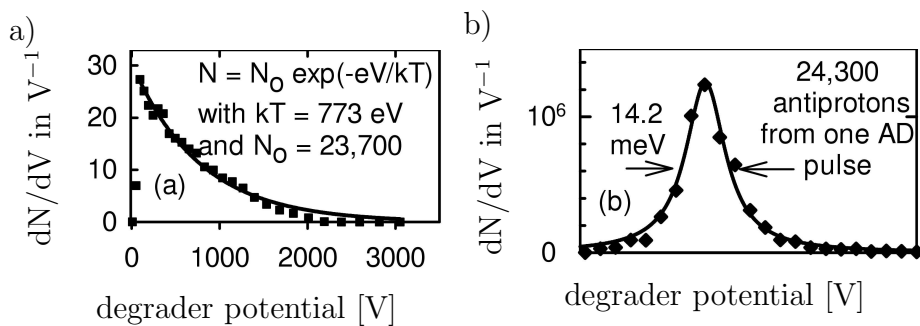


Figure 3.9: The energy spectra for antiprotons captured from an AD pulse without (a) and with (b) electron cooling. With the stacking technique (c) much more antiprotons can be trapped. Not absolute voltages are given since tiny offset voltages are not calibrated. The graph is taken from [GBO<sup>+</sup>02c].

In a third experiment, we have measured the energy distribution of the trapped antiprotons by slowly ramping the potential  $V$  of the degrader window back through zero and monitoring the number of antiproton annihilations  $N$  as a function of the degrader voltage. The result is depicted in Fig. 3.9 a, where the energy spectrum  $dN/dV$  is shown as a function of the degrader voltage  $V$ . The derivative with respect to  $V$  of an exponential energy spectrum given by  $N(E) = N_0 \exp(-eV/k_B T)$  has been fitted to the experimental data. Here  $e$  is the electric charge,  $k_B$  is the Boltzmann constant and  $T$  is a temperature.  $k_B T$  is thus the mean energy of the trapped antiprotons. The fit yields  $N_0 = 23\,700$  and  $k_B T = 773$  eV. The number of trapped antiprotons during this experiment is higher than the usual 14 000 to 16 000 because an extraordinary high number of antiprotons has been delivered from the AD. In conclusion, the trapped antiprotons have on average a mean energy of around  $k_B T \approx 800$  eV, which is a reduction in energy by a factor of  $\sim 1.5 \times 10^{-4}$  with respect to the energy of the incoming pulse of 5.3 MeV.

In a fourth experiment, the number of trapped antiprotons has been studied as a function of the time when the potential well at the degrader is switched from zero to -3 kV. The number of antiprotons normalized to the maximum trapped number is shown in Fig. 3.10 as a function of the time when the trapping well at DEG is established. The graph clearly indicates that the maximum number is trapped when the well is established immediately after the antiproton pulse enters the trap. The trapping efficiency drops quickly to about 0.85 which is due to the fact that the fastest antiprotons return to the degrader before capture and stays then rather flat (dashed line segment in the figure) until it drops quickly after about 800 ns. The round trip time for antiprotons at the mean energy of 800 eV is about 900 ns, which explains the large drop after about 800 ns since a large fraction of the trapped antiprotons has already been returned to the degrader before capture.

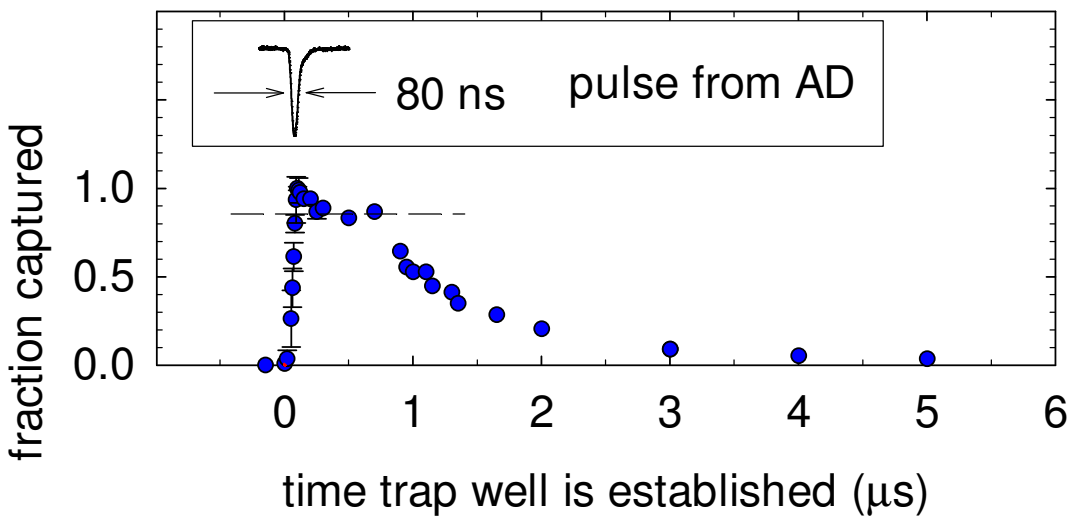


Figure 3.10: The number of trapped antiprotons is shown as a function of the time when the trapping potential is applied. It is obvious that the trap must be closed immediately after the bunch entered the trap. The graph is taken from [GBO<sup>+</sup>02c].

### 3.3.4 Electron Cooling of Antiprotons

In this section, it is described how the mean energy of the trapped antiprotons is reduced via interaction with stored electrons from about 800 eV to a mean energy corresponding to a temperature of 4.2 K. For this about four million electrons are loaded into either the potential structure depicted in Fig. 3.7b and c or into the potential structure which is depicted in Fig. 3.7 d. Antiprotons loaded into the long well by the same way as described above bounce back and forth the long well formed between HV and DEG and collide with the electrons. The kinetic energy of the antiprotons is transferred to the electrons which cool rapidly via synchrotron radiation to the 4.2 K environment as has been described in section 2.4.1. Due to this interaction, the energy of the antiprotons is reduced until they reside in the small electron wells. This cooling process is called electron cooling of antiprotons. We have carried out several experiments in order to understand this process in some detail.

In a first experiment, the potential  $V$  at the degrader is slowly ramped through zero after different electron cooling times. In that way the energy distribution  $dN/dV$ , which is the derivative of the number of antiprotons with respect to the potential, is measured as a function of the degrader voltage. The result is shown in Fig. 3.11 for specific electron cooling times. As can be seen, the number of antiprotons able to leave the trapping potential for a specific degrader voltage decreases with cooling time because more and more antiprotons are cooled into the small electron wells. Antiprotons which still leave the long well after a cooling time of 85 s are probably antiprotons with a large magnetron orbit and do not interact with the electron clouds which have typically a diameter of 8 mm.

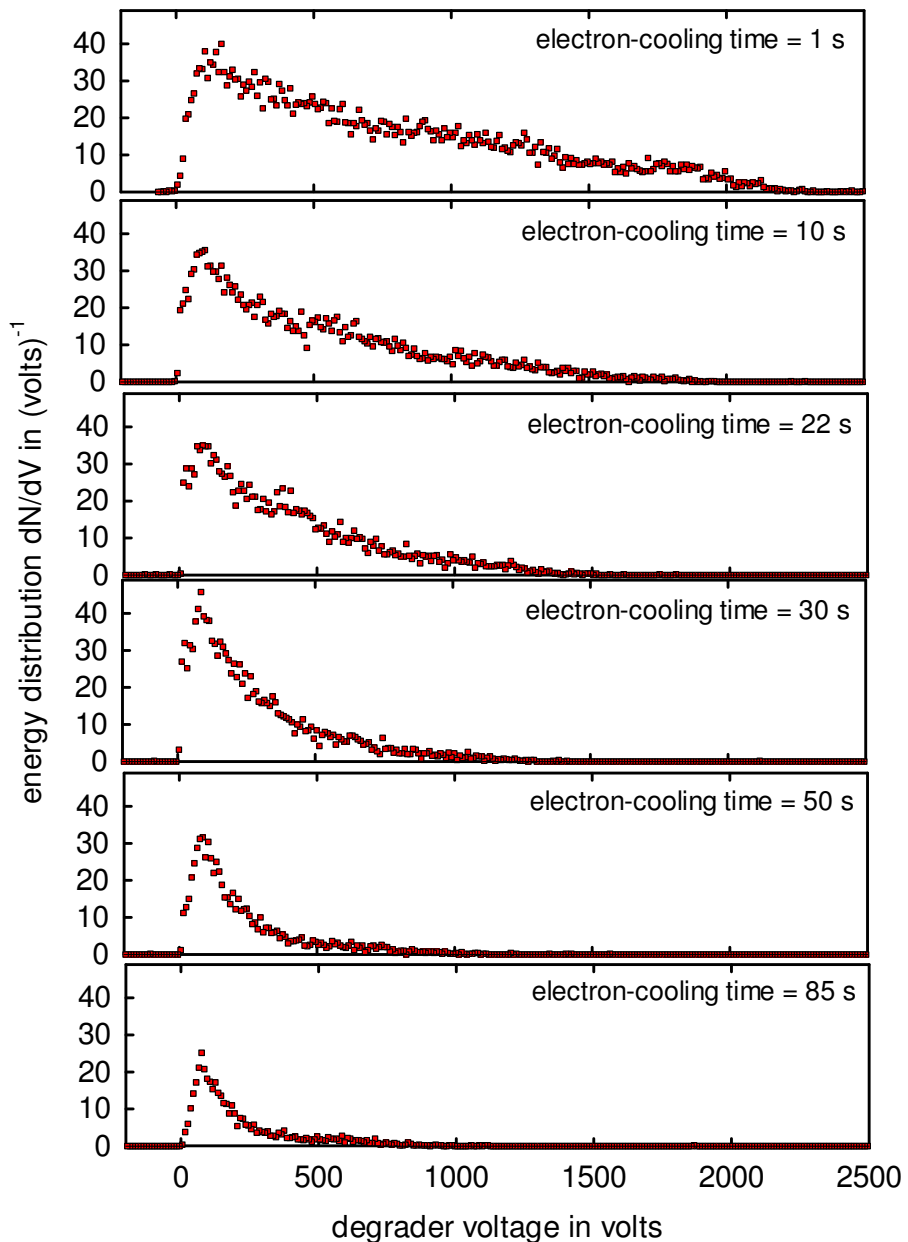


Figure 3.11: This series of pictures shows the energy distribution  $dN/dV$  of the antiprotons as a function of the degrader voltage for different electron cooling times. The number also decreases insofar as some antiprotons are cooled into the small well and others are lost from the trap [GBO<sup>+</sup>02c].

In a second experiment, the electrons are ejected from the small well after a cooling time of several minutes by opening the small well for about 100 ns. Since the electrons are lighter, they escape leaving the heavier antiprotons behind to be recaptured. The energy spectrum  $dN/dV$  of the electron-cooled antiprotons is then measured as a function of the degrader voltage and the result for a total number of 24 300 antiprotons is depicted in Fig. 3.9 b. The antiprotons have been cooled efficiently, since they spill out of the trap within a 14.2 meV change in degrader voltage. However, the actual width of the observed energy distribution is difficult to interpret. The electrons are in thermal equilibrium with their 4.2 K environment and the antiprotons in turn come to thermal equilibrium with the electrons. A 4.2 K energy width is only about 0.3 meV [GBO<sup>+</sup>02c] which is much smaller than the observed width. The width however depends also on space charge and a width of about 10 mV is estimated for 25 000 antiprotons [GBO<sup>+</sup>02c], which is only slightly smaller than the measured width of 14.2 meV. In conclusion for the experimental data presented in Fig. 3.9 b, about 24 300 antiprotons have been cooled by electrons to a temperature of approximately 4.2 K. Such large numbers can only be obtained from very intense AD pulses. In typical operating conditions 13 000-16 000 antiprotons can be trapped and cooled from a single AD pulse. Considering that the AD delivers about  $3 \times 10^7$  antiprotons at an energy of 5.3 MeV, this corresponds to a trapping efficiency of about  $5 \times 10^{-4}$  and a reduction of energy by ten orders of magnitude.

### 3.4 Stacking of Antiprotons

If more antiprotons are desired than the 13 000-16 000 which can be trapped from a single AD pulse it is necessary to accumulate antiprotons from more than one AD pulse. The method used to accumulate larger numbers of antiprotons is called stacking of antiprotons and is briefly discussed in the following. After a single bunch has been cooled into an electron well as described above the potential applied to the degrader can be lowered and a consecutive bunch of antiprotons can be loaded and electron cooled. This procedure can be repeated many times. In Fig. 3.12, the number of accumulated antiprotons is depicted as a function of the number of AD pulses. As indicated by the solid curve the number of trapped antiprotons rises linearly with the number of AD pulses. For the experimental data shown, about 13 400 antiprotons per bunch were trapped until about 430 000 antiprotons were accumulated in the Penning trap apparatus. The accumulation of one million antiprotons was demonstrated during the 2004 beam time and so far no variation from the linear dependence could be detected. Taken into account that an antiproton pulse arrives every 86 s it takes about one hour to accumulate 500 000 antiprotons and two hours to accumulate one million antiprotons. In conclusion, the method of stacking antiprotons is currently the only method to obtain large numbers (up to one million) of trapped antiprotons at cryogenic temperatures.

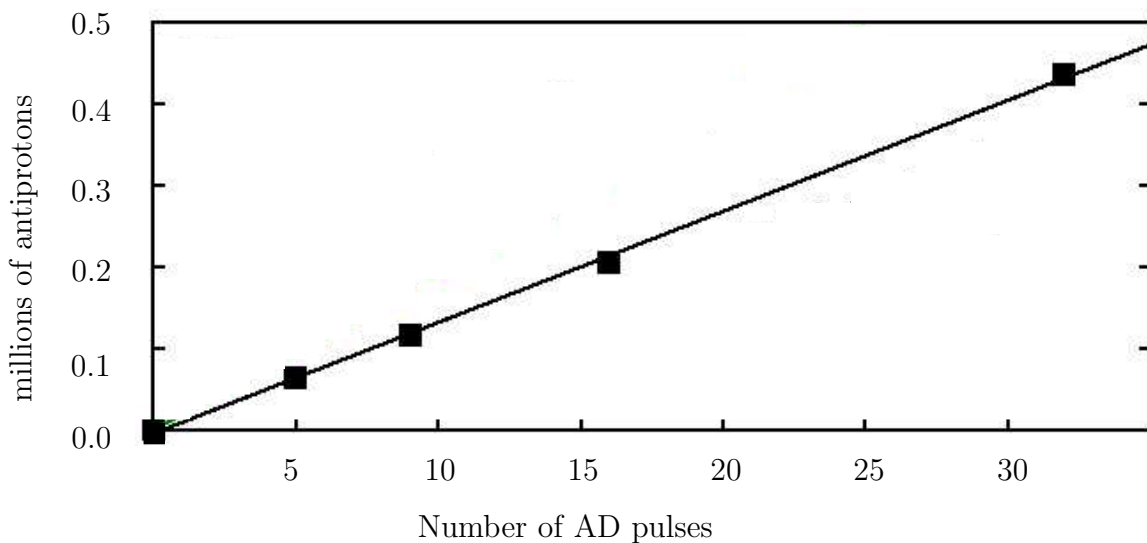


Figure 3.12: The number of antiprotons accumulated in the Penning trap is shown as a function of the number of antiproton pulses delivered from the AD. [GBO<sup>+</sup>02c].



# Chapter 4

## Antihydrogen Production in a Nested Penning Trap

In this chapter experiments are described by which antihydrogen atoms are produced during positron cooling of antiprotons [GET<sup>+</sup>01].

### 4.1 Introduction

In the preceding chapters, it has been described how antiprotons and positrons are accumulated in the Penning trap apparatus. The question now arises how antihydrogen atoms can be formed out of them. As a prerequisite the formation of antihydrogen from an antiproton and a positron requires the participation of a third body for energy and momentum to be conserved. The third “body” can for example be a photon. The properties of the so called radiative recombination process is discussed in section 4.1.1. A logical extension to the radiative recombination process is the stimulated radiative recombination process which is presented in 4.1.2. The third body can also be a positron. The properties of the so called three-body recombination (TBR) process are discussed in section 4.1.3.

#### 4.1.1 Antihydrogen Production by Radiative Recombination

In the radiative recombination process, antihydrogen is formed during the interaction of antiprotons and positrons by emission of a photon with the energy  $h\nu$  according to



where  $h$  is Planck's constant and  $\nu$  is the frequency. The formation rate per second and per antiproton is given by [GRHK88]

$$\Gamma_{RR} = 3 \times 10^{-11} \sqrt{\frac{4.2}{T}} n_{e^+}, \quad (4.2)$$

where  $T$  is the temperature given in Kelvin and  $n_{e^+}$  is the density of the positron plasma given in  $\text{cm}^{-3}$ .

For typical parameters of the ATRAP experiment,  $T = 4.2 \text{ K}$  and  $n_{e^+} = 2 \times 10^7 \text{ cm}^{-3}$ , a formation rate of  $\Gamma_{RR} = 6 \times 10^{-4} \text{ s}^{-1}$  and an antihydrogen production rate of  $N_{\bar{p}}\Gamma_{RR} = 60 \text{ s}^{-1}$  for  $N_{\bar{p}} = 100\,000$  antiprotons is obtained. The cross section for this process scales inversely to the third power of the principal quantum number of the recombined state and thus antihydrogen atoms in the ground state are preferentially created by this process [CEH<sup>+</sup>94].

#### 4.1.2 Stimulated Radiative Recombination

The formation rate of the radiative recombination process can be enhanced by exposing the interacting plasma clouds to intense laser light with frequency  $\nu$ , which stimulates recombination into a particular antihydrogen state with principal quantum number  $n$  according to



The production rate increases from  $\Gamma_{RR}$  to  $(1 + G)\Gamma_{RR}$ , where the gain  $G$  is given by [GRHK88]

$$G \approx 2 \cdot 10^{-5} \cdot n^5 \cdot I \quad (4.4)$$

for a positron plasma temperature of  $4.2 \text{ K}$  and for a laser intensity  $I$  given in  $\text{W/cm}^2$ .  $G$  is limited by photoionization at high  $n$  and by achievable laser intensities for stimulation into states with  $n \leq 8$  [GRHK88]. With laser light from a CO<sub>2</sub> laser recombination into the  $n = 11$  state can be stimulated. 10 W of laser light focused to a spot size of about 5 mm, which is a typical size of the interacting plasmas in the ATRAP experiment, yield a gain of  $G \approx 160$  and thus a total antihydrogen production rate of  $N\Gamma_{RR} \approx 9600 \text{ s}^{-1}$  for a positron density of  $n_{e^+} = 2 \times 10^7 \text{ cm}^{-3}$  and 100 000 antiprotons.

Though this process yields a higher formation rate, it is extremely difficult to implement in the Penning trap apparatus. The reason is that the current apparatuses are designed in a way that the only optical access is via optical fibers. Optical fibers for CO<sub>2</sub> lasers exists [Pol], but we did not put forward the idea to install any in the Penning trap apparatus for several reasons. The first reason is that the fiber is hollow and it is therefore extremely difficult to design vacuum feedthroughs. The second reason is that

the fiber is very rigid and therefore very difficult to bend from the vertical direction when running through the pinbase (compare Fig. 2.9 of the feedthrough for the silica fibers) to an angle of 30 degrees with respect to the vertical direction in order to mount the fiber end in a hole drilled into one of the electrodes so that the interacting particles could be exposed to laser light.

### 4.1.3 The Three–Body Recombination Process

A concurring process to radiative recombination is formation of antihydrogen via three–body collisions by which antihydrogen is formed in the collision between one antiproton and two positrons according to



so that one positron forms a bound state with the antiproton and the other positron carries away the excess energy and momentum. The collisional energy exchanged in this process is at the order of  $k_B T$  ( $\approx 0.36$  meV for  $T = 4.2$  K) and as a consequence the antihydrogen atoms are formed in highly excited states. De-excitation collisions stabilize this process but can only proceed to a binding energy of a few  $k_B T$  below the ionization limit [GO91]. The formation rate per second and per antiproton is given by [GRHK88]

$$\Gamma_{TBR} = 6 \times 10^{-12} \left( \frac{4.2}{T} \right)^{9/2} n_{e^+}^2, \quad (4.6)$$

where  $T$  is the temperature of the positron plasma given in Kelvin and  $n_{e^+}$  is the density of the positron cloud given in  $\text{cm}^{-3}$ . However, Glinsky and O’Neil [GO91] showed that this rate is reduced by a factor of about 10 because of the strong magnetic field present in the Penning trap. Thus a formation rate of  $\Gamma_{TBR} = 2400 \text{ s}^{-1}$  is obtained for typical parameters of the ATRAP experiment, namely a temperature  $T = 4.2$  K and a positron density of  $n_{e^+} = 2 \times 10^7 \text{ cm}^{-3}$ . The antihydrogen production rate is then  $N_{\bar{p}} \Gamma_{TBR} = 2.4 \times 10^8 \text{ s}^{-1}$  for  $N_{\bar{p}} = 100\,000$  antiprotons. This rate indicates that much more antihydrogen is produced via a TBR process than via a spontaneous recombination process.

It therefore seemed feasible to produce antihydrogen by merging simultaneously confined antiprotons and positron plasmas and relying upon the TBR process to occur. In order to let the two species of particles interact temporarily and spatially with each other, the concept of a nested Penning trap which is further discussed in section 4.2.1 has been proposed [GRHK88]. The ATRAP Collaboration could observe for the first time in 2001 positron cooling of antiprotons [GET<sup>+</sup>01] in a nested Penning trap, which has been a clear indication that the two species collisionally interact with each other, a prerequisite for the formation of antihydrogen via the TBR process. The challenge has

then been to detect any formed antihydrogen atom. An antihydrogen atom is electrically neutral and therefore free to leave the Penning trap. It annihilates when impinging for example at the trap electrodes. The most straightforward detection method, used by the ATHENA Collaboration [AAB<sup>+</sup>02] would then be to simultaneously detect the annihilation of an antiproton and a positrons by the detector system. In order to detect the 511 keV back-to-back  $\gamma$ -particles of the electron–positron annihilation events a segmented BGO detector (see Fig. 2.11a,b) was installed in addition to the fiber detector. Unfortunately, the antiproton annihilation events result in a large number of secondary interaction products including  $\gamma$ -particles and positrons from  $\gamma$  conversions. Therefore the background from pure antiproton annihilations is rather large. Due to the limited space a tracing system could not be installed which would improve the signal to background ratio as it is shown by the ATHENA experiment [AAB<sup>+</sup>02] where the annihilation vortex can be determined. An indication of antihydrogen production was observed with the BGO detector but the statistics and signal to noise ratio of about 1 : 3 was considered to be too low for a definite proof of antihydrogen production. Instead, the ATRAP Collaboration invented a method which relies on the field–ionization of antihydrogen and subsequent background–free detection. The first experiment carried out by the ATRAP Collaboration in fall 2002 and by which this detection method has been established is described in section 4.2. The method of field–ionization goes beyond a simple counting of antihydrogen atoms. It enabled us to measure the state distribution and the velocity of the antihydrogen atoms. These two experiments will be described in section 4.3 and in section 4.4, respectively. The chapter ends with a summary and conclusion, given in section 4.5.

## 4.2 First Observation of Antihydrogen Atoms

In this section, the experiment by which the ATRAP Collaboration has detected for the first time antihydrogen atoms produced during positron cooling of antiprotons [GET<sup>+</sup>01] in a nested Penning trap [GRHK88] is described. The result presented here has also been published in [GBO<sup>+</sup>02a].

### 4.2.1 The Experimental Setup

A cross sectional view of the lower electrode stack is shown in Fig. 4.1a. The electric potential applied to the electrodes is depicted in Fig. 4.1b and the corresponding electric field strength is given by the color code in Fig. 4.1a. The potential configuration can be divided into two regions. The electric potential from T1–T7 is used for the production of antihydrogen, while the ionization well at T8 and EET is used for the detection of antihydrogen. Central for the production of antihydrogen is the nested Penning trap [GRHK88] which is formed on the electrodes T4, T5, and T6. The nested Penning trap consists of a positron well at T5 which is centered between two potential wells for

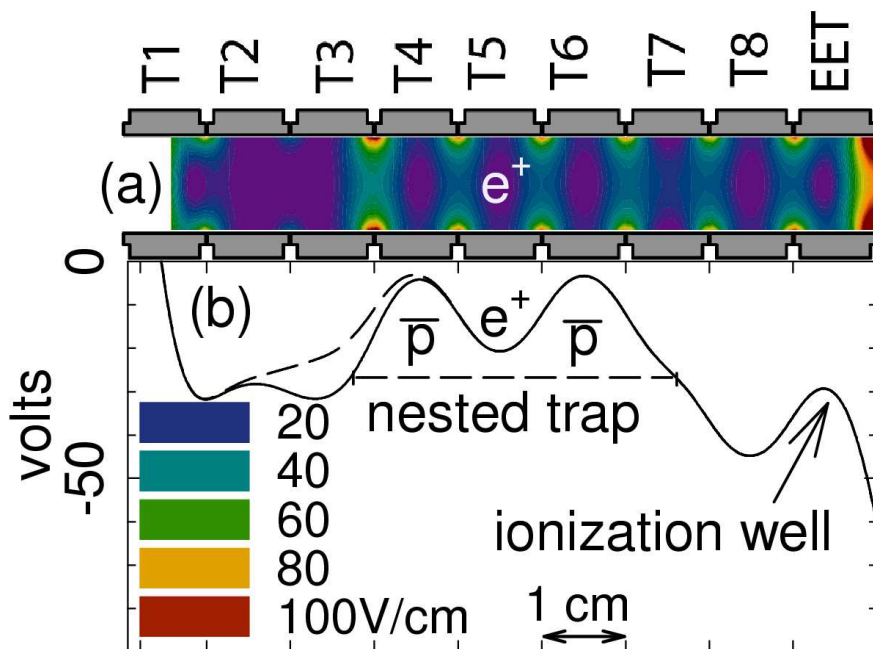


Figure 4.1: (a) A cross section of the bottom part of the hbar1 electrode stack as well as the electric field distribution due to the potential structure shown in (b) are depicted. (b) The potential along the central axis of the Penning trap. A nested Penning trap is constructed at the wells T4, T5, and T6. The antiprotons are launched into the structure from T2. An ionization well with a maximal electric field of 95 V/cm is constructed at EET.

antiprotons constructed at T5 and T6 in a way that the antiprotons are additionally axially confined by the long well between T4 and T6, which is indicated by the dotted line in Fig. 4.1b. A positron cloud is loaded into the potential well at T5. An antiproton cloud is initially stored in the potential well at the electrode T2. The antiprotons are launched into the nested Penning trap by pulsing the potential from the solid to the dashed form for  $1.5 \mu\text{s}$ . The antiprotons move then back and forth in the nested Penning trap and temporarily pass through the positron cloud. The antiprotons collisionally interact with the stored positrons and the kinetic energy of the antiprotons is transferred to the positrons which cool rapidly via synchrotron radiation to the 4.2 K environment. This process of positron cooling of antiprotons is similar to the electron cooling process used to accumulate antiprotons from the AD. A difference arises from the different sign of the electric charge of electrons and positrons. During the electron cooling process the antiprotons are cooled into the well of the electrons whereas during the positron cooling process the antiprotons are cooled into the side wells at T4 and T6 where interaction with the positron cloud stops. Any antihydrogen atom formed during this cooling process is due to its charge neutrality free to leave the nested Penning trap.

As mentioned in the introduction and as predicted theoretically [MK69, BM75, GO91, Fed97], the dominant antihydrogen formation process during the interaction of cold antiproton and positron plasmas is via the three-body recombination (TBR) process,  $\bar{p} + e^+ + e^+ \rightarrow \bar{H} + e^+$ . As a consequence the formed antihydrogen atoms are weakly bound. It is well known from experiments with Rydberg atoms [Gal93] that weakly bound atoms can be ionized by an electric field. Central to the detection region is the ionization well at EET. There, the maximum electric field is 95 V/cm. At the edge of the nested Penning trap, the maximum field strength is 35 V/cm. Therefore, any antihydrogen that passes through the ionization well and which ionizes at electric fields between 35 V/cm and 95 V/cm deposits its antiproton in the ionization well. The detection region is designed in a way that an antiproton alone cannot arrive in the ionization well since there is no mechanism for cooling. If an antiproton would have enough energy to climb over the potential hill at T8 (Fig. 4.1 b) it would bounce back and leave the trap at T1. The deposited antiproton remain stored in the ionization well until after positron cooling is completed in the nested well and the remaining antiprotons and positrons in the nested Penning trap are ejected in the direction away from the ionization well.

The antiprotons in the ionization well are ejected by ramping down the ionization well within 20 ms and the antiproton annihilations are detected by the detector system. The only background arises from cosmic rays that are on a rate of  $1.2 \text{ s}^{-1}$ . Since the ramp is so fast the cosmics contribute only 1 count in 50 and the antiprotons from the antihydrogen atoms are therefore detected background-free.

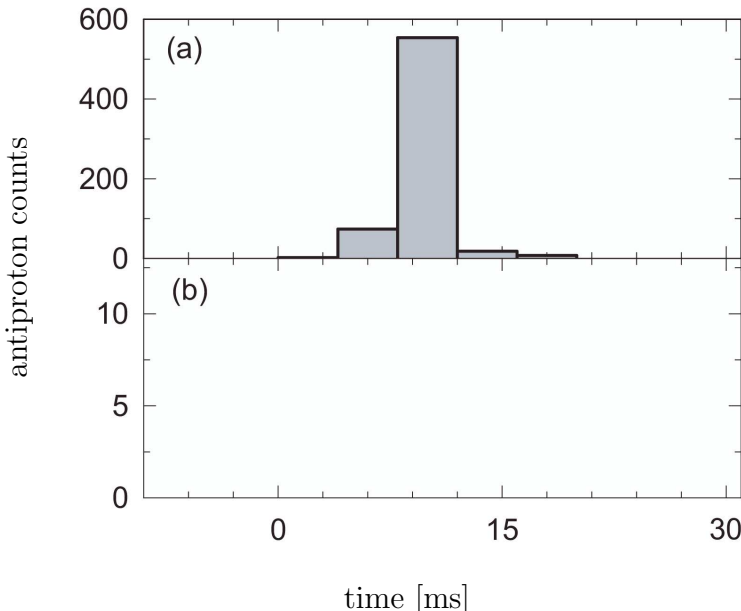


Figure 4.2: a) 657 antiproton counts in the ionization well within a time window of 20 ms with positrons in the nested Penning trap and b) zero counts seen without positrons.

#### 4.2.2 Experimental Results

Fig. 4.2 depicts the sum of all antiproton counts for the case a) with positrons present in the center of the nested Penning trap and b) without positrons. The data represents eleven trials with about 150 000 antiprotons per trial and 100 000 to 1.7 million positrons and 6 without positrons. In total 657 antihydrogen atoms have been detected within the 11 trials. Zero Counts have been observed for the case without positrons present in the center of the nested Penning trap. This clearly indicates that the potential structure ensures that an antiproton on its own cannot be trapped by the ionization well and that the antiprotons counts seen in the case with positrons present in the center of the nested Penning trap are from antihydrogen.

In conclusion, we have demonstrated by this experiment the production of antihydrogen atoms during positron cooling of antiprotons in a nested Penning trap and established the background-free detection method.

### 4.3 State Distribution of Antihydrogen

After antihydrogen has been detected, we focused on improving the production rate which lead to the invention of driving antiprotons over the positrons instead of releasing them from a side well. This method is briefly described in section 4.3.2. Due to the new production method, the production rate could be increased by more than an order

of magnitude so that about 500 to 3 000 antihydrogen atoms could be detected per experiment in the detection well. This large number enabled us to measure the state distribution of the antihydrogen (4.3.4) and as a side product, the dependence of the number of antihydrogen on the positron number could be measured (section 4.3.3). Many other results have already been reported in [GBO<sup>+</sup>02b, Oxl03, Bow03] and are therefore not presented here.

### 4.3.1 The Experimental Setup

A cross sectional view of the lower electrode stack of the hbar1 apparatus is shown in Fig. 4.3a. The potential and the corresponding electric field on axis is shown in Fig. 4.3b. The potential structure can be divided into several regions. The nested Penning trap which is used for the production of antihydrogen is formed between the electrodes T5 to EET and the potential structure and corresponding electric field on axis are additionally depicted in the inset in Fig. 4.3b. As can be seen from the inset, the magnitude of the electric field in the region of the nested Penning trap does not exceed 20 V/cm. To the left of the nested Penning trap, at the electrodes T2 to T4, a normalization well is constructed. This potential well structure is used for the detection of antihydrogen in the same way as the ionization well in the experiment described in section 4.2. The maximum electric field strength at the normalization well is 90 V/cm on axis and 120 V/cm 3 mm off axis. Any antihydrogen atom which leaves the nested Penning trap towards the normalization well and that ionizes at smaller electric fields is stripped while passing the normalization well and the freed antiproton is stored in the normalization well and is detected background-free later. To the right of the nested Penning trap, at the electrodes ER to B2, a state analysis region (indicated in Fig. 4.3b by pre-ionizing electric field) and a detection well are implemented. The electric field strength in the state analysis region is variable from 30 V/cm to 360 V/cm by changing the potentials on the corresponding electrodes. The maximum electric field strength at the detection well is 650 V/cm on axis and 860 V/cm 3 mm off axis. Any antihydrogen atoms which passes the pre-stripping field and which ionizes at lower electric fields deposits its antiproton in the detection well. The antiproton is detected background-free at the end of the experiment.

### 4.3.2 More Antihydrogen Atoms by Driving Antiprotons

The disadvantage of the experiment described in section 4.2 is that the antiprotons which have been cooled by the positrons finally reside in the antiproton wells of the nested Penning trap and interact not further with the positrons. In order to use antiprotons more efficiently, they are not any more launched from a separate well into the nested Penning trap but they are stored in the antiproton wells of the nested Penning trap, formed at T6 and T8 (see Fig. 4.3). A radio-frequency drive signal is applied

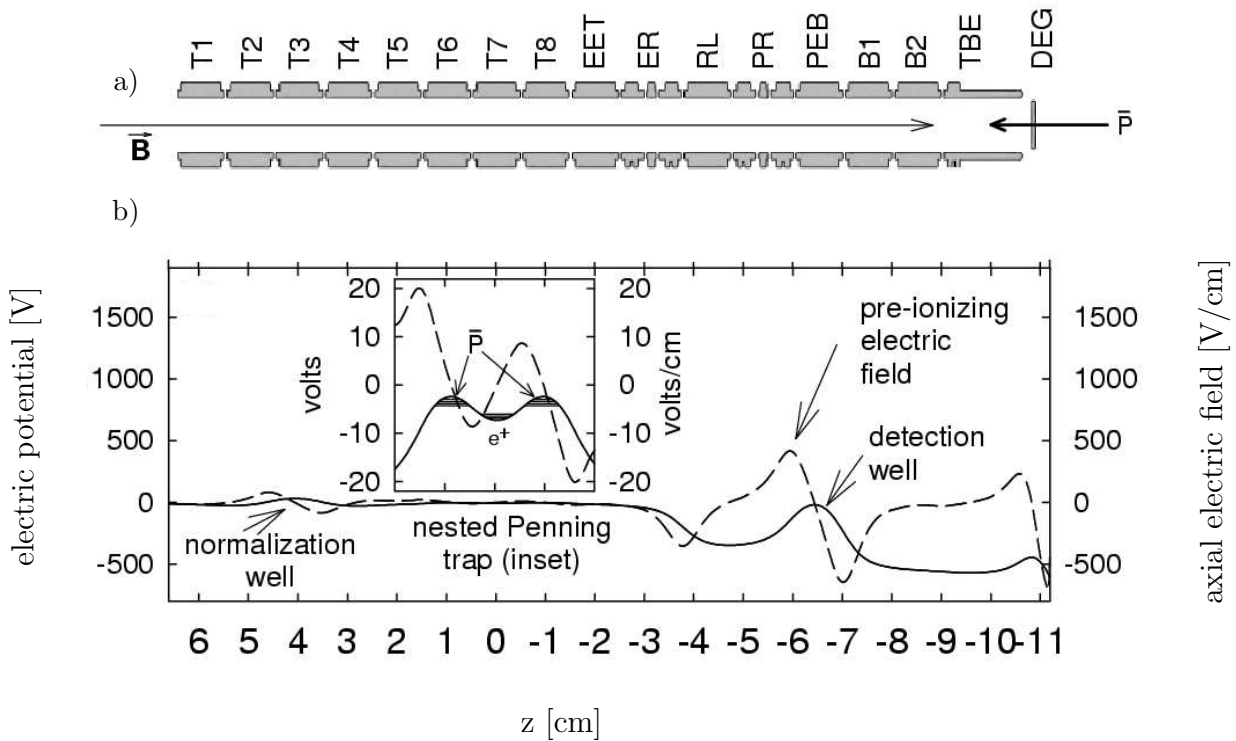


Figure 4.3: a) A cross sectional view of the lower electrode stack of the hbar1 Penning trap apparatus. b) Potential and corresponding electric field on axis used for the production and investigation of antihydrogen atoms.

alternatively to the electrodes T6 and T8 through which energy is put into the axial motion of the antiprotons. The resonance frequency of a single antiproton residing in a potential well of the nested Penning trap depends on its energy and on its position. The resonance frequency has been calculated for an antiproton on axis and 4 mm off axis by Paul Oxley in a numerical simulation [Oxl03] as a function of the antiproton energy and the result is shown in Fig. 4.4. As can be seen, a rf-frequency of 825 kHz (dotted line) is on resonance for both particle locations. A 1 V peak-to-peak drive at this frequency is applied up to 25 times alternatively for 10 s with 5 s without excitation in between to the electrodes T6 and T8. The driving capabilities of such a drive

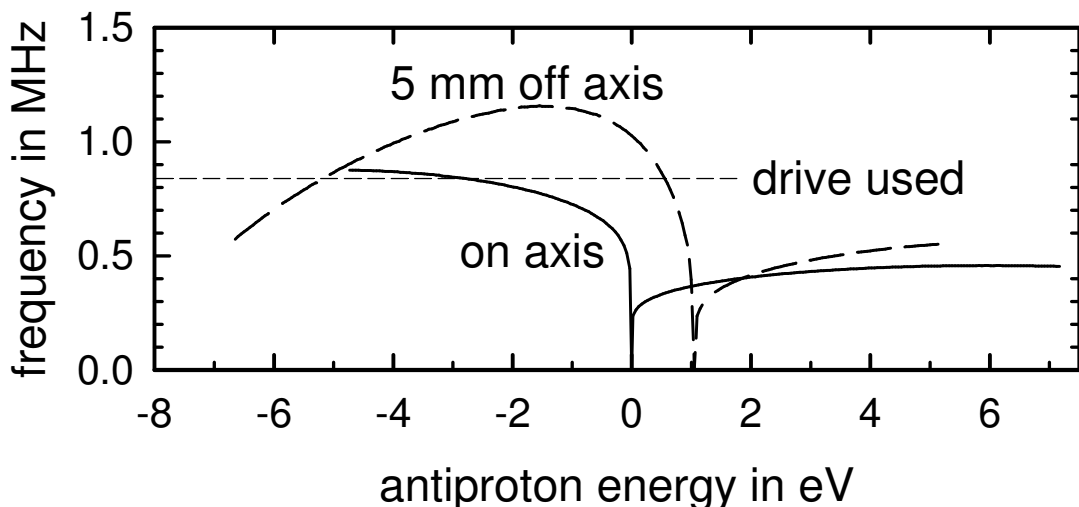


Figure 4.4: The axial oscillation frequencies in the side wells depend on the antiproton energy and radial position. The energy is calculated with respect to the energy on axis at the center of the nested well. The graph is taken from [GBO<sup>+</sup>02b].

are studied intensively by Paul Oxley and all details are presented in his PhD thesis [Oxl03]. In conclusion, due to the change of the experimental setup, from releasing the antiprotons from a side well into the nested Penning trap to driving them by a rf-drive, the antihydrogen production rate could be enhanced by a factor of 12 [GBO<sup>+</sup>02b]. For example, in a single experiment with 300 000 antiprotons and 2 million positrons, 718 antihydrogen atoms could be detected, which is more than the 657 antihydrogen atoms produced in eleven trials by releasing the antiprotons from a side well into the nested Penning trap as reported in section 4.2.

A very interesting result has been obtained from the analysis of an experimental trial with 290 000 antiprotons and  $4.5 \times 10^6$  positrons. In this trial we have detected 7600 antiprotons in the normalization well. The assumption that the antihydrogen atoms leave the nested Penning trap isotropically requires however about  $7600 \cdot 125 = 850\,000$  antiprotons for antihydrogen production, which is much more than the 290 000 used (The factor of 125 takes into account the solid angle of the detection well with respect

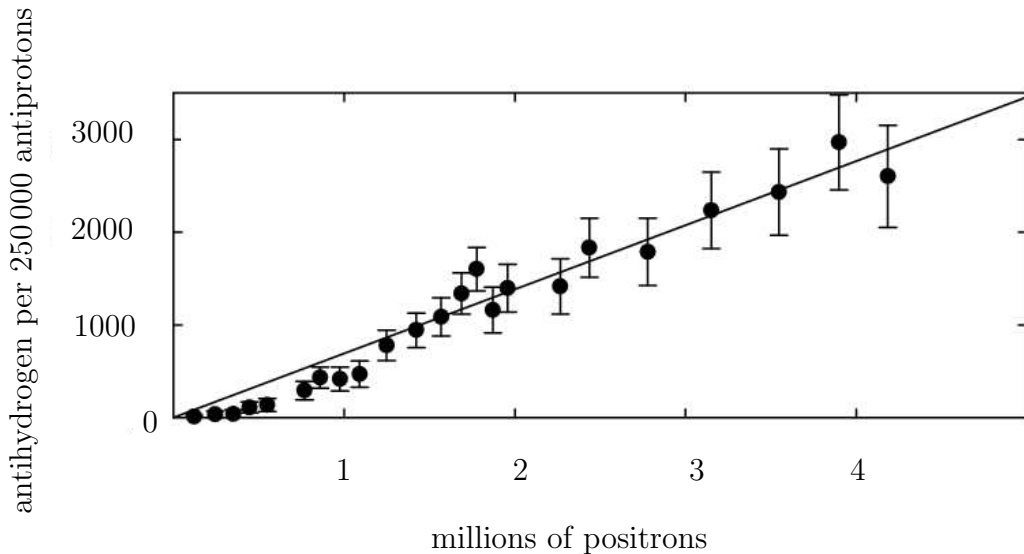


Figure 4.5: The number of antihydrogen atoms detected in the normalization well is shown as a function of the number of positrons used in the nested Penning trap for its production. The number of antihydrogen atoms is normalized to 250 000 antiprotons used in the nested Penning trap. The indicated uncertainties are statistical only, taking into account the statistical error in the measurement of the number of antiprotons in the normalization well as well as the statistical error in the measurement of the number of antiprotons in the nested Penning trap.

to the production region and the detection efficiency of the trigger counts as described in section 2.5.2.3). Thus the antihydrogen atoms are produced in a beam which is directed along the center axis of the Penning trap.

### 4.3.3 Dependence of Antihydrogen Production on the Number of Positrons

We have performed experiments over several weeks with about 300 000 antiprotons and a varying number of positrons using the driving method described above. The data can be used to investigate the dependence of the number of antihydrogen atoms detected in the normalization well on the number of positrons. The number of antiprotons (= number of antihydrogen atoms) detected in the normalization well is depicted in Fig. 4.5 as a function of the number of positrons. In order to compare the individual experiments, the number of antiprotons has been normalized with respect to 250 000 antiprotons in the nested Penning trap. As can be seen the number of antiprotons depends linearly on the number of positrons with a slight deviation from linearity for small numbers of positrons (< 1 million). In order to understand the linear dependence, the shape and density of the positron plasma have to be taken into account. The positron plasma shape and density have been studied by use of an aperture method, and the method

and results are published in [OBP<sup>+</sup>04, Oxl03], so that only a brief account is given in the following. In these studies, the positron cloud is pulsed through the aperture presented by the ball valve electrode of the hbar1 Penning trap apparatus (its inner diameter is only 6 mm, while the inner diameter of all other electrodes is 12 mm). From the measured transmission efficiency and the measured number of positrons, the shape and density of the plasma can be calculated by a numerical code written by Spencer et al. [SRV93] and Parrott [Par] which solves the Poisson equation self-consistently for charged particles confined in a Penning trap. These studies reveal that as the positron number increases from 1 million to 4.5 million particles the positron plasma diameter remains at 1 cm and the density remains within a few percent of  $2 \times 10^7 \text{ cm}^{-3}$ . The axial extent of the positron plasma however grows linearly from 1.5 mm to 3 mm. The antihydrogen production grows therefore linearly as the axial extent of the positron plasma. The observed deviation from linearity for less than one million positrons is due to the fact that the positron cloud still grows radially.

#### 4.3.4 The State Distribution of the Formed Antihydrogen

For the experimental results presented in the previous section, only the antihydrogen atoms stripped in the normalization well have been taken into account. When carrying out these experiments the electric field in the analysis region has been additionally varied from one experiment to the other between 30 V/cm and 360 V/cm. An antihydrogen atom stripped by the pre-ionizing electric field in the analysis region is unable to deposit its antiproton in the detection well and therefore the number of detected antihydrogen atoms in the detection well reduces with increasing electric field in the analysis region. The number of detected antihydrogen atoms is shown in Fig. 4.6 as a function of the maximum electric field  $F$  present in the state analysis region. The ordinate to the left gives the number of antihydrogen atoms normalized to 250 000 antiprotons and five million positrons. Such a normalization is possible because in each trial about 300 000 antiprotons have been used and a linear dependence of the produced number of antihydrogen atoms on the number of positrons has been measured as presented in the previous section. The ordinate to the right shows the number of detected antihydrogen atoms normalized to the number of antiprotons used in the nested Penning trap.

The number of antihydrogen atoms surviving an electric field  $F$  is proportional to  $F^{-2}$  or  $F^{-3/2}$  (see the dotted power laws in Fig. 4.6). This corresponds to state distributions  $dN/dF \propto F^{-3}$  or  $dN/dF \propto F^{-5/2}$ . This is a very interesting and important result for the understanding of the production mechanism, since the current theory of the three-body formation of antihydrogen [GO91, Fed97] cannot explain the measured distribution. A reason for the difficulties in the theoretical interpretation of the measured state distribution is that currently a numerical simulation of the antiproton–positron mixing process in a nested Penning trap seems unfeasible, because for a proper simulation the equations of motion during the mixing process have to be solved for each particle independently. In a particles' equations of motion the interactions of the particle with all

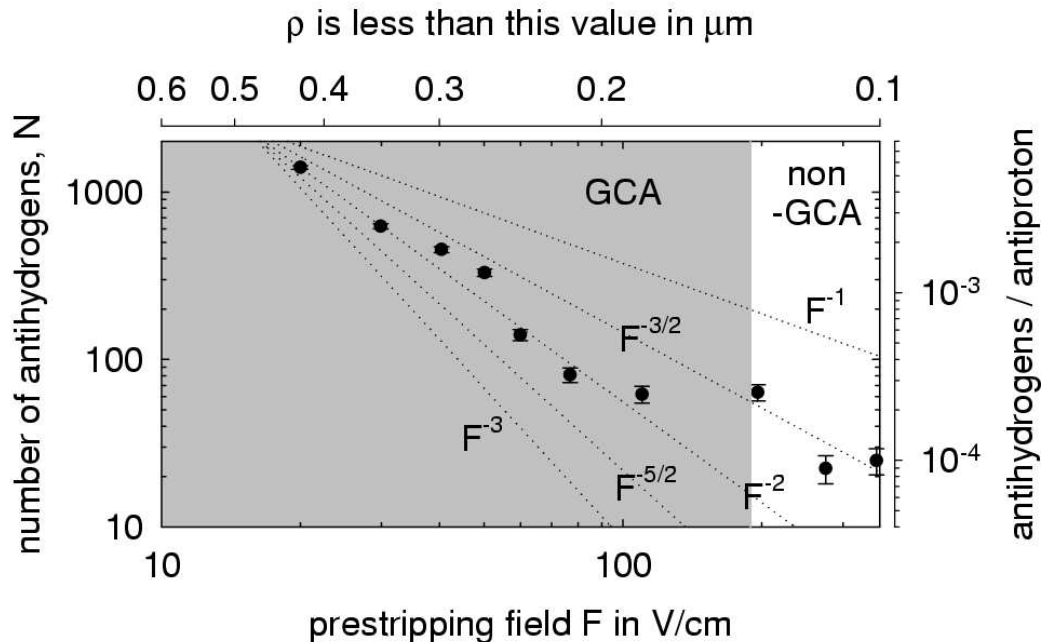


Figure 4.6: The number of antihydrogen atoms is shown as a function of the prestripping field  $F$  which the atoms have passed. The atoms can be characterized by their radial size  $\rho$ , which is less than indicated by the horizontal axis at the top. Antihydrogen atoms with radii in the gray-shaded region are guiding center atoms (GCA), while atoms with radii in the white region are non-GCA. The error bars are statistical due to the uncertainty in the detection of the antiprotons released from the detection well.

other particles have to be taken into account. Thus, a simulation of typical experiments with about one million positrons and about  $10^5$  antiprotons requires due to the relatively large number of particles storage and calculation time that are currently beyond the possibilities of modern computer technology. Moreover the physical interpretation of numerical simulations are intractable. Another reason for the difficulties in the theoretical interpretation of the measured state distribution is that so far theoretical treatments have only taken into account the relative simple model of guiding center atoms [GO91]. The interpretation of the measured state distribution requires probably the development of more advanced models. The results presented here have stimulated along with the results published by the ATHENA Collaboration new studies on the formation mechanism, see for example [Dri04, GBO<sup>+</sup>04, BD04, KO04a, KO04b, Rob04, RH04]. However, as mentioned above, so far no satisfying explanation for the measured state distribution has been found, see in particular [Dri04, GBO<sup>+</sup>04].

The electric field  $F$  by which an antihydrogen atom is ionized can be used to characterize the atoms. The most intuitive way to characterize an antihydrogen atom is by the

principal quantum state  $n$  to which the positron is excited. In the following a relation between  $F$  and  $n$  is derived. Consider an antihydrogen atom with the antiproton at the origin in the presence of an electric field in the z-direction. The potential experienced by the positron moving along the z-axis is given by the combined potential  $V(r)$  of the atomic core and the potential due the external electric field  $F$

$$V(r) = -qFr - \frac{q^2}{4\pi\epsilon_0 r}, \quad (4.7)$$

where  $q$  is the unit charge,  $\epsilon_0$  is the permittivity of the vacuum, and  $r$  is the classical distance between the positron and antiproton. The maximum potential energy is obtained by solving  $V'(r_{max}) = 0$  with respect to  $r_{max}$  and ensuring that  $V''(r_{max}) < 0$ . This yields  $r_{max} = \sqrt{\frac{q}{2\pi\epsilon_0 F}}$  and  $V_{max} = V(r_{max}) = -\frac{3q\sqrt{qF}}{2\sqrt{2\pi\epsilon_0}}$ . The energy of a positron in an atomic state with principal quantum number  $n$  is given by  $E(n) = -\frac{Ryd}{n^2}$ , where  $Ryd \approx 13.6$  eV is the Rydberg energy. The antihydrogen atom is ionized when the energy of the positron is larger than the maximum energy of the combined potential. The minimum electric field by which an antihydrogen atom in a state with principal quantum number  $n$  is stripped is then given by solving  $E(n) > V_{max}(F)$  for  $F$  which yields

$$F \geq 2.85 \times 10^8 \text{ V/cm} \times \frac{1}{n^4}. \quad (4.8)$$

The quantum state which are ionized can be obtained by solving  $E(n) > V_{max}(F)$  for  $n$  which yields

$$n \geq \sqrt[4]{\frac{2.85 \times 10^8 \text{ V/cm}}{F}}. \quad (4.9)$$

As shown in Fig. 4.6, antihydrogen atoms that have passed a pre-stripping field between 30 V/cm and 360 V/cm are detected. Atoms that are not ionized by an electric field of 30 V/cm are according to Eq. 4.9 in an atomic state with  $n \leq 55$ . Antihydrogen atoms which have passed a pre-stripping field of 360 V/cm are in a state with  $n \leq 29$ . A lower limit of the detected quantum states is given by  $n \geq 24$  set by the maximum electric field of the detection well, which is 860 V/cm.

The characterization of the detected highly excited antihydrogen atoms by the principal quantum number  $n$  is very intuitive and practical for any further estimates, as for example presented in chapter 5. However, due to the presence of the magnetic field of the Penning trap  $n$  is not a good quantum number for such highly excited states. The reason is that at a magnetic field strength of about [RGHW94]

$$B_{critical} \approx 8.3 \left(\frac{30}{n}\right)^3 \text{ T}, \quad (4.10)$$

the Lorentz force acting on the positron is of similar size as the Coulomb force caused by the atomic core on the positron. The Lorentz force cannot be treated as a perturbation

and as a consequence  $n$  is not a good quantum number [RGHW94]. Using the magnetic field of the Penning trap,  $B_0 = 5.3$  T, Eq. 4.10 can be solved for  $n$ , which yields  $n \approx 35$ , confirming that the detected antihydrogen atoms are in the regime, where  $n$  is not a good quantum number.

Due to the mixing of the highly excited  $n$ -states a different approach for the description of the formed antihydrogen atoms had to be developed, which is a reason why the theory of TBR-processes in nested Penning traps is so challenging. Progress has been made by a recent theory paper [VGP<sup>+</sup>04] which discusses field-ionization of antihydrogen atoms in a strong magnetic field. The authors suggest to characterize the highly excited and highly magnetized antihydrogen atoms by their radius  $\rho = \sqrt{x^2 + y^2}$  in the plane perpendicular to the magnetic field of the Penning trap. According to [VGP<sup>+</sup>04], an antihydrogen atom which survives an electric field  $F$  has a radius  $\rho$  smaller than

$$\rho = \frac{a^{1/4}}{2\sqrt{F}} \sqrt{\frac{q}{\pi\epsilon_0}} \quad (4.11)$$

where  $a = \left(\frac{4}{27}\right)^{1/4} \approx 0.62$ ,  $q$  is the unit charge and  $\epsilon_0$  is the permittivity of the vacuum. The maximum atomic radius, determined by Eq. 4.11 is indicated by the horizontal axis at the top of Fig. 4.6. As can be seen, a typical radius of the detected antihydrogen atoms is in the range between  $0.4 \mu\text{m}$  and  $0.15 \mu\text{m}$  and the radius of the deepest bound atoms is less than  $0.1 \mu\text{m}$ .

As mentioned before, the formation of the highly excited antihydrogen atoms is probably due to the three-body recombination (TBR) process and subsequent collisional de-excitation. Theoretical studies carried out by Glinsky and O'Neil [GO91] and by Fedichev [Fed97] have used the model of guiding center atoms (GCA) in order to describe the formed antihydrogen atom. The guiding center approximation however breaks down for an atomic radius of  $\rho < 0.14 \mu\text{m}$  [GSS<sup>+</sup>05] and the orbit of the positron is chaotic [DKN84]. For more clarity the antihydrogen atoms for which GCA is a reasonable approximation are separated by the grey shaded part of Fig. 4.6, while non-GCA lie in the white part the graph. We have thus for the first time produced and detected antihydrogen atoms which are too deeply bound to be described by the GCA-model. So far no theory exists to explain the formation of such deeply bound antihydrogen atoms.

## 4.4 Measuring the Velocity of Antihydrogen Atoms

In addition to the measurement of the state distribution, the velocity of the antihydrogen atoms could also be measured during the beam time 2003. The experimental result is published in [GSS<sup>+</sup>04] and will be briefly described and discussed in this section.

#### 4.4.1 Experimental Setup

The experimental setup is shown in Fig. 4.7a–d. Fig. 4.7a shows the lower part of the hbar1 electrode stack and the potential which is present on the center axis is depicted in Fig. 4.7b. The corresponding electric fields on axis and 3 mm off axis are shown in Fig. 4.7c and d, respectively. The potential structure and electric fields can be divided into several regions. The nested Penning trap used for antihydrogen production is constructed between the electrodes T5 and EET, while a normalization well is designed at T3 which is used for antihydrogen detection. As can be seen the maximum electric field in the normalization well is 85 V/cm on axis and 120 V/cm off axis and any antihydrogen which passes through this well and which ionizes at lower fields deposits its antiproton in the normalization well. The stored antiproton is detected at the end of the experiment background-free in the same way as in the experiments described above. The potential structure formed between the electrodes RL and TBE is used for measuring the velocity of antihydrogen. It consists of a pre-stripping field and a subsequent detection well. The pre-stripping field consists of a static component  $F_{DC}(\rho, z)$  and a time varying component  $F_{AC}(\rho, z)\cos(\omega t + \Phi)$ , which are both functions of the radial coordinate  $\rho = \sqrt{x^2 + y^2}$  and the axial coordinate  $z$  with respect to the magnetic field. The dashed and the dotted curve in Fig. 4.7c and d show the maximum variation in amplitude of the pre-stripping field. As can be seen, the maximum electric field in this region does not exceed 65 V/cm on axis and 85 V/cm 3 mm off axis. Therefore, according to the results presented in section 4.3.4, only the weakest bound atoms are sensitive to the electric fields in this region and therefore only the velocity of these atoms is measured. The idea of the velocity measurement is rather simple. Consider such a weakly bound antihydrogen atom which could be ionized by the maximum pre-stripping field traveling from the nested Penning trap towards the detection well. The probability that the electric field is high enough to strip the atom while it moves through the pre-stripping region increases with frequency  $\omega$  of the AC-component of the electric field. The number of antihydrogen atoms detected in the detection well therefore decreases with increasing  $\omega$  which allows to determine the velocity of the atoms by comparing the experimental data with a model as presented below.

#### 4.4.2 The Experimental Results

For the experimental results presented here, typical 250 000 antiprotons and 400 000 positrons have been accumulated and mixed in the nested Penning trap. Fig. 4.8 shows the fraction of antihydrogen atoms detected in the detection well relative to the number measured in the normalization well as a function of the oscillating pre-stripping well. For the result represented by the open square, no frequency is associated with it. It is the ratio of counts in the detection well to the normalization well with the oscillating field turned off. The solid points are measured with the oscillating fields turned on. The vertical scale for Fig. 4.8. is chosen so that the measurement with no oscillating field is

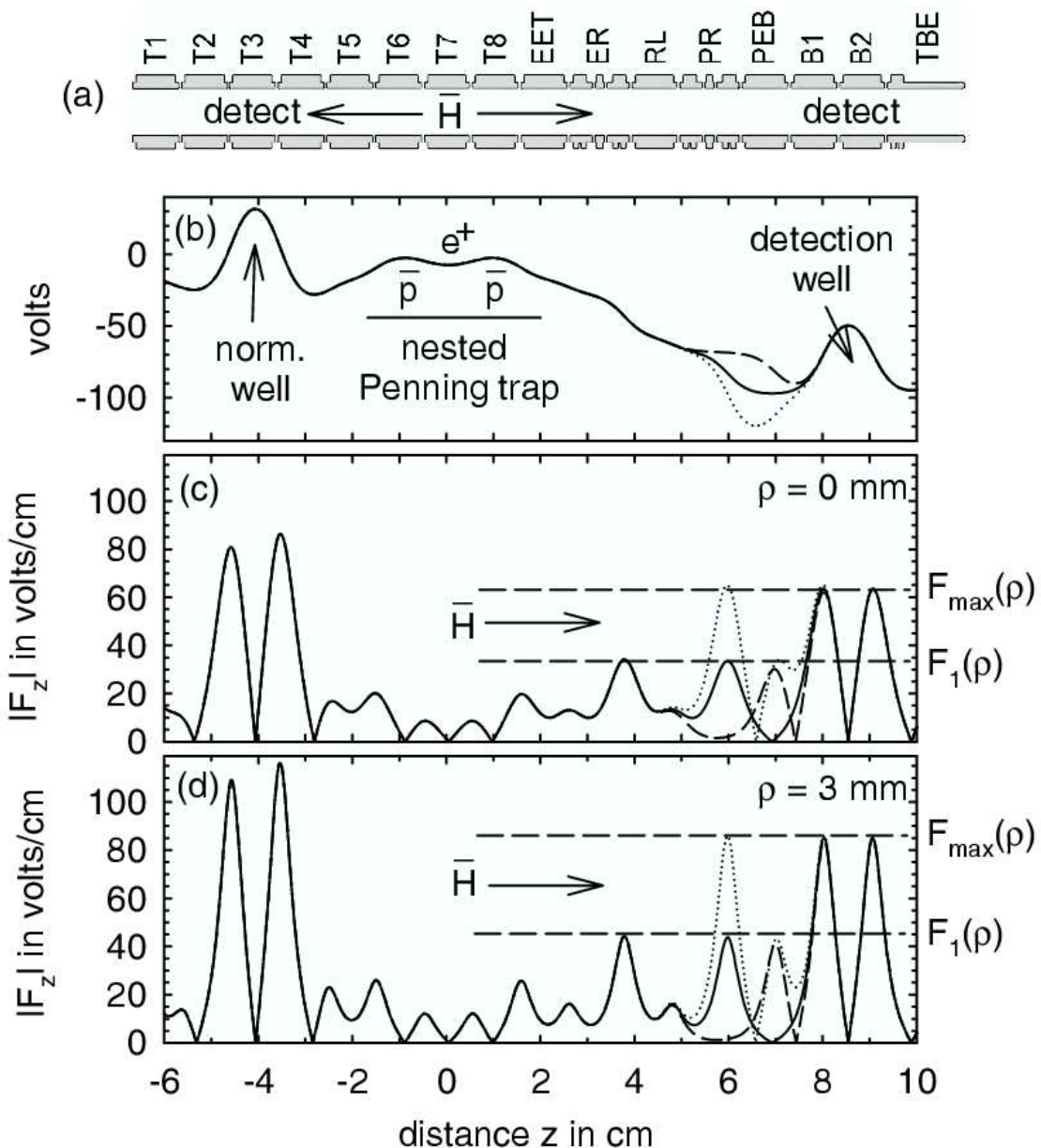


Figure 4.7: a) Cross section of the lower electrode stack of the hbar1 apparatus. b) Potential on axis and the magnitude of the electric field on axis (c) and 3 mm off axis (d). The solid curves are the static potentials and the fields magnitudes. The dashed and dotted curves show the maximum variation of these when the oscillating potential is added [GSS<sup>+</sup>04].

consistent with 1 and that the measured  $\omega \rightarrow 0$  limit is consistent with 0.62. The latter is the fraction of the time that the magnitude of the oscillating electric field, along the trajectory of an antihydrogen atom traveling to the detection well, is less than the maximum static field along this path. In this limit 0.62 of all the antihydrogen atoms traveling to the detection well should thus not be ionized by the oscillating field.

#### 4.4.3 Discussion of the Experimental Results

In order to determine a velocity of the antihydrogen atoms from the experimental data shown in Fig. 4.8, we have developed a simple numerical model. Consider that  $N(\rho, v, F) d\rho dv dF$  antihydrogen atoms are produced at  $z=0$  and  $t=0$  within a radius of  $\rho$  and  $\rho + d\rho$ , with a velocity towards the detection well between  $v$  and  $v + dv$ , and in an atomic state which ionizes at a electric fields between  $F$  and  $F + dF$ . Without a time varying field, the antihydrogen atom experience  $F_{DC}(\rho, z = vt)$  on their way to the detection well. The number of antihydrogen atoms detected is then

$$N_0 = \int_0^\infty d\rho \int_0^\infty dv \int_{F_{DC}(\rho)}^{F_{max}(\rho)} N(\rho, v, F) dF. \quad (4.12)$$

A value for  $\rho_{max}$  is given below and  $F_{max}(\rho)$  is the maximum electric field present in the detection well.

When the time varying component of the pre-stripping field is switched on, then the atoms which travel towards the detection well pass an electric field given by

$$F(\rho, z, \omega/v, \Phi) = F_{DC}(\rho, z) + F_{AC}\rho, z \cos\left(\frac{\omega z}{v} + \Phi\right). \quad (4.13)$$

The number of detected antihydrogen atoms is then given by

$$N = \int_0^\infty d\rho \int_0^\infty dv \int_0^{2\pi} \frac{1}{2\pi} d\phi \int_{F'(\rho, \omega/v, \phi)}^{F_{max}(\rho)} N(\rho, v, F) dF \quad (4.14)$$

The lower border of the last integral,  $F'(\rho, \omega/v, \phi)$  is the maximum field magnitude that the antihydrogen atoms encounter in the pre-stripping region.

In order to derive a numerical result, we assume that the antihydrogen atoms are produced uniformly out to a radius of  $\rho_{max} = 3$  mm, which is approximately the radius of a positron plasma cloud with 400 000 positrons. We also assume that  $N \propto F^{-3}$  which has been measured by the experiment presented in section 4.3.4. Additionally it is assumed that all antihydrogen atoms have a velocity of  $v_0$ . We therefore obtain

$$N(\rho, v, F) = \frac{2\rho}{\rho_{max}^2} \delta(v - v_0) F^{-3}. \quad (4.15)$$

The integral given in Eq. 4.12 is then solved numerically by usage of the approximations for  $F_{DC}(\rho)$  and  $F_{max}(\rho)$  and by use of Eq. 4.15. The result is depicted in Fig. 4.8 by the

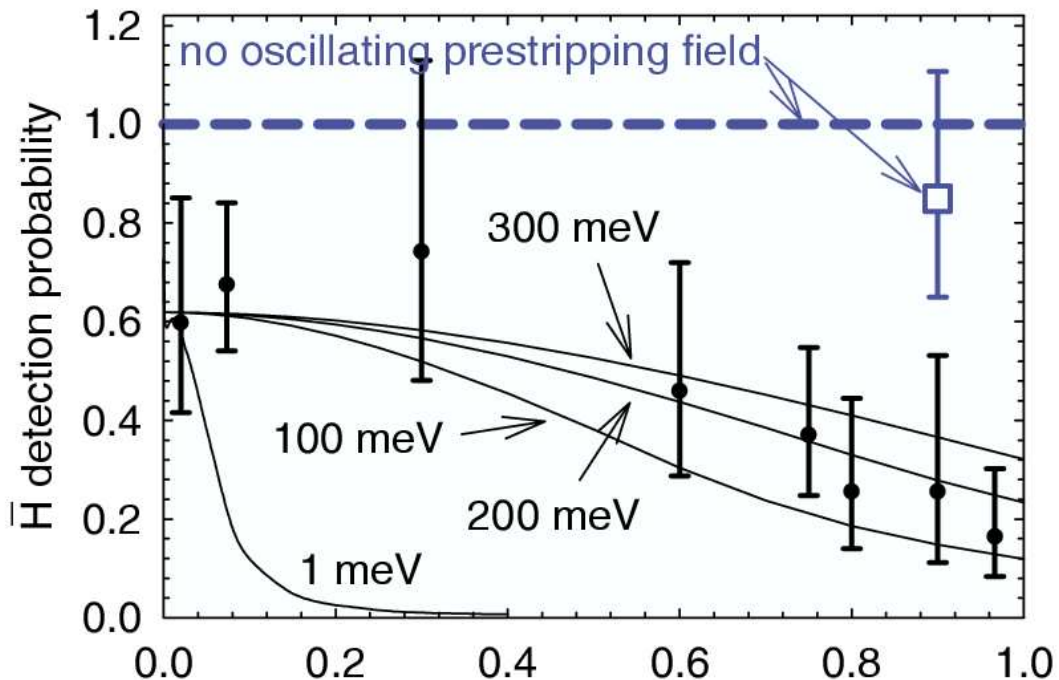


Figure 4.8: The fraction of the antihydrogen atoms detected in the detection well relative to the number detected in the normalization well is shown by the solid points as a function of the frequency  $\omega/(2\pi)$  of the oscillating pre-stripping field [GSS<sup>+</sup>04]. The error bars are statistical due to the uncertainties in the determination of the number of antiprotons in the normalization and detection well. The open square shows a measurement with the oscillating field switched off. The measured points are compared to a simple model discussed in the text (solid curve), which reveals that the average kinetic energy of the antihydrogen atom is about 200 meV.

blue dashed curve. The scale in that graph is chosen so that the curve is at a detection probability of one. The integral given in Eq. 4.14 is also solved numerically by usage of the approximations for  $F'(\rho)$  and  $F_{max}(\rho)$  and by use of Eq. 4.15. The solid curves in Fig. 4.8 show the functional behavior of the integral for several velocities  $v_0$ . The velocities are given in the graph via the corresponding kinetic energy  $1/2m_{\bar{H}}v_0^2$ , where  $m_{\bar{H}}$  is the antihydrogen mass. As can be seen a kinetic energy of 200 meV is a good fit to the experimental data. This result is rather insensitive to the assumptions. For example, if we had assumed that all antihydrogen atoms are produced on the central axis, then best fit would correspond to a kinetic energy of 100 meV. If we had assumed that all antihydrogen is produced 4 mm off axis, then we would have concluded that the antihydrogen velocity is about 300 meV. 200 meV correspond to an antihydrogen temperature of about 2300 K, which is much higher than the 0.36 meV kinetic energy corresponding to a temperature of 4.2 K.

The measured average antihydrogen energy of 200 meV corresponds to an antihydrogen velocity of about 6200 m/s. It is up to now unknown if this relative high velocity is caused by the rf-signal used to drive the antiprotons over the positrons or whether such a high velocity is characteristic of this production method. An antiproton speed that seems important for antihydrogen formation is the one that equals the most probable speed of the positrons, because in this case a relative large fraction of the positrons move collinearly with the antiprotons when these pass the positron cloud and one would expect an increased antihydrogen production. The most probable positron velocity  $v_{e^+}$  for a temperature of  $T = 4.2 \text{ K}$  is given by

$$v_{e^+} = \sqrt{\frac{2k_B T}{m_{e^+}}} \approx 11300 \text{ m/s}, \quad (4.16)$$

where  $k_B$  is the Boltzmann constant and  $m_{e^+}$  is the mass of a positron. The most probable positron velocity is about a factor of two larger than the measured velocity of the antihydrogen atoms.

Another important antiproton speed can be calculated from the average rate of deexcitation collisions [GO91] between an initially bound positron and another positron. The expected  $e^+ - e^+$  collision rate should be of order  $n_{e^+}(\pi b^2)v_{e^+}$  [GO91], where  $n_{e^+} = 1.6 \times 10^7 \text{ cm}^{-3}$  is a typical positron density and  $v_{e^+}$  is the positron velocity calculated above. The distance of closest approach  $b$  comes from equating the potential energy  $\frac{e^2}{4\pi\epsilon_0 b^2}$  between two positrons and the thermal energy  $k_B T$ . This yields a collision rate of about  $9 \times 10^6 \text{ s}^{-1}$  and hence a mean time between two collisions of about  $t = 1.1 \times 10^{-7} \text{ s}$ . Thus for a least one deexcitation collision to occur while passing a positron plasma of a typical size  $s \approx 1 \text{ mm}$ , the antiproton velocity has to be lower than  $v' = s/t \approx 9100 \text{ m/s}$ , which is about 1.5 times larger than what has been observed experimentally. From this simple model the conclusion can therefore be drawn that the weakest bound atoms of which we have measured the velocity are formed from only one deexcitation collision. Notice that the antiproton speed  $v'$  scales as  $n_{e^+} s T^{-3/2}$ . Hence

a positron plasma with lower density, shorter length and higher temperature should produce –somehow counter-intuitively – antihydrogen atoms with lower velocities.

Antihydrogen with lower velocities might also be produced by driving the antiprotons so that they have just enough energy to go through the positron plasma. In addition, the positrons can be kept in a deep potential well so that weakly bound antihydrogen atoms will strip at the edge of the well, thereby giving the antiprotons further time to cool and to form more deeply bound states.

In conclusion, the average velocity of the most weakly bound atoms has been measured to about 6200 m/s which corresponds to a kinetic energy of about 200 meV. These atoms are far too hot to be trapped in a neutral particle trap, which requires atoms below a temperature of 1 K [Wal93]. A simple model suggest that the antihydrogen atoms are formed from a single deexcitation collision. By use of a lower density and shorter and hotter positron plasma, a weaker rf-drive, and deeper potential wells of the nested Penning trap the temperature of these atoms might be reduceable.

## 4.5 Summary and Conclusion

In this chapter experiments have been presented by which antihydrogen atoms are formed during positron cooling of antiprotons in a nested Penning trap. From a comparison of the number of antiprotons detected in the detection well with the number of antiprotons used for antihydrogen formation it could be deduced by taking into account the detection efficiency and the solid angle of the detection well with respect to the production region that the antihydrogen atoms are formed in a beam which is directed along the center axis of the Penning trap. A new detector system which is currently constructed for the new Penning–Ioffe trap apparatus and which will probably be available for beamtime 2006 allows to track the locations of the antihydrogen annihilation events. By use of this detector system it should therefore be possible in the future to investigate the properties of the antihydrogen beam in detail.

A linear dependence of the number of detected antihydrogen atoms on the number of positrons could be established. Additionally, the state distribution of the antihydrogen atoms could be measured, revealing that the antihydrogen atoms are produced in highly excited states. The high production rate and the highly excited states suggest that these atoms are produced via three-body recombination processes and subsequent collisional deexcitations. However, the current theory cannot yet account for the measured state distribution, which is  $dN/dF \propto F^{-3}$  or  $dN/dF \propto F^{-5/2}$ . Reasons for the difficulties in interpreting the experimental results are as discussed in detail above that it is currently impossible to numerically simulate the antiproton–positron mixing process in a nested Penning trap mainly due to the large numbers of particles involved and that so far theoretical treatments have only taken into account the relative simple model of guiding center atoms [GO91]. The results of the

ATRAP Collaboration have however stimulated along with the results published by the ATHENA Collaboration new studies of the formation mechanism, see for example [Dri04, GBO<sup>+</sup>04, BD04, KO04a, KO04b, Rob04, RH04] and certainly many more will follow. A theoretical paper by Vrinceanu et al. [VGP<sup>+</sup>04] suggests to characterize the highly excited and highly magnetized antihydrogen atoms by their radii in the plane perpendicular to the magnetic field of the Penning trap which yields typical radii of the detected antihydrogen atoms in the range between  $0.4\text{ }\mu\text{m}$  and  $0.15\text{ }\mu\text{m}$ . The radii of the deepest bound atoms are below  $0.1\text{ }\mu\text{m}$ . According to [GSS<sup>+</sup>05] the GCA approximation breaks down for atomic radii below  $0.14\text{ }\mu\text{m}$  and hence antihydrogen atoms that are too deeply bound to be described by the GCA–model have been detected for the first time.

The kinetic energy of the weakest bound atoms could be measured to about 200 meV which corresponds to an antihydrogen velocity of about 6200 m/s. The kinetic energy of these atoms is too hot to allow trapping in a neutral particle trap. For at least one deexcitation collision to occur while passing through a 1 mm positron cloud, the antihydrogen velocity needs to be below 9100 m/s, a velocity that is comparable with the measured antihydrogen velocity. Thus the weakest bound antihydrogen atoms are probably formed from only one deexcitation collision. The simple model given in section 4.4 suggests that a positron plasma with lower density, shorter length and higher temperature should produce – somehow counter–intuitively – antihydrogen atoms with lower velocities. Moreover, by use of a weaker rf–drive and deeper potential wells for the nested Penning trap the mean antihydrogen velocity might be reduceable.

# Chapter 5

## Trapped Antiprotons exposed to Laser Light

### 5.1 Introduction

In this chapter experiments in which trapped antiprotons have been exposed to laser light are presented. These experiments have been carried out against the background of the future ATRAP project to confine antihydrogen atoms in a combined Penning–Ioffe trap and then to carry out laser spectroscopy on the stored antihydrogen atoms. A consequence of the ultra-low pressure of about  $5 \times 10^{-17}$  torr (section 2.4.2) that exists in the trap can is the long lifetime of trapped antiprotons. Similar lifetimes of trapped antiprotons are expected because the collision cross section of antiprotons and antihydrogen atoms with background gas are of similar size. Laser light in the trap might however cause an increase of the pressure for example by liberating adsorbed gases from cryogenic surfaces. The purpose of the experiments presented in this chapter is therefore to investigate if laser light induces any extra loss on trapped antiprotons and therefore to investigate if laser experiments on trapped antihydrogen might be feasible. For these experiments, a Titanium:Sapphire laser system has been built which is described in section 5.2. In order to deliver the laser light into the inside of the hbar2 electrode stack, new electrodes have been designed which are presented in section 5.3. The experimental studies carried out on trapped antiprotons are presented in section 5.4. The chapter ends with a summary and conclusion given in section 5.5.

### 5.2 The Titanium:Sapphire Laser System

In this section, the design and the specifications of the Titanium:Sapphire laser system are presented. The laser system is depicted schematically in Fig. 5.1. It consists of the

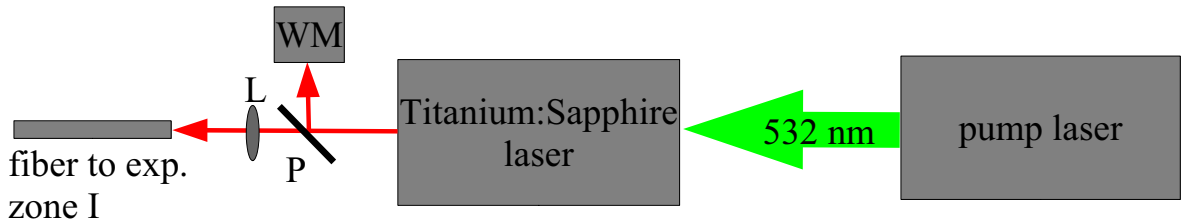


Figure 5.1: Setup of the Titanium Sapphire laser system. The pump laser is a Coherent Corona, which emits green light at 532 nm. P is a glass plate which is AR-coated on one side. A fraction of about 4% of the laser power is deflected from P and used to measure the wavelength via the wavemeter (WM). The remaining laser power is focused by a lens (L) with focal length of 5 mm into the type II optical fiber that guides the light into zone I.

actual Titanium:Sapphire laser and a pump laser, which is a Coherent Corona laser, a commercial, Q-switched, diode-pumped, intra-cavity frequency doubled Nd:YVO<sub>4</sub> laser. This laser was borrowed from the group of Kjeld Eikema (Vrije Universiteit, Amsterdam, NL). It emits green laser light at a wavelength of 532 nm in pulses with a length of about 160 ns. The pulse repetition rate is adjustable between one and 25 kHz, and the output power is adjustable from zero to 75 W. The laser light emitted by the Titanium:Sapphire laser is focused by a lens (L, focal length 50 mm) into the type II optical fiber (section 2.4.3) which delivers the light to the experimental zone I. A fraction of about 4% of the laser power is deflected off a single-sided AR coated plate (P) which is used to measure the wavelength via a Highfinesse WS/7 [Hig] wavemeter (WM).

The basic design of the Titanium:Sapphire laser is a copy of the system described in the PhD thesis of R. Horn [Hor03] and is shown schematically in Fig. 5.2. The laser consists of a z-type laser resonator which is formed by the mirrors M1, M2, M3, and M4, a Titanium:Sapphire laser crystal, a Lyot filter and a Fabry-Perot etalon. The specifications of the four mirrors are:

- **M1:** material: fused silica, diameter: 1", thickness:  $\frac{1}{8}$ ", reflectivity: 75 % at the center wavelength of 820 nm
- **M2 and M3:** material: BK7, diameter: 1", thickness:  $\frac{3}{8}$ ", reflectivity: > 99 % at the center wavelength of 820 nm, transmittivity: > 99 % at the wavelength of 532 nm, the mirrors are concave spherical mirrors with a radius of curvature of  $r = 75$  mm
- **M4:** material: BK7, diameter: 1", thickness:  $\frac{1}{4}$ ", reflectivity: > 99 % at the center wavelength of 820 nm.

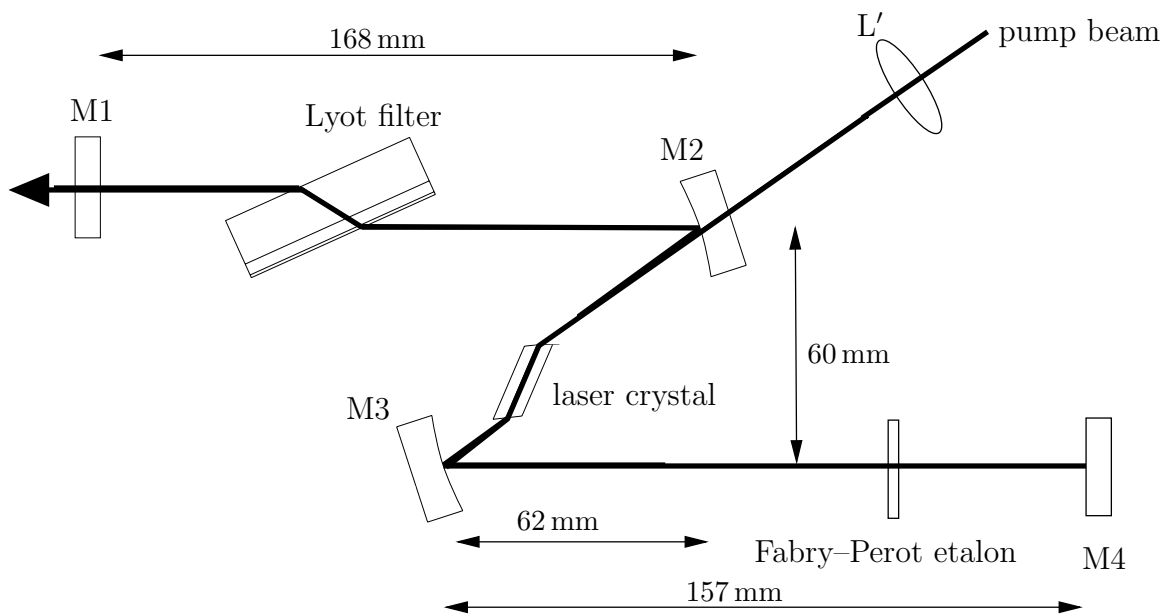


Figure 5.2: Design of the Titanium:Sapphire laser.

The Titan:Sapphire crystal has a diameter of 6.35 mm and a length of 20 mm. Both end surfaces are cut in the Brewster angle. The outer surface is wrapped in a 0.2 mm thick indium foil in order to heat sink the crystal to a home-made water cooled copper block into which the crystal is bracketed. The copper block is mounted in an angular adjustment stage (Owis, product number 14.439.2001) by which the crystal can be turned around its center axis for optimal alignment. The pump beam is focused by the lens ( $L'$  focal length 88.3 mm) through the mirror M2 into the laser crystal.

The laser wavelength is continuously tunable by use of the Fabry–Perot etalon and the Lyot filter. The Lyot filter (Coherent, Part-Nr. 0157-415-0) consists of three quartz plates. The ratio of the thicknesses of the three plates is 1:4:16. The free spectral range (FSR) of the thickest plate is  $208 \text{ cm}^{-1}$  for a wavelength of 600 nm [Hor03]. The Lyot filter is held by a home-made mount through which it can be turned around the axis given by the direction of the laser beam.

The Fabry–Perot etalon is made of BK7 and has a diameter of 25 mm and a thickness of 0.3 mm. The free spectral range is  $\text{FSR}_{\text{FPE}} = 330 \text{ GHz}$ . Both etalon sides are coated so that the reflectivity per side is  $R_{\text{FPE}} \approx 67\%$  for a center wavelength of 820 nm. The Finesse  $\mathcal{F}_{\text{FPE}}$  is then  $\mathcal{F}_{\text{FPE}} = \pi\sqrt{R_{\text{FPE}}}/(1 - R_{\text{FPE}}) \approx 8$ , where the relation between the Finesse and the reflectivity is taken from [Dem95]. The etalon is held by an optical mount (Thorlabs KC1-T/M) through which the etalon can be tilted around the two axes which are perpendicular to the direction of the laser beam.

The repetition rate of the Titanium:Sapphire laser is given by the repetition rate of the Corona. The pulse length of a Titanium:Sapphire laser pulse has been measured to

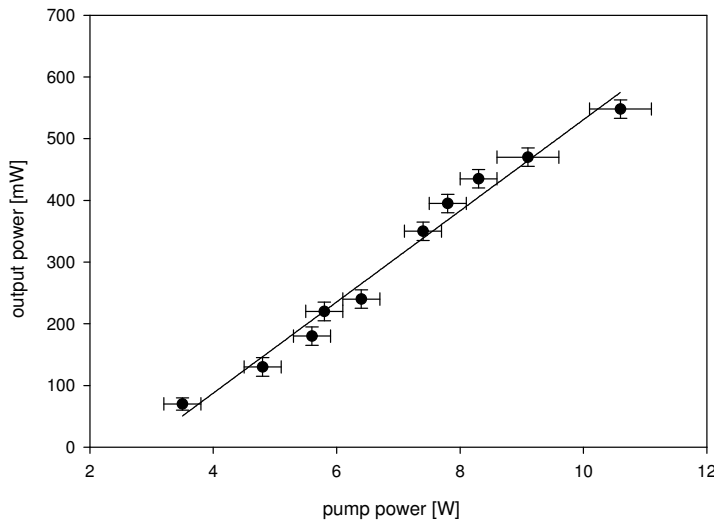


Figure 5.3: Output power of the Titanium:Sapphire laser as a function of the pump power delivered by the Coherent Corona. The horizontal error bars are observed fluctuations of the pump power. The vertical error bars are fluctuations of the output power. The pump power has been read of the control unit of the Corona laser system.

wavelength tuning range	770–845 nm
output power	see Fig. 5.3
pulse repetition rate $f_{rep}$	1–25 kHz
pulse length $\tau_{Pulse}$	20–25 ns

Table 5.1: Specifications of the Titanium:Sapphire laser. The pulse repetition rate of the Titanium:Sapphire laser is identical to the pulse repetition rate of the pump laser.

be between 20 and 25 ns, and the tuning range has been measured to be between 770 and 845 nm. Fig. 5.3 shows the average output power of the Titanium:Sapphire laser as a function of the pump power. A straight line has been fitted to the experimental data by use of SigmaPlot [Sig]. The fit yields the functional form for the output power  $P_{out} = 73.9 \cdot P_{in} - 208.0$ , where  $P_{out}$  is given in mW with respect to the input power  $P_{in}$  of the Corona given in W. For completeness and further reference, the specifications of the Titanium:Sapphire laser that are relevant for the experiments presented in this chapter are summarized in Tab. 5.1.

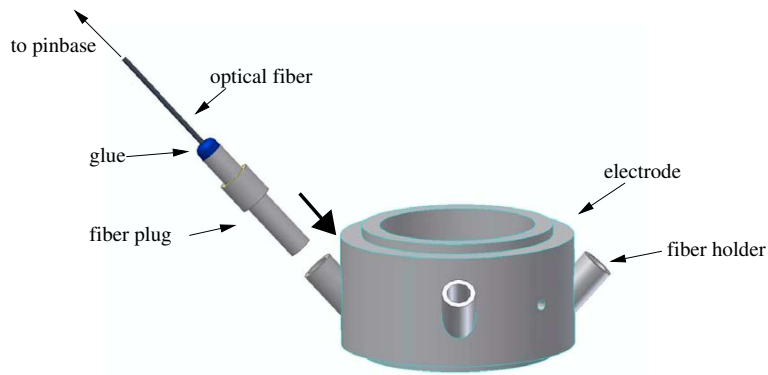


Figure 5.4: Laser electrode. The optical fiber is glued into the fiber plug which is plugged into one of the four fiber holders. The fourth fiber holder is on the back and therefore not visible in the figure.

### 5.3 Laser Electrodes

New electrodes have been designed in order to expose antiprotons and antihydrogen atoms to laser light. These electrodes are referred to in the following as laser electrodes. A laser electrode is depicted in Fig. 5.4. It contains four holes into which the fiber holders are soldered into (the fourth fiber holder is on the back side and therefore not visible in Fig. 5.4). Each end of the two type II optical fibers is glued (Emerson Cumming, Styccast 2850 FT with Catalyst 24 LV) into the so called fiber plug, so that the fiber tip pokes out of the fiber plug but by not more than one millimeter. The fiber plug is depicted on the left side of Fig. 5.4 along with the optical fiber. Due to this design, the optical fiber can be installed in situ into a laser electrode which is mounted in the electrode stack. The dimensions of the laser electrode are given in Fig. 5.5a, which shows a cut through the laser electrode that lies in the plane defined by the center axis of two opposing holes. Fig. 5.5b and c show cuts through the fiber holder and fiber plug, respectively. The dimensions of the inner and outer radius as well as the height of the laser electrodes are chosen to be identical with the T-electrodes of the hbar2 apparatus. For the experiments presented in the following, the electrodes T4 and T7 of the hbar2 apparatus (see Fig. 2.7b) have been replaced by two laser electrodes and an optical fiber has been installed in both laser electrodes.

The mode of operation of a laser electrode is explained by use of Fig. 5.6. This figure shows a cut view of the assembly of two laser electrodes with an optical fiber installed into the upper electrode. As has been pointed out before, it is ensured that the optical fiber does not poke out of the fiber plug by more than one millimeter. The optical fiber is therefore not ‘visible’ for particles that are stored in the laser electrode, because the fiber is located as seen from the particles stored in this electrode behind the inner surface of the laser electrode. The optical fiber, which is an insulator and might electrically

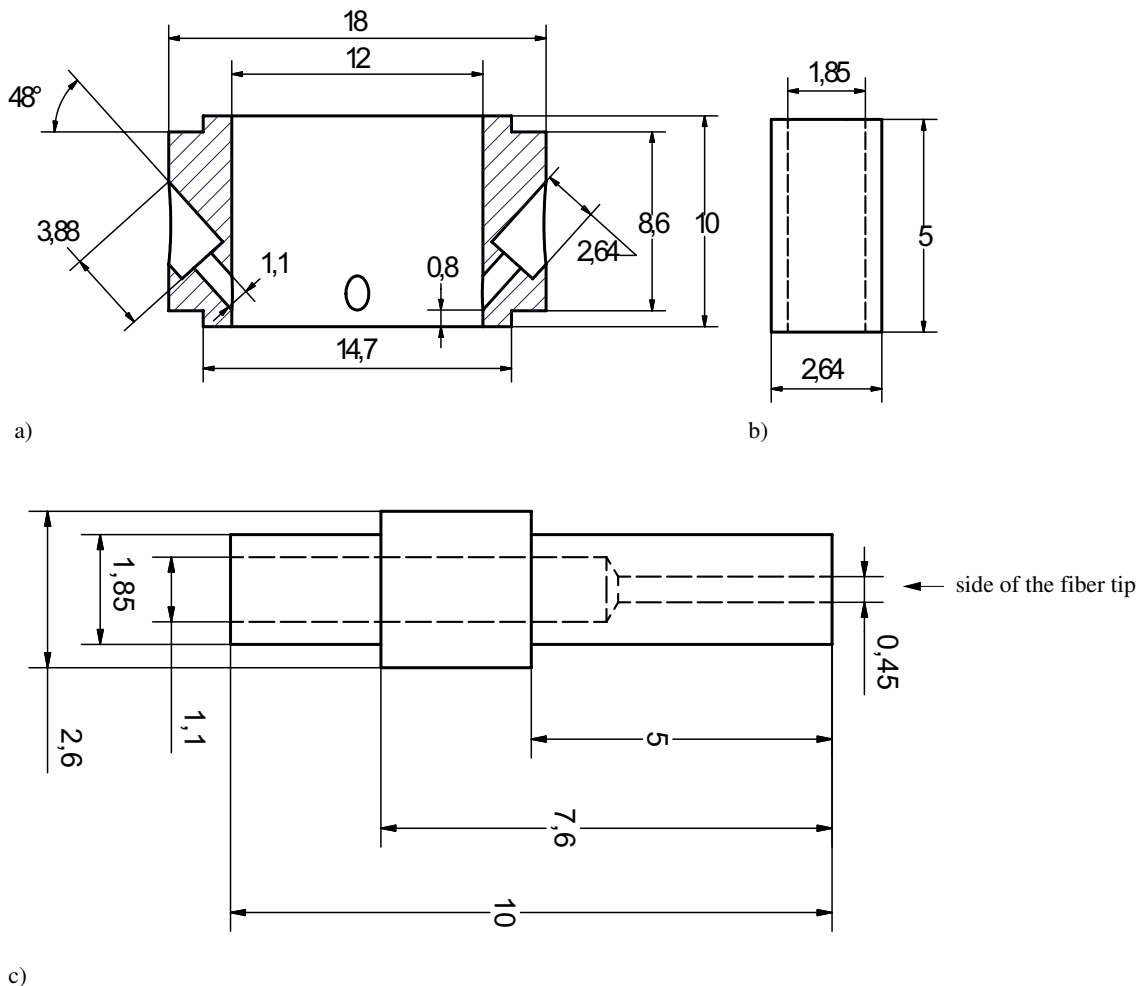


Figure 5.5: a) Basic design of the laser electrodes. b) Fiber holder, which is soldered into the holes of the laser electrodes. c) Fiber plug. The end of the optical fiber is glued at the left side into the fiber plug so that the fiber tip does poke out but not more than 1 mm on the right side. The three graphs are not intended to be technical drawings, since for example the tolerances are not specified. All lengths are given in millimeters. All pieces consist of OFHC copper and the surfaces are gold-plated.

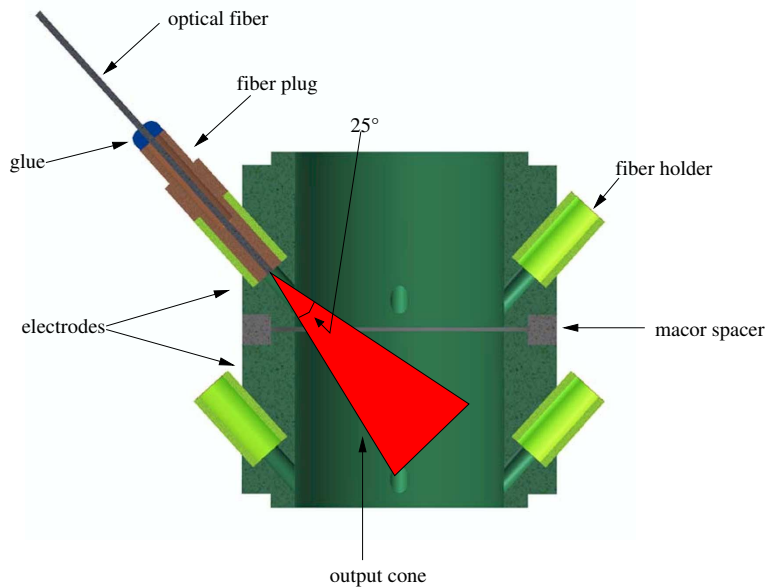


Figure 5.6: Cut view of the assembly of two laser electrodes. An optical fiber is installed into the upper electrode.

charge up, does therefore not disturb the electric potential at the inside of the laser electrode. The only perturbation on the electric potential might then arise from the presence of the four holes in the otherwise plain inner electrode surface. The four holes cause a quadrupolic perturbation on the electric potential, while a single hole would cause an asymmetric perturbation and trapped particle clouds tend to be more stable in quadrupolic perturbations than in symmetric perturbations. This is actually the reason, why we have chosen to build in four instead of one hole which would be sufficient for the installation of an optical fiber. The laser light emerges from the optical fiber within an output cone, whose opening angle is as determined in section 7.2 about  $25^\circ$ . The angle of  $48^\circ$  which is indicated in Fig. 5.5 is chosen so that the output cone of the laser light covers the center of the neighboring electrode as depicted in Fig. 5.6. Particles stored or passing through the center of the neighboring electrode are thus exposed to the laser light. The spot size of the laser beam in the center of this electrode is about 5 mm.

## 5.4 Experiments on Trapped Antiprotons

### 5.4.1 Introduction

The availability of laser light within the electrode stack is a major improvement of the design of the hbar2 Penning trap apparatus, since it allows for the first time to carry out laser experiments on antihydrogen atoms. However, the change in the design might

also cause problems. A problem might be that antiproton and positron clouds might not be stable any more when trapped in a laser electrode due to perturbations on the electric potential distribution caused by the four holes in the laser electrode. It has been shown that this is not the case simply by storing antiprotons and positrons in a laser electrode and by detecting no particle loss for several hours.

The situation could however change if the trapped particles are exposed to laser light. The question if laser light delivered by the Titanium:Sapphire laser causes an increase in antiproton loss is addressed by the experiments presented in the following.

### 5.4.2 Experimental Setup

A side view of the lower electrode stack from electrodes T2 to UB of the hbar2 Penning trap apparatus is shown in Fig. 5.7. In order to study the loss rate of trapped antiprotons that are exposed to laser light, an antiproton cloud is stored in the center of the U1, U3 or T5 electrode and the laser light is sent into the electrode stack via the laser electrode at T4. The output cone of the laser light is depicted in Fig. 5.7 by the red triangle and as can be seen, antiprotons stored in T5 are directly exposed to the light, while when stored in U1 or U3 they are exposed to stray light.

The laser light is sent into the electrode stack in a sequence of four consecutive ten seconds long cycles with a ten seconds long break in between two cycles. The cycles are produced by opening an optical shutter which is placed in front of the lens L (L is shown in Fig. 5.1) four times for ten seconds with a break in between of ten seconds. The laser repetition rate is set to  $f_{rep} = 5\text{ kHz}$  and the wavelength is set to 820 nm. All values of the laser power that are given in the following are measured in zone I at the output of the optical fiber which delivers the light from the laser cabin into the zone before this fiber is connected by use of a fiber to fiber coupler to the fiber installed in the apparatus.

The antiproton loss rate is detected by monitoring the trigger count rate which is measured by the ATRAP detector system as described in section 2.5.2.3.

### 5.4.3 Experimental Results

The experimental results presented in the following have been obtained from experiments carried out during beam time 2003. The first set of experiments has been carried out before a cesium beam, which is used for the experiments presented in chapters 6 and 7 has been run through the CS electrode. For these experiments, the measured antiproton loss rates are given in Tab. 5.2. As can be seen no loss at all is detected for antiprotons stored in U1 and U3 up to laser powers of 810 mW, and no loss is also detected for antiprotons stored in T5 up to a laser power of 590 mW.

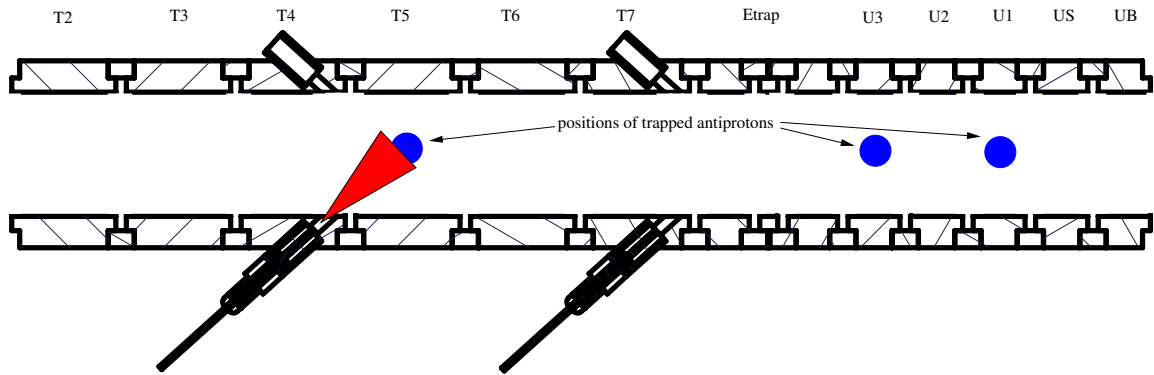


Figure 5.7: Part of the lower electrode stack from electrodes T2 to UB of the hbar2 apparatus. Laser light is sent into the electrode stack via the T4 laser electrode. The light cone of the laser light is depicted by the red triangle. The antiprotons are stored in the electrodes U1, U3, and T5, while laser light is sent into the electrode stack and the annihilation rate is monitored.

	225 mW	320 mW	400 mW	590 mW	810 mW
laser power →	225 mW	320 mW	400 mW	590 mW	810 mW
number of $\bar{p}$ →	78 000	60 000	60 000	60 000	74 000
↓ electrode					
U1	0	0	0	0	0
U3	0	0	0	0	0
T5	0	0	0	0	10–15

Table 5.2: The table shows the antiproton loss per second for an antiproton cloud stored at the electrode indicated by the first column. The laser power and the total number of trapped antiprotons are given at the top of the last five columns. The loss rates have been measured in a trap where no cesium beam which is employed in experiments described in chapters 6 and 7 has been run before.

In contrast, a loss of 10–15 antiprotons per second is detected for antiprotons trapped in T5 and exposed to a laser power of 810 mW, which corresponds to an intensity of about  $40 \text{ kW/m}^2$  taking into account a spot size of 5 mm in the center of the T5 electrode. This antiproton loss only occurs during the time when the laser light is sent into the electrode stack. After the shutter closes, the loss rate drops within one or two seconds back to the usual background trigger count rate of  $1.2 \text{ s}^{-1}$ .

Another set of experiments has been carried out after the cesium beam was running through the electrode stack. In the very first experimental trial about 50 000 antiprotons were stored in U1 and then exposed in four 10 second long cycles with a 10 second long break in between two cycles to laser light at a power of 800 mW. The detected loss rate has been 20 antiprotons per second. The particles were then moved to U3 where they are closer to the laser beam. There, an antiproton loss rate of 5 per second has been

detected under the same laser conditions. The particles were subsequently stored in T5, where they have been directly exposed to the laser light. Employing again the same laser conditions, a loss of 20 antiprotons per second has been detected. Finally the antiprotons were moved back to U1 and a loss of 5–10 per second has been measured, which is between a forth and a half of the loss rate measured previously in this electrode.

The experimental results can be interpreted as follows. Cesium atoms are adsorbed due to cryopumping at the inner surfaces of the 4.2 K cold electrodes while the cesium beam is running through the electrode stack. The laser beam locally heats up the electrodes and therefore liberates cesium atoms. The freed cesium atoms can annihilate with the trapped antiprotons and as a result cause an increase of the antiproton loss rate. They get however also readsorbed by other locations that remain at 4.2 K so that as a net effect the number of liberated cesium atoms decreases from one experimental trial to the next.

As a consequence of this interpretation, we have put about 0.5 W of laser light for about one minute into the electrode stack after the cesium beam was running again. We could then measure an antiproton loss rate which is of similar size as the antiproton loss given in Tab. 5.2 for similar laser conditions. By these experiments, we therefore have demonstrated that trapped antiprotons are stable when exposed to a laser power of up to 590 mW. An increase of antiproton loss after a cesium beam was running through the electrode stack could be cured by shining laser light into the electrode stack before accumulating antiprotons and exposing them to laser

## 5.5 Summary and Conclusion

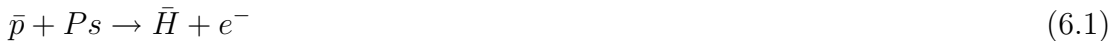
In this chapter, the first experiments on trapped antiprotons exposed to laser light have been presented. A Titanium:Sapphire laser system has been built and the electrodes with integrated optical fibers have been designed. The experiments have shown by exposing antiprotons to laser light that the laser light does not cause an antiproton loss for laser powers up to 590 mW. Moreover, a higher loss due to cesium atoms adsorbed to the inner surface of the electrodes could be cured by sending laser light of about 500 mW for about one minute into the electrode stack. This is a very important result against the background of the future ATRAP project to confine antihydrogen atoms in a combined Penning–Ioffe trap and then to carry out spectroscopy on trapped antihydrogen. The reason is that the zero or low loss of trapped antiprotons induced by laser light indicates that a comparable loss rate can be expected for trapped antihydrogen atoms when exposed to comparable laser power. Thus it indicates that spectroscopy of antihydrogen in a combined cyrogenic Penning–Ioffe trap might be feasible with respect to antihydrogen losses due to laser light.

# Chapter 6

## Antihydrogen via a Two-Stage Rydberg Charge-Exchange Process

### 6.1 Introduction

In this chapter, the first experiment by which cold antihydrogen atoms were produced via charge-exchange collisions between stored antiprotons and Rydberg positronium atoms ( $Ps^*$ ) is presented [SSS<sup>+</sup>04]. A positronium atom is the bound state of a positron ( $e^+$ ) and an electron ( $e^-$ ). For an overview of its general properties, see for example [Ric81]. The initial idea to produce antihydrogen in charge-exchange collisions between trapped antiprotons  $\bar{p}$  and ground state positronium atoms ( $Ps$ ) according to



was proposed by Humberston et al. [HCJD87]. The counterpart process in which a proton is substituted for an antiproton has been used for the production of hydrogen [MBC<sup>97</sup>] but the observed rate was low and many fewer antiprotons than protons are available, so no attempt has been put forward to produce antihydrogen by this method.

Charlton [Cha90] however pointed out that the charge-exchange cross section  $\sigma_n$  of collisions between antiprotons and positronium atoms with principal quantum state  $n$  scales as the fourth power of  $n$  with respect to the charge-exchange cross section  $\sigma_0$  of collisions between antiprotons and ground state positronium,  $\sigma_n \propto \sigma_0 n^4$ . The antihydrogen formation rate is therefore enormously larger if Rydberg positronium atoms are used instead of ground state positronium atoms. This antihydrogen formation process can be schematically described by



Here,  $\bar{H}^*$  refers to an antihydrogen atom in a Rydberg state. Trapped antiprotons are readily available at the ATRAP experiment. The difficulty to implement this formation

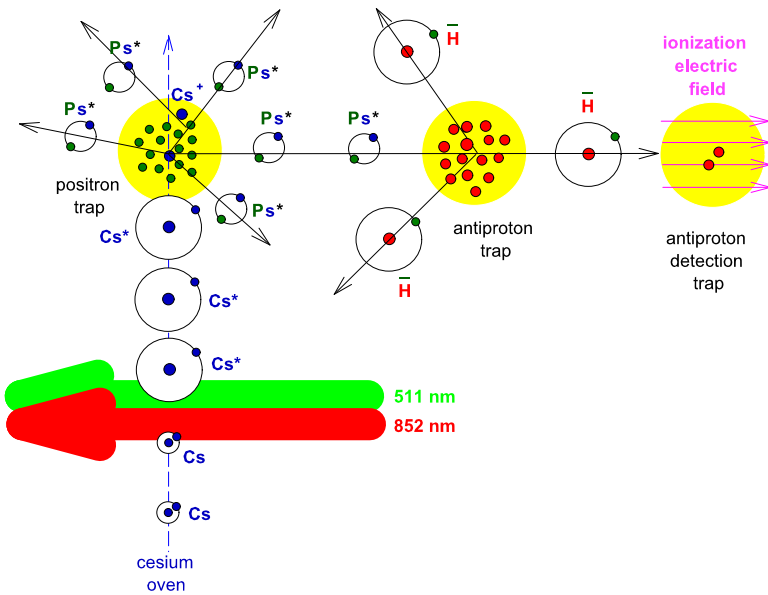
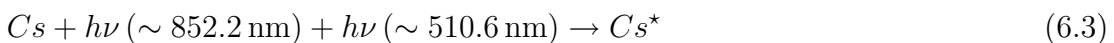


Figure 6.1: A schematic overview of the experiment is depicted.

process in our Penning trap has been the production of the Rydberg positronium atoms. Since positrons can also be routinely trapped in the ATRAP Penning traps, we followed the route proposed by Hessels et al. [HHC98], where Rydberg positronium atoms are produced in foregoing charge-exchange reactions between trapped positrons and Rydberg cesium atoms ( $Cs$ ) which were excited by laser light in a two-step excitation scheme to a Rydberg state. The production process can be summarized by



A schematic overview of the experiment is depicted in Fig. 6.1. The yellow regions indicate from left to right trapped positrons, trapped antiprotons, and an initially empty trap which is used for antihydrogen detection. The cesium atoms come from a cesium oven located outside the Penning trap electrode stack and are excited by a two-step excitation scheme according to Eq. 6.3 to a Rydberg state. A simplified excitation scheme is depicted schematically in Fig. 6.2. A diode laser at about 852.2 nm excites the cesium atoms from the  $6S_{1/2}$  ground state to the  $6P_{3/2}$  state ( $D_2$  line) from which the atoms are excited by a copper vapor laser at about 510.7 nm to a state which would be the  $37D$  state for the case of zero magnetic field. The neutral positronium atoms formed in charge-exchange collisions according to Eq. 6.4 are not sensitive to the trapping fields and therefore leave the region and a fraction collides with the trapped antiprotons. Antihydrogen atoms in highly excited states are then formed in charge-exchange reactions according to Eq. 6.5. The neutral antihydrogen

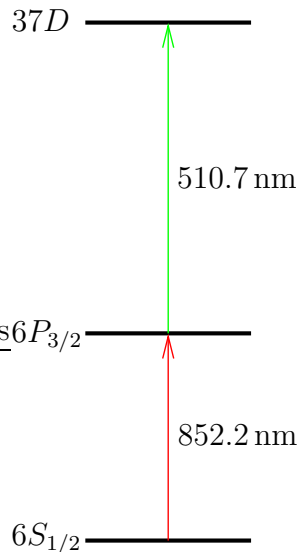


Figure 6.2: A simplified depiction of the two-step excitation scheme.

atoms are also insensitive to the trapping fields and move out. A small fraction of the antihydrogen atoms enters the antiproton detection trap. They are field-ionized by the electric field present at the edge of the detection well and similar to the experiments presented in chapter 4, the antiprotons are deposited in the detection well in order to be detected background-free at the end of an experiment.

As mentioned before, trapped antiprotons and positrons are readily available. They can be loaded and stored in the Penning trap apparatus by methods described in chapter 3. The challenge of this experiment has been the implementation of a cesium beam in the Penning trap apparatus and the development of a laser system by which the cesium atoms are excited effectively to a Rydberg state. Most of this chapter is therefore devoted to a detailed description of the excitation scheme and of the setup for the Rydberg cesium beam.

In the subsequent theoretical overview, the excitation scheme is discussed theoretically and the calculated properties of the two-stage charge-exchange process as given by Eq. 6.4–Eq. 6.5 are presented. In section 6.3 the experimental setup in the Penning trap apparatus and the basic properties of the laser system are described. The actual experiment has been carried out in three steps. In a first step it has been demonstrated that cesium atoms have been excited by the diode laser from the  $6S_{1/2}$  state to the  $6P_{3/2}$  state. This is presented in section 6.4.1. In a second step we have demonstrated that Rydberg cesium atoms have been produced in a two-step excitation scheme according to Eq. 6.4.2. In a third step, a complete antihydrogen experiment according to Eq. 6.3–Eq. 6.5 has been carried out which is presented in section 6.4.3. This chapter ends with a summary and conclusion which is given in 6.5.

## 6.2 Theoretical Overview

In the following, a theoretical overview of the production process given by Eq. 6.3–6.5 is presented. The overview is organized as follows. In section 6.2.1, the laser excitation scheme employed for the production of Rydberg cesium atoms is discussed, while in section 6.2.2 the properties of the two consecutive charge-exchange processes given by Eq. 6.4 and Eq. 6.5 are described.

### 6.2.1 The Excitation Scheme

#### 6.2.1.1 Excitation Efficiency

The choice of the excitation scheme which is depicted schematically in Fig. 6.2 and which is used for the production of antihydrogen is somewhat arbitrary since the only requirement for the production of antihydrogen via Eq. 6.3–Eq. 6.5 is the availability of Rydberg atoms. Maximilian Herrmann [Her03] therefore investigated this excitation scheme and four alternative schemes when working on his diploma thesis. All schemes are tabulated in the first column of Tab. 6.1. For each excitation scheme, he solved rate equations of the population dynamics of the corresponding atomic states. He has taken realistic parameters for commercial available lasers that are suited to induce the various transitions and the experimental setup of the ATRAP experiment into account. However, he neglected the presence of the strong magnetic field. The excitation efficiency which is given in the second column of Tab. 6.1 is defined as the probability that a cesium atom is excited to the final state. The calculations indicate that the chosen scheme yields an excitation efficiency of 23.7 %. Only the excitation scheme  $6S_{1/2} \rightarrow 7P_{3/2} \rightarrow 50D_{5/2}$  can be excited with a higher efficiency of about 32.8 %. We have however chosen not to employ this scheme because the Rydberg cesium atoms produced by this scheme are more sensitive to the electric field present in the Penning trap region. The reason is that the final state has a principal quantum number of  $n = 50$  and is therefore according to Eq. 4.8 ionized by an electric field of about 45 V/cm, while a  $n = 37$  state is ionized by an electric field of about 150 V/cm.

#### 6.2.1.2 The $6S_{1/2} - 6P_{3/2}$ Transition in 0 T and in the Magnetic Field of the Penning Trap

In order to excite the cesium atoms effectively from the  $6P_{3/2}$  state to a Rydberg state, the first transition induced by a diode laser has to be saturated. As a consequence, the diode laser frequency has to be stabilized to a transition frequency of the  $D_2$  line. The transition frequencies of the cesium  $D_2$  line have been measured for the case without any magnetic field with an absolute accuracy of 110 kHz by Udem et al. [URHK00]. The strong magnetic field of the Penning trap shifts however the transition frequencies. In

Transition Sequence	Excitation Efficiency
$6S_{1/2} \rightarrow 6P_{3/2} \rightarrow 37D_{5/2}$	23.7 %
$6S_{1/2} \rightarrow 50P_{3/2}$	1.5 %
$6S_{1/2} \rightarrow 7P_{3/2} \rightarrow 50D_{5/2}$	32.8 %
$6S_{1/2} \rightarrow 6P_{3/2} \rightarrow 7S_{1/2} \rightarrow 50P_{3/2}$	0.9 %
$6S_{1/2} \rightarrow 6P_{3/2} \rightarrow 8S_{1/2} \rightarrow 50P_{3/2}$	0.2 %

Table 6.1: Possible excitation schemes for the production of Rydberg cesium atoms are given along with the corresponding excitation efficiencies. The excitation efficiencies are taken from [Her03].

order to measure the transition frequencies on the cesium beam running in the Penning trap apparatus we have calculated in a first step the level scheme and the shifted transition frequencies of the  $D_2$  line for a magnetic field in the range between 5.3 and 5.5 T.

As a starting point, we used the well known level structure of the cesium  $D_2$  for the zero magnetic field case [Ste02]. The level structure of the  $6S_{1/2}$  and  $6P_{3/2}$  state is depicted in Fig. 6.3a. The transition additionally shows hyperfine structure which is due to the  $I = 7/2$  nuclear spin of cesium-133. The quantum number of the total angular momentum is labeled by  $F$ .  $F$  can take the values  $|J-I|, |J-I+1|, \dots, |J+I-1|, |J+I|$ . For the  $S$  state,  $J = 1/2$  which results in a splitting into two levels with  $F = 3$  and  $F = 4$ . For the  $P$  state,  $J = 3/2$  which results in a splitting into four levels with  $F = 2, 3, 4$ , and 5.

The selection rules for optical transitions between the hyperfine components are  $\Delta F = 0, \pm 1$ . Udem et al. [URHK00] have obtained for the splitting of the hyperfine centroids, depicted to the left in Fig. 6.3a the frequency

$$f_{D_2} = 351.725\,718\,50(11) \text{ THz.} \quad (6.6)$$

A magnetic field in the range between 5.3 and 5.5 T destroys the coupling between  $I$  and  $J$  to  $F$ . We are in the Paschen–Back regime for the hyperfine structure [Ste02], where  $F$  is not a good quantum number. Additionally we are in the Zeeman regime for the fine structure, where  $J$  is still a good quantum number [Ste02]. As a result, the hyperfine levels split with respect to their magnetic quantum number  $m_J$  and  $m_I$ . For the case of the  $6S_{1/2}$  state,  $m_J = \pm 1/2$  and  $m_I = -7/2 \dots + 7/2$ . The energy shift  $\Delta E_{6S_{1/2}}(m_J, m_I)$  for a given  $m_J, m_I$  sublevel with respect to the  $6S_{1/2}$  centroid is given by [Ste02]

$$\Delta E_{6S_{1/2}}(m_J, m_I) = g_{6S_{1/2}}\mu_B B_0 m_J + A_{6S_{1/2}} m_I m_J - g_{6S_{1/2}}\mu_k B_0 m_I. \quad (6.7)$$

For the case of the  $6P_{3/2}$  state,  $m_J = \pm 1/2, \pm 3/2$  and  $m_I = -7/2 \dots + 7/2$ . The energy shift  $\Delta E_{6P_{3/2}}(m_J, m_I)$  for a given  $m_J, m_I$  sublevel with respect to the  $6P_{3/2}$  centroid is

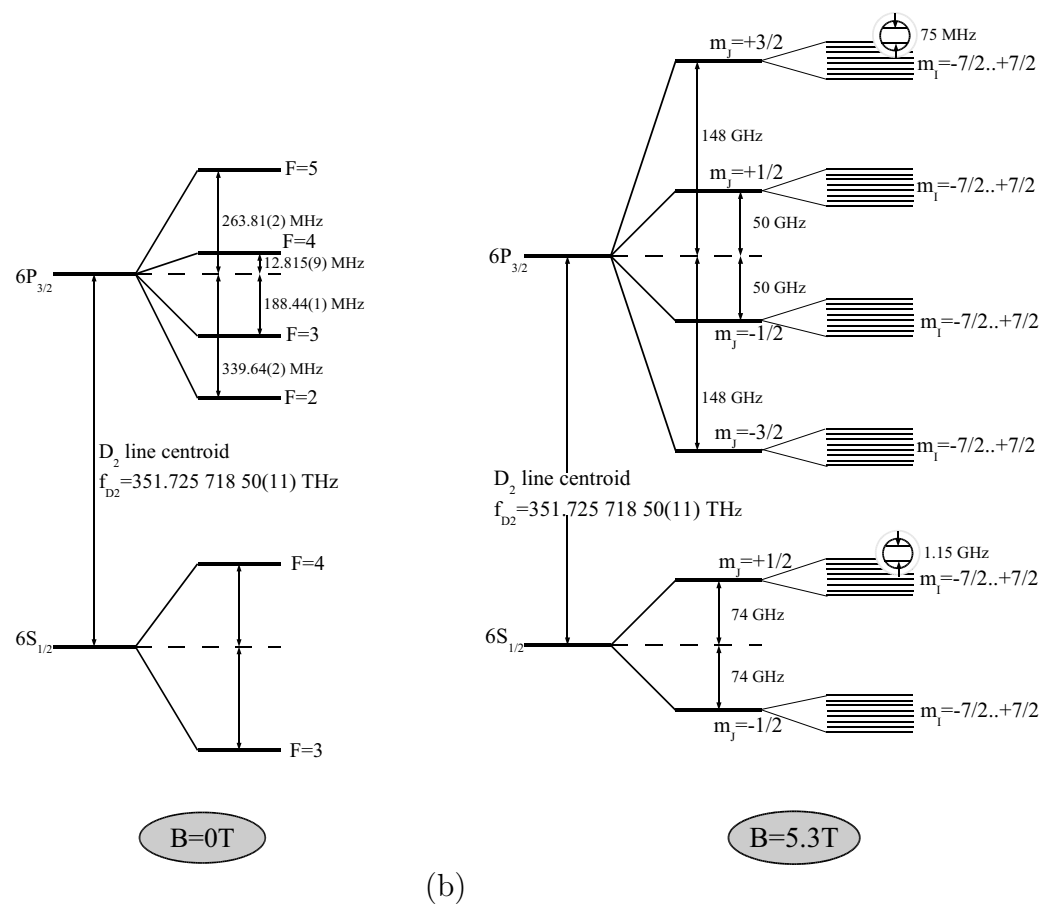


Figure 6.3: Cs level structure of the  $6S_{1/2}$  and  $6P_{3/2}$  state for  $0\text{T}$  and  $5.3\text{T}$ .

Magnetic Dipole Constant $A_{6S_{1/2}}$	$h \times 2.298\,157\,942\,5$ GHz
Magnetic Dipole Constant $A_{6P_{3/2}}$	$h \times 50.275(3)$ MHz
Electric Quadrupole Constant $B_{6P_{3/2}}$	$-h \times 0.53(2)$ MHz
Fine Structure Landé g-factor $g_J(6S_{1/2})$	2.002 540 32(20)
Fine Structure Landé g-factor $g_J(6P_{3/2})$	1.3340(3)
Nuclear g-factor $g_I$	0.000 398 853 95(52)
Planck's constant $h$	$6.626\,0755 \times 10^{-34}$ Js
Bohr magneton $\mu_B$	$9.274\,0154 \times 10^{-24}$ J/T
Nuclear magneton $\mu_k$	$5.050\,786\,6 \times 10^{-27}$ J/T

Table 6.2: The table gives the values used to calculate the frequency shifts due to the magnetic field. All values are taken from [Ste02].

given by [Ste02]

$$\begin{aligned} \Delta E_{6P_{3/2}}(m_J, m_I) = & g_{6P_{3/2}} \mu_B B_0 m_J + A_{6P_{3/2}} m_I m_J - g_{6P_{3/2}} \mu_k B_0 m_I \\ & + B_{6P_{3/2}} \frac{3(m_I m_J)^2 + \frac{3}{2} m_J m_I - I(I+1)J(J+1)}{2J(2J-1)I(2I-1)}. \end{aligned} \quad (6.8)$$

Numerical values for the constants used in Eq. 6.7 and 6.8 are given in Table 6.2. By use of Eq. 6.7 and 6.8 the level scheme of a cesium atom exposed to the magnetic field of the Penning trap can be calculated. The level scheme for  $B = 5.3$  T is given in Fig. 6.3b.

The selection rules for optical transitions are given by  $\Delta m_J = 0, \pm 1$  and  $\Delta m_I = 0$  [HW96]. We have chosen to excite from the  $6S_{1/2}, m_J = +1/2$  state to the  $6P_{3/2}, m_J = +3/2$  state because it is a cycling transition. This means that an excited atom can only decay to the initial state. From  $\Delta m_I = 0$  follows that there are eight possible transitions between the hyperfine components of the  $6S_{1/2}, m_J = +1/2$  and  $6P_{3/2}, m_J = +3/2$  state with the same  $m_I$  quantum state. The transition frequencies are then given as a function of  $m_I$  and of the magnetic field  $B$  by

$$f(m_I, B) = f_{D_2} + \frac{\Delta E_{6P_{3/2}}(+3/2, m_I)}{h} - \frac{\Delta E_{6S_{1/2}}(+1/2, m_I)}{h}, \quad (6.9)$$

where Eq. 6.7 and Eq. 6.8 have been used and  $h$  is Planck's constant. In Fig. 6.4 the transition frequencies of the  $D_2$  line are plotted as a function of the magnetic field ranging from 5.3 to 5.5 T. It can be seen from the graph, that the frequency spacing between neighboring lines is about 1 GHz. The diode lasers which are used to excite a transition have a linewidth of a few hundred kHz as will be described in section 6.3.2.1 and therefore one transition out of the eight can be excited per diode laser.

### 6.2.1.3 Excitation from the $6P_{3/2}$ State to a Rydberg State

The copper vapor laser whose properties will be given in section 6.3.2.2 emits green laser light at a fixed wavelength of 510.7 nm which corresponds to a frequency of  $f_{CVL} \approx$

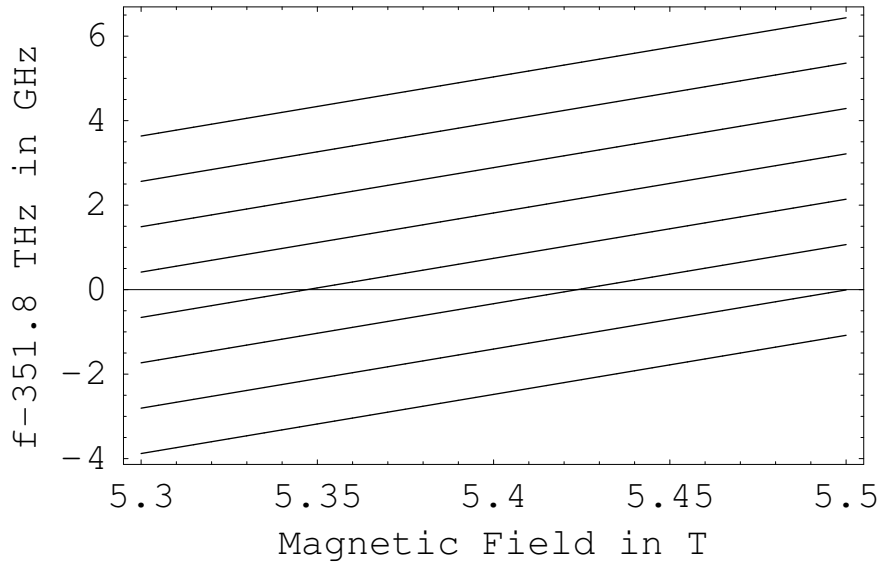


Figure 6.4: The calculated transition frequencies are given as a function of the magnetic field ranging from 5.3 to 5.5 T. The highest frequency corresponds to a transition between states with a magnetic sublevel of  $m_I = -7/2$ , the second highest frequency correspond to a transition between states with a magnetic sublevel of  $m_I = -5/2$  and so on.

	$nS_{1/2}$	$nD_{5/2}$
$n = 36$	511.1 nm	510.8 nm
$n = 37$	510.9 nm	510.7 nm
$n = 38$	510.7 nm	510.5 nm
$n = 39$	510.6 nm	510.4 nm
$n = 40$	510.4 nm	510.3 nm

Table 6.3: Rydberg states that are separated by about 510.7 nm from the  $6P_{3/2}$  state.

587 THz. It is used to excite the cesium atoms from the  $6P_{3/2}$  state to a Rydberg state. As mentioned in the introduction, the laser excites the atoms to a state which would be  $37D$  if no magnetic field would be present. In this section, the final Rydberg states will be discussed in more detail.

Let us start with a determination of the atomic states to which the cesium atoms can be excited from the  $6P_{3/2}$  centroid by the copper vapor laser for the zero magnetic field case. In this case, the principal quantum numbers of the Rydberg states can be calculated by use of the modified Ritz formula [WS87]

$$E(n) = E_\infty - \frac{R}{(n - \mu_n)^2}, \quad (6.10)$$

which gives the energy  $E(n)$  in wavenumbers of the energy level with principal quantum

	$nS_{1/2}$	$nD_{5/2}$
$E_\infty$	31 406.46 796 cm <sup>-1</sup>	31 406.467 65 cm <sup>-1</sup>
$A$	4.049 356 6(38)	2.466 315 24(63)
$B$	0.237 703 7	0.013 577
$C$	0.255 401	-0.374 57

Table 6.4: Numeric values used in Eq. 6.10. The values are taken from [WS87].

number  $n$  with respect to the  $6S_{1/2}$  ground state. Here  $E_\infty$  is the ionization limit,  $R$  is the Rydberg constant (109 736.862 24 cm<sup>-1</sup> for  $^{133}\text{Cs}$  [WS87]) and  $\mu_n$  is the quantum defect given by

$$\mu_n \approx A + \frac{B}{(n - A)^2} + \frac{C}{(n - A)^4}. \quad (6.11)$$

The values for  $E_\infty$ ,  $A$ ,  $B$ , and  $C$  are given in Tab. 6.4 for a  $nS_{1/2}$  and a  $nD_{5/2}$  state, since according to the selection rules for electric dipole transitions a single photon transition from the  $6P$  state can only be induced to a  $S$  or a  $D$  state. The transition frequency  $f(n)$  of a transition from the  $6P_{3/2}$  centroid state to a Rydberg state with principal quantum number  $n$  is then given by

$$f(n) = 100 \cdot c \cdot E(n) - f_{D_2}. \quad (6.12)$$

Here,  $f_{D_2}$  is given in Eq. 6.6 and  $c$  is the speed of light. The principal quantum number  $n$  of Rydberg states which are approximately separated by  $f_{CVL}$  from the  $6P_{3/2}$  state can then be calculated by solving  $f(n) = f_{CVL}$  for  $n$ . This yields for both,  $nS_{1/2}$  and  $nP_{3/2}$  final states with principal quantum numbers in the range between  $n = 36$  and 40. The states are tabulated in Tab. 6.3 along with the corresponding wavelengths. As can be seen, the  $37D_{5/2}$  state and the  $38S_{3/2}$  state are separated by 510.7 nm from the  $6P_{3/2}$  state. They are however still off resonance, but the  $37D_{5/2}$  state only within a few GHz. The copper vapor laser is a pulsed laser and has a linewidth of about 6 GHz, the copper vapor laser would excite to the  $37D_{5/2}$  state for the case of zero magnetic field. The excitation scheme from the  $6P_{3/2}$  state to a Rydberg state is depicted schematically for the above calculated zero magnetic field case to the left of Fig. 6.5.

The presence of the strong magnetic field of the Penning trap apparatus changes however the level structure. The level structure of the cesium Rydberg states in a  $\sim$ 5.3 T magnetic field is not an easy task to calculate. The reason is that at a magnetic field strength of about  $B_{\text{critical}} \approx 8.3(\frac{30}{n})^3$  Tesla [RGHW94], the Lorentz force on the valence electron is similar to the Coulomb force caused by the atomic core on the valence electron. In  $B_{\text{critical}}$ ,  $n$  is the principal quantum number of the Rydberg state. With  $n = 37$ ,  $B_{\text{critical}} \approx 4.4$  T confirming that we are in the range where the Lorentz force is of similar size than the Coulomb force. The Lorentz force cannot be treated any more as a perturbation on the Coulomb force as it has been the case for the  $6S_{1/2}$  and

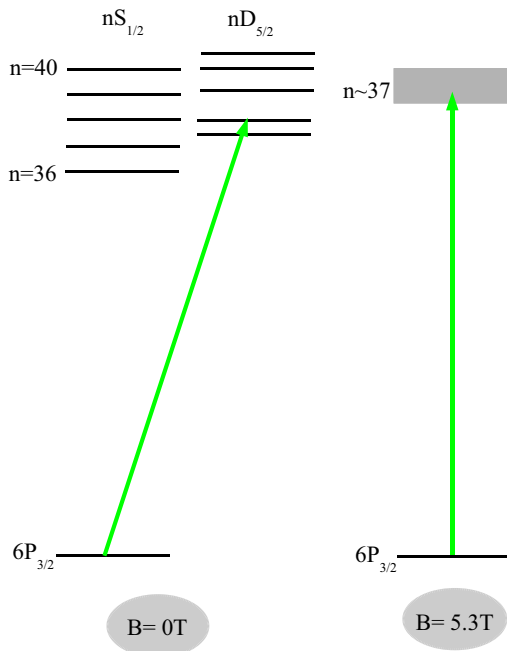


Figure 6.5: The second excitation step to a Rydberg state is shown for the zero magnetic field case and schematically for the 5.3 T magnetic field case.

$6P_{3/2}$  states and the full Hamiltonian for a cesium atom has to be solved numerically. This has so far only been achieved for the case of a Rydberg hydrogen atom in a strong magnetic field by the use of supercomputers [RGHW94]. We therefore restrict ourselves to some plausible explanations and are comfortable with the experimental detection of the production of Rydberg cesium atoms presented in section 6.4.2.1.

The effect caused by a magnetic field of  $\sim 5.3$  T is that it mixes the different Rydberg  $n$  states of cesium atoms [Gal93]. As a result, a whole manifold of lines is created with some  $S$  and  $D$  character which are accessible from the  $6P_{3/2}$  state by laser light at 510.7 nm. The transition from the  $6P_{3/2}$  state to the Rydberg state in a 5.3 T magnetic field is depicted schematically to the left in Fig. 6.5. The Rydberg states in the magnetic field are now depicted graphically by a band, but it has been pointed out that this region still consists of many well separated lines.

### 6.2.2 The Two-Stage Charge-Exchange Process

In this section, the two-stage charge-exchange processes as described by Eq. 6.4 and Eq. 6.5 are discussed theoretically. Charge-exchange collisions between ions and Rydberg atoms have been studied intensively for various types of atoms and ions. For a general overview, see [Gal93] and references therein. It has been found that charge-exchange collisions have extremely large cross sections at the order of the geometric

area of the Rydberg atom. The geometric area of a Rydberg atom is approximately given by  $\pi a_0^2 n^4$ , where  $a_0$  is the Bohr radius and  $n$  is the principle quantum number of the Rydberg state.

For the calculation of charge-exchange cross sections classical trajectory Monte Carlo (CTMC) methods are commonly employed [Gal93]. In these calculations, the incoming ion, the ion at the core of the Rydberg atom, and the Rydberg electron are all treated as classical particles and their trajectories are obtained by integrating the Newtonian equations of motion. A set of initial conditions for the Rydberg electron is chosen to correspond to the quantum numbers  $n$  and  $l$  of the Rydberg electron. At the end of the collision, the final trajectory of the electron is analyzed to determine whether it has been captured by the ion, and to determine its state from its final energy and angular momentum. Hessels et al. [HHC98] conducted CTMC calculations for the two-stage charge-exchange process described by Eq. 6.4 and Eq. 6.5. Their numerical results are presented in the following, because their results are quite useful for the interpretation of our experimental results, since they took the experimental parameters of the ATRAP experiment into account. That is that they assumed the positrons and antiprotons to reside at a temperature of 4.2 K and they assumed that the Rydberg cesium atoms travel with an average speed of about 300 m/s towards the positron cloud. This velocity is reasonably close to the mean velocity of the cesium atoms in the actual experiment. As will be described in detail in section 6.3.1, the cesium atoms come from a cesium oven heated to a temperature of about T=317 K which yields a mean velocity of

$$v_{Cs} = \sqrt{\frac{3k_B T}{m_{Cs}}} \approx 250 \frac{m}{s}, \quad (6.13)$$

where  $k_B$  is Boltzmann's constant and  $m_{Cs} = 133m_u$  the atomic weight of cesium. Hessels and coworkers however neglected the strong magnetic field present in the ATRAP Penning trap apparatus. But it has been shown theoretically and experimentally, that the presence of magnetic or electric fields does not greatly affect charge-exchange cross sections [HEHP<sup>+</sup>93, WO93, HCH94, MHMS97].

In their simulations, they assumed that the cesium atoms have been excited to a  $n = 50$  state. For the first charge-exchange process described by Eq. 6.4, they obtained from the CTMC calculations the charge-exchange cross section as a function of the final positronium  $n$  states as depicted in Fig. 6.6. For the second charge-exchange process described by Eq. 6.5, they obtained the charge-exchange cross section as a function of the final antihydrogen  $n$  state distribution as depicted in Fig. 6.7. Note that both  $n$  state distributions are sharply peaked. The final  $n$  state distribution for positronium is sharply peaked near  $n_{Ps} = n_{Cs}/\sqrt{2}$ , which is due to the fact that the binding energy is approximately conserved before and after the charge-exchange process. The positronium binding energy is  $E_{Ps} = -\frac{Ryd}{2n_{Ps}^2}$  and the cesium binding energy is  $E_{Cs} = -\frac{Ryd}{n_{Cs}^2}$ . Here  $Ryd$  is the Rydberg energy ( $\sim 13.6$  eV). The same energy conservation argument holds approximately for the second charge-exchange process and

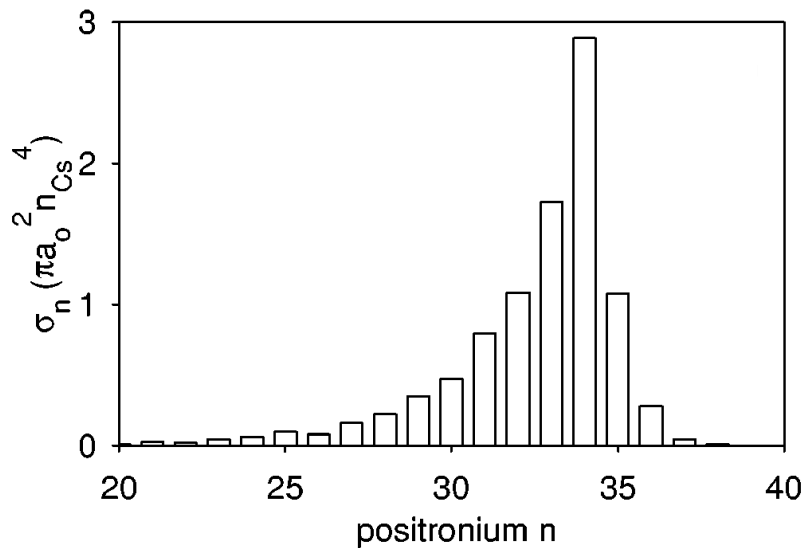


Figure 6.6: The calculated charge-exchange cross sections for the process described by Eq. 6.4 is depicted as a function of the final  $n$  state distribution of the formed positronium atoms. The graph is taken from [HHC98].

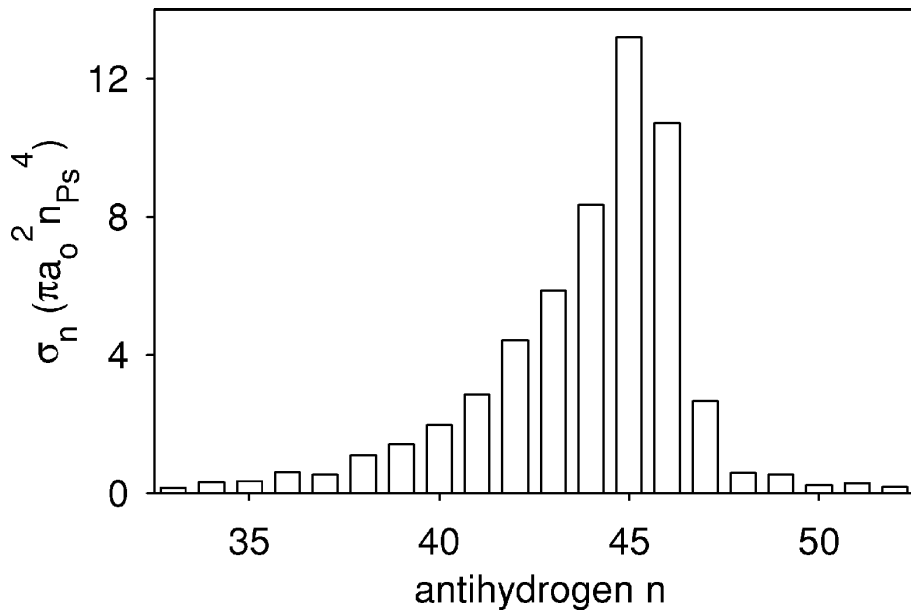


Figure 6.7: The calculated charge-exchange cross sections for the process described by Eq. 6.5 is depicted as a function of the final  $n$  state distribution of the formed antihydrogen atoms. The graph is taken from [HHC98].

according to the simulation the final  $n$  state distribution is very narrow and is centered near  $n = 45$  for  $n_{Cs} = 50$ . The narrow distribution of the final antihydrogen  $n$  states is one of the advantages of this production scheme over the formation process in a nested Penning trap, which has been described in chapter 4. There, the final state distribution is spread over more than 25  $n$  states. Another advantage is that one can directly control the  $n$  state distribution of the formed antihydrogen. The reason is that the final  $n$  state distribution depends on the cesium Rydberg state and this state is controllable via the laser excitation scheme employed for its production.

As it has already derived in the previous section, Rydberg cesium atoms in a  $n = 37$  state (neglecting the magnetic field) are produced by the excitation scheme employed by us. Accordingly, we expect to produce Rydberg positronium atoms in states around  $n = 26$  and antihydrogen atoms in states with principal quantum numbers of about 32. The peak in Fig. 6.6 corresponds to  $\frac{\sigma}{\pi a_0^2 n_{Cs}^4} \approx 2.8$ , which yields  $\sigma_{Cs^* - e^+} \approx 4.6 \times 10^{-14} \text{ m}^2$  for  $n_{Cs} = 37$ . The peak in Fig. 6.7 corresponds to  $\frac{\sigma}{\pi a_0^2 n_{Ps}^4} \approx 13.0$ , which yields  $\sigma_{Ps^* - \bar{p}} \approx 5.2 \times 10^{-14} \text{ m}^2$  for  $n_{Ps} = 26$ .

The calculations of Hessels and coworkers show that basically all trapped positrons are transformed into Rydberg positronium leaving the positron trap isotropically. The trapped antiprotons in our Penning trap apparatus can be stored at the minimum distance of about  $d = 0.6 \text{ cm}$  away from the positronium cloud. The fraction of positronium that enters the solid angle approximately given by  $\frac{1}{4\pi d^2}$  collide with the trapped antiprotons. For one experimental trial with  $N_{e^+} = 2 \times 10^6$  stored positrons and  $N_{\bar{p}} = 3 \times 10^5$  stored antiprotons,  $\frac{1}{4\pi d^2} \sigma_{Ps^* - \bar{p}} N_{e^+} N_{\bar{p}} \approx 70$  antihydrogen atoms are therefore predicted to be produced which leave the production region isotropically.

## 6.3 The Experimental Setup

In section 6.3.1 an overview of the experimental setup which is used for the production and detection of the Rydberg cesium beam is given. In section 6.3.2, the basic properties of the diode laser and the copper vapor laser are presented.

### 6.3.1 The Penning Trap Apparatus

It has already been mentioned in section 2.4.2, that the hbar2 Penning trap apparatus has been designed in order to carry out the experiment described in this chapter. In particular the lower electrode stack from the electrodes U3 to L3 is designed for this experiment. These electrodes have in contrast to such standard electrodes as T1-T7 a height of only 5 mm so that the distance between two particle clouds loaded into two adjacent electrodes is reduced and the solid angle covered by a particle cloud viewed from a neighboring cloud is enlarged. Additionally, the setup for the production and detection of the Rydberg cesium beam is mounted around the CS electrode.

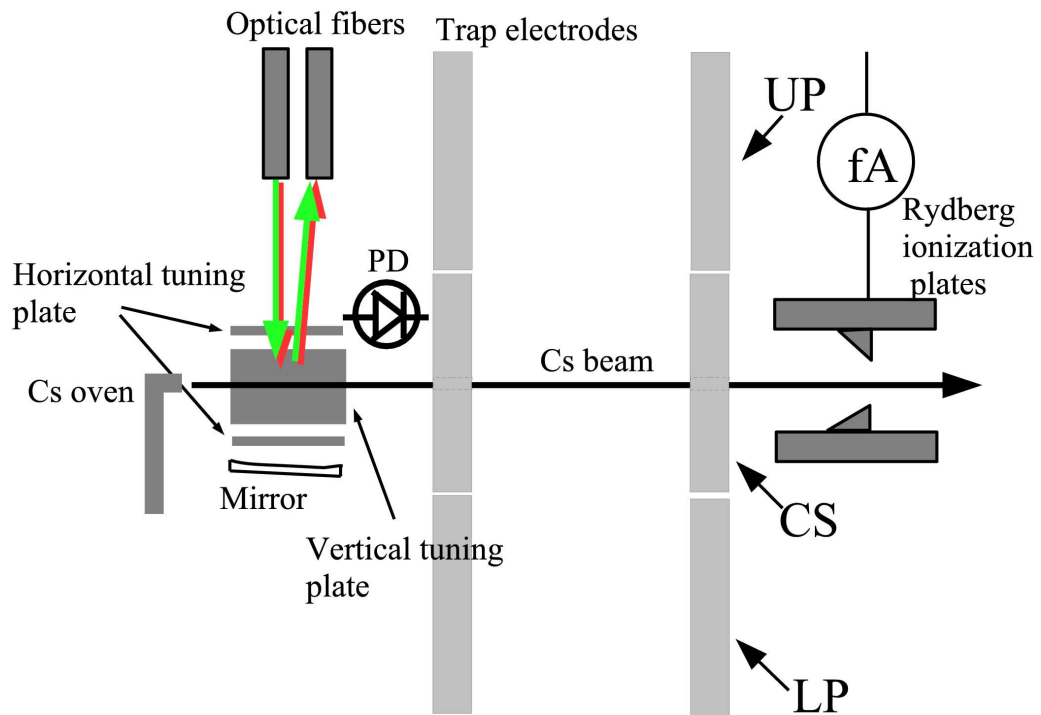


Figure 6.8: Sketch of the experimental setup for the production and detection of the Rydberg cesium beam. The cesium beam comes from an oven and is excited to a Rydberg state by laser light which is sent into the Penning trap apparatus by an optical fibers. The light reflects on a curved mirror and illuminates the cesium atoms again. Thus, the laser power which excites the atoms is effectively doubled. The laser light is focused by a mirror into a second fiber which guides it out of the Penning trap apparatus. The photodiode is used to detect fluorescence light. The cesium beam passes through the CS electrode and the Rydberg ionization plates are used to detect the Rydberg atoms by field-ionization.

A schematic drawing of the region around the CS electrode is given in Fig. 6.8. It shows in the center the three electrodes UP, CS, and LP. The cesium beam is produced by the cesium oven, which is depicted to the left. The cesium oven is a  $\sim 5 \text{ mm}^3$  glass container filled with a few milligrams of 95% pure cesium (Strem Chemicals). Its outer surface is gold plated and electrically connected to the ground of the Penning trap apparatus, which prevents the oven from charging up. The oven is normally at a temperature of 4.2 K. It can be heated by a current through a constantan wire which is wound many times around the oven. Its temperature is measured by a temperature sensor which is mounted to the oven. Careful thermal isolation of this oven, heat sinking and thermal shielding keep all other components in the vicinity of the oven close to liquid helium temperature. The cesium beam emerges from the oven when it is heated well above the melting point of cesium, which is 28.44°C at atmospheric pressure [Lid94]. We generally operate the oven at a temperature of 317 K. The most probable velocity of the cesium atoms is then according to Eq. 6.13 given by  $v_{Cs} \approx 250 \text{ m/s}$ .

The cesium beam emerges from the oven nozzle and then passes through the laser excitation region. There, a fraction of the cesium atoms are excited by a diode laser at a wavelength around 852 nm from the  $6S_{1/2}$  ground state to the  $6P_{3/2}$  state ( $D_2$  line) from which they are excited by a copper vapor laser at a wavelength of about 511 nm to a Rydberg state. The laser light of both lasers is guided from the laser cabin to the excitation region by a silica multimode fiber (OFS CF01493-54). For this experiment, two optical fibers are implemented in the Penning trap apparatus as described in section 2.4.3. Both fibers are mounted as shown schematically in Fig. 6.8 right next to each other so that the fiber ends are about 13 mm above the cesium beam. The laser light which is delivered by the fiber to the left to the excitation region illuminates the cesium beam, reflects from a spherical mirror and illuminates the cesium beam again. The mirror focuses it into the second fiber which guides the light out of the trap apparatus. This design ensures that as less power as possible is dissipated inside the cryogenic system.

A large area silicon photodiode ( $15 \text{ mm}^2$ ) that views the excitation region is mounted to the frame which holds the spherical mirror and the oven. It is used to detect fluorescence light due to the excitation from the diode laser. A green-blocking filter in front of the detector prevents that stray light from the copper vapor laser is detected.

Horizontal and vertical tuning plates consisting of OFHC copper are placed around the cesium beam in the excitation region. The copper vapor laser which excites the atoms from the  $6P_{3/2}$  state to a Rydberg state is at a fixed frequency. A voltage can be applied to each tuning plate and as an effect an electric field is created at the excitation region. In section 6.2.1.3 it has been calculated that the copper vapor laser excites the cesium atoms to the  $37D_{5/2}$  for the zero magnetic field case. Since the level structure of the Rydberg cesium levels cannot be calculated in the presence of a strong magnetic field, these tuning plates are foreseen to Stark-tune the Rydberg levels into resonance with the fixed frequency laser in the case if no Rydberg atoms are detected by use of the Rydberg ionization plates which are described below.

The cesium beam enters the trapping region through a 0.3 mm aperture at the entrance of a 1 mm hole in the CS electrode and leaves through a second 1 mm hole on the opposite side, where Rydberg ionization plates are mounted. Strong electric fields ( $> 100 \text{ V/cm}$ ) are produced between the plates because of the two tips when a voltage is applied to one plate while the other is kept at ground. These plates are used to field ionize the Rydberg cesium atoms. By measuring the fA-current produced by the  $\text{Cs}^+$ -ions or the electrons collected on one of the ionization plates, the production of Rydberg cesium atoms can be proved.

### 6.3.2 Lasers

#### 6.3.2.1 Grating-Stabilized Diode Lasers

We use grating-stabilized diode lasers for the excitation of the  $D_2$  line. The actual lasers have been built by Maximilian Herrmann when he was working on his diploma thesis and are extensively described therein [Her03]. They are basically copies of the diode laser system developed by Ricci et al. [RWE<sup>+</sup>95]. Very detailed information about grating-stabilized diode lasers can be obtained from the two references cited above and from [WH90]. This overview will therefore be rather short.

The mechanical setup is depicted in Fig. 6.9. A diode laser, an optical collimator and a diffraction grating are mounted on a metal block. The diffraction grating and the rear facet of the laser diode form an external cavity. The grating is mounted in a Littrow configuration where the first diffraction order is coupled back into the laser diode and therefore the grating causes a frequency selective feedback. Single-mode operation can be achieved and the linewidth is reduced to a few kHz [RWE<sup>+</sup>95]. The actual diode lasers are of the type SDL 5411-G1 with a nominal output power of about 100 mW which is reduced because of the grating to about 30 mW.

A coarse adjustment of the laser frequency is achieved by changing the micrometer adjustment screw so that the laser frequency is within a few GHz of the desired value (usually, this needs only to be done when the diode laser is used for the first time). The laser frequency is further controlled by changing the temperature of the laser system through a Peltier element which is mounted below the metal block. A temperature change causes a variation of the cavity length and thus a change of the resonance frequency of the longitudinal modes of the cavity. The diode laser system is tunable over several nanometers at a rate of about 0.3 nm/K, however not continuously. The phenomenon of mode hopping occurs [WH90]. In practice, the frequency is set by varying the temperature closer than 2 GHz to the desired value.

Fine tuning is achieved by tweaking the laser diode's drive current and the piezo-electric transducer (PZT) which tilts the position of the grating. The laser frequency can be tuned continuously by about 50 MHz by varying the drive current. We usually just tweak the drive current in order to achieve single-mode operation and then tune the

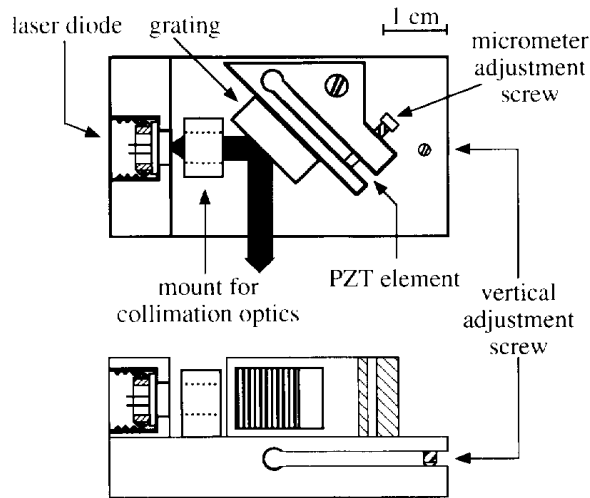


Figure 6.9: Mechanical setup of a grating-stabilized diode laser. [RWE<sup>+</sup>95].

laser via the PZT to the desired wavelength. If the voltage on the PZT is changed slowly, for example at a rate of 0.1 V/s, then the laser frequency can be pulled by about 2 GHz without any mode hops.

### 6.3.2.2 The Copper Vapor Laser

The copper vapor laser is a turn-key system bought from Spectronika Ltd., Model OM5WCVL Ogi. The laser specifications are given in Tab. 6.5. As can be seen, it emits 20 ns long pulses at the fixed wavelengths of 510.6 nm and of 578 nm at a repetition rate of between 19-20 kHz.

## 6.4 The Experiments

The experiment which has lead to the detection of antihydrogen atoms via a two-stage charge-exchange process according to Eq. 6.3–6.5 has been carried out in several steps. At first it has been demonstrated in a series of preliminary experiments that the cesium atoms are excited by the diode laser from the  $6S_{1/2}$  ground state to the  $6P_{3/2}$  state. These experiments are presented in section 6.4.1. In a second step the production of Rydberg cesium atoms according to Eq. 6.3 has been demonstrated and this experiment is presented in section 6.4.2.1. Finally, in a third step, the production of antihydrogen via two consecutive charge-exchange processes according to Eq. 6.3-Eq. 6.5 has been demonstrated which is presented in section 6.4.3.

Average power	6.5 W
Wavelength	510.6 nm , 578.2 nm
Green/ yellow (gold) ratio	1.4/1
Pulse duration	30 ns (FWHM)
(Green	20 ns
Yellow	20 ns)
Pulse repetition rate	19–20 kHz
Beam diameter	14 mm
Divergence	2.0 mrad (full angle)
Pointing stability	0.2 mrad typically
power stability	less than ±3 % absolutely

Table 6.5: Specifications of the copper vapor laser from Spectronika Ltd., Model OM5WCVL Ogi [Spe]

### 6.4.1 Excitation from the $6S_{1/2}$ Ground State to the $6P_{3/2}$ State

In this section, the experiment by which we have demonstrated that a fraction of the cesium beam running in the Penning trap apparatus is excited from a hyperfine level of the ground state to a hyperfine level of the  $6P_{3/2}$  state is presented. This experiment itself is carried out in several steps. It has been calculated in section 6.2.1.2 that there are eight possible transitions between the hyperfine components of the  $6S_{1/2}$  and the  $6P_{3/2}$  state and that the lines are separated by about 1 GHz. The line width of a grating stabilized diode laser is a few 100 kHz and thus only one out of the eight transitions can be excited per diode laser stabilized to a transition frequency. However, the appropriate transition frequency is not known apriori because the magnetic field of the Penning trap apparatus is not known precisely enough. In a first step, a transition frequency of the cesium atoms in the Penning trap had therefore to be measured. This required a robust detection method, which is presented in section 6.4.1.1 and the actual measurement of a transition frequency is presented in section 6.4.1.2. Once a transition frequency had been measured, a method to stabilize the diode laser to the transition had to be developed in order to effectively excite the atoms. This method is presented in section 6.4.1.3. As a side product, the measured transition frequencies can be used to determine the actual magnetic field in the Penning trap apparatus, which is presented in section 6.4.1.4.

#### 6.4.1.1 Demonstration of the Detection Method by Saturation Spectroscopy

The method employed to measure the transition frequencies of the  $D_2$  line has not been developed directly on the cesium beam running in the Penning trap apparatus. The reasons are that we intended to be as independent as possible on the proper functioning

of the Penning trap apparatus and that we intended to run the cesium beam as little as possible in order to preserve the ultrahigh vacuum of the Penning trap apparatus. Instead, we developed the method presented in the following by spectroscopy on cesium atoms situated in a cesium cell without any magnetic field. The cesium cell has been at room temperature, which introduces an additional problem only relevant for this external cesium cell and not for the excitation of the cesium cell within the Penning trap. The problem is that the thermal motion of the cesium atoms broadens the transition frequencies of the  $D_2$  line due to the first order Doppler effect to about

$$\Delta\nu_{\text{Doppler}} = \frac{2}{\lambda} \sqrt{\frac{2k_B T \ln 2}{m_{Cs}}} \approx 375 \text{ MHz.} \quad (6.14)$$

where the formula has been taken from [EE98] and  $\lambda = 852.2 \text{ nm}$ ,  $k_B$  is the Boltzmann constant,  $T = 300 \text{ K}$ , and  $m_{Cs}$  is the atomic mass of Cs-133. The Doppler width is much larger than the natural linewidth of the cesium hyperfine components ( $\Delta f_{\text{nat.}} = 5.2 \text{ MHz}$  [Her03]) and it is also much larger than the separation of neighboring transitions, which is at the order of 25–200 MHz [URHK00]. Hence, the cesium hyperfine components can only be resolved by a Doppler-free detection technique for the zero magnetic field case. We have used a saturation spectroscopy technique which is a method to eliminate the first order Doppler effect and therefore to resolve the hyperfine components. Saturation spectroscopy on a cesium cell is intensively discussed in many publications, see for example [Dem95] or [SKWM94] and we will therefore immediately continue with a description of the experiment.

In a first saturation spectroscopy experiment, we have repeated the experiment carried out by Udem et al. [URHK00]. The experimental setup is shown in Fig. 6.10. A small fraction ( $\sim 4\%$ ) of the power in the laser beam which is coming from the diode laser (LD) and which has passed an optical insulator (OI) is deflected at a single-sided AR coated plate (AR) and guided into the fiber input of the wavemeter (WM), Model Highfinesse WS/7 with an absolute accuracy of 100 MHz and a relative accuracy of  $10^{-7}$ . The other part of the laser beam is split by a beam splitter (BS) into a strong pump beam and a weak probe beam. The intensities of the beams are adjusted by two attenuator plates (A). The pump and the probe beam pass through the cesium cell (Cs) in opposite directions. The pump beam is chopped by an optical chopper (C) and the intensity of the probe beam is measured by a photodiode and a lock-in detector (SRS SR 510) as a function of the laser frequency. Here, the chopper frequency serves also as the reference frequency for the lock-in detector. The laser frequency is tuned continuously over the known transition frequencies [URHK00] by modulating the PZT with a  $3 \text{ V}_{pp}$  triangular wave at a frequency of 0.01 Hz. The laser frequency and the lock-in signal are recorded by a Labview VI on a computer (PC).

The result of a measurement is shown in Fig. 6.11, where the signal from the lock-in detector is plotted as a function of the frequency. Here, we have measured the hyperfine resonances of the cesium  $D_2$  line starting from the ground state total angular momentum  $F_g = 3$  to the excited states  $F_e = 2, 3, 4$  and the cross over resonances

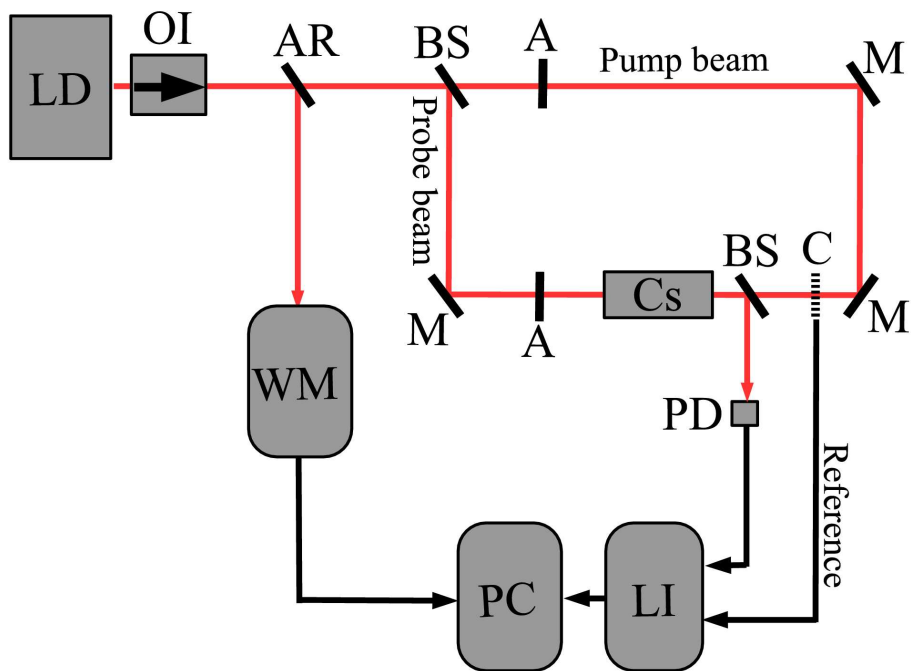


Figure 6.10: Experimental setup for saturation spectroscopy on a cesium cell. The symbols refer to: diode laser (LD), optical insulator (OI), single-sided AR (for 852 nm) coated plate (AR), beam splitter (BS), attenuator plate (A), mirror (M), cesium cell (Cs), optical chopper (C), photodiode (PD), lock-in detector (LI), computer (PC), wavemeter (WM).

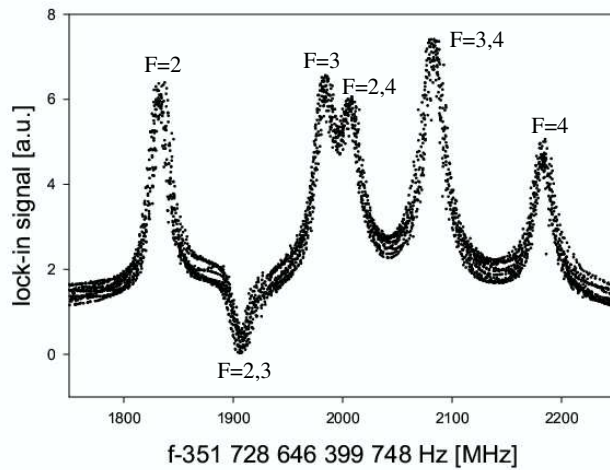


Figure 6.11: Measurement of the hyperfine components of the  $D_2$  line starting from the  $6S_{1/2}, F_g = 3$  state to the indicated  $6P_{3/2}, F$  states.

$F_e = 2, 3$ ,  $F_e = 2, 4$ , and  $F_e = 3, 4$ . The crossover resonances occur if two components within the Doppler width share a common level. In this case a velocity class of atoms with  $v \neq 0$  is probed giving rise to a resonance that is halfway in between the two transitions [URHK00]. We found the line center of the resonances by fitting the peaks separately with a Lorentzian and linear background as shown in Fig. 6.12. The result is tabulated in Tab. 6.6 along with the corresponding exact transition frequencies given in [URHK00]. In the last column of the table, the difference frequency  $\Delta f$  between the measured values and the exact values is given.  $\Delta f$  is therefore the absolute error of the measurement. The measured values are on average 72.5 MHz below the absolute values with a standard deviation of 2.2 MHz. It can be deduced from Tab. 6.6 that the frequency spacing between adjacent transitions is measured with an accuracy of better than 5 MHz. For example the spacing between the transition  $F_g = 3 \rightarrow F_e = 2$  and  $F_g = 3 \rightarrow F_e = 3$  is measured to 150 MHz and the precise spacing is 151 MHz. With these measurements, we have demonstrated that the setup for saturation spectroscopy and our data acquisition system worked correctly. Moreover, we checked the specifications of the wavemeter, which enables us to measure transition frequencies with an absolute accuracy of 100 MHz and a relative accuracy of better than  $10^{-7}$ .

However, for a measurement of the transition frequencies of the cesium atom inside the Penning trap apparatus, the reference signal for the lock-in detector had to be generated differently. Simply chopping the laser beam does not work, because it is not possible to prevent that any stray light is detected by the photodiode and since the stray light is also chopped it is therefore detected by the lock-in detector as well. Instead, the chopper is removed from the experimental setup depicted in Fig. 6.10 and a reference signal is generated by a modulation of the PZT of the diode laser with a fast 313.3 Hz, 0.1 V<sub>pp</sub> sinusoidal signal superposed on the slow 0.01 Hz 3 V<sub>pp</sub> triangular wave.

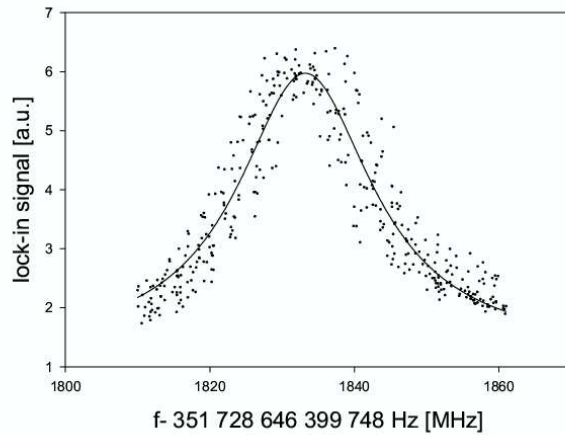


Figure 6.12: A Lorentzian has been fitted to the peak corresponding to the  $F_g = 3 \rightarrow F_e = 2$  transition, from which the center frequency is determined to  $f = 351.730\,477\,\text{THz}$ .

Transition	$f_C$ [THz]	$f_a$ [THz]	$\Delta f = f_C - f_a$ [MHz]
$F_g = 3 \rightarrow F_e = 2$	351.730 477	351.730 549 611	-73
$F_g = 3 \rightarrow F_e = 2, 3$	351.730 556	351.730 625 488	-69
$F_g = 3 \rightarrow F_e = 3$	351.730 627	351.730 700 968	-74
$F_g = 3 \rightarrow F_e = 2, 4$	351.730 651	351.730 726 043	-75
$F_g = 3 \rightarrow F_e = 3, 4$	351.730 728	351.730 801 568	-73
$F_g = 3 \rightarrow F_e = 4$	351.730 831	351.730 902 214	-71

Table 6.6: The measured transition frequencies corresponding to the transitions indicated in the first column are given in the second column. The absolute values as given by [URHK00] are given in the third column. In the last column, the difference is given, which is the error of the measured values.

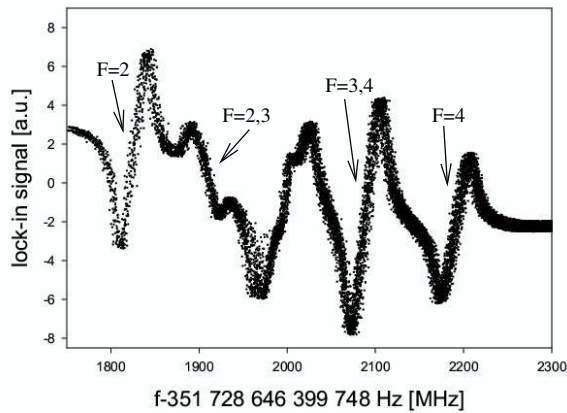


Figure 6.13: Measurement of the hyperfine components of the  $D_2$  line starting from the  $6S_{1/2}, F_g = 3$  state to the indicated  $6P_{3/2}, F$  states. A first derivative signal is measured because of the change in the modulation.

Transition	$f_{PZT}$ [THz]	$\Delta f' = f_{PZT} - f_C$ [MHz]
$F_g = 3 \rightarrow F_e = 2$	351.730 471	-6
$F_g = 3 \rightarrow F_e = 2, 3$	351.730 554	-1
$F_g = 3 \rightarrow F_e = 3, 4$	351.730 735	+7
$F_g = 3 \rightarrow F_e = 4$	351.730 836	+5

Table 6.7: The measured transition frequencies  $f_{PZT}$  of the transitions indicated in the first column are given in the second column. The difference to the frequencies  $f_C$  is given in the last column.

The fast modulation corresponds to a frequency modulation of about 100 MHz. The wavemeter measures the frequency on a time interval of 20 ms. The fast modulation is therefore averaged out and as a result it does not disturb the frequency measurement.

The result of this measurement is shown in Fig. 6.13, where the output signal of the lock-in detector is plotted over the laser frequency. A first derivative signal is measured, because of the change in the modulation. The first derivative signals depicted in Fig. 6.13 which correspond to the various peaks in Fig. 6.11 are identified by a comparison of the two figures and the so found zero crossings of the first derivative signals are marked in Fig. 6.13 by the quantum number  $F$  of the excited state. As can be seen, the two transitions  $F_g = 3 \rightarrow F_e = 3$  and  $F_g = 3 \rightarrow F_e = 2, 4$  cannot be resolved. The reason is that these two transitions are separated according to Tab. 6.6 by about 25 MHz which is less than the fast frequency modulation of 100 MHz caused by the modulation of the PZT. The transition frequencies of all other transitions are found by fitting to the slopes separately the derivative of a Lorentzian with linear background as shown in Fig. 6.14 and the transition frequencies are given in Tab. 6.7.

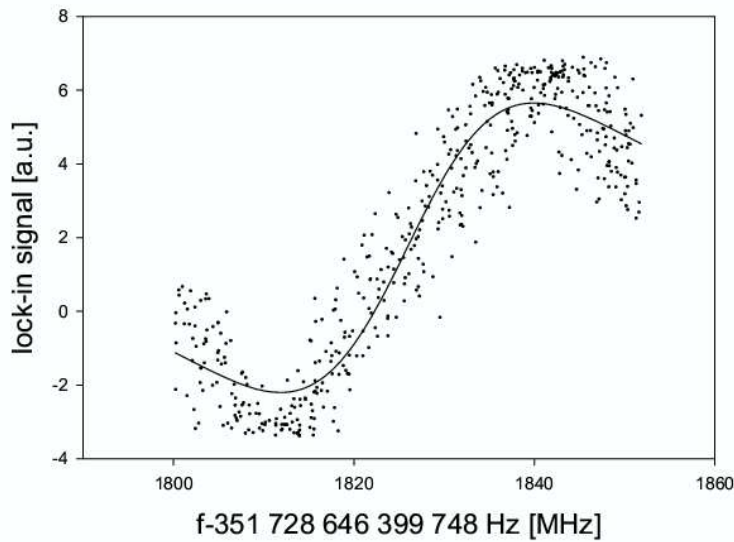


Figure 6.14: A Lorentzian with linear background is fitted to the slope. The center frequency is determined by the abscissa of the turning point of the Lorentzian. Here it is 351.730 471 THz.

The frequency spacing between the  $F_g = 3 \rightarrow F_e = 2$  and the  $F_g = 3 \rightarrow F_e = 2, 3$  transition is about 83 MHz and the two lines are clearly resolved. It has been calculated in section 6.2.1.2 that the frequency spacing between neighboring transitions of the  $D_2$  line for the case of a cesium atom in the Penning trap magnetic field is about 1 GHz. Therefore, these transition can be resolved by this detection method. In conclusion, by carrying out saturation spectroscopy on a cesium cell, we have developed and demonstrated a simple and robust method which can be applied to measure the transition frequencies of the  $D_2$  line of the cesium atoms in the Penning trap apparatus with an absolute accuracy of 100 MHz.

#### 6.4.1.2 Measurement of the Transition Frequencies

In this section, the experiment carried out to measure the transition frequencies of the cesium  $D_2$  line in the Penning trap apparatus is presented. The experimental setup is shown schematically in Fig. 6.15. A small fraction ( $\sim 4\%$ ) of the power in the laser beam which is coming from the diode laser (LD) and which has passed an optical insulator (OI) is deflected at a single-sided AR coated plate (AR) and guided into the fiber input of the wavemeter (WM), Model Highfinesse WS/7 with an absolute accuracy of 100 MHz and a relative accuracy of  $10^{-7}$ . About 10 mW of the diode laser power is focused into the optical fiber which guides the laser light to the excitation region as described in section 6.3.1. The diode laser is set to a frequency of about 351.803 THz and then tuned by about 1.5 GHz by  $2 V_{pp}$ , 0.01 Hz triangular signal applied to the

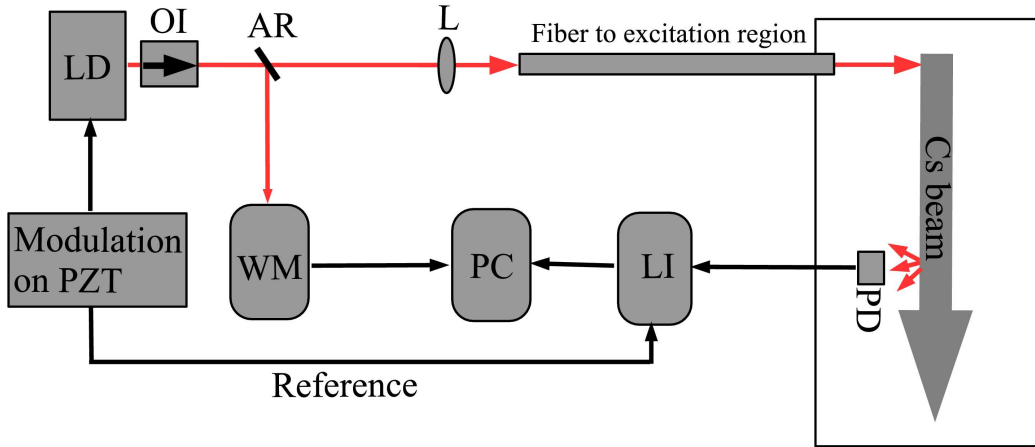


Figure 6.15: The laser setup used to find the transition frequencies of cesium atoms in the Penning trap apparatus.

PZT. It is therefore ensured that the laser frequency sweeps according to Fig. 6.4 on page 84 over a resonance. A fast 313.3 Hz,  $0.1 \text{ V}_{pp}$  sinusoidal modulation is superposed on the slow modulation of the PZT, which causes a fast frequency sweep of about 100 MHz. When the laser frequency is on resonance, the cesium atoms are excited and the photodiode viewing the excitation region detects fluorescence light. The photodiode signal is measured with a lock-in detector with the fast modulation on the PZT as reference signal. Here we have not employed a Doppler-free detection technique, since the frequency spacing between neighboring transitions has been calculated in section 6.2.1.2 to be at about 1 GHz.

The measured signal of the lock-in detector is shown in Fig. 6.16 as a function of the laser frequency. The derivative of a Gaussian line is fitted to the data. The center frequency is determined by the abscissa of the turning point of the curve, which yields  $351\,803\,770 \pm 100$  MHz, where the error is due to the resolution of the wavemeter. The full width at half maximum (FWHM) of the transition is determined by the frequency spacing of the maximum and minimum of the dispersion curve which yields  $46 \pm 2$  MHz.

In order to ensure that a real transition has been identified, the experiment is repeated for a laser frequency which is close to 351.800 THz (according to section 6.2.1.2, the fourth next transition with respect to the transition identified above should then be detected). The detected signal is shown in Fig. 6.17 as a function of the laser frequency. The center frequency is determined to  $351\,799\,471 \pm 100$  MHz and the FWHM is  $57 \pm 2$  MHz.

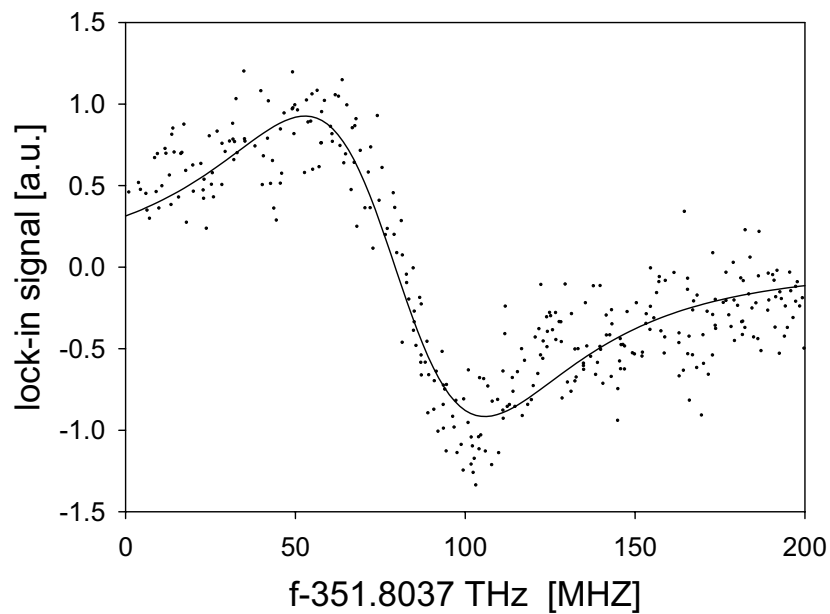


Figure 6.16: The lock-in signal from the photodiode is depicted as a function of the laser frequency. The derivative of a Gaussian line is fitted to the curve. The center frequency is determined by the abscissa of the turning point which yields  $351\,803\,770 \pm 100$  MHz. The line width is given by the FWHM, which is  $46 \pm 2$  MHz.

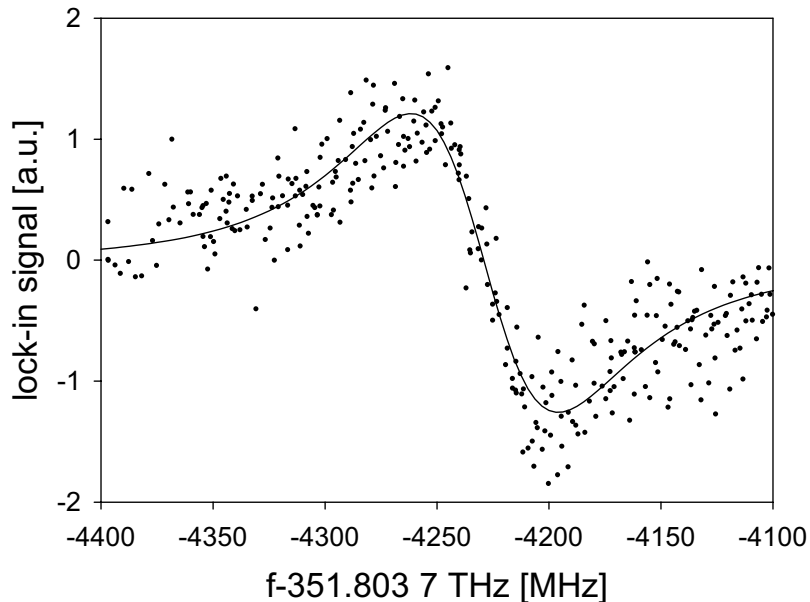


Figure 6.17: The lock-in signal from the photodiode is depicted as a function of the laser frequency. The derivative of a Gaussian line is fitted to the curve. The center frequency is determined by the abscissa of the turning point which yields  $351\,799\,471 \pm 100$  MHz. The line width is given by the FWHM, which is  $57 \pm 2$  MHz.

#### 6.4.1.3 Locking Scheme of the Diode Laser to a Transition Frequency

The method which is used to stabilize the diode laser in all subsequent experiments to a transition frequency is described in this section. For all experiments presented subsequently, we have arbitrarily chosen to excite the transition with center frequency of  $351\,803\,779 \pm 100$  MHz. The diode laser is stabilized to the transition in a three step procedure, carried out before each experiment. In a first step, the diode laser is tuned to 351.803 779 THz ensuring that the frequency is within 100 MHz close to the actual transition frequency. A 313 Hz,  $0.1\text{ V}_{pp}$  sinusoidal modulation is applied to the PZT of the diode laser which serves as a reference signal for the lock-in detector. The lock-in detector is used to amplify any fluorescence signal seen by the photodiode which views the excitation region in the same way as described in the previous section. In a second step, the diode laser is manually swept over  $\pm 100$  MHz by changing the offset voltage additionally applied to the PZT. As a result, the laser frequency is swept through the resonance and the lock-in detector monitors the dispersion signal similar to the signal depicted in Fig. 6.16. The laser frequency at the zero crossing of the lock-in signal corresponds to the center frequency of the transition (neglecting a small offset, which might be present). The short term stability of the wavemeter is within a few MHz. Therefore in a third step the measured frequency at the zero crossing of the lock-in signal is used as a set point for the frequency stabilization. The frequency stabilization

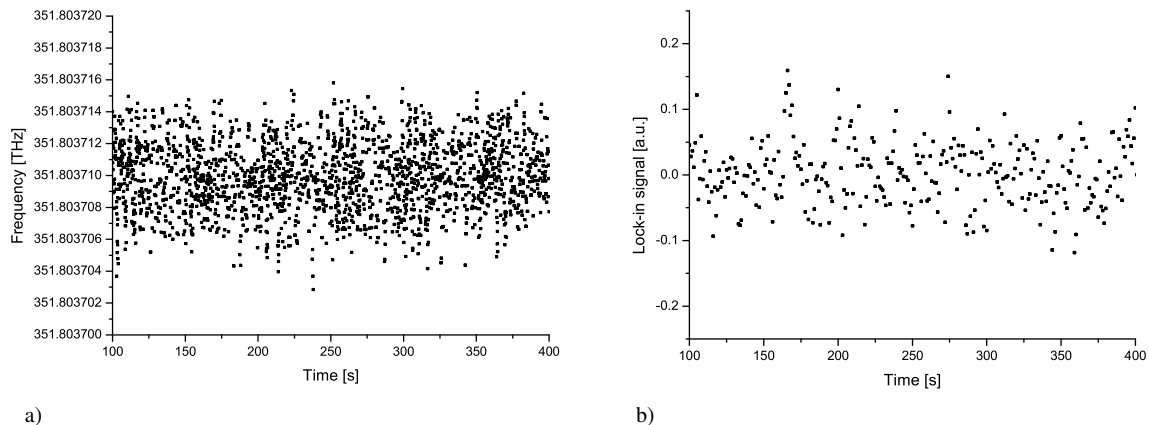


Figure 6.18: The laser diode is stabilized to the center frequency of 371.803 710 THz. The stabilization keeps the diode laser to within about  $\pm 5$  MHz to the set point.

system is a software PI-controller written in Labview [Lab]. It reads out every 0.1 s the diode laser frequency from the wavemeter and keeps the laser frequency within about  $\pm 5$  MHz close to the set point by adjusting the offset voltage applied to the PZT. Fig. 6.18a shows the diode laser frequency stabilized to 371.803 710 THz as a function of time and Fig. 6.18b shows the corresponding lock-in detector signal. As can be seen, the control system keeps the laser frequency within about  $\pm 5$  MHz to the stabilization point over a time of more than 400 s, a time far longer than necessary for carrying out an antihydrogen experiment. It seems to be even more straightforward to lock the laser frequency directly to the output signal of the lock-in detector. However, the photodiode mounted in the trap can resides at 4.2 K and is heated during an antihydrogen experiment by the copper vapor laser used to excite the atoms from the  $6P_{3/2}$  state to a Rydberg state. The heating causes a change in the noise spectrum of the photodiode and causes sometimes strong fluctuations of the lock-in signal which would unlock the laser. We therefore did not consider this alternative method.

#### 6.4.1.4 Determination of the Penning Trap Magnetic Field

The transition frequencies measured in section 6.4.1.2 can be used to determine the magnetic field  $B_0$  of the Penning trap apparatus. The transition frequency is given in Eq. 6.9 on page 83 as a function of the  $m_I$  quantum number of the states between which the transition is induced and as a function of the magnetic field  $B_0$ . Thus, in order to determine the magnetic field of the Penning trap, the  $m_I$  quantum number for the measured transition frequencies have to be determined.

This has been achieved by the following method. The grating-stabilized diode laser is locked to the transition with center frequency  $f = 351\,803\,779 \pm 100$  MHz as described in the previous section. Additionally, the cesium beam is exposed to about 5 mW of

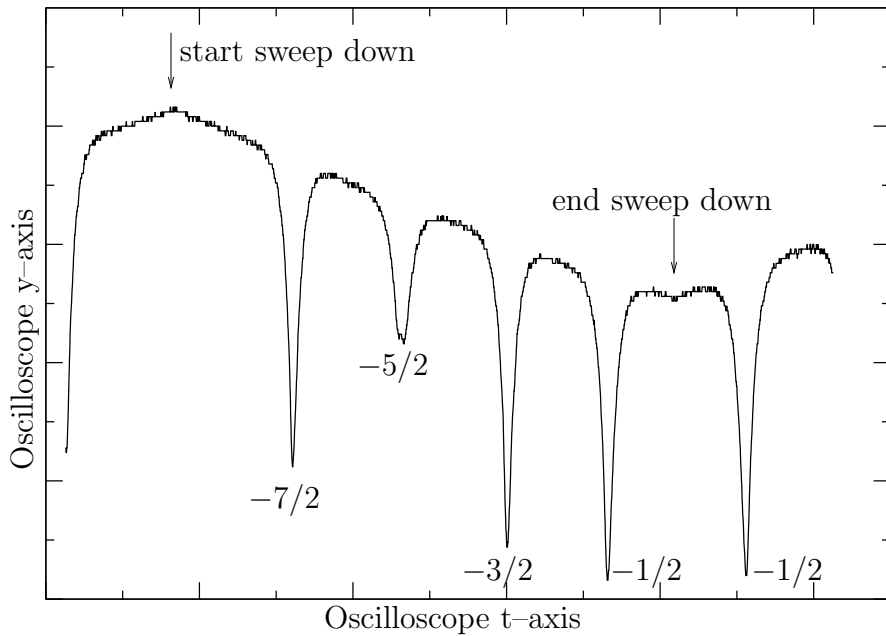


Figure 6.19: Scope trace of the fluorescence signal induced by a free-running diode laser. The time between the start and the end of the sweep down corresponds to  $\frac{1}{2} \cdot \frac{1}{780}$  s.

laser light delivered by a laser diode which is not grating-stabilized. The frequency of the laser diode is set to about 351.803779 THz and then modulated over a frequency range of a few GHz by a triangular modulation (780 Hz, 1 V<sub>pp</sub>) of the injection current. The fluorescence signal detected by the photodiode which views the excitation region is monitored by an oscilloscope triggered to the triangular modulation signal. This fluorescence signal can be observed by an oscilloscope operated in an averaging mode without usage of a lock-in detector when the cesium oven is running in steady state at 317 K. The oscilloscope signal is shown in Fig. 6.19. The vertical axis depicts the intensity of the photodiode as a function of time. At the position marked by the arrow to the left (begin sweep down), the triangular modulation is at its maximal value and correspondingly the laser frequency is also at its maximum. The modulation signal and correspondingly the laser frequency is steadily decreased until they reach their minimum value at the position marked by the arrow to the right (end sweep down). As can be seen by the four equally spaced dips, the laser frequency sweeps over four transitions. The dip to the left corresponds to the highest frequency at which we observe a dip and therefore according to the calculations presented in section 6.2.1.2 to a transition between hyperfine states with  $m_I = -7/2$ . The other dips correspond then from left to right to transitions between hyperfine states with  $m_I = -5/2, -3/2, -1/2$  as indicated in Fig. 6.19. The dip to the very left corresponds already to the half cycle in which the laser frequency is swept from low to high values and therefore to a transition between hyperfine states with  $m_I = -1/2$ . The depth of the dip with  $m_I = -5/2$  is half of the depth of the other dips. The reason is that this transition is also excited by the

grating-stabilized diode laser. Thus, the center frequency  $f = 351\,803\,779 \pm 100$  MHz corresponds to transitions between hyperfine levels with  $m_I = -5/2$ . The transition measured at  $351\,799\,471 \pm 100$  MHz is about 4.3 GHz lower than  $351\,803\,779 \pm 100$  MHz and corresponds therefore to the transition which is the fourth next neighbor and thus  $m_I = +3/2$ .

The magnetic field  $B_0$  of the Penning trap apparatus is obtained by solving Eq. 6.9 for the magnetic field  $B$  which yields

$$B(f, m_I) = \frac{h(f - f_{D_2}) - \frac{1}{2}m_I \left( 3A_{6P_{3/2}} + A_{6S_{1/2}} \right) - B_{6P_{3/2}} \left( \frac{3}{56}m_I^2 + \frac{1}{56}m_I - \frac{15}{32} \right)}{\frac{1}{2}\mu_B \left( 3g_{6P_{3/2}} - g_{6S_{1/2}} \right) - \mu_k m_I \left( g_{6S_{1/2}} + g_{6P_{3/2}} \right)}, \quad (6.15)$$

where the values for the constants are given in Tab. 6.2 on page 83. The uncertainty  $\Delta B$  in the magnetic field is determined by the uncertainty in the measurement of the transition frequencies, which is  $\Delta f = 100$  MHz and  $\Delta B$  can then be calculated by

$$\Delta B(m_I) = \frac{dB}{df} \Delta f = \frac{h}{\frac{1}{2}\mu_B \left( 3g_{6P_{3/2}} - g_{6S_{1/2}} \right) - \mu_k m_I \left( g_{6S_{1/2}} + 3g_{6P_{3/2}} \right)} \Delta f. \quad (6.16)$$

Using  $f = 351\,803\,779 \pm 100$  MHz and  $m_I = -5/2$  yields  $B = 5.387 \pm 0.007$  T and  $f = 351\,799\,471 \pm 100$  MHz and  $m_I = +3/2$  yields  $B = 5.386 \pm 0.007$  T. By taking the average, the magnetic field of the Penning trap apparatus is determined to  $B_0 = 5.387 \pm 0.007$  T.

### 6.4.2 Excitation from the $6P_{3/2}$ State to a Rydberg State

It has been demonstrated in the previous section, that the cesium atoms are excited by a diode laser from a hyperfine level of the ground state to a hyperfine level of the  $6P_{3/2}$  state. From this state, they are excited to a Rydberg state by a copper vapor laser. The experiment by which we have demonstrated that Rydberg cesium atoms are produced in the Penning trap apparatus is presented in section 6.4.2.1. The experimental results of this section can be used to derive an estimate for the Rydberg cesium flux passing through the trapping region, which is given in section 6.4.2.2.

#### 6.4.2.1 Detection of Rydberg Cesium Atoms

The laser setup used to excite the cesium atoms to a Rydberg state is depicted in Fig. 6.20. Green laser light from the copper vapor laser (CVL) is focused by a lens (L) into the optical fiber which guides the laser light to the excitation region. The

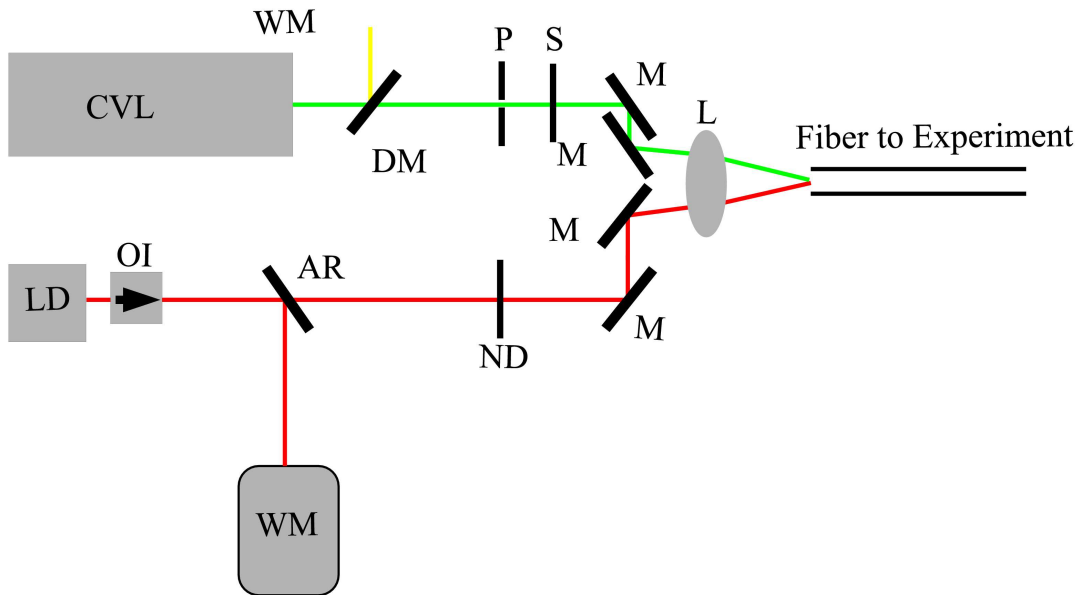


Figure 6.20: Laser setup for the production of Rydberg cesium atoms. CVL: copper vapor laser, LD: grating-stabilized diode laser, OI: optical insulator, DM: dichroic mirror, I: continuously variable iris, S: shutter, M: mirror, L: lens, ND: neutral density filter, AR: single-sided antireflection-coated plate, WM: wavemeter.

beam can be blocked by a remotely controlled shutter (S) and the laser power sent to the experiment can be adjusted by a continuously variable iris (P). If nothing else is stated, we send  $0.5 \pm 0.01$  W of green laser light to the experiment. The yellow line is filtered out by use of a dichroic mirror (DM), which has a high reflectivity for yellow and a high transmittivity for green light. Infrared laser light coming from the grating-stabilized laser diode (LD) is focused into the same optical fiber. The laser power can be adjusted by a neutral density filter (ND). If nothing else is stated, about 10 mW are sent to the excitation region. A fraction of the laser light is deflected from a single-sided anti-reflection coated plate (AR) and focused into the fiber input of the wavemeter (WM).

In a first step, the diode laser is tuned to the transition frequency of the  $6S, m_J = +1/2, m_I = -5/2$  to  $6P, m_J = +3/2, m_I = -5/2$  transition which has been found in section 6.4.1.2 to be at  $351\,803\,779 \pm 100$  MHz and the fluorescence signal due to the excitation of the cesium atoms is detected. Then, the frequency of the diode laser is modulated by a  $0.5\text{ V}_{pp}$  square wave signal at a frequency of 4.117 Hz delivered from a SRS DS 345 function generator, which is applied to the PZT of the diode laser. As a result, the laser frequency jumps from being on resonance at 351.803 779 THz to being off resonance at 351.803 400 THz. In a third step, the shutter which has blocked the green laser beam is opened and a voltage is applied to one Rydberg ionization plate depicted in Fig. 6.8 while the other plate is kept at ground, which produces an electric field between the

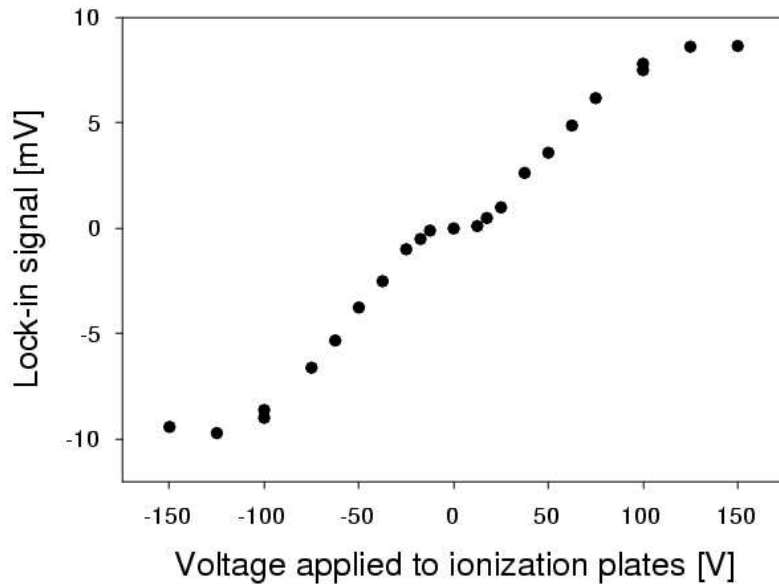


Figure 6.21: The signal of the ionized Rydberg cesium atoms measured by the lock-in detector as a function of the voltage applied to one ionization plate.

plates. If the electric field is strong enough ( $> 150 \text{ V/cm}$ ), it will ionize the Rydberg atoms. Depending on the sign of the applied voltage, a current from the  $\text{Cs}^+$ -ions or from the electrons can be collected on one of the ionization plates. The current is in the fA-range. It is amplified by a home-made current amplifier with a gain of  $G = 10^{11} \text{ V/A}$ . The amplified signal is measured by a lock-in detector (SRS SR830). The square wave signal applied to the PZT, which switches on and off the excitation of the 6P state and therefore the production of Rydberg cesium atoms serves as reference signal for the lock-in detector.

The measured signal is depicted in Fig. 6.21 as a function of the voltage applied to an ionization plate. The signal is antisymmetric with respect to 0 V, which is expected because depending on the sign of the voltage either the current due to the electrons or the cesium ions is measured. In the range from zero to  $\pm 15 \text{ V}$ , no current is measured. The electric field between the plates is still too weak to ionize any atom. For higher voltages, the signal increases linearly. As depicted in Fig. 6.8, the Rydberg ionization plates are not flat but contain two tips facing each other. The electric field close to the tips is already strong enough to ionize the Rydberg atom passing through. The signal saturates at voltages of less than  $-100 \text{ V}$  and of more than  $+100 \text{ V}$  indicating that the electric field between the Rydberg ionization plates is strong enough to ionize all Rydberg atoms passing through.

During the experiment, the intensity of the infrared light has been changed by a change of the neutral density filter. This had basically no effect on the measured lock-in

signal indicating that the transition induced by the diode laser is saturated. We also temporarily decreased the intensity of the green light from 0.5 W to 0.25 W. As an effect, the signal on the lock-in detector dropped to -3.8 mV indicating that the green laser does not saturate the transition to a Rydberg state.

As a result, we demonstrated that Rydberg cesium atoms are produced by the two step excitation scheme according to Eq. 6.3.

#### 6.4.2.2 Determination of the Rydberg Cesium Flux

The Rydberg cesium flux  $N_{Cs^*}$  is defined here as the number of Rydberg cesium atoms which pass through the trapping region. The cesium flux can be deduced from the lock-in signal which is measured in the saturated region for applied voltages larger than +100 V or less than -100 V. A lock-in detector measures a RMS-voltage signal [SRSb]. A 1 V<sub>pp</sub> square wave signal is measured to 0.45 V<sub>RMS</sub> [SRSb]. Consider that the signal measured by the lock-in detector is x mV<sub>RMS</sub>. The current  $I$  in the ionization plate is then given by  $I = \frac{2}{G} \frac{1}{0.45} x \times 10^{-3}$ , where x is given in mV,  $G = 10^{11}$  A/V is the gain of the current amplifier and the result is given in Ampere. The extra factor of 2 is taken into account because the diode laser is locked to a transition during an actual antihydrogen experiment instead of being off resonance for half the measurement time and it is the Rydberg cesium flux during an actual experiment which is interesting to us. The Rydberg cesium flux through the Rydberg ionization plates is then given by  $I/q$ , where q is the unit electric charge.

The question now arises, how many cesium atoms that pass through the trapping region actually pass through the cesium ionization plates and contribute to the fA-current measured by the lock-in detector. The geometry of the experimental setup for the Rydberg cesium beam, which is schematically depicted in Fig. 6.8, is designed so that for geometrical arguments all atoms that pass through the 0.3 mm aperture in the trap electrode also pass through the second 1 mm hole before entering the Rydberg cesium detection region. Thus if any collisional effects that the Rydberg cesium atoms encounter on their way from the trapping to the excitation region are neglected, the cesium flux in the trapping region is approximately given by

$$N_{Cs^*} = \frac{I}{q} \approx 3 \times x \times 10^5 \text{ 1/s.} \quad (6.17)$$

For the experiment described above in section 6.4.2.1, the lock-in signal in the saturation region is on average x=8.7 mV, which yields a Rydberg cesium flux according to Eq. 6.17 of about  $2.6 \times 10^6$  Rydberg cesium atoms per second. For this experiment, the cesium oven was operated at a temperature of about 350 K in order to obtain a clear lock-in signal. As mentioned before, during an actual antihydrogen experiment, the oven is run at a lower temperature of about 317 K. At this temperature, the lock-in signal is 3.4 mV which yields to a Rydberg cesium flux of about  $10^6 \text{ s}^{-1}$ . The copper

vapor laser is a pulsed laser with a repetition rate  $f_{rep} = 19 - 20 \text{ kHz}$ . Hence, about 50 Rydberg cesium atoms pass through the Penning trap per laser pulse.

### 6.4.3 The Production of Antihydrogen

In this section, the actual experiment by which antihydrogen atoms are produced in a two-stage Rydberg charge-exchange experiment according to Eq. 6.3, Eq. 6.4, and Eq. 6.5 is presented.

#### 6.4.3.1 The Experimental Setup

A cross sectional view of the bottom part of the lower electrode stack (electrodes U2 to TBE) of the hbar2 Penning trap apparatus is shown in Fig. 6.22a. The electric potential structure on axis is depicted along with the corresponding electric field as a function of the axial position in Fig. 6.22b. As can be seen from Fig. 6.22, the positrons are loaded into a static potential well formed at the CS electrode and the antiprotons are loaded into the adjacent potential well formed at the LP electrode. The positrons and antiprotons are loaded into these static potential wells by methods described in chapter 3. The number of positrons is counted before an experiment by a radio-frequency counting technique as described in section 2.5.1. The number of antiprotons is counted after an experiment by summing over all detected antiproton losses that occurred during an experiment and by adding the number of antiprotons that remained in the antiproton well after an experiment. They are also detected destructively by ejecting them from the well and by counting the number of annihilations.

The positrons are exposed to the Rydberg cesium beam as indicated in Fig. 6.22a. The laser system used to excite the cesium atoms to a Rydberg state is given in Fig. 6.20 on page 107. The production of the Rydberg cesium beam is intensively described in the previous sections. The cesium oven is operated at a temperature of 317 K and the cesium atoms are excited by about 10 mW of infrared laser light and by 0.5 W of green laser light to a Rydberg state. These parameters yield according to section 6.4.2.2 a Rydberg cesium flux of about  $10^6$  Rydberg cesium atoms per second, which pass through the positron cloud. The electric field in the region of the positron cloud is less than 20 V/cm which ensures that the Rydberg cesium atoms are not field-ionized.

The produced Rydberg antihydrogen atoms are detected in the detection well. The axial electric field in this region exceeds 400 V/cm for all radii in the detection trap, which is much more than enough in order to ionize the Rydberg antihydrogen atoms which should ionize already at 150 to 200 V/cm. An ionized antihydrogen atom deposits its antiproton in the detection well and the antiproton can be counted background-free later. The detection well is constructed in a way that only an antiproton ionized from

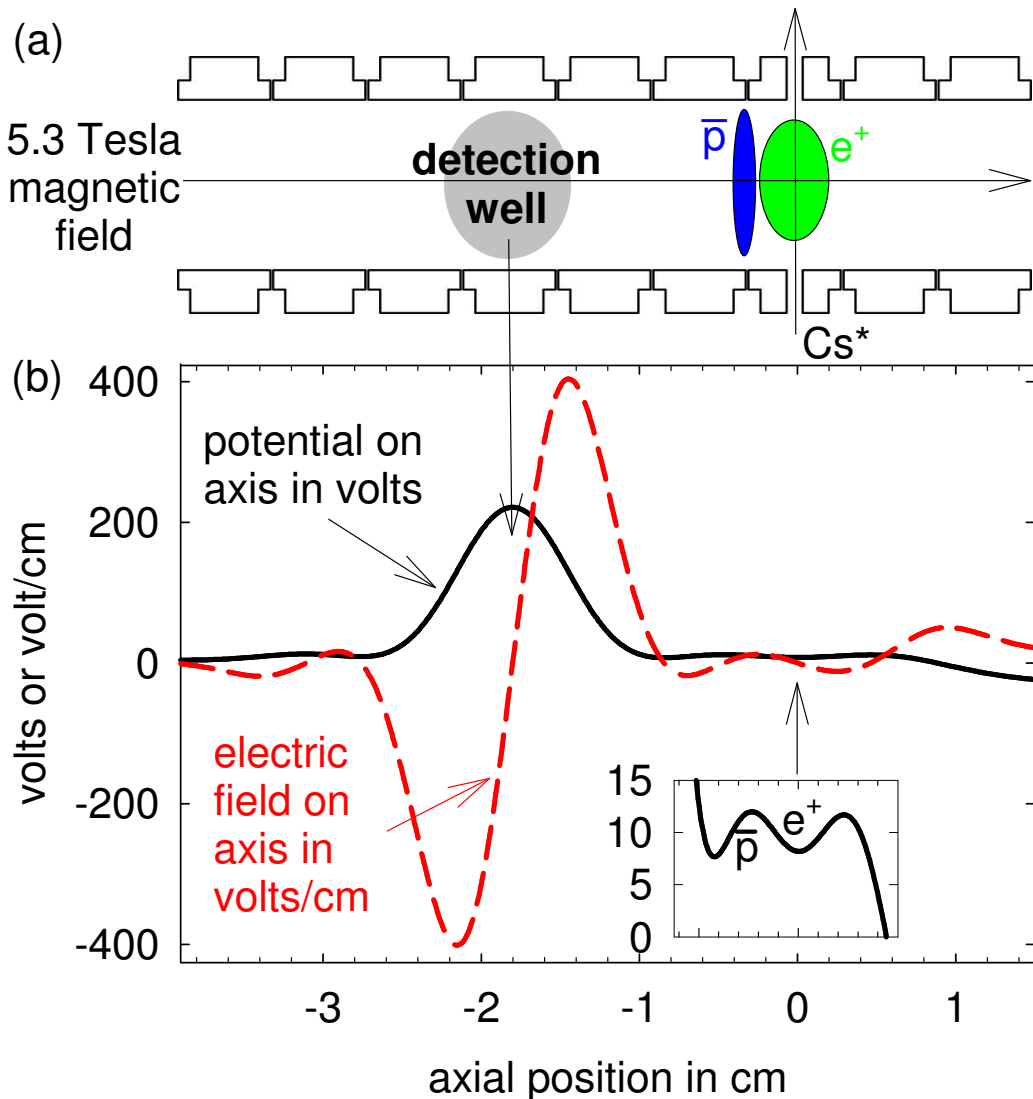


Figure 6.22: a) Trap electrode cross section with particle location. b) The potential structure on axis along with the corresponding electric field is shown. The potential structure to the right is used for particle storage and this region is magnified by the small picture. The potential well to the left is used for the detection of antihydrogen via field-ionization.

an antihydrogen atom can be collected there. If an antiproton does manage to escape the antiproton trap and pass through the detection trap, it cannot be captured unless a collision with an already stored particle in the detection well lowers the antiproton energy. Typical collisional energies are at the order of  $k_B T \ll 1 \text{ eV}$ . As a precaution the left side of the detection well is kept lower by 1 eV than the right side in Fig. 6.22b (although the offset is too small in order to be visible).

#### 6.4.3.2 Experimental Results

For the detection of antihydrogen atoms, the antiprotons captured in the detection well are released and the annihilation signals are detected. However, the production rate and hence the number of stored antiprotons is low and in order to be able to identify a signal, the time information of the detected antiproton annihilations has also to be considered. For a calibration of the time information, about 15 000 antiprotons are stored in the detection well. The detection well depth is shown as a function of time by the solid blue curve in Fig. 6.23b. It is ramped down within 40 ms while the number of antiproton annihilations is monitored. The histogram in the same graph shows the number of antiprotons detected as a function of time. All stored antiprotons annihilate in a window of less than 4 ms.

In the actual antihydrogen experiment, the electric field in the detection well is strong enough to ionize any Rydberg positronium atom passing through that region. We actually observe electrons in the detection well. The so deposited electrons cool radiatively to the 4.2 K environment and in addition collisionally cool the antiprotons to 4.2 K. Thus, we expect that the detected antiprotons will be at the bottom of the trap potential and therefore we use the very right edge of the histogram in Fig. 6.23b to select a  $700 \mu\text{s}$  time window that contains annihilation signal from antiprotons released from the very bottom of the detection well. The antiprotons captured from antihydrogen are released in the same way as in the calibration. Six experiments with changing numbers of antiprotons and positrons have been carried out. The identification number of the experiment as it is stored in our data acquisition, the number of antiprotons and positrons as well as the number of counts within the  $700 \mu\text{s}$  time window is given for each of the six experiments in Tab. 6.8. A count indicates a coincidence of signals of at least two scintillating fibers located in different layers of the fiber detector. The total number of counts in the expected channel is 13. The sum of all signals in that channel is depicted as a histogram in Fig. 6.23a. 13 counts correspond to 14 antihydrogen atoms in the detection trap when the  $94 \pm 6\%$  [Grz] detection efficiency of the fiber detectors is taken into account. On average 2.4 background counts [Grz] are expected in the 40 ms width of Fig. 6.23a and two counts are seen outside the  $700 \mu\text{s}$  window. Statistically, there is therefore a 4% chance that a background count is in the peak of the  $700 \mu\text{s}$  time window. The statistical error in the number of detected antihydrogen atoms is given by  $\sigma = \sqrt{14} \approx 3.7$ . Thus  $14 \pm 4$  antihydrogen atoms are detected in the six trials.

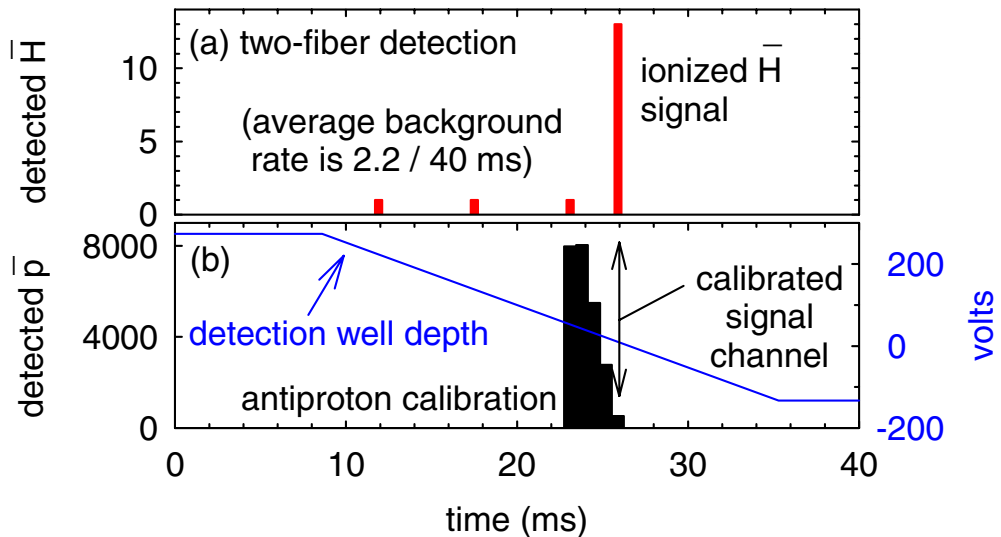


Figure 6.23: a) Antihydrogen detected as the potential well whose axial well depth is indicated by the blue curve in b) is ramped down. b) antiproton annihilation histogram as the potential well (solid curve and right scale) is reduced through zero.

RUN#	Number of $\bar{p}$	Number of $e^+$	$\bar{H}$ Counts
3394	140 000	2 200 000	2
3397	150 000	1 500 000	1
3399	130 000	1 500 000	2
3400	100 000	700 000	0
3409	420 000	2 500 000	4
3411	450 000	2 200 000	4

Table 6.8: The number of antiprotons and positrons and the antihydrogen counts are tabulated for the six experiments in which antihydrogen is detected. The error in the number of antiprotons results from statistics and is given by the square root of the tabulated numbers. The uncertainty of the number of positrons is due to the rf-counting technique and is about 20% of the measured value.

RUN #	Type	Number of $\bar{p}$	Number of $e^+$
3401	no $e^+$	138 500	0
3404	DL off resonance	40 500	2 340 435
3407	DL off resonance	210 200	837 812
3412	no $e^+$	206 800	0

Table 6.9: The control experiments from which we have detected zero counts as expected. It is specified in the second column, if no positrons have been used or if the diode laser frequency has been off resonance with a transition between the hyperfine levels of the  $6S_{1/2}$  to  $6P_{3/2}$  state.

Although the most convincing evidence that the detected signals are from antihydrogen atoms is that the potential wells are arranged so that an antiproton by its own cannot be trapped in the detection well for reasons described above, we have additionally carried out four control experiments in which either the diode laser frequency has been tuned off resonance or no positrons have been present in the positron well. The experiments are tabulated in Tab. 6.9. In the first case, the diode laser frequency has been tuned and locked by 500 MHz away from resonance and we ensured that the same laser power of 10 mW was sent to the excitation region. By setting the laser frequency off resonance, only ground state cesium atoms pass through the trapping region. The charge-exchange cross section between ground state cesium atoms and stored positrons is according to section 6.2.2 low and therefore no antihydrogen atoms are expected to be produced. In the control experiment without positrons no Rydberg positronium atoms are produced and thus no antihydrogen atoms. In all four experiments, no counts in the selected channel were detected as expected.

## 6.5 Summary and Conclusion of this Chapter

By the experiment presented here, antihydrogen atoms have been produced for the first time via a consecutive charge-exchange mechanism. The experimental result has been published in [SSS<sup>+</sup>04]. The experiment has been carried out in the last week of the 2003 beam run and therefore only  $14 \pm 4$  antihydrogen atoms could be detected because of the small number of trials.

If one thinks about possibilities to increase the number of produced antihydrogen atoms per trial, one has to distinguish two problems. The first problem is how to increase the total number of produced antihydrogen atoms. This can be done by increasing the number of antiprotons and positrons used for antihydrogen formation, since the total number depends according to section 6.2.2 linearly on these parameters. Additionally, the distance between the antiproton and positron clouds can still be optimized. With the detector system that is currently constructed for the new Penning-Ioffe trap is will

be possible to track the antihydrogen annihilation events and thus to count the total number of produced antihydrogen atoms. This system will probably be available for beamtime 2006.

The second problem is how to increase the number of detected antihydrogen atoms. This could be achieved by decreasing the distance between the detection well and the antiproton well. Because of solid angle arguments, the detected number should increase with the inverse of the distance squared. The distance between the center of the detection well and the antiproton well is in the current setup about 1.6 cm. The large distance is mainly due to the fact that for the field-ionization method to work, the detection well needs to have a depth of more than 200 V in order to generate the large electric fields between the detection and ionization well. An better optimized potential structure might allow a decrease of the distance between the production and detection regions. A factor of two in the detection efficiency can also be gained by placing an additional detection well to the opposite site of the production region.

Despite the number of antihydrogen atoms is currently much lower than by the merging antiproton and positron plasmas in nested Penning traps, this method offers several advantages. The state distribution of the formed antihydrogen atoms is much narrower and the atomic states can be selected by choice of the cesium Rydberg state. In that sense the antihydrogen states can be controlled by the lasers used to excite the cesium atoms. The narrower state distribution and the controllability of the atomic states would for example allow to deexcite trapped Rydberg antihydrogen atoms with a laser source, for example by use of the Titanium:Sapphire laser system presented in chapter 5 to the  $n = 3$  state from which the atoms would decay within a few nanoseconds to the ground state. Moreover, it is expected that the formed antihydrogen atoms have the velocity distribution of the antiprotons from which they are formed. The antiprotons remain trapped in a static potential well and are therefore at a temperature of 4.2 K. If indeed antihydrogen is produced at that temperature, the antihydrogen atoms at the lower end of the Maxwell–Boltzmann distribution should be trapable by a superposed Ioffe trap.



# Chapter 7

## Towards a Temperature Measurement of the Antihydrogen Atoms Produced in the Two-Step Charge-Exchange Process

### 7.1 Introduction

In the previous chapter an experiment has been presented by which antihydrogen atoms have been produced in a two-step charge-exchange process according to Eq. 6.3–Eq. 6.5. These antihydrogen atoms are expected to have a temperature of 4.2 K because they are produced from trapped antiprotons which reside at that temperature. However, this assumption has yet to be verified experimentally. In this chapter, an experiment is therefore presented by which a determination of the antihydrogen temperature might be feasible.

The most straightforward way to measure the temperature or equivalently the mean kinetic energy of the antihydrogen atoms would be by adding an oscillating pre-stripping field to the experimental setup depicted in Fig. 6.22 which would be placed between the trapped antiprotons and the detection well. The average kinetic energy of the antihydrogen atoms would then be determined in the same way as by the velocity measurement carried out on the antihydrogen atoms produced in a nested Penning trap as presented in section 4.4, namely by measuring the number of antiprotons in the detection well as a function of the frequency of the pre-stripping field. For such a measurement, the detection well would have to be moved away from the antiproton well in order to provide enough space for the pre-stripping field. The number of antiprotons in the detection well would then drop because of solid angle arguments. Since only about two to four antiprotons are detected per experiment with the detection well at

the minimum possible distance away from the antiproton well such a measurement of the antihydrogen mean kinetic energy is not feasible.

The basic idea of an experiment by which the temperature of the antihydrogen atoms might be measurable is as follows: The Rydberg cesium atoms are produced in bunches since they are excited by the pulsed copper vapor laser to a Rydberg state. Hence, the Rydberg positronium atoms and subsequently the antihydrogen atoms are produced in bunches. The antihydrogen atoms leave the production region according to [HHC98] isotropically and annihilate at the trap electrodes. The time delay between the annihilation events of an antihydrogen bunch with respect to the laser pulse that initiated its production via the excitation of the cesium atoms can be measured. Consider the time delay of a single antihydrogen annihilation event with respect to the laser pulse. It is determined by the time a Rydberg cesium atom travels from the location where it has been excited by the copper vapor laser to the location within the positron cloud where it forms positronium according to Eq. 6.4 plus the time the positronium travels to the location within the antiproton cloud where it forms antihydrogen according to Eq. 6.5 plus the time the antihydrogen atom travels to the electrodes and annihilates. The time the antihydrogen atom travels is given by the ratio between the path length between the location of its production and its annihilation and its velocity. A measurement of the time distribution of many antihydrogen annihilation events therefore contains information about the velocity distribution of the antihydrogen atoms and thus about the antihydrogen temperature.

In order to investigate quantitatively the influence of the antihydrogen temperature on the time distribution of the annihilation signals and in order to evaluate an experimentally measured time distribution of antihydrogen annihilations, a numerical analysis of the experiment has been carried out, which is presented in section 7.2. An actual experiment to measure the antihydrogen temperature is presented in section 7.3. The chapter finishes with a conclusion in section 7.5.

## 7.2 Numerical Analysis

The procedure of the numerical analysis is described in section 7.2.1. The results are presented in section 7.2.2.

### 7.2.1 Description of the Algorithm

The time distribution of  $\mathcal{N}$  antihydrogen annihilations is calculated by the algorithm described in the following. The basic concept is to calculate  $\mathcal{N}$  times the time of flight of a Rydberg cesium atom from the excitation region to the location where the first charge-exchange occurs plus the time of flight of a positronium atom from the location of the first to the second charge-exchange plus the time of flight of an antihydrogen

atom from the location of the second charge exchange to the location of its annihilation at the electrodes taking into account different antihydrogen and cesium velocities as well as different antihydrogen and cesium paths from one repetition to the next. The sum of these three times of flight will be referred to in the following as total time of flight. The laser pulse length of about 20 ns is neglected for the calculation of the total time of flight because it is much smaller than the three times of flight and therefore considered to be of minor influence on the time distribution of the time annihilation spectrum.

In order to account for the effect caused by the temperature on the time distribution of antihydrogen annihilations, the velocities which are assigned per repetition to a Rydberg cesium atom and an antihydrogen atom are chosen so that the ensemble of all  $\mathcal{N}$  Rydberg cesium atoms and antihydrogen atoms obey a Maxwell–Boltzmann velocity distribution for a temperature  $T_{Cs}$  and  $T_{\bar{H}}$ , respectively. This is implemented in the numerical code as follows. The temperature of the cesium atoms is taken to be  $T_{Cs} = 320$  K, which is about the temperature of the cesium oven during an experiment as described in the previous chapter. Then, the most probable velocity of the cesium atoms given by

$$v_{Cs} = \sqrt{\frac{2k_B T_{Cs}}{m_{Cs}}}, \quad (7.1)$$

where  $k_B$  is the Boltzmann constant and  $m_{Cs}$  is the atomic mass of cesium is calculated. A random velocity between zero and  $4 \cdot v_{Cs}$  is then assigned to the cesium atom by use of the following method. Let  $r_1$  be a random number between zero and one. A value for the velocity  $v$  is then calculated by  $v = 4 \cdot v_{Cs} \cdot r_1$ . The probability of this velocity is given by the Maxwell–Boltzmann probability function according to [Vog95]

$$f(v) = \sqrt{\frac{2}{\pi}} \left( \frac{m}{k_B T} \right)^{3/2} v^2 \exp \left( -\frac{mv^2}{2k_B T} \right), \quad (7.2)$$

with  $m = m_{Cs}$ , and  $T = T_{Cs}$ . The ratio  $q = f(v)/f(v_{Cs})$  is compared with a second random number  $r_2$ . If  $r_2$  is larger than  $q$  then a new velocity  $v$  is calculated. If  $r_2$  is less or equal than  $q$  than  $v$  is assigned to the cesium atom.

Accordingly, the most probable antihydrogen velocity  $v_{\bar{H}}$  for an antihydrogen temperature  $T_{\bar{H}}$  is calculated by

$$v_{\bar{H}} = \sqrt{\frac{2k_B T_{\bar{H}}}{m_{\bar{H}}}}, \quad (7.3)$$

where  $m_{\bar{H}}$  is the antihydrogen mass. Again, a random velocity between zero and  $4 \cdot v_{\bar{H}}$  is assigned to an antihydrogen atom by the same method as described above for a cesium atom.

All positronium atoms are taken to be at the most probable velocity  $v_{Ps} = 10\,000 \text{ m/s}$  according to the numerical result of Hessels et al. [HHC98]. A specific velocity distribution for the positronium atoms is not taken into account because due to the high mean velocity the time of flight of a positronium atom is two orders of magnitude smaller than the times of flight of an antihydrogen atom or a cesium atom and is therefore considered to be of minor influence on the time distribution of the antihydrogen annihilations.

With the particle velocities specified, what remains to be done is to specify the path lengths that are covered by each particle species. Fig. 7.1 shows schematically the cesium excitation region by the green hatched triangle and the inner electrode surface of the lower electrode stack by the black rectangle.

For a cesium atom it is assumed that it is excited at a random spot within the 5.7 mm wide cesium excitation region and then travels the 14.8 mm long path to the center of the positron cloud, which is depicted by the bottom black dot in Fig. 7.1. The cesium path length is thus calculated by  $s_{Cs} = (14.8 + 5.7 \cdot x) \text{ mm}$ , where  $x$  is a random number between zero and one, inclusively.

For a positronium atom it is assumed that it travels three millimeters, the distance between the centers of an antiproton and a positron cloud in a real experiment. The time of flight of all positronium atoms is then given by  $t_{Ps} = s_{Ps}/v_{Ps} = 300 \text{ ns}$ .

The specifications of the cesium path and the positronium path imply that the radial and axial extensions of the antiproton and positron clouds are neglected in the numerical analysis. The reason is that the smearing of the time distribution due to the extensions of the clouds is considered to be negligible in view of the large uncertainties in the involved path lengths.

For an antihydrogen atom it is assumed that it leaves the antiprotons in a straight line and in a random direction within the white half plain inside the trap wall (because of the cylinder symmetry of the Penning trap electrodes, only this half plain needs to be considered in the simulation). The crossing point with the trap wall is determined numerically. The antihydrogen path is then obtained by the distance between the center of the antiproton cloud and the crossing point with the trap wall. For clarity, several arbitrarily chosen antihydrogen paths are indicated in Fig. 7.1 by the dashed red arrows.

In order to obtain a time distribution of the  $\mathcal{N}$  calculated annihilations, an array with 1024 elements called  $counts[n]$  ( $n = 0, 1, \dots, 1023$ ) is defined. All elements of the array are set to zero at the beginning of the algorithm. In each repetition, the element of  $counts[n]$  for which  $n$  is the closest integer number to the ratio between the calculated total time of flight and  $0.64 \mu\text{s}$  is increased by one.

As a summary of this section, the basic algorithm is summarized by the following list.

- For  $j = 1$  to  $\mathcal{N}$ 
  1. Determine a random velocity  $v_{Cs,j}$  for the cesium atom in the range between zero and  $4 \cdot v_{Cs}$ .

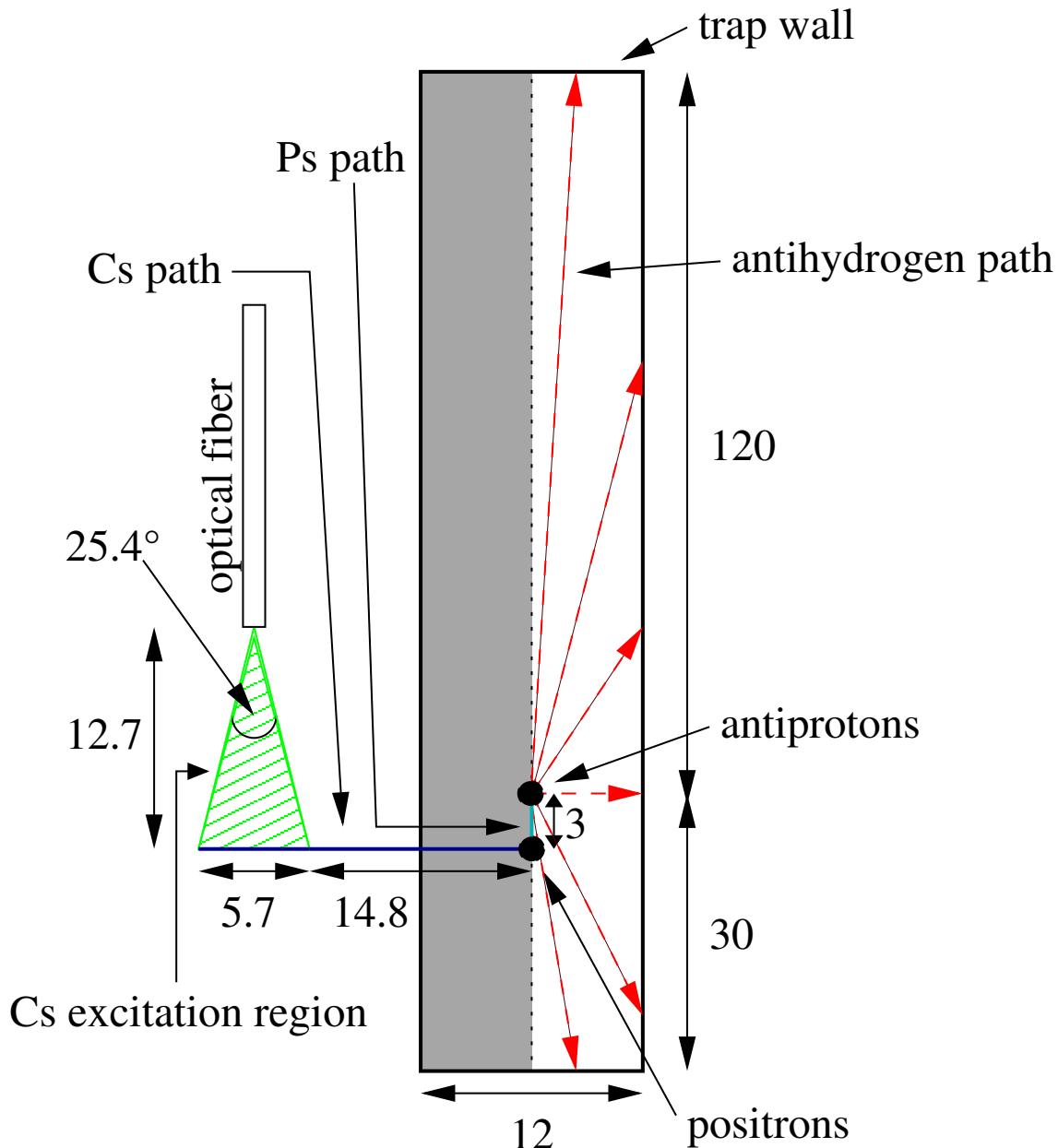


Figure 7.1: The graph depicts schematically the cesium excitation region (green hatched triangle) and the electrode walls of the lower electrode stack (black rectangle). The upper horizontal electrode wall is assumed in the numerical code to be the ball valve, the lower horizontal line represents the degrader. All dimensions are given in millimeters. The width of the cesium excitation region along the path of the cesium beam is given by the diameter of the output cone (green hatched triangle) of the optical fiber along the cesium path. The specified value of 5.7 mm is obtained by the following consideration: The distance from the tip of the fiber to the cesium beam is as indicated in the graph 12.7 mm. According to section 2.4.3 the numerical aperture (NA) of the optical fiber is  $NA = 0.22$ . The relation between the numerical aperture and the half angle  $\alpha/2$  of the output cone is given by  $NA = \sin(\alpha/2)$ . The relation yields  $25.4^\circ$  as indicated in the figure for the full angle of the output cone. From geometrical arguments follows then a width of 5.7 mm for the cesium excitation region.

$T_{\bar{H}}$ [K]	$t_{avg}$ [ $\mu s$ ]	$t_{stdev}$ [ $\mu s$ ]
4.2	159.6	1.7
5	154.7	1.7
7	146.2	1.6
10	138.5	1.4
25	124.2	1.2
50	117.0	1.1
250	107.4	1.1
500	105.1	1.1
1000	103.5	1.1
2000	102.3	1.1
2500	102.1	1.0
3000	101.8	1.1

Table 7.1: The first column gives the antihydrogen temperature specified in the numerical calculation. The second column gives the average time of flight and the last column gives the standard deviation from the average.  $t_{avg}$  and  $t_{stdev}$  have been calculated from 1000 time distributions of 5000 annihilation events.

2. Determine a random velocity  $v_{\bar{H},j}$  for the antihydrogen atom in the range between zero and  $4 \cdot v_{\bar{H}}$ .
3. Determine the random path length for the cesium atom via  $s_{Cs,j} = 14.8 + 2.8 \cdot x$  mm.
4. Cesium time of flight  $t_{Cs,j} = s_{Cs,j}/v_{Cs,j}$ .
5. Determine random antihydrogen path  $s_{\bar{H},j}$ .
6. Antihydrogen time of flight  $t_{\bar{H},j} = s_{\bar{H},j}/v_{\bar{H},j}$ .
7. Total time  $t_j = t_{Cs,j} + t_{Ps} + t_{\bar{H},j}$ .
8. Increase the element of  $counts[n]$  for which  $n$  is the next closest integer of the value  $t_j/0.64 \mu s$  by 1.
- End of loop

### 7.2.2 Numerical Results

By use of the algorithm described in the previous section, the time distribution of  $N = 5000$  annihilation events has been calculated by taking into account the antihydrogen temperatures given in Tab. 7.1. For a specific temperature, the time distribution of the  $N = 5000$  annihilation events has been calculated 1000 times. For each of the 1000 time distributions, the average value  $\bar{t}$  of the total time of flight is calculated. The value  $t_{avg}$  given in the second column of Tab. 7.1 is the average of the 1000 values of  $\bar{t}$ , and

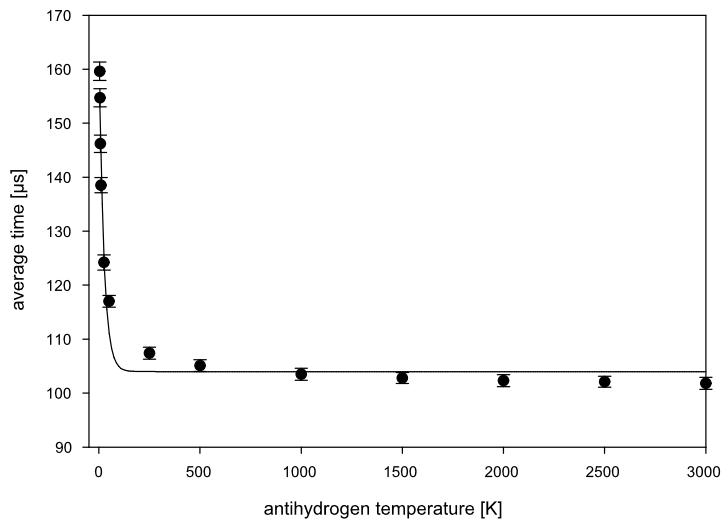


Figure 7.2: The average time of the antihydrogen annihilations is plotted as a function of the antihydrogen temperature. An exponential curve of the form  $y = 60.7 \exp(-0.04x) + 104.0$  has been fitted by use of Sigmaview [Sig].

the value  $t_{stdev}$  given in the third column is the standard deviation  $t_{stdev}$  of the 1000 values of  $\bar{t}$  with respect to  $t_{avg}$ . The tabulated values of  $t_{avg}$  are plotted with  $t_{stdev}$  as error bars in Fig. 7.2 as a function of the temperature  $T_{\bar{H}}$ . An exponential curve of the form  $y = 60.7 \exp(-0.04x) + 104.0$  has been fitted by use of Sigmaview [Sig].

As can be seen in the table and in the figure, the higher the antihydrogen temperature, the earlier on average the antihydrogen annihilations occur. Moreover the time intervals  $t_{avg} \pm t_{stdev}$  are well separated for the various antihydrogen temperatures. According to the simulation the antihydrogen temperature can therefore be determined with an accuracy of better than 1 K by taking the average time of 5000 antihydrogen annihilation events.

In view of the experimental setup and of the interpretation of the experimental results, three calculated time distributions are given in the following. Fig. 7.3 shows the calculated time distributions as given by the array counts[n] for  $n = 0, 1, \dots, 1000$  for  $T_{\bar{H}} = 4.2$  K (red dots) and for  $T_{\bar{H}} = 25$  K (blue triangles). Fig. 7.4 shows the calculated time distribution as given by the array counts[n] for  $n = 0, 1, \dots, 1000$  for  $T_{\bar{H}} = 4.2$  K (red dots) and for  $T_{\bar{H}} = 1000$  K (blue triangles). From the graphs can be seen, as already described above, that on average the annihilation events occur later for lower antihydrogen temperatures. Moreover, the first count for an antihydrogen temperature of 1000 K occurs at after  $37 \times 0.64 \mu\text{s}$  with respect to the laser pulse, while the first counts for  $T_{\bar{H}} = 25$  K occurs at  $47 \times 0.64 \mu\text{s}$  and at  $75 \times 0.64 \mu\text{s}$  for an antihydrogen temperature of 4.2 K.

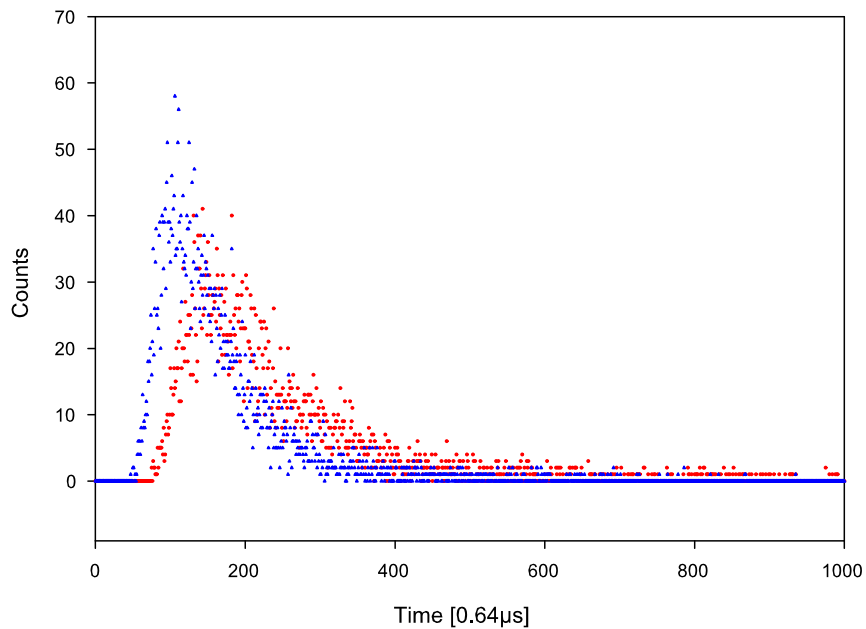


Figure 7.3: Calculated time distribution of 5000 annihilations from antihydrogen at 4.2 K (red dots) versus 5000 annihilations at 25 K (blue triangles).

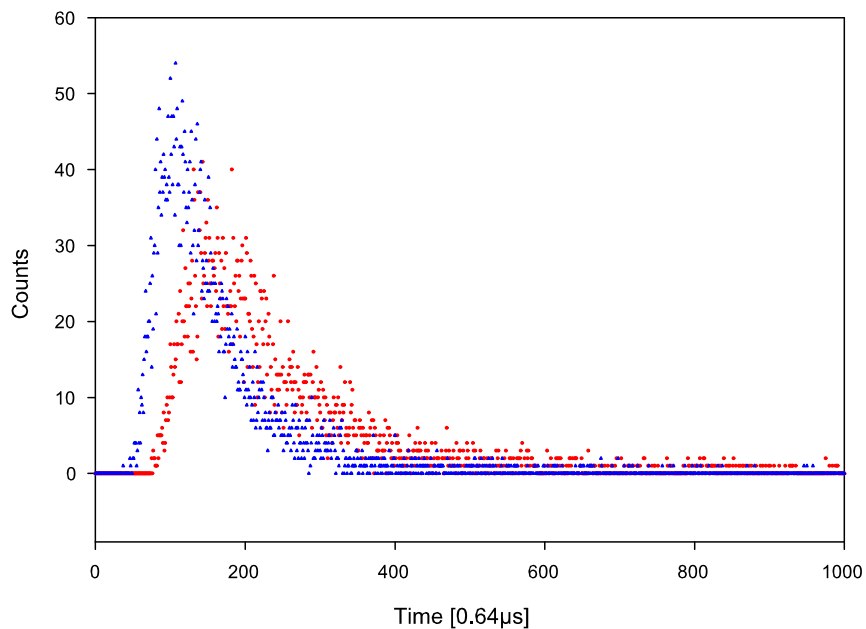


Figure 7.4: Calculated time distribution of 5000 annihilations from antihydrogen at 4.2 K (red dots) versus 5000 annihilations at 1000 K (blue triangles).

## 7.3 Experimental Setup

In this section, the experimental setup is described. In the first part, the laser system and the data acquisition is described, while in the second part, the potential structure used to confine antiprotons and positrons is presented.

### 7.3.1 The Laser System and the Data Acquisition

A schematic overview of the laser system is given in Fig. 7.5. The diode laser (DL) is locked as has been described in section 6.4.1.3 to the transition between the sublevels with  $m_I = -5/2$  of the  $6S_{1/2}$  state and the  $6P_{3/2}$  state which is at a frequency of  $351\,803\,779 \pm 100$  MHz. About 10 mW of laser light is sent via the optical fiber to the excitation region ensuring according to the results presented in section 6.4.2.1 that the transition is saturated. The specifications of the copper vapor laser (CVL) have been summarized in Tab. 6.5. It emits green and yellow laser light pulses with a duration of 20 ns and at a repetition rate of 19-20 kHz. The yellow line which is of no use for the experiment is deflected of a dichroic mirror (DM) which has a high reflectivity ( $> 99\%$ ) for yellow at 578 nm and a high transmittivity ( $> 99\%$ ) for green at 511 nm. A small fraction ( $\sim 4\%$ ) of the power in the green line is reflected of a glass plate (GP) onto the photodiode PD1. PD1 is used to measure the repetition rate  $f_{rep}$  of the copper vapor laser. The photodiode signal is transformed by a discriminator into a TTL signal which is used to synchronize an optical chopper to  $f_{rep}/4$ . The home-made chopper wheel has been designed to not block one in 24 consecutive pulses when it is spinning at  $f_{rep}/4$ . Since the holes of the chopper wheel are smaller than the beam size, the laser beam is focused through the chopper wheel by the lens (L) to the left and again collimated to its original spot size behind the chopper wheel by the lens to the right. A small fraction ( $\sim 4\%$ ) of the laser power is deflected from another glass plate (GP) situated behind the chopper wheel onto the photodiode PD2. PD2 measures the repetition rate of the laser pulses behind the chopper wheel. It is used before an experiment to control the phase delay between the TTL signal and the chopper wheel so that it is ensured that the repetition rate is indeed  $f_{CVL}/24$ . A laser power of  $500 \pm 10$  mW measured in the zone I when the chopper wheel was not spinning has been sent into the trap can for these experiments. Thus according to section 6.4.2.2 about 50 cesium atoms are produced at a repetition rate of  $f_{CVL}/24$ .

During an experiment, the signal is used as a trigger signal for a multichannel scaler (Stanford Research Systems Model SR 430 [SRSA]). After being triggered, the multichannel scaler counts incoming “trigger” counts (section 2.5.2.3) delivered by the detector system in  $N = 1024$  successive time bins each with a length of  $t_{bin} = 640$  ns. Each new trigger (from PD2) starts a record whose data is added to the bin by bin accumulation of all the previous records. The result is a record of the sum of all counts in each time bin. The multichannel scaler can only be triggered by pulses that are

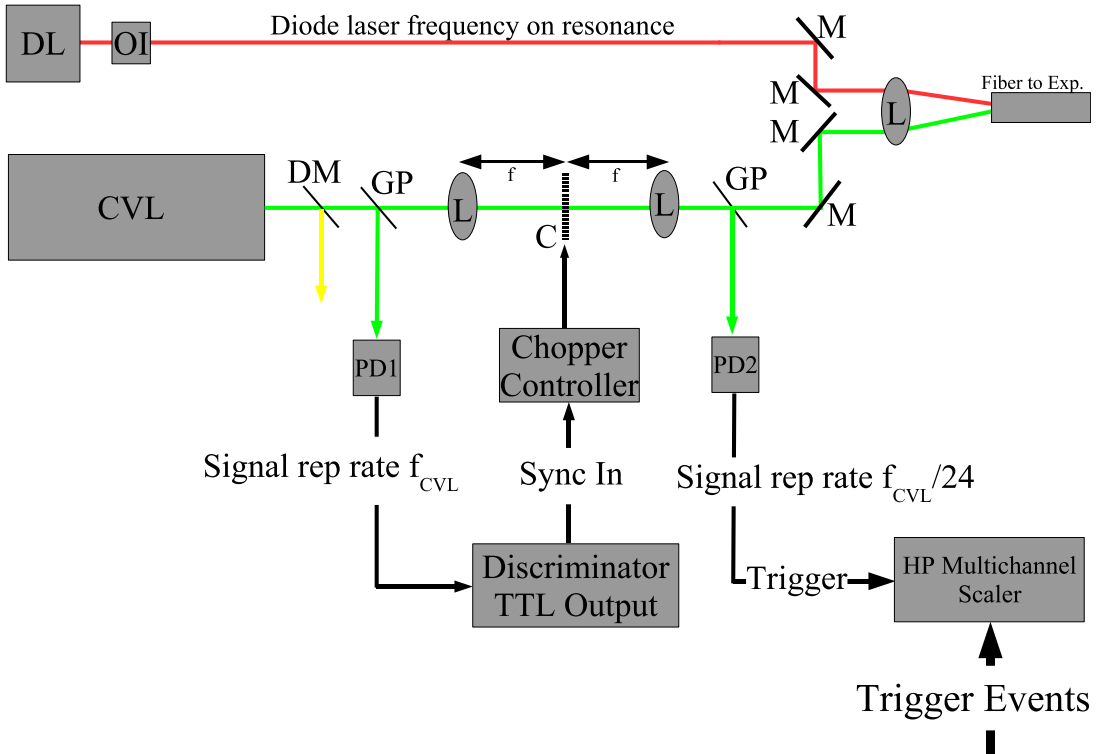


Figure 7.5: The laser setup used to measure the velocity of the cesium atoms. The symbols refer to: (DL) diode laser, (OI) optical insulator, (CVL) copper vapor laser, (L) lens with focal length  $f = 10\text{ mm}$ , (C) optical wheel, (PD1, PD2) photodiodes, (DM) dichroic mirror, (GP) glass plate.

separated in time by more than  $t_{delay} = N \cdot t_{bin} + N \cdot 250\text{ ns} + 150\text{ }\mu\text{s} = 1.06\text{ }\mu\text{s}$  [SRS99]. This yields to a maximum trigger rate of  $\approx 940\text{ Hz}$  and this is the reason why we had to reduce the repetition rate of the copper vapor laser to  $f_{CVL}/24$ . The maximum value of  $f_{CVL}$  is according to the specifications  $20\text{ kHz}$  and thus the multichannel scaler is triggered at a maximum rate of  $833\text{ Hz}$ , a value below the maximum possible trigger rate of  $\approx 940\text{ Hz}$ .

### 7.3.2 Experimental Setup in the Penning Trap Apparatus

The experiment has been carried out in the hbar2 Penning trap apparatus. The basic properties of this trap have been described in section 2.4.2 and the setup for the production of the Rydberg cesium has been depicted in chapter 6. Fig. 7.6 shows in the top part a side view of the lower electrode stack of the hbar2 Penning trap apparatus and in the bottom part the potential structure on axis used to confine antiprotons ( $\bar{p}$ ) at the electrode UP and positrons ( $e^+$ ) at the electrode CS. The Rydberg cesium beam ( $\text{Cs}^*$ )

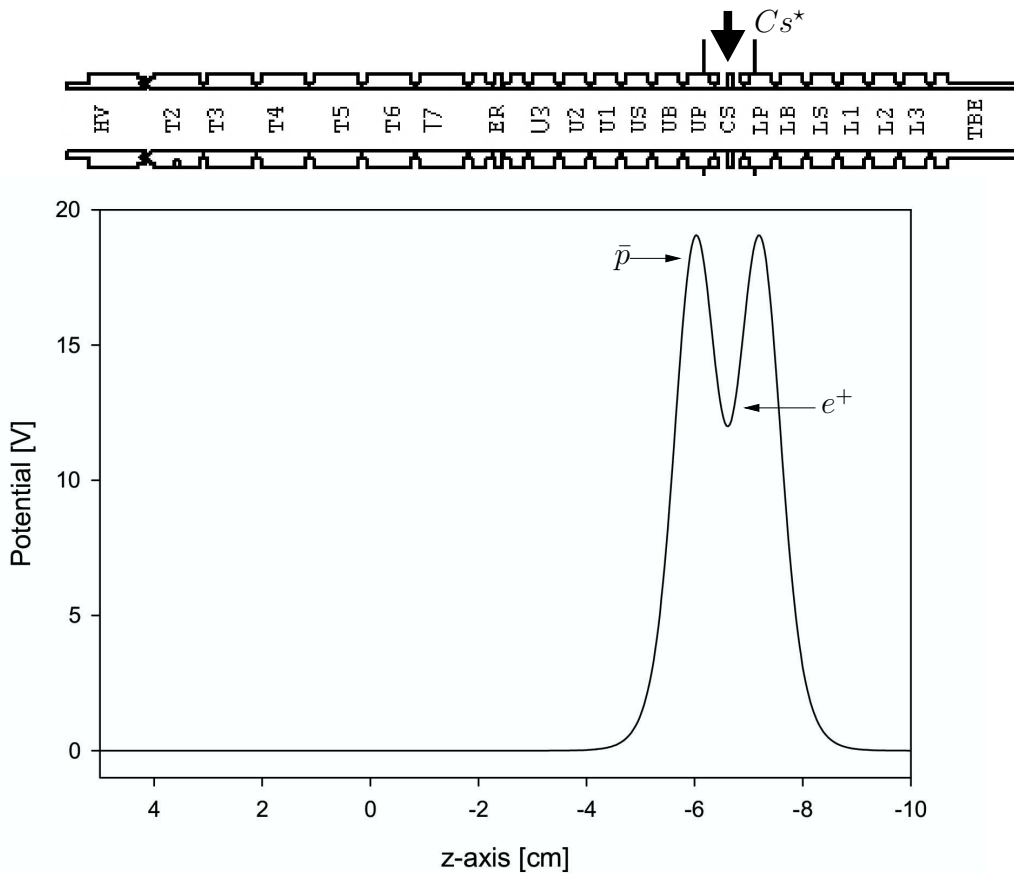


Figure 7.6: A side view of the lower electrode stack of the hbar2 Penning trap apparatus is shown in the upper part of the figure. The Rydberg cesium ( $Cs^*$ ) is passing through the CS electrode. The lower part of the figure shows the potential on axis which is used to confine antiprotons ( $\bar{p}$ ) at the electrode UP and positrons ( $e^+$ ) at the electrode CS.

which passes through the electrode CS collides with the stored positrons and initiates the production of antihydrogen via a two-step charge-exchange process according to Eq. 6.3–6.5. A detection well for antihydrogen detection via field-ionization as has been used in the experiment presented in chapter 6 has not been employed in the potential structure. The reason is that we have carried out a few trials with a detection well and for unknown reasons the antiprotons residing at UP have not been stable.

## 7.4 Experimental Results

Unfortunately, only four experiments could be carried out within the last few days of the 2004 beam run in order to measure the time distribution of the antihydrogen annihilation events. The numbers of antiprotons and positrons used in each experiment

Run#	Number of Antiprotons	Number of Positrons
4014	$2.3 \times 10^5$	$1.2 \times 10^6$
4038	$3.8 \times 10^5$	$1.5 \times 10^6$
4051	$1.5 \times 10^5$	$1.7 \times 10^6$
4053	$1.5 \times 10^5$	$1.1 \times 10^6$
Control Experiment		
4037	$1.5 \times 10^5$	zero

Table 7.2: The table gives in the first column the Run number as it is stored in the data acquisition system. The second column gives the number of antiprotons and the third the number of positrons loaded into UP and CS, respectively.

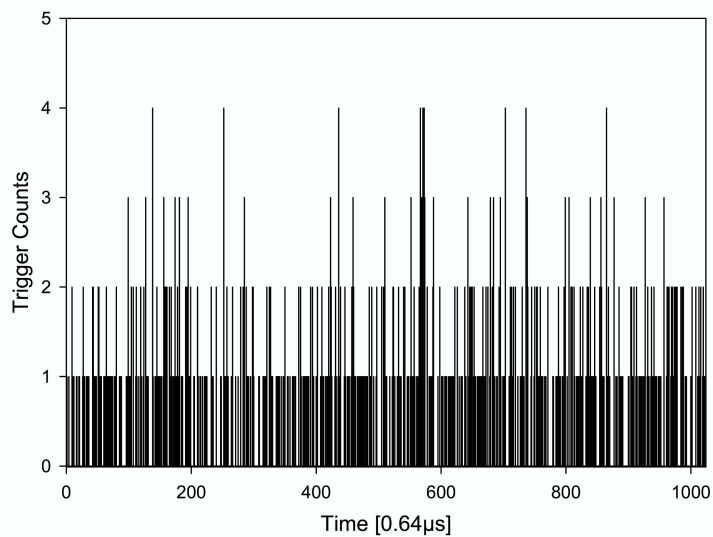


Figure 7.7: The sum of the trigger counts detected in four experimental trials is shown over all 1024 time bins.

is given in Tab. 7.2. Fig. 7.7 shows the detected trigger counts of all four experiments over the 1024 time bins with a length of an individual bin of  $0.64\mu\text{s}$ . Fig. 7.8 depicts the trigger counts of all four experiments that occurred within the 50th and 300th time bin, the region where we expect according to the numerical results presented in section 7.2.2 the antihydrogen annihilations to take place. In addition, a control experiment has been carried out with  $1.5 \times 10^5$  antiprotons and zero positrons (also given in Tab. 7.2) by which no antihydrogen is produced. Fig. 7.9 shows the detected counts over the 1024 time bins and Fig. 7.10 depicts the trigger counts that occurred within the 50th and 300th time bin.

The background trigger count rate due to cosmic rays is about  $1.2\text{ s}^{-1}$  [Grz] and thus the probability to detect a cosmic event within a  $0.64\mu\text{s}$  long time bin is very low. The detected distribution of antiproton annihilations in the control experiment is thus

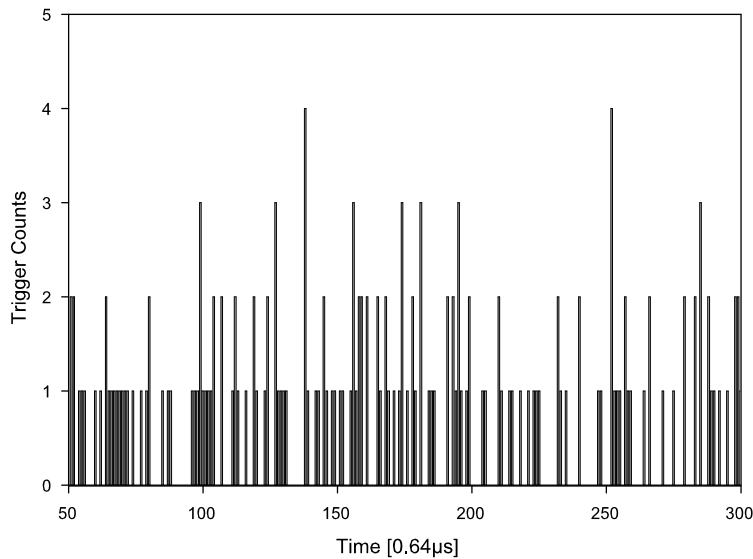


Figure 7.8: The sum of the trigger counts detected in four experimental trials is shown over the 50th to 300th time bin, the region where according to the numerical analysis presented in section 7.2 the antihydrogen annihilations are expected to take place.

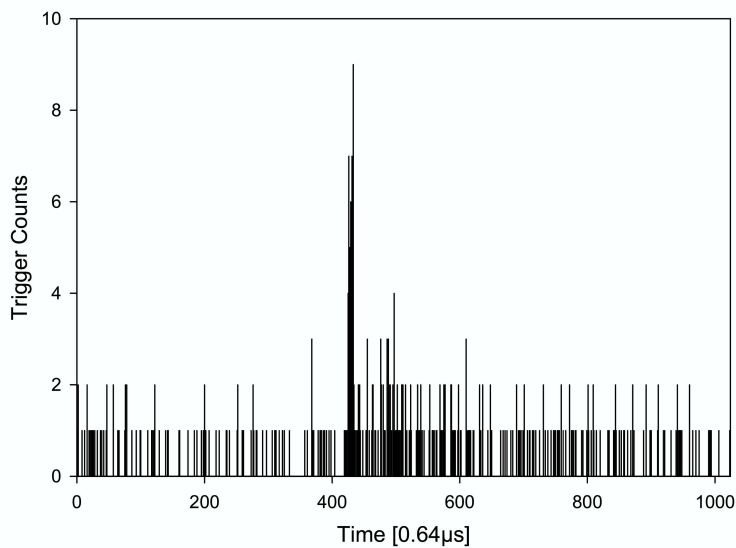


Figure 7.9: The trigger counts detected in one null experiment without positrons are shown over all 1024 time bins. The counts are due to antiproton loss out of the static potential well at UP.

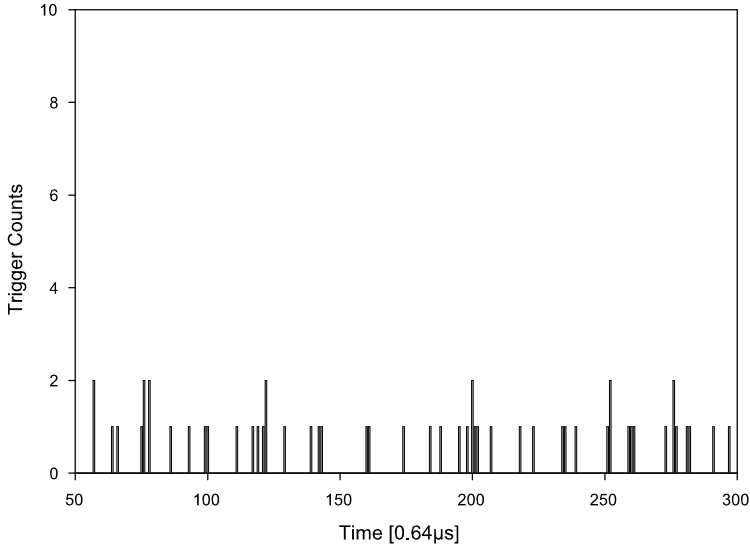


Figure 7.10: The trigger counts detected in one null experiment without positrons are shown over the 50th to 300th time bin, the region where according to the numerical analysis presented in section 7.2 the antihydrogen annihilations are expected to take place.

due to antiprotons leaking out of the static potential well. The background count rate measured in the control experiment is as high as 9 trigger counts per time bin and within the 50th and 300th time bin as high as 2 trigger counts per time bin. The maximum count rate for the four experimental trials is four per bin. The detected counts clearly exceed the background level but the number is much too low so that no conclusion can be drawn from the experimental data for the antihydrogen temperature.

## 7.5 Summary and Conclusion

In this chapter, a method to determine the antihydrogen temperature from a measurement of the time delay between antihydrogen annihilation events and the laser pulse that initiates the antihydrogen production via the excitation of Rydberg cesium is proposed. A numerical model has been developed in order to evaluate the effect of the antihydrogen temperature on the time distribution of the antihydrogen annihilations events. According to the numerical model it should be possible to determine the antihydrogen temperature to an accuracy of better than 1 K if 5000 annihilations events are measured. Four experimental trials have been carried out within the last days of the 2004 beam time, but the number of detected annihilations are much too low for any estimate of the antihydrogen temperature. Thus no conclusion for the antihydrogen temperature can be drawn so far.

# Chapter 8

## Outlook

In this work, two methods have been presented by which the first step towards a precise comparison of antihydrogen and hydrogen has been taken: the production of antihydrogen itself.

By the first method, antihydrogen atoms have been produced as presented in chapter 4 from interacting antiproton and positron clouds in a nested Penning trap. The atoms have been detected background-free via ATRAP's field-ionization method. In subsequent experiments the antihydrogen state-distribution could be measured, which revealed that the antihydrogen atoms are formed in highly excited states. This suggests that three-body recombination is the formation process, however current theory cannot yet account for the measured state distribution. A fraction of the detected antihydrogen atoms is too deeply bound to be described by a GCA model. For these atoms no theory exists so far to explain the formation mechanism. The experimental results have already triggered along with the results obtained by the ATHENA Collaboration studies on the formation mechanism [Dri04, GBO<sup>+</sup>04, BD04, KO04a, KO04b, VGP<sup>+</sup>04, Rob04, RH04] and certainly many more studies will follow.

By the second method, antihydrogen atoms are formed via two-step charge-exchange processes as described in chapter 6, and so far  $14 \pm 4$  have been detected. According to theory, the atomic state distribution is much narrower compared with the state distribution of the antihydrogen atoms produced in a nested Penning trap and the atomic states can be selected by choice of the cesium Rydberg states. Future projects might be focused on increasing the number of antihydrogen atoms and on a measurement of the state distribution. Since the antiprotons remain trapped in a static potential well during the experiment, it is expected that the temperature of the antihydrogen atoms is 4.2 K. A method to determine the antihydrogen temperature and initial experiments have been presented in chapter 7. These experiments will probably be continued after the AD startup in the year 2006.

The next major step towards high precision experiments on antihydrogen is to confine the antihydrogen atoms in a neutral particle trap. To achieve this step, a new Penning

trap apparatus is currently constructed by the Harvard group. This trap will house a superconducting Ioffe trap that is currently developed by the Jülich group. The combined Penning–Ioffe trap will probably be built before the start-up of the AD in 2006. The consequences for charged particle trapping have been studied in such a combined trap and the results look favorable, at least in the low particle limit (for further references, see [Gab04] and references therein). The experiments to produce antihydrogen as mentioned above will then probably be repeated in the combined Penning–Ioffe apparatus so that antihydrogen is synthesized within the neutral particle trap. The antihydrogen atoms that are at the cold end of the Maxwell–Boltzmann distribution are the most probable for magnetic trapping. Trapped antihydrogen atoms might then decay to the ground state while remaining trapped. The trapped ground state antihydrogen atoms can then be cooled by the Lyman- $\alpha$  source developed by the Garching group to temperatures of about 1 mK. The final step will then be a high-precision measurement of the 1S–2S transition frequency and to compare it with hydrogen for an accurate test of the CPT theorem. Many challenges lie ahead but great progress has been made.

# Appendix A

## Author's List of Publications

In the following the author's publications are listed. The papers published in Physical Review Letters are attached to the end of the thesis.

1. [GBO<sup>+02a</sup>]  
G. Gabrielse, N. S. Bowden, P. Oxley, A. Speck, C. H. Storry, J. N. Tan, M. Wessels, D. Grzonka, W. Oelert, G. Schepers, T. Sefzick, J. Walz, H. Pittner, T. W. Hänsch and E. A. Hessel.  
Background-Free Observation of Cold Antihydrogen with Field-Ionization Analysis of its States. *Phys. Rev. Lett.*, 89:213401, 2002.
2. [GBO<sup>+02b</sup>]  
G. Gabrielse, N. S. Bowden, P. Oxley, A. Speck, C. H. Storry, J. N. Tan, M. Wessels, D. Grzonka, W. Oelert, G. Schepers, T. Sefzick, J. Walz, H. Pittner, T. W. Hänsch and E. A. Hessel.  
Driven Production of Cold Antihydrogen and the First Measured Distribution of Antihydrogen States. *Phys. Rev. Lett.*, 89:233401, 2002.
3. [GSS<sup>+04</sup>]  
G. Gabrielse, A. Speck, C. H. Storry, D. Le Sage, N. Guise, D. Grzonka, W. Oelert, G. Schepers, T. Sefzick, H. Pittner, J. Walz, T. W. Hänsch, D. Comeau and E. A. Hessels.  
First Measurement of the Velocity of Slow Antihydrogen Atoms. *Phys. Rev. Lett.*, 93:073401, 2004.
4. [SSS<sup>+04</sup>]  
C. H. Storry, A. Speck, D. Le Sage, N. Guise, G. Gabrielse, D. Grzonka, W. Oelert, G. Schepers, T. Sefzick, H. Pittner, M. Herrmann, J. Walz, T. W. Hänsch, D. Comeau and E. A. Hessels.  
First Laser-Controlled Antihydrogen Production. *Phys. Rev. Lett.*, 93:263401, 2004.

5. [GBO<sup>+</sup>02c]  
G. Gabrielse, N. S. Bowden, P. Oxley, A. Speck, C. H. Storry, J. N. Tan, M. Wessels, D. Grzonka, W. Oelert, G. Schepers, T. Sefzick, J. Walz, H. Pittner, T. W. Hänsch and E. A. Hessel.  
Stacking of cold antiprotons. *Phys. Lett. B*, 548:140, 2002.
6. [OBP<sup>+</sup>04]  
P. Oxley, N. S. Bowden, R. Parrott, A. Speck, C. H. Storry, J. N. Tan, M. Wessels, G. Gabrielse, D. Grzonka, W. Oelert, G. Schepers, T. Sefzick, J. Walz, H. Pittner, T. W. Hänsch and E. A. Hessels.  
Aperture method to determine the density and geometry of antiparticle plasmas. *Phys. Lett. B*, 595:60, 2004.
7. [GSS<sup>+</sup>05]  
G. Gabrielse, A. Speck, C. H. Storry, D. Le Sage, N. Guise, D. Grzonka, W. Oelert, G. Schepers, T. Sefzick, H. Pittner, J. Walz, T. W. Hänsch, D. Comeau and E. A. Hessels.  
First Evidence for Atoms of Antihydrogen too Deeply Bound to be Guiding Center Atoms. submitted to *Phys. Lett. B*
8. [WFH<sup>+</sup>03]  
J. Walz, P. Fendel, M. Herrmann, M. König, A. Pahl, H. Pittner, B. Schatz and T. W. Hänsch.  
Towards laser spectroscopy of antihydrogen. *J. Phys. B*, 36:649, 2003.
9. [WPH<sup>+</sup>03]  
J. Walz, H. Pittner, M. Herrmann, P. Fendel, B. Henrich and T. W. Hänsch.  
Cold antihydrogen atoms. *Appl. Phys. B*, 77:713, 2003

# Bibliography

- [AAB<sup>+</sup>02] M. Amoretti, C. Amsler, G. Bonomi, A. Bouchta, P. Bowe, C. Carraro, C. L. Cesar, M. Charlton, M. J. T. Collier, M. Doser, V. Filippini, K. S. Fine, A. Fontana, M. C. Fujiwara, R. Funakoshi, P. Genova, J. S. Hangst, R. S. Hayano, M. H. Holzscheiter, L. J. Jorgensen, V. Lagomarsino, R. Landua, D. Lindelo, E. Lodi-Rizzini, M. Marcy, N. Madsen, G. Manuzio, M. Marchesoti, P. Montagna, H. Pruys, C. Regenfuß, P. Riedler, J. Rochet, A. Rotondi, G. Rouleau, G. Testera, A. Variola, T. L. Watson, and D. P. van der Werf. Production of antihydrogen. *Nature*, 419:456, 2002.
- [Ams98] C. Amsler. Proton–antiproton annihilation and meson spectroscopy with the Crystal Barrel. *Rev. Mod. Phys.*, 70(4):1293–1339, 1998.
- [And32] C. D. Anderson. *Science*, 76:238, 1932.
- [ASA97] ASACUSA proposal to the CERN SPSLC. CERN SPSCL/P307, March 1997.
- [ATH96] ATHENA proposal to the CERN SPSLC. CERN SPSCL/P302, October 1996.
- [ATR97] ATRAP proposal to the CERN SPSLC. CERN SPSCL/P306, March 1997.
- [BBB<sup>+</sup>96] G. Baur, G. Boero, S. Brauksiepe, A. Buzzo, W. Eyrich, R. Geyer, D. Grzonka, J. Hauffe, K. Kilian, M. LoVetre, M. Macri, M. Moosburger, R. Nellen, W. Oelert, S. Passaggio, A. Pozzo, K. Röhricht, K. Sachs, G. Schepers, T. Seifzick, R. S. Simon, R. Stratmann, F. Stinzing, and M. Wolke. Production of antihydrogen. *Phys. Lett. B*, 368:251, 1996.
- [BCG<sup>+</sup>98] G. Blanford, D. C. Christian, K. Gollwitzer, M. Mandelkern, C. T. Munger, J. Schultz, and G. Zioulas. *Phys. Rev. Lett.*, 80:3037, 1998.
- [BD04] E. M. Bass and D. H. E. Dubin. *Phys. Plasmas*, 11:1240, 2004.
- [Bel55] J. S. Bell. *Proc. Roy. Soc.*, A231:479, 1955.

- [BEM04] P. Belochitskii, T. Eriksson, and S. Maury. The CERN antiproton decelerator (AD) in 2002: status, progress and machine development results. *Nucl. Instr. and Meth. in Phys. Res. B*, 214:176–180, 2004.
- [BG86] L. S. Brown and G. Gabrielse. Geonium theory: Physics of an electron or ion in a Penning trap. *Rev. Mod. Phys.*, 58:233, 1986.
- [BKR99] R. Bluhm, V. A. Kostelecky, and N. Russell. CPT and Lorentz Tests in Hydrogen and Antihydrogen. *Phys. Rev. Lett.*, 82(11):2254–2257, 1999.
- [BM75] D. R. Bates and I. Mendas. Calculation of ionic recombination coefficient in an ambient gas taking specific account of angular momentum . *J. Phys. B.*, 8:1770–1775, 1975.
- [Bow] N. S. Bowden. Harvard University, private communication.
- [Bow03] Nathaniel Sean Bowden. *Production of Antihydrogen during the Positron Cooling of Antiprotons*. PhD thesis, Harvard University, Cambridge, Massachusetts, September 2003.
- [BW84] J. J. Bollinger and D. J. Wineland. *Phys. Rev. Lett.*, 53:348, 1984.
- [CCC<sup>+</sup>90] R. Carosi, P. Clarke, D. Coward, D. Cundy, N. Doble, L. Gatignon, V. Gibson, P. Grafström, R. Hagelberg, and G. Kesseler et al. *Phys. Lett. B*, 237:303–312, 1990.
- [CCFT64] J. H. Christenson, J. W. Cronin, V. L. Fitch, and R. Turlay. *Phys. Rev. Lett.*, 13:138, 1964.
- [CEH<sup>+</sup>94] M. Charlton, J. Eades, D. Horvath, R. J. Hughes, and C. Zimmermann. Antihydrogen Physics. *Phys. Rep.*, 241:65–117, 1994.
- [CFK<sup>+</sup>96] C. L. Cesar, D. G. Fried, T. C. Killian, A. D. Polcyn, J. C. Sandberg, I. A. Yu, T. J. Gretyak, D. Kleppner, and J. M. Doyle. Two-Photon Spectroscopy of Trapped Atomic Hydrogen. *Phys. Rev. Lett.*, 77:255, 1996.
- [Cha90] M. Charlton. Antihydrogen Production in Collisions of Antiprotons with Excited States of Positronium. *Phys. Lett. A*, 143:143–146, 1990.
- [CK99] C. L. Cesar and D. Kleppner. Two-photon Doppler-free spectroscopy of trapped atoms. *Phys. Rev. A*, 59:4564–4570, 1999.
- [CSWY55] O. Chamberlain, E. Segrè, C. Wiegand, and T. Ypsilantis. Observation of Antiprotons. *Phys. Rev.*, 100:947, 1955.
- [DAD<sup>+</sup>01] C. F. Driscoll, F. Anderegg, D. H. E. Dubin, D. Z. Jin, J. M. Kriesel, E. M. Hollman, and T.M. O’Neil. *Phys. Plasmas*, 9:1905, 2001.

- [Dem95] W. Demtröder. *Laser Spectroscopy*. Springer Verlag, Berlin, 2nd edition, 1995.
- [Dir28] P. A. M. Dirac. *Proc. Roy. Soc.*, A117:610, 1928.
- [DKN84] J. B. Delos, S. K. Knudson, and D. W. Noid. Trajectories of an atomic electron in a magnetic field. *Phys. Rev. A*, 30:1208, 1984.
- [Dri04] C. F. Driscoll. Comment on Driven Production of Cold Antihydrogen and the First Measured Distribution of Antihydrogen States. *Phys. Rev. Lett.*, 92, 2004.
- [DROM92] T. W. Darling, F. Rossi, G. I. Opat, and G. F. Moorhead. *Rev. Mod. Phys.*, 64:237, 1992.
- [DSD87] R. S. Van Dyck, P. B. Schwinberg, and H. G. Dehmelt. *Phys. Rev. Lett.*, 59:26, 1987.
- [DSY<sup>+</sup>91] J. M. Doyle, J. C. Sandberg, I. A. Yu, C. L. Cesar, D. Kleppner, and T. J. Greytak. Hydrogen in the submillikelvin regime: Sticking probability on superfluid  $^4\text{He}$ . *Phys. Rev. Lett.*, 67:603, 1991.
- [Dub99] D. Dubin. Trapped nonneutral plasmas, liquids, and crystals (the thermal equilibrium states). *Rev. Mod. Phys.*, 58:233, 1999.
- [EE98] J. Eichler and H. J. Eichler. *Laser*. Springer–Verlag, Berlin, 3rd edition, 1998.
- [EH99] J. Eades and F. J. Hartmann. Forty years of antiprotons. *Rev. Mod. Phys.*, 71(1):373–419, 1999.
- [EJW99] K. S. E. Eikema and T. W. Hänsch J. Walz. Continuous Wave Coherent Lyman–alpha Radiation. *Phys. Rev. Lett.*, 83:3828, 1999.
- [ERTG00] J. Estrada, T. Roach, J. N. Tan, and G. Gabrielse. Field Ionization of Strongly Magnetized Rydberg Positronium: A New Physical Mechanism for Positron Accumulation. *Phys. Rev. Lett.*, 84:859, 2000.
- [Est02] John Karl Estrada. *Cold Trapped Positrons and Progress to Cold Antihydrogen*. PhD thesis, MIT, Cambridge, Massachusetts, January 2002.
- [Fed97] P. O. Fedichev. Formation of antihydrogen atoms in an ultra–cold positron–antiproton plasma. *Phys. Lett. A*, 226:289–292, 1997.
- [Gab01] G. Gabrielse. Comparing the antiproton and proton, and opening the way to cold antihydrogen. *Advances in Atomic, Molecular, and Optical Physics*, 45:1–39, 2001.

- [Gab04] G. Gabrielse. Atoms Made Entirely of Antimatter: Two Methods Produce Slow Antihydrogen. *submitted to Advances in Atomic, Molecular, and Optical Physics*, anticipated 2004.
- [Gal93] T. F. Gallagher. *Rydberg Atoms*. Cambridge University Press, 1993.
- [GBB<sup>+</sup>93] L. K. Gibbons, A. R. Barker, R. A. Briere, G. Makoff, V. Papadimitriou, J. R. Patterson, B. Schwingenheuer, S. V. Somalwar, Y. W. Wah, B. Winstein, R. Winston, M. Woods, and H. Yamamoto. *Phys. Rev. Lett.*, 70:1199–1202, 1993.
- [GBO<sup>+</sup>02a] G. Gabrielse, N. S. Bowden, P. Oxley, A. Speck, C. H. Storry, J. N. Tan, M. Wessels, D. Grzonka, W. Oelert, G. Schepers, T. Sefzick, J. Walz, H. Pittner, T. W. Hänsch, and E. A. Hessels. Background-Free Observation of Cold Antihydrogen with Field–Ionization Analysis of its States. *Phys. Rev. Lett.*, 89:213401, 2002.
- [GBO<sup>+</sup>02b] G. Gabrielse, N. S. Bowden, P. Oxley, A. Speck, C. H. Storry, J. N. Tan, M. Wessels, D. Grzonka, W. Oelert, G. Schepers, T. Sefzick, J. Walz, H. Pittner, T. W. Hänsch, and E. A. Hessels. Driven Production of Cold Antihydrogen and the First Measured Distribution of Antihydrogen States. *Phys. Rev. Lett.*, 89, 2002.
- [GBO<sup>+</sup>02c] G. Gabrielse, N. S. Bowden, P. Oxley, C. H. Storry, J. N. Tan, M. Wessels, D. Grzonka, W. Oelert, G. Schepers, T. Sefzick, J. Walz, H. Pittner, T. W. Hänsch, and E. A. Hessels. Stacking of cold antiprotons. *Phys. Lett. B*, 548:140, 2002.
- [GBO<sup>+</sup>04] G. Gabrielse, N. S. Bowden, P. Oxley, C. H. Storry, A. Speck, J. N. Tan, M. Wessels, D. Grzonka, W. Oelert, T. Sefzick, G. Schepers, J. Walz, H. Pittner, T. W. Hänsch, and E. A. Hessels. Gabrielse et al. Reply. *Phys. Rev. Lett.*, 92:149304–1, 2004.
- [GET<sup>+</sup>01] G. Gabrielse, J. Estrada, J. N. Tan, P. Yesley, N. S. Bowden, P. Oxley, T. Roach, C. H. Storry, M. Wessels, J. Tan, D. Grzonka, W. Oelert, G. Schepers, T. Sefzick, W. H. Breunlich, M. Cargnelli, H. Fuhrmann, R. King, R. Ursin, J. Zmeskal, H. Kalinowsky, C. Wesdorp, J. Walz, K. S. E. Eikema, and T. W. Hänsch. First positron cooling of antiprotons. *Phys. Lett. B*, 507:1–6, 2001.
- [GFO<sup>+</sup>90] G. Gabrielse, X. Fei, L. A. Orozco, R. L. Tjoelker, J. Haas, H. Kalinowsky, T. Trainor, and W. Kells. Thousandfold Improvement in the Measured Antiproton Mass. *Phys. Rev. Lett.*, 65:1317, 1990.
- [GHR89] G. Gabrielse, L. Haarsma, and S. L. Rolston. *Int. J. of Mass Spec.*, 88:319, 1989.

- [GHR<sup>+</sup>99] G. Gabrielse, D. S. Hall, T. Roach, P. Yesley, A. Khabbaz, J. Estrada, C. Heimann, and H. Kalinowsky. Ingredients of cold antihydrogen: Simultaneous confinement of antiprotons and positrons. *Phys. Lett. B*, 455:311–315, 1999.
- [GKH<sup>+</sup>99] G. Gabrielse, A. Khabbaz, D. S. Hall, C. Heimann, H. Kalinowsky, , and W. Jhe. Precision Mass Spectroscopy of the Antiproton and Proton Using Simultaneously Trapped Particles. *Phys. Rev. Lett.*, 82:3198–3201, 1999.
- [GN82] T. Goldman and M. M. Nieto. *Phys. Lett.*, 112B:437, 1982.
- [GO91] M. E. Glinsky and T. M. O’Neil. Guiding center atoms: Three-body recombination in a strongly magnetized plasma. *Phys. Fluids B*, 3(5):1279–1293, 1991.
- [GRHK88] G. Gabrielse, S. L. Rolston, L. Haarsma, and W. Kells. Antihydrogen production using trapped plasmas. *Phys. Lett. A*, 129(1):38–42, 1988.
- [Grz] D. J. Grzonka. IKP, FZ Jülich, private communication.
- [GSS<sup>+</sup>04] G. Gabrielse, A. Speck, C. H. Storry, D. Le Sage, N. Guise, D. Grzonka, W. Oelert, G. Schepers, T. Sefzick, H. Pittner, J. Walz, T. W. Hänsch, D. Comeau, and E. A. Hessels. First Measurement of the Velocity of Slow Antihydrogen Atoms. *Phys. Rev. Lett.*, 93(7):073401, 2004.
- [GSS<sup>+</sup>05] G. Gabrielse, A. Speck, C. H. Storry, D. Le Sage, N. Guise, D. Grzonka, W. Oelert, G. Schepers, T. Sefzick, H. Pittner, J. Walz, T. W. Hänsch, D. Comeau, and E. A. Hessels. First Evidence for Atoms of Antihydrogen too Deeply Bound to be Guiding Center Atoms. *to be published in Phys. Lett. B*, anticipated 2005.
- [HAD00] E. M. Hollman, F. Anderegg, and C. F. Driscoll. *Phys. Plasmas*, 7:1767, 2000.
- [Hal99] D. S. Hall. *Positrons, Antiprotons, and Interactions for Cold Antihydrogen*. PhD thesis, Harvard University, Cambridge, Massachusetts, 1999.
- [HCH94] D. Homan, M. J. Cavagnero, and D. A. Harmin. Charge transfer in ion collisions with circular Rydberg atoms. *Phys. Rev. A*, 50:R1965–R1968, 1994.
- [HCJD87] J. W. Humberston, M. Charlton, F. M. Jacobsen, and B. I. Deutch. On antihydrogen formation in collisions of antiprotons with positronium. *J. Phys. B: At. Mol. Phys.*, 20, 1987.

- [HEHP<sup>+</sup>93] S. B. Hansen, T. Ehrenreich, E. Horsdal-Petersen, K. B. MacAdam, and L. J. Dubé. Electron capture from circular Rydberg atoms. *Phys. Rev. Lett.*, 71:1522–1525, 1993.
- [Her03] Maximilian Herrmann. Untersuchungen zur Produktion von Antiwasserstoff mittels zweifachem Ladungstransfer. Master’s thesis, Diplomarbeit TU München & Max-Planck-Institut für Quantenoptik, Garching, 2003.
- [HHC98] E. A. Hessels, D. M. Homan, and M. J. Cavagnero. Two-stage Rydberg charge exchange: An efficient method for production of antihydrogen. *Phys. Rev. A*, 57:1668–1671, 1998.
- [Hig] HighFinesse GmbH, Auf der Morgenstelle 14, 72076 Tübingen, Germany.
- [HKD<sup>+</sup>87] H. F. Hess, G. P. Kochanski, J. M. Doyle, N. Masuhara, D. Kleppner, and T. J. Greytak. Magnetic trapping of spin-polarized atomic hydrogen. *Phys. Rev. Lett.*, 59:672, 1987.
- [Hor03] Roland Erich Horn. *Aufbau eines Systems gepulster, abstimmbarer Festkörperlaser zum Einsatz in der Resonanzionisations-Massenspektrometrie*. PhD thesis, Johannes Gutenberg-Universität, Mainz, 2003.
- [HW96] H. Haken and H. C. Wolf. *Atom- und Quantenphysik*. Springer Verlag, Berlin, 6th edition, 1996.
- [HZ93] T. W. Hänsch and C. Zimmermann. Laser spectroscopy of hydrogen and antihydrogen. *Hyperfine Interact.*, 76:47, 1993.
- [Jac98] J. D. Jackson. *Classical Electrodynamics*. John Wiley and Sons, New York, 3rd edition, 1998.
- [Jos65] R. Jost. *The General Theory of Quantised Fields*. Am. Math. Soc., Providence, 1965.
- [Kab70] P. K. Kabir. *Phys. Rev. D*, 2:540, 1970.
- [KD01] J. M. Kriesel and C. F. Driscoll. *Phys. Rev. Lett.*, 87:135003–1, 2001.
- [KO04a] S. G. Kuzmin and T. M. O’Neil. Guiding center drift atoms. *Phys. Plasmas*, 11(5):2383–2393, 2004.
- [KO04b] S. G. Kuzmin and T. M. O’Neil. Motion of guiding center drift atoms in the electric and magnetic field of a Penning trap . *preprint*, 2004.
- [Lab] Labview. National Instruments Corporation, 6504 Bridge Point Parkway, Austin, TX 78730–5039, USA.

- [Lid94] D. R. Lide. *Handbook of Chemistry and Physics*. CRC Press, 74th edition, 1994.
- [Lüd57] G. Lüders. *Ann. Phys.*, 2:1, 1957.
- [LWS<sup>+</sup>93] O. J. Luiten, H. G. C. Werij, I. D. Setija, M. .W. Reynolds, T. W. Hijmans, and J. T. M. Walraven. Lyman-alpha spectroscopy of magnetically trapped atomic hydrogen. *Phys. Rev. Lett.*, 70:544, 1993.
- [MBC<sup>+</sup>97] J. P. Merrison, H. Bluhme, J. Chevallier, B. I . Deutch, P. Hvelplund, L. V. Jorgensen, H. Knudsen, M. R. Poulsen, and M. Charlton. Hydrogen Formation by Proton Impact on Positronium. *Phys. Rev. Lett.*, 78(14):2728–2731, 1997.
- [MDS<sup>+</sup>88] N. Masuhara, J. M. Doyle, J. C. Sandberg, D. Kleppner, T. J. Greytak, H. F. Hess, and G. P. Kochanski. Evaporative Cooling of Spin-Polarized Atomic Hydrogen. *Phys. Rev. Lett.*, 61:935, 1988.
- [MH88] D. H. McIntyre and T. W. Hänsch. *Metrologia*, 25:61, 1988.
- [MH03] C. Maggiore and M. Holzscheiter. CERN/SPSC 2003-020, SPSC-M-702, May 2003.
- [MHMS97] K. B. MacAdam, D. M. Homan, O.P. Makarov, and O. P. Sorokina. In *Proceedings of the 14th International Conference on the Application of Accelerators in Research and Industry*, New York, 1997. AIP Press.
- [MK69] P. Mansback and J. C. Keck. Monte Carlo Trajectory Calculations of Atomic Excitation and Ionization by Thermal Electrons. *Phys. Rev.*, 181(1):275–289, 1969.
- [MPTvdM80] D. Möhl, G. Petrucci, L. Thorndahl, and S. van der Meer. *Phys. Rept.*, 58:76, 1980.
- [MvdS99] H. J. Metcalf and P. van der Straten. *Laser Cooling and Trapping*. Springer Verlag, 2nd edition, 1999.
- [NG91] M. M. Nieto and T. Goldman. The Arguments against Antigravity and the Gravitational Acceleration of Antimatter. *Phys. Rep.*, 205:221, 1991.
- [NHR<sup>+</sup>00] M. Niering, R. Holzwarth, J. Reichert, P. Pakasov, T. Udem, M. Weitz, T. W. Hänsch, P. Lemonde, G. Santarelli, M. Abgrall, P. Laurent, C. Salomon, and A. Clairon. Measurement of the Hydrogen 1S–2S Transition Frequency by Phase Coherent Comparison with a Microwave Cesium Fountain Clock. *Phys. Rev. Lett.*, 84:5496–5499, 2000.

- [NPWW83] R. Neumann, H. Poth, A. Winnacker, and A. Wolf. Laser-Enhanced Electron-Ion Capture and Antihydrogen Formation. *Z. Phys. A*, 313:253, 1983.
- [OBP<sup>+</sup>04] P. Oxley, N. S. Bowden, R. Parrott, A. Speck, C. H. Storry, J. N. Tan, M. Wessels, G. Gabrielse, D. Grzonka, W. Oelert, G. Schepers, T. Sefzick, J. Walz, H. Pittner, T. W. Hänsch, and E. A. Hessels. Aperture method to determine the density and geometry of antiparticle plasmas. *Phys. Lett.B*, 595:60–67, 2004.
- [OFS] *OFS Optical Fiber Solutions*. 2000 NE Expressway, Norcross, GA 30071, USA.
- [O'N80] T. M. O'Neil. A confinement theorem for nonneutral plasmas. *Phys. Fluids*, 23:2216–2218, 1980.
- [OT68] A. I. Oksak and I. T. Todorov. *Comments Math. Phys.*, 11:125, 1968.
- [Oxl03] P. K. Oxley. *Production of Slow Antihydrogen from Cold Antimatter Plasmas*. PhD thesis, Harvard University, Cambridge, Massachusetts, October 2003.
- [Par] R. Parrott. *to be published*. PhD thesis, Harvard University, Cambridge, Massachusetts.
- [Pau55] W. Pauli. *Niels Bohr and the Development of Physics*, page 30. Pergamon Press, 1955.
- [PDG00] The Particle Data Group. *The European Physical Journal*, C15:1, 2000.
- [Pol] *Polymicron Technologies*.
- [Pri83] D. E. Pritchard. Cooling neutral atoms in a magnetic trap for precision spectroscopy. *Phys. Rev. Lett.*, 51:1336, 1983.
- [Ram90] N. F. Ramsey. Atomic hydrogen hyperfine structure experiments. In T. Kinoshita, editor, *Quantum Electrodynamics*, pages 673–695. World Scientific, Singapore, 1990.
- [RGHW94] H. Ruder, F. Geyer, H. Herold, and G. Wunner. *Atoms in Strong Magnetic Fields*. Springer Verlag, Berlin, 1994.
- [RH04] F. Robicheaux and J. D. Hanson. Three-body recombination for protons moving in a strong magnetic field. *Phys. Rev. A*, 69:010701, 2004.
- [Ric81] Arthur Rich. Recent experimental advances in positronium research. *Rev. Mod. Phys.*, 53(1):127–165, January 1981.

- [Rob04] F. Robicheaux. Simulation of antihydrogen formation. *Phys. Rev. A*, 70:022501, 2004.
- [RWE<sup>+</sup>95] L. Ricci, M. Weidemüller, T. Esslinger, A. Hemmerich, C. Zimmermann, V. Vuletic, W. König, and T. W. Hänsch. A compact grating–stabilized diode laser system for atomic physics. *Optics Communications*, 117:541, 1995.
- [Sig] SPSS, Inc., Chicago, IL. *Sigmaplot 8.0*.
- [SKWM94] O. Schmidt, K. M. Knaak, R. Wynands, and D. Meschede. Cesium saturation spectroscopy revisited: How to reverse peaks and observe narrow resonances. *Appl. Phys. B*, 59:167–178, 1994.
- [SL88] P. J. Schultz and K. G. Lynn. *Rev. Mod. Phys.*, 60:701, 1988.
- [Spe] Spektronika. *Laser Specifications*. Spektronika Ltd., Sofia, Bulgaria.
- [SRSa] Stanford Research Systems, 1290-D Reamwood Ave., Sunnyvale, CA 94089, USA .
- [SRNb] Stanford Research Systems, 1290-D Reamwood Ave., Sunnyvale, CA 94089, USA. *Model SR830 DSP Lock-in Amplifier*.
- [SRS99] Stanford Research Systems, 1290-D Reamwood Ave., Sunnyvale, CA 94089, USA. *Multichannel Scaler/Averager Model SR430*, October 1999.
- [SRV93] R. L. Spencer, S. N. Rasband, and R. R. Vanfleet. Numerical calculation of axisymmetric non–neutral plasma equilibria. *Physics of Fluids B*, 5(12):4267–4272, 1993.
- [SSS<sup>+</sup>04] C. H. Storry, A. Speck, D. Le Sage, N. Guise, G. Gabrielse, D. Grzonka, W. Oelert, G. Schepers, T. Sefzick, H. Pittner, M. Herrmann, J. Walz, T. W. Hänsch, D. Comeau, and E. A. Hessels. First Laser–Controlled Antihydrogen Production. *Phys. Rev. Lett.*, 93:263401, 2004.
- [ST68] D. T. Stoyonoy and I. T. Todorov. *J. Math. Phys.*, 9:2146, 1968.
- [Ste76] H. Stelzer. A large area parallel plate avalanche counter. *Nucl. Inst and Methods*, 133:409, 1976.
- [Ste02] D. A. Steck. Cesium D Line Data. <http://steck.us/alkalidata>, 2002.
- [SWL<sup>+</sup>93] I. D. Setija, H. G. C. Werij, O. J. Luiten, M. W. Reynolds, T. W. Hijmans, and J. T. M. Walraven. Optical cooling of atomic hydrogen in a magnetic trap. *Phys. Rev. Lett.*, 70:2257–2260, 1993.

- [SYG01] T. M. Squires, P. Yesley, and G. Gabrielse. Stability of a combined Penning–Ioffe trap. *Phys. Rev. Lett.*, 86:5266–5269, 2001.
- [URHK00] T. Udem, J. Reichert, T. W. Hänsch, and M. Kourogi. Absolute optical frequency measurement of the cesium  $D_2$  line. *Phys. Rev. A*, 62:031801(R), 2000.
- [VGP<sup>+</sup>04] D. Vrinceanu, B. E. Granger, R. Parrott, H. R. Sadeghpour, L. Cederbaum, A. Mody, J. Tan, and G. Gabrielse. Strongly Magnetized Antihydrogen and Its Field Ionization. *Phys. Rev. Lett.*, 92:133402, 2004.
- [Vog95] Helmut Vogel. *Gerthsen Physik*. Springer Verlag, Berlin, 18th edition, 1995.
- [vRB JW88] R. van Roijen, J. J. Berkhout, S. Jaakkola, and J. T. M. Walraven. Experiments with Atomic Hydrogen in a Magnetic Trapping Field. *Phys. Rev. Lett.*, 61:931, 1988.
- [WAH<sup>+</sup>57] C. S. Wu, E. Ambler, R. W. Hayward, D. D. Hoppes, and R. P. Hudson. *Phys. Rev.*, 105:1413, 1957.
- [Wal80] R. M. Wald. *Phys. Rev. D*, 21:2742, 1980.
- [Wal93] J. T. M. Walraven. Trapping and cooling of (anti)hydrogen. *Hyperfine Interact.*, 76:205–220, 1993.
- [WEH<sup>+</sup>03] E. Widmann, J. Eades, R. S. Hayano, T. Ishikawa, W. Pirkl, M. Hori, Y. Yamazaki, A. Mohri, T. Yamazaki, D. Horváth, B. Juhász, and E. Takács. Measurement of the antihydrogen hyperfine structure. *Letter of Intent to the AD: CERN/SPSC 2003–009*, 2003.
- [WFH<sup>+</sup>03] J. Walz, P. Fendel, M. Herrmann, M. König, A. Pahl, H. Pittner, B. Schatz, and T. W. Hänsch. Towards laser spectroscopy of antihydrogen. *J. Phys. B*, 36:649, 2003.
- [WH90] C. E. Wieman and L. Hollberg. Using diode lasers for atomic physics. *Rev. Sci. Instrum.*, 62:1, 1990.
- [WH04] J. Walz and T. W. Hänsch. A proposal to measure antimatter gravity using ultracold antihydrogen atoms. *General Relativity and Gravitation*, 36:361, 2004.
- [Wil81] C. M. Will. *Theory and Experiment in Gravitational Physics*. Cambridge University Press, Cambridge, 1981.
- [WO93] J. Wang and R. E. Olsen. Dominance of the Thomas mechanism for electron capture from orientated Rydberg atoms. *Phys. Rev. Lett.*, 72:332–335, 1993.

- [WPH<sup>+</sup>03] J. Walz, H. Pittner, M. Herrmann, P. Fendel, B. Henrich, and T. W. Hänsch. Cold antihydrogen atoms. *Appl. Phys. B*, 77:713, 2003.
- [WS87] K.-H. Weber and C. J. Sansonetti. Accurate energies of nS, nP, nD, nF, and nG levels of neutral cesium. *Phys. Rev. A*, 35(11):4650, 1987.
- [Yes01] P. S. Yesley. *The Road to Antihydrogen*. PhD thesis, Harvard University, 2001.
- [YMH<sup>+</sup>02] T. Yamazaki, N. Morita, R. S. Hayano, E. Widmann, and J. Eades. *Phys. Rep.*, 366:183, 2002.



## Background-Free Observation of Cold Antihydrogen with Field-Ionization Analysis of Its States

G. Gabrielse,<sup>1,\*</sup> N. S. Bowden,<sup>1</sup> P. Oxley,<sup>1</sup> A. Speck,<sup>1</sup> C. H. Storry,<sup>1</sup> J. N. Tan,<sup>1</sup> M. Wessels,<sup>1</sup> D. Grzonka,<sup>2</sup> W. Oelert,<sup>2</sup>  
G. Schepers,<sup>2</sup> T. Seifzick,<sup>2</sup> J. Walz,<sup>3</sup> H. Pittner,<sup>4</sup> T. W. Hänsch,<sup>4,5</sup> and E. A. Hessels<sup>6</sup>

(ATRAP Collaboration)

<sup>1</sup>*Department of Physics, Harvard University, Cambridge, Massachusetts 02138*

<sup>2</sup>*IKP, Forschungszentrum Jülich GmbH, 52425 Jülich, Germany*

<sup>3</sup>*CERN, 1211 Geneva 23, Switzerland*

<sup>4</sup>*Max-Planck-Institut für Quantenoptik, Hans-Kopfermann-Strasse 1, 85748 Garching, Germany*

<sup>5</sup>*Ludwig-Maximilians-Universität München, Schellingstrasse 4/III, 80799 München, Germany*

<sup>6</sup>*York University, Department of Physics and Astronomy, Toronto, Ontario, Canada M3J 1P3*

(Received 11 October 2002; published 31 October 2002)

A background-free observation of cold antihydrogen atoms is made using field ionization followed by antiproton storage, a detection method that provides the first experimental information about antihydrogen atomic states. More antihydrogen atoms can be field ionized in an hour than all the antimatter atoms that have been previously reported, and the production rate per incident high energy antiproton is higher than ever observed. The high rate and the high Rydberg states suggest that the antihydrogen is formed via three-body recombination.

DOI: 10.1103/PhysRevLett.89.213401

PACS numbers: 36.10.-k

Antihydrogen ( $\bar{H}$ ) atoms that are cold enough to be trapped for laser spectroscopy [1] promise to provide the most stringent *CPT* tests with baryons and leptons [2], along with more sensitive tests for possible extensions to the standard model [3], building on the high accuracy of hydrogen spectroscopy [4]. It may even be possible to directly observe the gravitational force on antimatter atoms [5].  $\bar{H}$  atoms with a temperature near to the 0.5 K depth of a realistic magnetic trap are greatly preferred since trapping atoms from a thermal distribution is much less likely with increasing temperature.

The ATRAP Collaboration demonstrated the first positron cooling of antiprotons [6,7] in a nested Penning trap [8] more than a year ago. Detailed studies of this cooling (to 4 K) have since been carried out [9] to ensure that the antiproton ( $\bar{p}$ ) loss we observed during positron ( $e^+$ ) cooling corresponds to  $\bar{H}$  formation. This Letter reports an observation of cold  $\bar{H}$  produced during such cooling that is insensitive to other  $\bar{p}$  loss mechanisms. Field ionization of  $\bar{H}$  followed by  $\bar{p}$  storage provides the first experimental information about  $\bar{H}$  excited states. Every recorded event comes from  $\bar{H}$  production, with no background. Another very recent report of cold  $\bar{H}$  formation [10], also during positron cooling in a nested Penning trap, instead identifies  $\bar{p}$  and  $e^+$  annihilations within  $\pm 8$  mm and 5  $\mu$ s as  $\bar{H}$ , subtracting a background larger than the signal. Observations of high velocity  $\bar{H}$  also used simultaneous annihilation detection [11,12].

More antiprotons from ionized  $\bar{H}$  atoms can now be captured in an hour than the sum of all antimatter atoms reported so far. If the  $\bar{H}$  leave the production region isotropically, then 11% of the  $\bar{p}$  in the nested Penning

trap form  $\bar{H}$ . The 657  $\bar{p}$  we capture from  $\bar{H}$  ionization in the sample used here would then correspond to nearly 170 000 cold  $\bar{H}$  atoms. Even if the distribution is not isotropic, the high rate supports the feasibility of spectroscopic investigations to follow. Rydberg states formed at a high rate likely start with a three-body recombination collision [8] between a  $\bar{p}$  and two  $e^+$ , with deexcitation continuing via other processes [13,14].

The apparatus (Fig. 1) alternates between the one used to demonstrate positron cooling of antiprotons [6] and a close copy. A 5.4 T magnetic field from a superconducting solenoid is directed along the vertical symmetry axis of a stack of gold-plated copper rings. Applied voltages form Penning traps that confine the  $\bar{p}$ ,  $e^-$ , and  $e^+$  and control their interactions. Captured  $\bar{p}$  accumulate in the volume below the rotatable electrode. Above, injected  $e^+$  accumulate simultaneously. The electrodes and surrounding vacuum enclosure are cooled to 4.2 K via a thermal contact to liquid helium. Cryopumping reduces the pressure within the trap to less than  $5 \times 10^{-17}$  Torr, as measured in a similar apparatus [15] using the lifetime of trapped  $\bar{p}$  as a gauge.

All experiments pursuing antihydrogen, and other experiments requiring the lowest energy antiprotons, make use of CERN's unique Antiproton Decelerator (AD). A standard set of techniques that some of us developed over the last 15 years [2] is also used to accumulate cold  $\bar{p}$  in a trap, at an energy that can be more than a factor of  $10^{10}$  times lower than that of  $\bar{p}$  in the AD. Every 100 s, the AD ejects a short pulse of  $\bar{p}$ . The  $\bar{p}$  slow in matter, are captured in a trap that is closed electronically while they are within, and electron cool in the trap to 4.2 K.

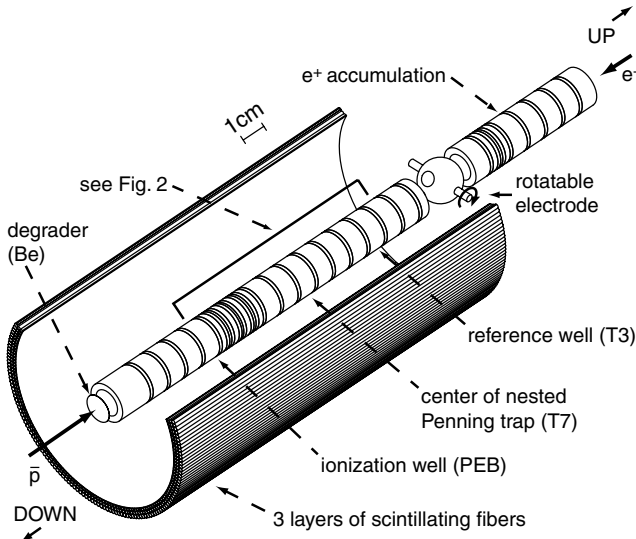


FIG. 1. Overview of the trap and detectors. Antiprotons are loaded from below (left), into the trap electrodes below the rotatable electrode. Positrons are simultaneously loaded from above (right) into the electrodes above the rotatable electrode.  $\bar{H}$  formation is observed within the lower region detailed in the next figure.

A  $\bar{p}$  stacking technique [16] allows the accumulation of as many  $\bar{p}$  from successive AD pulses as time permits. Typically 150 000 antiprotons end up suspended within electrode T2 [Fig. 2(a)].

The accumulated  $e^+$  [17] originate in a 69 mCi  $^{22}\text{Na}$  source that is lowered through a He dewar to settle against the 4.2 K trap enclosure. Fast  $e^+$  follow magnetic field lines and enter the trap vacuum through a thin Ti window. Some slow as they enter the trapping region through a thin single crystal of tungsten. Others slow while turning around within a thick tungsten crystal that rotates to the trap axis when the rotatable electrode goes to its closed position. Slow  $e^+$  that pick up  $e^-$  while leaving the thin crystal form highly magnetized, Rydberg positronium atoms. These travel parallel to the trap axis until they are ionized by the electric field of a Penning trap well, whereupon the  $e^+$  are captured. With the rotatable electrode in its closed position, neither crystal can be struck by  $\bar{p}$ , thus protecting an essential layer of adsorbed gas on the thin crystal, without which  $e^+$  accumulation ceases [17,18]. With this electrode rotated open,  $e^+$  can be pulsed through and caught in the lower trap region. Particle motions induce detectable currents in resonant RLC circuits attached to trap electrodes, making it possible to nondestructively detect the  $e^+$  number before and after the transfer. Up to  $1.7 \times 10^6$  cold  $e^+$  are located in electrode T5 [Fig. 2(a)] for these studies.

The nested Penning trap [Figs. 2(a) and 2(b)] is central to the production of cold  $\bar{H}$ . The  $e^+$  and  $\bar{p}$  have opposite charge signs, and thus cannot be confined or made to interact within the same Penning trap well. Some of us

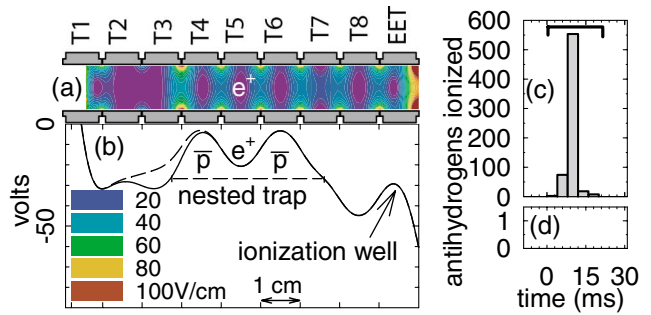


FIG. 2 (color). (a) Electrodes for the nested Penning trap. Inside is a representation of the magnitude of the electric field that strips  $\bar{H}$  atoms. (b) Potential on axis for positron cooling of antiprotons (solid line) during which  $\bar{H}$  formation takes place, with the (dashed line) modification used to launch  $\bar{p}$  into the well. (c) Antiprotons from  $\bar{H}$  ionization are released from the ionization well during a 20 ms time window. (d) No  $\bar{p}$  are counted when no  $e^+$  are in the nested Penning trap.

proposed the nested Penning trap [8], with  $e^+$  within a small inverted well at the center of a larger well for  $\bar{p}$ , as the solution to this challenge. We investigated its properties with  $e^-$  and  $p$  [19], loaded cold  $\bar{p}$  and  $e^+$  together in a nested Penning trap [18], and then used it to observe the positron cooling of antiprotons [6].

To start positron cooling and  $\bar{H}$  formation, the  $\bar{p}$  are launched into the nested Penning trap by pulsing from the solid to the dashed potential [Fig. 2(b)] for  $1.5 \mu\text{s}$ . The  $\bar{p}$  oscillate back and forth through the cold  $e^+$  within a nearly symmetrical nested Penning trap, restored before the  $\bar{p}$  return to their launch point. They lose energy via collisions with  $e^+$ , which cool via synchrotron radiation to the 4.2 K of their surroundings.

Antihydrogen should form most efficiently when  $e^+$  cool  $\bar{p}$  to the point where the two species have low relative velocities. Upon observing  $\bar{p}$  losses during positron cooling, and intriguing indications of  $\bar{H}$  production, we undertook a more detailed study of positron cooling [9] to ensure that other mechanisms would not generate signals that could be confused with  $\bar{H}$  production. The ambipolar diffusion mechanism [20] is particularly troubling since unbound  $e^+$  and  $\bar{p}$  correlate enough to diffuse out of the trap, perhaps even generating simultaneous annihilations of  $\bar{p}$  and  $e^+$ .

Detailed studies of the positron cooling of antiprotons in a nested Penning trap reveal some intricacy, as illustrated with small numbers of  $\bar{p}$  and  $e^+$  in Fig. 3. The average  $\bar{p}$  energy decreases exponentially for short times [Fig. 3(a)], with a time constant that varies with the particle number and density. However, the  $\bar{p}$  energy spectra taken at a sequence of cooling times [Figs. 3(b)–3(e)] reveals a great deal of structure, not yet completely understood. The  $\bar{H}$  atoms presumably form when the energies of the  $\bar{p}$  (histograms) and  $e^+$  (vertical dashed line) overlap, since their relative velocities are then lowest. On a 10 times longer time scale, the  $\bar{p}$  cool into the side wells

of the nested trap, out of contact with the  $e^+$ . The new cooling mechanism here seems to be a recycled evaporative cooling of the  $\bar{p}$ , whereby hot  $\bar{p}$  that “evaporate” to higher energies in the nested well are cooled by the  $e^+$  before they leave the well. With no  $e^+$  in the nested well, evaporative cooling cools the  $\bar{p}$  on the slower time scale. There is also radial loss of  $\bar{p}$  near the potential maximum at the center of the nested Penning trap.

Any  $\bar{H}$  atom formed is free to move in the initial direction of its  $\bar{p}$ , unconfined by the nested Penning trap.  $\bar{H}$  atoms passing through the field-ionization well in a state that can be ionized by the electric field will leave their  $\bar{p}$  trapped in this well. The ionization well [within electrode EET in Fig. 2(a)] is carefully constructed so that its electric field ensures that no  $\bar{p}$  from the nested Penning trap can get into it (e.g., a  $\bar{p}$  liberated from the nested well by ambipolar diffusion), except if it travels about 4 cm bound within an  $\bar{H}$  atom. Any  $\bar{p}$  heated out of the nested Penning trap escapes over the lower potential barrier in the other direction. Even if a  $\bar{p}$  did acquire enough energy to go over the ionization well in one pass it would not be trapped because there is no mechanism to lower its energy while over this well. In addition, positron cooling lowers the energy of the  $\bar{p}$  in the nested well, taking them farther from the energy required to even pass over the ionization well.

Electric fields [Fig. 2(a)] ionize  $\bar{H}$  Rydberg states. Numerical modeling indicates the capture of  $\bar{p}$  from  $\bar{H}$  atoms that ionize in electric fields between 35 and 95 V/cm. A rough estimate comes from the classical formula [21] for the electric field  $F = 3.2 \times 10^8 n^{-4}$  V/cm that would strip a Rydberg atom entering this field. The binding energy,  $E = 13.6n^{-2}$  eV, defines  $n$  even though it is not a good quantum number in these fields. This suggests the field ionization and capture of  $\bar{p}$  from  $\bar{H}$  atoms with binding energies corresponding to

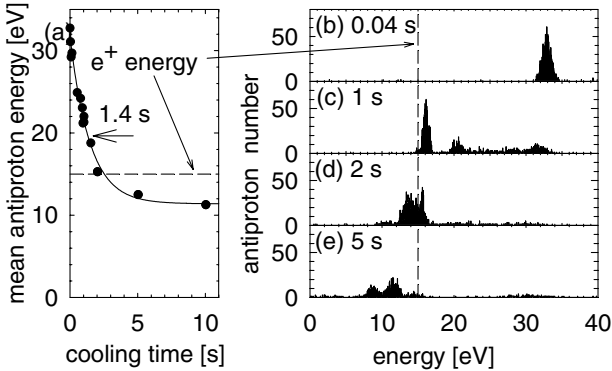


FIG. 3. (a) Antiproton average energy decreases exponentially in time until the antiprotons and positrons have the lowest relative velocity. Cooling then continues but at a 10 times slower rate. (b)–(e) Energy spectra of the  $\bar{p}$  as a function of the positron cooling time. (For this example, 5000  $\bar{p}$  are used, along with 200 000  $e^+$  in a 15 V well.)

$n = 43$  to  $n = 55$ . Refined estimates are needed using methods suited to strong fields.

Only signals from  $\bar{H}$  are detected with this field-ionization method—there is no background at all. Figure 2(c) represents 657 ionized  $\bar{H}$  atoms captured in the ionization well during the course of this experiment—more than all of the  $\bar{H}$  atoms that have been reported so far. In many trials without  $e^+$  we have never seen a single  $\bar{p}$  in the ionization well [Fig. 2(d)]. Antiprotons from  $\bar{H}$  ionization are stored in the ionization well until after positron cooling is completed in the nested well, and all  $e^+$  and  $\bar{p}$  in the nested well are released in the direction away from the ionization well. We then eject the trapped  $\bar{p}$  by ramping down the potential of the ionization well in 20 ms. The ejected  $\bar{p}$  annihilate upon striking electrodes, generating pions and other charged particles that produce light pulses in the scintillators. The ramp is fast enough so that the 1.2 s<sup>-1</sup> cosmic ray background contributes a count in our window only 1 time in 50 in Figs. 2(c) and 2(d). Our experimentally calibrated detection efficiency [22] corresponds to 1 in 2.7 of the stored  $\bar{p}$  producing a coincidence signal in surrounding scintillators.

The number of ionized  $\bar{H}$  atoms increases with the number of  $e^+$  in the nested well [Fig. 4(a)] as might be expected, though this curve is surprisingly insensitive to the total number of  $e^+$  for larger  $e^+$  number. We are exploring some indications that the shape of this measured curve is related to a quadratic dependence of the production rate upon  $e^+$  density. The ionization well can be moved farther away from the center of the nested well, using identical electrodes to the right of EET in Fig. 2(a). The decrease in the number of ionized  $\bar{H}$  [Fig. 4(b)] seems consistent with a quadratic dependence on distance, showing that the  $\bar{H}$  angular distribution is broader than the small solid angle subtended by our ionization well. Isotropic  $\bar{H}$  production and a broad  $\bar{H}$  “beam” along the direction of the magnetic field are both consistent

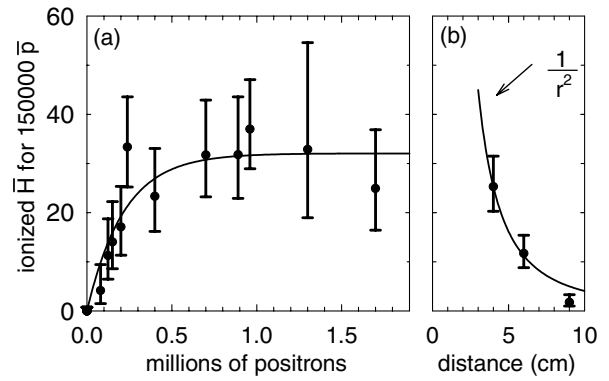


FIG. 4. (a) The number of field-ionized  $\bar{H}$  atoms increases with the number of  $e^+$  in the nested Penning trap of Fig. 2, and then levels off. (b) This number decreases when the ionization well is moved away from the nested Penning trap.

with Fig. 4(b). More study is required to see if the trajectories of the highly polarizable Rydberg atoms could be significantly modified by the electric and magnetic fields.

To give some idea of how efficiently  $\bar{H}$  atoms are stripped and detected we use one trial in which eight AD injection pulses are used to accumulate 148 000 cold  $\bar{p}$ , with 430 000 cold  $e^+$  accumulating simultaneously. After the positron cooling of the antiprotons we determine that 66  $\bar{H}$  atoms have field ionized and left their  $\bar{p}$  in the ionization well. This means that we observe about eight  $\bar{H}$  atoms per AD injection pulse, and about one  $\bar{H}$  atom per 2200 antiprotons in the nested well. (For comparison, smaller values of about 1/4 and 1/12 000 pertain to the very recent implementation of positron cooling of  $\bar{p}$  in a larger trap using more  $e^+$  [10], perhaps because of a higher temperature and a higher background gas pressure.)

If the  $\bar{H}$  production at ATRAP is isotropic, then the 657 ionized  $\bar{H}$  would represent nearly 170 000 cold  $\bar{H}$ . This would mean that a remarkable 11% of the  $\bar{p}$  in the nested Penning trap are forming  $\bar{H}$  atoms—comprising a substantial portion of the large  $\bar{p}$  losses we have been observing during positron cooling of antiprotons since this cooling was first observed. (The ionization well covers only about 1/260 of the total solid angle.)

In conclusion, more  $\bar{H}$  atoms are observed than the sum of all previously reported, and many more are observed per high energy  $\bar{p}$  sent to our apparatus, and per  $\bar{p}$  cooled in our apparatus.  $\bar{H}$  atoms are produced during positron cooling of antiprotons in a nested Penning trap. Improved implementations of such cooling will certainly increase the  $\bar{H}$  production rate. Repeatedly driving  $\bar{p}$  from one side of the nested well to the other with a resonant radio frequency drive, for example, yields 720 ionized  $\bar{H}$  atoms in 1 h [9]. The  $\bar{H}$  signals being observed should allow optimization of techniques and further rate increases.

The electric field ionization of  $\bar{H}$ , followed by  $\bar{p}$  storage until all  $\bar{p}$  losses cease, allows the detection of  $\bar{H}$  atoms without any background at all; only  $\bar{H}$  atoms are observed. The field ionization also gives the first glimpse of  $\bar{H}$  atomic states, with  $n$  roughly between about 43 and 55 here. Changing the ionizing electric field should reveal a more detailed picture and indicate how difficult it may be to deexcite  $\bar{H}$  atoms to states that can be trapped and used for spectroscopic studies. It will be interesting to see if the highly polarizable Rydberg states could be trapped in an electric field minimum for some time, but trapping of  $\bar{H}$  in a magnetic trap superimposed on the Penning traps for charge particles [23] awaits deexcitation of the highly magnetized, highly excited states that have been observed.

We are grateful to CERN, its PS Division and the AD team for delivering the 5.3 MeV antiprotons. This work

was supported by the NSF, AFOSR, the ONR of the U.S., the BMBF, FZ-J, and MPG of Germany, and the NSERC, CRC, and PREA of Canada.

\*ATRAP spokesperson.

Email address: gabrielse@physics.harvard.edu

- [1] G. Gabrielse, in *Fundamental Symmetries*, edited by P. Bloch, P. Paulopoulos, and R. Klapisch (Plenum, New York, 1987), p. 59.
- [2] G. Gabrielse, *Adv. At. Mol. Opt. Phys.* **45**, 1 (2000).
- [3] R. Bluhm, V. A. Kostelecký, and N. Russell, *Phys. Rev. D* **57**, 3932 (1998).
- [4] M. Niering *et al.*, *Phys. Rev. Lett.* **84**, 5496 (2000).
- [5] G. Gabrielse, *Hyperfine Interact.* **44**, 349 (1988).
- [6] G. Gabrielse, J. Estrada, J. N. Tan, P. Yesley, N. S. Bowden, P. Oxley, T. Roach, C. H. Storry, M. Wessels, J. Tan, D. Grzonka, W. Oelert, G. Schepers, T. Seifzick, W. Breunlich, M. Carnegalli, H. Fuhrmann, R. King, R. Ursin, H. Zmeskal, H. Kalinowsky, C. Wesdorp, J. Walz, K. S. E. Eikema, and T. W. Hänsch, *Phys. Lett. B* **507**, 1 (2001).
- [7] In Fig. 6c of the previous reference, the center of the  $e^+$  well should be  $-4$  V. Our current understanding is that recycled evaporative cooling produces the low energy  $\bar{p}$  peak in Fig. 6, while the intermediate energy peak represents  $\bar{p}$  and  $e^+$  with low relative velocities.
- [8] G. Gabrielse, S. L. Rolston, L. Haarsma, and W. Kells, *Phys. Lett. A* **129**, 38 (1988).
- [9] G. Gabrielse *et al.* (to be published).
- [10] M. Amoretti *et al.*, *Nature (London)* **419**, 456 (2002).
- [11] G. Baur *et al.*, *Phys. Lett. B* **368**, 251 (1996).
- [12] G. Blanford *et al.*, *Phys. Rev. Lett.* **80**, 3037 (1998).
- [13] M. Glinsky and T. O'Neil, *Phys. Fluids B* **3**, 1279 (1991).
- [14] P. O. Fedichev, *Phys. Rev. A* **226**, 289 (1997).
- [15] G. Gabrielse, X. Fei, L. A. Orozco, R. L. Tjoelker, J. Haas, H. Kalinowsky, T. A. Trainor, and W. Kells, *Phys. Rev. Lett.* **63**, 1360 (1989).
- [16] G. Gabrielse, N. S. Bowden, P. Oxley, A. Speck, C. H. Storry, J. N. Tan, M. Wessels, D. Grzonka, W. Oelert, G. Schepers, T. Seifzick, J. Walz, H. Pittner, T. W. Hänsch, and E. A. Hessels, *Phys. Lett. A* **548**, 140 (2002).
- [17] J. Estrada, T. Roach, J. N. Tan, P. Yesley, D. S. Hall, and G. Gabrielse, *Phys. Rev. Lett.* **84**, 859 (2000).
- [18] G. Gabrielse, D. S. Hall, T. Roach, P. Yesley, A. Khabbaz, J. Estrada, C. Heimann, and H. Kalinowsky, *Phys. Lett. B* **455**, 311 (1999).
- [19] D. S. Hall and G. Gabrielse, *Phys. Rev. Lett.* **77**, 1962 (1996).
- [20] R. J. Goldston and P. H. Rutherford, *Introduction to Plasma Physics* (IOP, London, 1995).
- [21] T. F. Gallagher, *Rydberg Atoms* (Cambridge, New York, 1994).
- [22] X. Fei, Ph.D. thesis, Harvard University, 1990.
- [23] T. M. Squires, P. Yesley, and G. Gabrielse, *Phys. Rev. Lett.* **86**, 5266 (2001).

# Driven Production of Cold Antihydrogen and the First Measured Distribution of Antihydrogen States

G. Gabrielse,<sup>1,\*</sup> N. S. Bowden,<sup>1</sup> P. Oxley,<sup>1</sup> A. Speck,<sup>1</sup> C. H. Storry,<sup>1</sup> J. N. Tan,<sup>1</sup> M. Wessels,<sup>1</sup> D. Grzonka,<sup>2</sup> W. Oelert,<sup>2</sup> G. Schepers,<sup>2</sup> T. Seifzick,<sup>2</sup> J. Walz,<sup>3</sup> H. Pittner,<sup>4</sup> T. W. Hänsch,<sup>4,5</sup> and E. A. Hessels<sup>6</sup>

(ATRAP Collaboration)

<sup>1</sup>Department of Physics, Harvard University, Cambridge, Massachusetts 02138

<sup>2</sup>IKP, Forschungszentrum Jülich GmbH, 52425 Jülich, Germany

<sup>3</sup>CERN, 1211 Genève 23, Switzerland

<sup>4</sup>Max-Planck-Institut für Quantenoptik, Hans-Kopfermann-Strasse 1, 85748 Garching, Germany

<sup>5</sup>Ludwig-Maximilians-Universität München, Schellingstrasse 4/III, 80799 München, Germany

<sup>6</sup>York University, Department of Physics and Astronomy, Toronto, Ontario M3J 1P3, Canada

(Received 25 October 2002; published 19 November 2002)

Cold antihydrogen is produced when antiprotons are repeatedly driven into collisions with cold positrons within a nested Penning trap. Efficient antihydrogen production takes place during many cycles of positron cooling of antiprotons. A first measurement of a distribution of antihydrogen states is made using a preionizing electric field between separated production and detection regions. Surviving antihydrogen is stripped in an ionization well that captures and stores the freed antiproton for background-free detection.

DOI: 10.1103/PhysRevLett.89.233401

PACS numbers: 36.10.-k

Observations of cold antihydrogen ( $\bar{H}$ ) were recently reported by the ATHENA [1] and ATRAP [2] collaborations. Both used nested Penning traps, proposed [3] and developed [4,5] to allow oppositely charged antiprotons ( $\bar{p}$ ) and positrons ( $e^+$ ) to interact while confined. Both observed  $\bar{H}$  production during the positron cooling of antiprotons in a nested Penning trap, following the earlier ATRAP demonstration [6]. The two experiments differed sharply in the way that cold  $\bar{H}$  was detected. ATHENA identified  $\bar{p}$  and  $e^+$  annihilations within  $\pm 8$  mm and  $5 \mu s$  as  $\bar{H}$ , subtracting a background (from  $\bar{p}$  annihilations generating  $e^+ e^-$ ) that was larger than the signal. No information about the  $\bar{H}$  states was provided [1]. ATRAP used a background-free, field-ionization method to detect more  $\bar{H}$  in an hour than all other reported  $\bar{H}$  observations. The first glimpse of  $\bar{H}$  states was provided insofar as states ionized by electric fields between 35 and 95 V/cm were detected [2].

More knowledge of  $\bar{H}$  excited state distributions is required to prepare states that can be trapped and used for precision spectroscopy. This long term goal [7] remains attractive for greatly improved *CPT* tests with baryons and leptons [8] and sensitive tests of extensions to the standard model [9], building on accurate hydrogen spectroscopy [10]. It may even be possible to directly observe the gravitational force on cold antimatter atoms [11].

In this Letter, a measured distribution of  $\bar{H}$  states is reported for the first time, for  $\bar{H}$  produced at a high rate by driving  $\bar{p}$  into collisions with cold  $e^+$ . The  $\bar{H}$  states are analyzed as they pass through an electric field that is

varied without changing the separated  $\bar{H}$  production and detection. The  $\bar{p}$  are resonantly driven through trapped  $e^+$ , back and forth from one side of a nested Penning trap to the other, in a new and efficient  $\bar{H}$  production method.  $\bar{H}$  forms during the positron cooling of antiprotons over many cycles, until most of the trapped  $\bar{p}$  have formed  $\bar{H}$  or are otherwise lost from the trap. A higher  $\bar{H}$  production rate, per  $\bar{p}$  coming to our apparatus, compensates for the reduced detection solid angle caused by the clean spatial separation of production and detection. The high rate and observed Rydberg states are what is expected for a three-body recombination mechanism [3,12,13].

The apparatus and many techniques are similar to those ATRAP used to first demonstrate positron cooling of antiprotons in a nested Penning trap [6], and to observe the cold  $\bar{H}$  produced during this cooling [2]. A  $B = 5.4$  T magnetic field from a superconducting solenoid is directed along the symmetry axis of a stack of gold-plated copper rings (Fig. 1). Applied voltages form Penning traps [Figs. 2(a) and 2(b)] that confine the  $\bar{p}$ ,  $e^-$ , and  $e^+$ , and control their interactions. The electrodes and surrounding vacuum enclosure are cooled to 4.2 K via thermal contact to liquid helium. Cryopumping reduces the pressure within the trap to less than  $5 \times 10^{-17}$  Torr, as measured in a similar apparatus using the lifetime of trapped  $\bar{p}$  as a gauge [14].

Antiprotons from CERN's Antiproton Decelerator (AD) are slowed, trapped, electron cooled, and stacked [8,15] in the volume below the rotatable electrode. Above, positrons from a  $^{22}\text{Na}$  source slow and form Rydberg

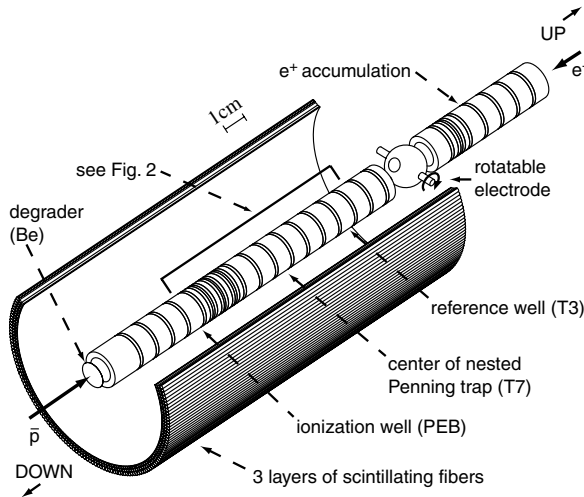


FIG. 1. Antiprotons are loaded from below (left), into the trap electrodes below the rotatable electrode. Positrons are simultaneously loaded from above (right) into the electrodes above the rotatable electrode.  $\bar{H}$  formation is observed within the region detailed in Fig. 2.

positronium atoms that are then ionized to accumulate  $e^+$  [16], at the same time as the  $\bar{p}$  accumulate.

The nested Penning trap [3–6] is central to  $\bar{H}$  production [Figs. 2(a) and 2(b)], as it was for the two earlier experiments [1,2]. The  $e^+$  are in an inverted well at the center of a larger well for  $\bar{p}$ , to allow  $e^+$  and  $\bar{p}$  to be confined and interact despite their opposite charge signs. For these studies, typically 300 000 cold  $e^+$  are located in the center well (within electrode T7). Typically 200 000  $\bar{p}$  are either divided between the two sides of the nested Penning trap (within T6 and T8) or placed in one side well.

The ionization and normalization wells [Figs. 2(a)–2(c)], to the right and left of the nested Penning trap,

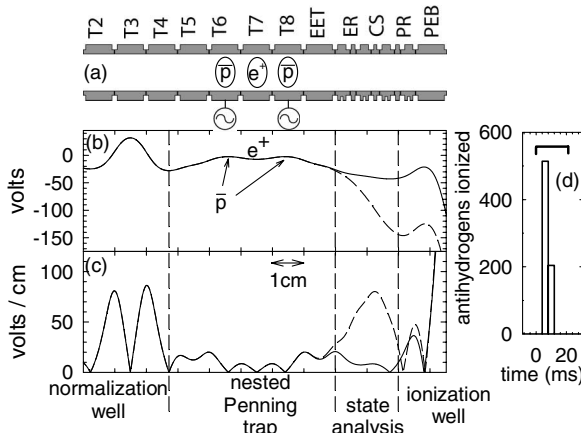


FIG. 2. Trap electrodes (a). Two values of the potential (b) and electric field magnitude (c) on axis. In a one-hour trial, 718  $\bar{p}$  from  $\bar{H}$  are captured in the ionization well (d).

are carefully constructed to prevent  $\bar{p}$  not bound in  $\bar{H}$  from being captured. A  $\bar{p}$  heated out of the nested Penning trap will escape over the normalization well, unless there is a mechanism to lower the  $\bar{p}$  energy within this well. To make capture harder the potential on the left of this well is lower by 3 V (on axis) than that on its right side. Getting a  $\bar{p}$  into the ionization well not only requires an energy loss within the well, but also requires that the  $\bar{p}$  climb a substantial potential barrier. Positron cooling keeps the  $\bar{p}$  from being heated and thus makes it less likely that  $\bar{p}$  will be able to pass through the ionization and normalization wells when  $e^+$  are in the nested well.

Electric fields within the ionization and normalization wells can ionize  $\bar{H}$  passing through, leaving freed  $\bar{p}$  in one of these wells. Figure 2(c) shows the electric field on the trap axis; in the critical state-analysis region, it varies by only about 10% off the axis. Numerical modeling of  $\bar{H}$  trajectories shows that  $\bar{p}$  in the ionization well come from  $\bar{H}$  stripped by fields between 25 and 150 V/cm, while  $\bar{p}$  in the normalization well come from  $\bar{H}$  stripped by fields between 35 and 140 V/cm.

$\bar{H}$  state analysis, a central feature of this work, is done by varying the potential offset between the nested well and the ionization well. This varies the state-analyzing field that  $\bar{H}$  encounter on their way to the ionization well, as illustrated by two examples in Fig. 2(c). Any  $\bar{H}$  stripped by this field is unable to deposit its  $\bar{p}$  in the ionization well, causing the measured number  $N$  of  $\bar{p}$  in this well to decrease. (The stripping field in this well is stronger than are the state-analysis fields.) The number  $N_{\text{norm}}$  of  $\bar{p}$  from  $\bar{H}$  ionization in the normalization well provides a normalization.

Crucial radiofrequency drive potentials applied alternatively to electrodes T6 or T8 [Fig. 2(a)] drive  $\bar{p}$  between the sides of the nested Penning trap. During each cycle, positron cooling allows the  $\bar{p}$  to settle into the opposite, undriven side well of the nested Penning trap, and some form  $\bar{H}$  during this cooling. Because the  $\bar{p}$  are not exactly positioned at the center of these electrodes, their symmetry does not prevent driving  $\bar{p}$  axial motion.

The 825 kHz frequency of a 1 V peak-to-peak drive is chosen to resonate with the calculated axial bounce frequency (Fig. 3) for  $\bar{p}$  oscillating along the magnetic field direction near the axis and near the bottom of either side of the nested well. The axial bounce frequency depends on  $\bar{p}$  energy, here referenced to the potential energy of a  $\bar{p}$  at the center of the nested Penning trap. This frequency discontinuously halves as the  $\bar{p}$  are excited out of a side well into the wider region of the nested Penning trap. The  $\bar{p}$  interact with the  $e^+$  when the  $\bar{p}$  energy is between zero and  $-0.2$  eV, the latter due to the slightly negative space charge energy of the  $e^+$ . Some optimization of the drive frequency and amplitude was done, but most of a large parameter space remains to be explored. (Another option we have used, though not for this data sample, is noise broadening the drive's frequency spectrum.)

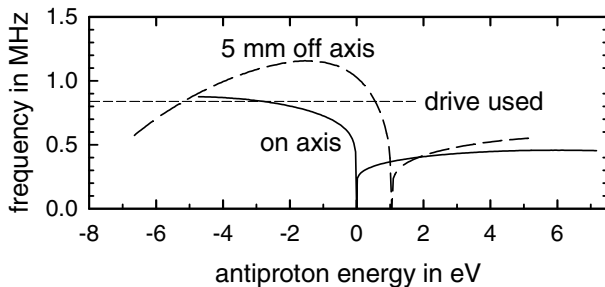


FIG. 3. Axial bounce frequency for  $\bar{p}$  oscillating along the magnetic field direction in the nested Penning trap depends upon their energy, calculated with respect to their potential energy on axis at the center of the nested well. The chosen drive frequency is indicated.

We alternately drive  $\bar{p}$  in one side then the other of the nested well for 10 s, with 5 s between, up to 25 times. Figure 4 shows what our detectors indicate is radial  $\bar{p}$  loss from the trap. Typically we transfer most  $\bar{p}$  from one side to the other, though asymmetries make it common for a constant remnant of a few ten thousands of  $\bar{p}$  to remain in one side well during the whole sequence. The drive cycle timing was not optimized.

To detect  $\bar{p}$  deposited in the ionization and normalization wells from  $\bar{H}$  ionization, we ramp down these potential wells in 20 ms, after the driving and associated particle loss are over. Ejected  $\bar{p}$  annihilate upon striking electrodes, generating pions and other charged particles that produce light pulses in surrounding scintillators. The ramp is fast enough that the  $1.2 \text{ s}^{-1}$  cosmic ray background contributes a count in our window only 1 time in 50—essentially no background at all. Our experimentally calibrated detection efficiency [17] corresponds to 1 in 2.7 of the stored  $\bar{p}$  producing a coincidence signal in surrounding scintillators. Figure 2(d) represents 718  $\bar{p}$  captured in an ionization well from  $\bar{H}$  ionization in a single, one-hour trial. Without  $e^+$  in the nested well, no  $\bar{p}$  from  $\bar{H}$  ionization are detected in the ionization well.

The observed  $\bar{H}$  production rate, per  $\bar{p}$  and per detection solid angle, is up to a factor of 12 greater than that observed using one-time positron cooling of antiprotons [2]. The  $\bar{H}$  rate seems very sensitive to the number of  $e^+$  in the nested well, unlike what was observed for the one-time cooling. This makes some sense insofar as the driving process continually heats the  $\bar{p}$  and hence the  $e^+$  they collide with. More  $e^+$  would transfer this heat more

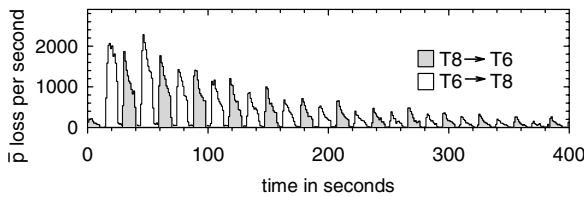


FIG. 4. Antiprotons lost while being driven from one side of the nested Penning trap to the other.

rapidly into synchrotron radiation, and increase  $\bar{p}$  and  $e^+$  overlap. Here much parameter space also remains to be explored. We presume that the  $\bar{H}$  are cold, insofar as the  $\bar{H}$  is likely made after very effective positron cooling of  $\bar{p}$ , but this must also be checked.

The first measured distribution of  $\bar{H}$  states is displayed in Fig. 5(a). The ratio ( $R$ ), of the number of  $\bar{p}$  from  $\bar{H}$  stripped in the ionization well ( $N$ ) to the corresponding number in the normalization well ( $N_{\text{norm}}$ ), is plotted as a function of the state-analysis field ( $F$ ). The number of  $\bar{H}$  that survive this field decreases linearly until consistent with zero. The error bars prevent seeing curvature near this point, so we use a simple linear dependence going to zero to explore principal features. Thus  $dR/dF$  [Fig. 5(b)] is constant up to a cutoff. As many  $\bar{H}$  states are ionized by fields between 30 and 35 V/cm as between 55 and 60 V/cm, for example. No observed  $\bar{H}$  states require a stripping field greater than 62 V/cm.

It would be more satisfying to characterize the distribution of  $\bar{H}$  excited states by their principle quantum number  $n$ , rather than by the electric field that strips them. The first difficulty is that  $n$  is not a good quantum number in the strong  $B = 5.4 \text{ T}$  field, though we still use  $n$  as a rough parametrization of binding energy, using  $E = -13.6 \text{ eV}/n^2$ . Ionization likely takes place in the direction of  $B$  [18], giving some hope that it may not be strongly modified by  $B$ , but this must be investigated.

The second difficulty is that the type of Rydberg states formed determines the electric field that will ionize them, even in the absence of any magnetic field [19–21]. The field that strips a Rydberg atom entering it with principal quantum number  $n$  is given (in atomic units) by

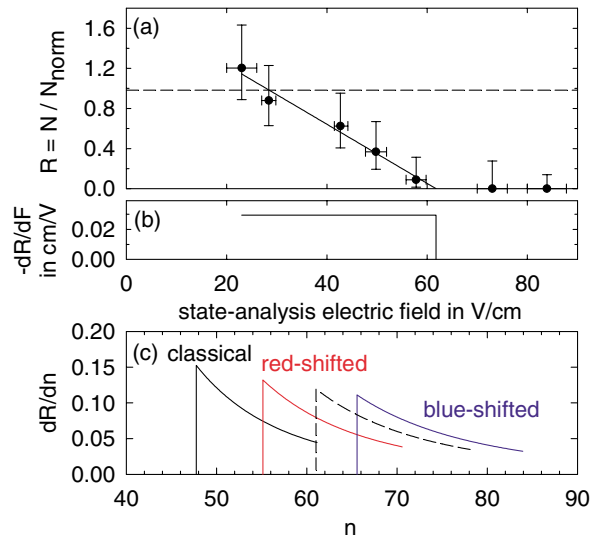


FIG. 5 (color online). (a) The ratio of ionized  $\bar{H}$  in ionization and normalization wells decreases linearly with state-analysis electric field  $F$ . (b) Distribution  $dR/dF$  is flat up to a cutoff. (c) The distribution  $dR/dn \sim n^{-5}$  depends upon the choice of  $A$  used in Eq. (1) to relate  $F$  and  $n$ .

$$F = \frac{A}{16n^4}. \quad (1)$$

This form and the flat distribution of Fig. 5(b) indicate that the shape of the  $n$  distribution goes as  $dR/dn \sim n^{-5}$ .

Several examples of  $dR/dn$  are shown in Fig. 5(c) since the appropriate  $A$  for three-body recombination in a strong  $B$  field is not known. The classical “saddle point” formula, used to give some interpretation of the  $\bar{H}$  produced in our one-time positron cooling of antiprotons [2], has  $A = 1$  and gives the lowest  $n$  distribution with  $n \geq 48$ . Some calculations [19,21] and hydrogen measurements [20] (all unfortunately for  $B = 0$ ) give  $A$  values ranging between red and blue Stark-shifted values of  $A \approx 1.8$  and 3.6, with a weak  $n$  dependence in some cases [19]. This latter value is also close to that for circular Rydberg states in parallel electric and magnetic fields [18]. The dashed distribution midway between the extremes with  $A \approx 2.7$  gives  $n \geq 65$ , and the range of possibilities suggests that these  $n$  values are uncertain by at least  $\pm 10\%$ . Calculations of the  $\bar{H}$  states produced in three-body recombination, and their ionization, are clearly needed to complete the interpretation of the measured distribution of  $\bar{H}$  states.

Finally, further enhancements of  $\bar{H}$  production seem likely with optimizations and variations on our method of arranging for many cycles of positron cooling of antiprotons. One variation would be to simultaneously drive  $\bar{p}$  on both sides of the nested Penning trap. Another would be to lift  $\bar{p}$  from the bottom of the nested well in a potential “bucket” for launching back into the nested Penning trap.

In conclusion, the observed  $\bar{H}$  production per  $\bar{p}$  injected into the ATRAP apparatus is encouragingly high when  $\bar{p}$  are driven into collisions with cold  $e^+$  in a nested Penning trap. The distribution of  $\bar{H}$  states has been measured for the first time with an analyzing electric field in a separate region between where the  $\bar{H}$  are produced and detected. The observed distribution  $dR/dF$  is constant as a function of the state-analysis field, up to cutoff, and implications for the distribution in principal quantum number are explored. The Rydberg states and high production rate are consistent with a three-body recombination mechanism [3,12,13].

The high  $\bar{H}$  production rate suggests the possibility to devise a way to deexcite Rydberg atoms with a range of binding energies and still get enough atoms for trapping and spectroscopy. Some temporary confinement of these highly polarizable states may be possible, but conventional trapping awaits deexcitation to the ground state, whereupon a goal is to superimpose a magnetic trap for  $\bar{H}$  with the Penning traps needed for its  $\bar{p}$  and  $e^+$  ingredients [22].

We are grateful to CERN, its PS Division, and the AD team for delivering the 5.3 MeV antiprotons. This work was supported by the NSF, AFOSR, the ONR of the U.S.,

the BMBF, MPG, and FZ-J of Germany, and the NSERC, CRC, and PREA of Canada.

\*Corresponding author.

Email address: gabrielse@physics.harvard.edu

- [1] M. Amoretti *et al.*, Nature (London) **419**, 456 (2002).
- [2] G. Gabrielse, N. S. Bowden, P. Oxley, A. Speck, C. H. Storry, J. N. Tan, M. Wessels, D. Grzonka, W. Oelert, G. Schepers, T. Seifzick, J. Walz, H. Pittner, T. W. Hänsch, and E. A. Hessels, Phys. Rev. Lett. **89**, 213401 (2002).
- [3] G. Gabrielse, S. L. Rolston, L. Haarsma, and W. Kells, Phys. Lett. A **129**, 38 (1988).
- [4] D. S. Hall and G. Gabrielse, Phys. Rev. Lett. **77**, 1962 (1996).
- [5] G. Gabrielse, D. S. Hall, T. Roach, P. Yesley, A. Khabbaz, J. Estrada, C. Heimann, and H. Kalinowsky, Phys. Lett. B **455**, 311 (1999).
- [6] G. Gabrielse, J. Estrada, J. N. Tan, P. Yesley, N. S. Bowden, P. Oxley, T. Roach, C. H. Storry, M. Wessels, J. Tan, D. Grzonka, W. Oelert, G. Schepers, T. Seifzick, W. Breunlich, M. Carnegelli, H. Fuhrmann, R. King, R. Ursin, H. Zmeskal, H. Kalinowsky, C. Wesdorp, J. Walz, K. S. E. Eikema, and T. W. Hänsch, Phys. Lett. B **507**, 1 (2001).
- [7] G. Gabrielse, in *Fundamental Symmetries*, edited by P. Bloch, P. Paulopoulos, and R. Klapisch (Plenum, New York, 1987), p. 59.
- [8] G. Gabrielse, Adv. At. Mol. Opt. Phys. **45**, 1 (2001).
- [9] R. Bluhm, V. A. Kostelecký, and N. Russell, Phys. Rev. D **57**, 3932 (1998).
- [10] M. Niering, R. Holzwarth, J. Reichert, P. Pokasov, Th. Udem, M. Weitz, T. W. Hänsch, P. Lemonde, G. Santarelli, M. Abgrall, P. Laurent, C. Salomon, and A. Clairon, Phys. Rev. Lett. **84**, 5496 (2000).
- [11] G. Gabrielse, Hyperfine Interact. **44**, 349 (1988).
- [12] M. Glinsky and T. O’Neil, Phys. Fluids B **3**, 1279 (1991).
- [13] P. O. Fedichev, Phys. Lett. A **226**, 289 (1997).
- [14] G. Gabrielse, X. Fei, L. A. Orozco, R. L. Tjoelker, J. Haas, H. Kalinowsky, T. A. Trainor, and W. Kells, Phys. Rev. Lett. **63**, 1360 (1989).
- [15] G. Gabrielse, N. S. Bowden, P. Oxley, A. Speck, C. H. Storry, J. N. Tan, M. Wessels, D. Grzonka, W. Oelert, G. Schepers, T. Seifzick, J. Walz, H. Pittner, T. W. Hänsch, and E. A. Hessels, Phys. Lett. B **548**, 140 (2002).
- [16] J. Estrada, T. Roach, J. N. Tan, P. Yesley, and G. Gabrielse, Phys. Rev. Lett. **84**, 859 (2000).
- [17] X. Fei, Ph.D. thesis, Harvard University, 1990.
- [18] W. Ihra, F. Mota-Furtado, and P. F. O’Mahony, Phys. Rev. A **58**, 3884 (1998).
- [19] D. Banks and J. G. Leopold, J. Phys. B **11**, L5 (1978).
- [20] P. M. Koch and K. A. H. van Leeuwen, Phys. Rep. **255**, 289 (1995).
- [21] T. F. Gallagher, *Rydberg Atoms* (Cambridge University Press, New York, 1994).
- [22] T. M. Squires, P. Yesley, and G. Gabrielse, Phys. Rev. Lett. **86**, 5266 (2001).

# First Measurement of the Velocity of Slow Antihydrogen Atoms

G. Gabrielse,<sup>1,\*</sup> A. Speck,<sup>1</sup> C. H. Storry,<sup>1</sup> D. LeSage,<sup>1</sup> N. Guise,<sup>1</sup> D. Grzonka,<sup>2</sup> W. Oelert,<sup>2</sup> G. Schepers,<sup>2</sup> T. Sefzick,<sup>2</sup> H. Pittner,<sup>3</sup> J. Walz,<sup>3</sup> T. W. Hänsch,<sup>3,4</sup> D. Comeau,<sup>5</sup> and E. A. Hessels<sup>5</sup>

(ATRAP Collaboration)

<sup>1</sup>Department of Physics, Harvard University, Cambridge, Massachusetts 02138, USA

<sup>2</sup>IKP, Forschungszentrum Jülich GmbH, 52425 Jülich, Germany

<sup>3</sup>Max-Planck-Institut für Quantenoptik, Hans-Kopfermann-Strasse 1, 85748 Garching, Germany

<sup>4</sup>Ludwig-Maximilians-Universität München, Schellingstrasse 4/III, 80799 München, Germany

<sup>5</sup>York University, Department of Physics and Astronomy, Toronto, Ontario M3J 1P3, Canada

(Received 31 March 2004; published 10 August 2004)

The speed of antihydrogen atoms is deduced from the fraction that passes through an oscillating electric field without ionizing. The weakly bound atoms used for this first demonstration travel about 20 times more rapidly than the average thermal speed of the antiprotons from which they form, if these are in thermal equilibrium with their 4.2 K container. The method should be applicable to much more deeply bound states, which may well be moving more slowly, and should aid the quest to lower the speed of the atoms as required if they are to be trapped for precise spectroscopy.

DOI: 10.1103/PhysRevLett.93.073401

PACS numbers: 36.10.-k

When the goal of producing “cold” antihydrogen ( $\bar{H}$ ) was laid out long ago [1], the objective was  $\bar{H}$  atoms that were cold enough to be confined in a neutral particle trap for precise spectroscopy and gravitation studies. This stringent definition of “cold” requires  $\bar{H}$  energies significantly below the 0.5 K depth of superconducting magnetic traps, when these are placed in the  $\sim 1$  Tesla bias field needed to confine the antiprotons ( $\bar{p}$ ) and positrons ( $e^+$ ) for  $\bar{H}$  production.

Antihydrogen produced during the positron cooling of antiprotons [2] in a nested Penning trap [3] was called “cold” antihydrogen in reports of its observation [4–6]. However, no  $\bar{H}$  energy, velocity, or temperature was actually measured. The observed atoms were clearly cold compared to  $\bar{H}$  moving at nearly the speed of light [7,8]. Almost certainly the  $\bar{H}$  energy was less than the tens of eV well depths of the potential wells used to confine the  $\bar{p}$  and  $e^+$  from which the  $\bar{H}$  were formed. It was naturally hoped that the  $\bar{H}$  were in thermal equilibrium with the 4.2 K [5,6] or 15 K [4] temperature of the electrodes confining the  $\bar{p}$  and  $e^+$ .

In this Letter we report the first measurement of the velocity of  $\bar{H}$  atoms. The change in  $\bar{H}$  transmission efficiency through an oscillating electric field is measured as a function of the field’s oscillation frequency. ATRAP’s background-free field ionization detection method [5] registers only  $\bar{H}$  that reach the detection well intact. Atoms moving slowly enough will never make it through the electric field without being ionized. Faster atoms are sometimes able to pass while the oscillating field is too weak to ionize them, depending upon the phase of the field. In this first demonstration we deduce that the most weakly bound  $\bar{H}$  that we detect have an energy that is about 200 meV, a speed that is about 20 times higher than

an average thermal speed at 4.2 K. More deeply bound  $\bar{H}$  observed to survive a 360 V/cm electric field may move more slowly; this method should make it possible to check, though the measurements will take much more time than has been available so far. No attempt has yet been made to minimize the  $\bar{p}$  driving forces that bring  $\bar{p}$  and  $e^+$  into repeated contact [6].

The ATRAP apparatus is represented in Fig. 1, with a cross section of the crucial volume in Fig. 2(a). In preparation for  $\bar{H}$  production, typically  $2 \times 10^5 \bar{p}$  from CERN’s Antiproton Decelerator are accumulated for this demonstration. The well-established techniques for slowing, trapping, cooling, and stacking [9,10] are now used in all  $\bar{H}$  experiments. The  $\bar{p}$  cool by collisions to equilibrium with trapped, 4.2 K electrons. (The electrons

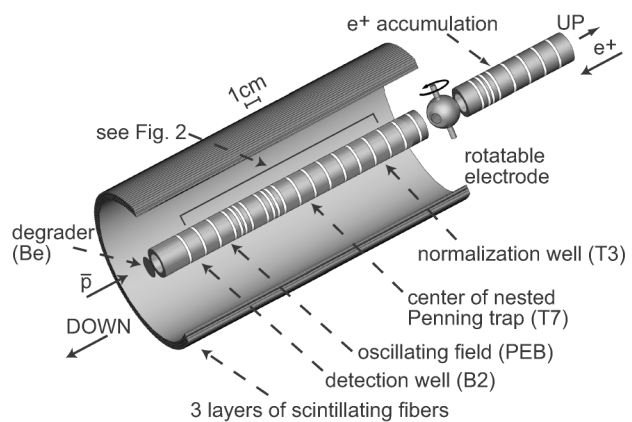


FIG. 1. Antiprotons are loaded from below (left), into the trap electrodes below the rotatable electrode. Positrons are simultaneously loaded from above (right) into the electrodes above the rotatable electrode.

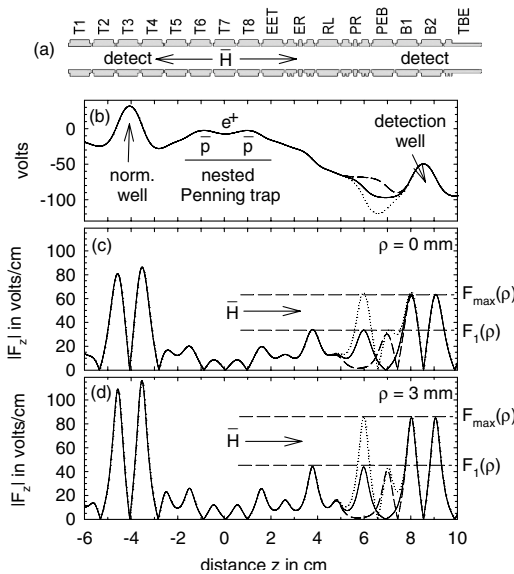


FIG. 2. Cross section of trap electrode (a), potential on axis (b) and the magnitude of the axial electric field on axis (c) and 3 mm off axis (d). Solid curves are the static potentials and axial electric fields magnitudes. Dashed and dotted curves show the maximum variation of these when the oscillating potential is added.

cool via synchrotron radiation to thermal equilibrium with the 4.2 K trap electrodes.) The  $\bar{p}$  are then positioned in the side wells of a nested Penning trap [Fig. 2(b)] by manipulating the potentials applied to the vertical stack of ring electrodes. A magnetic field,  $B\hat{z}$  with  $B = 5.2$  T, is parallel to trap axis. Typically  $4 \times 10^5 e^+$  are accumulated at the same time as the  $\bar{p}$  [11]. They are then positioned in the center of the nested Penning trap [Fig. 2(b)], between the side wells for antiprotons. Like the electrons they cool to 4.2 K by radiating synchrotron radiation.

$\bar{H}$  atoms are produced near the center of the nested Penning trap, at the location of electrode T7 as indicated by “ $\bar{H}$ ” in Fig. 2(a).  $\bar{H}$  atoms are produced when the  $\bar{p}$  are driven from one side well [Fig. 2(b)], by a radiofrequency driving force, through the  $e^+$  [6]. The  $\bar{p}$  that do not form  $\bar{H}$  get more chances when they are driven back and forth from one well to the other. The drives give  $\bar{p}$  velocities along the axis of the trap, either in the direction of the normalization well or in the direction of the detection trap. (Likely such weakly driven  $\bar{H}$  production can produce slower atoms than those produced by injecting higher energy  $\bar{p}$  into a nested Penning trap for cooling [4,5].) If an  $\bar{H}$  is formed before the  $e^+$  completely cool the  $\bar{p}$ , then the  $\bar{H}$  will have a residual axial velocity that is larger than the average thermal velocity of the  $\bar{p}$  at the 4.2 K temperature of the  $e^+$  awaiting  $\bar{H}$  production.

Atoms traveling in the  $-\hat{z}$  direction travel along the magnetic field axis to the normalization well [Fig. 2(b)]. No potentials or fields are varied along this trajectory. The  $\bar{H}$  ionized by the strong electric fields in this well [Figs. 2(c) and 2(d)] leave their  $\bar{p}$  in the well for back-

ground free detection. This well is emptied at a later time and the  $\bar{p}$  annihilations are detected in surrounding scintillators. We use this count to normalize all other  $\bar{H}$  measurements, thereby reducing the effect of variations in the  $\bar{H}$  production due to slightly different numbers of  $\bar{p}$  and  $e^+$ .

Atoms traveling in the  $\hat{z}$  direction will be similarly counted in the detection well [Fig. 2(d)] if they are not ionized by the electric field they pass through on their way to this well. An atom will ionize if the magnitude of the axial electric field it encounters along its trajectory exceeds a value  $F$  which is directly related to the size of its internal orbit [12]. The field along an  $\bar{H}$  trajectory always has a static component  $F_{dc}(\rho, z)\hat{z}$ , and we can add a time varying axial field  $F_{ac}(\rho, z)\cos(\omega t + \phi)\hat{z}$ .

While we can only measure the number of  $\bar{H}$  atoms that travel into the very small solid angle of our detection well, a simple example gives clear evidence that driven  $\bar{H}$  production sends  $\bar{H}$  preferentially directed along the magnetic field axis,  $\pm\hat{z}$ . From  $4.5 \times 10^6 e^+$  and  $2.9 \times 10^5 \bar{p}$  we detect  $7.6 \times 10^3 \bar{H}$  in the detection and normalization wells. Since the combined solid angle of the detection and normalization wells is less than  $4\pi/100$ , the  $\bar{H}$  production cannot be isotropic since several times more  $\bar{p}$  would be required than the number available.

A measurement of the  $\bar{H}$  velocity is very simple in principle. With the oscillating field turned off, the ratio of  $\bar{H}$  atoms ionized in the detection and normalization wells is obtained (open square in Fig. 3). This point has no frequency associated with it, but is plotted on the same vertical scale as the other points on the graph. These come from measurements with the oscillating field turned on, for different values of oscillation frequency  $\omega/(2\pi)$  (solid points in Fig. 3). The fraction of  $\bar{H}$  atoms detected decreases as  $\omega$  increases. As  $\omega$  increases, fewer atoms travel quickly enough through the oscillating field to avoid ionization, and fewer atoms are thus detected. The  $\bar{H}$  atoms are produced under the same conditions for each measurement, and the count from the detection well is normalized as discussed above. Electric field gradients can change the speed of a highly excited and polarizable  $\bar{H}$  atom, but this is a small affect here since the preionizing field is relatively spatially uniform [12].

The vertical scale for Fig. 3 is chosen so that the measurement with no oscillating field is consistent with 1, and so that the measured  $\omega \rightarrow 0$  limit of the oscillating field measurements is consistent with 0.62. The latter is the fraction of the time that the magnitude of the oscillating electric field, along the trajectory of an  $\bar{H}$  traveling to the detection well, is less than the maximum static field along this path. In this limit 0.62 of all the  $\bar{H}$  traveling to the detection well should thus not be ionized by the oscillating field.

To interpret our measurements quantitatively we consider the  $N(\rho, v, F)d\rho dv dF$  antihydrogen atoms produced at  $z = 0$  and  $t = 0$ , at a radius between  $\rho$  and  $\rho + d\rho$ , with an axial velocity between  $v$  and  $v + dv$ , and which

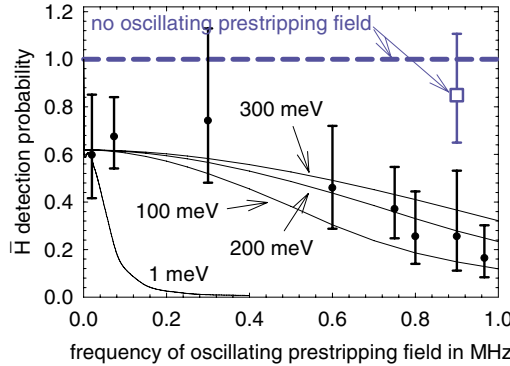


FIG. 3 (color online). The fraction of the  $\bar{H}$  atoms detected in the detection well decreases as the frequency  $\omega/(2\pi)$  of the oscillating electric field is increased (solid points). More atoms are detected when there is no oscillating field (open square). This point is plotted on the same scale as the others but it has no frequency associated with it. The measured points are compared to a simple model discussed in the text; the solid curves apply when the oscillating electric field is applied, and the dashed curve when it is not.

are in a state that will be ionized by an axial electric field between  $F$  and  $F + dF$ .

When no time varying electric field is applied, the  $\bar{H}$  atoms on their way to the detection well experience an axial electric field  $F_{dc}(\rho, z = vt)$ . Figure 2 shows  $F_{dc}(\rho, z)$  for  $\rho = 0$  (c) and  $\rho = 3$  mm (d), along with the corresponding values  $F_1(\rho = 0) = 34$  V/cm and  $F_1(\rho = 3 \text{ mm}) = 45$  V/cm. The number of detected  $\bar{H}$  is thus

$$N_o = \int_0^{\rho_{max}} d\rho \int_0^\infty dv \int_{F_1(\rho)}^{F_{max}(\rho)} dFN(\rho, v, F). \quad (1)$$

Detected atoms are those that ionize between  $F_1(\rho)$  and  $F_{max}(\rho)$ , the maximum values of  $F_{dc}(\rho, z)$  that they encounter before and within the detection well, respectively.

When the alternating axial electric field,  $F_{ac}(\rho, z) \times \cos(\omega t + \phi)$ , is applied the  $\bar{H}$  atoms traveling towards the detection well encounter a net axial field

$$F(\rho, z, \omega/v, \phi) = F_{dc}(\rho, z) + F_{ac}(\rho, z) \cos\left(\frac{\omega z}{v} + \phi\right), \quad (2)$$

where we must later average over all phases  $\phi$ . The number of detected  $\bar{H}$  is

$$N = \int_0^{\rho_{max}} d\rho \int_0^\infty dv \int_0^{2\pi} \frac{d\phi}{2\pi} \int_{F_2(\rho, \omega/v, \phi)}^{F_{max}(\rho)} dFN(\rho, v, F). \quad (3)$$

The limit  $F_2(\rho, \omega/v, \phi)$  is the maximum axial field magnitude (i.e., the maximum  $|F(\rho, z, \omega/v, \phi)|$ ) that an  $\bar{H}$  sees at any  $z$  before the detection well begins.

We make the simplest assumption—that the  $\bar{H}$  are produced uniformly out to a radius  $\rho_{max} = 3$  mm—approximately the measured extent of our  $e^+$  plasma [13]. (Later we show that we are not very sensitive to this

assumption.) We also assume the measured power law dependence  $N \sim F^{-3}$  [14]. Finally we assume that the  $\bar{H}$  have a velocity  $v_o \hat{z}$ , since we expect that driven  $\bar{H}$  production produces atoms traveling along the magnetic field direction. We would expect the same result for any velocity spread that is narrow compared to the average velocity. Thus

$$N(\rho, v, F) \sim \frac{2\pi\rho}{\pi\rho_{max}^2} \delta(v - v_o) F^{-3}. \quad (4)$$

The solid curves in Fig. 3 show the fraction of  $\bar{H}$  atoms that should be detected when the oscillating electric field is turned on, for various values of the  $\bar{H}$  kinetic energy  $\frac{1}{2}Mv_o^2$ , where  $M$  is the  $\bar{H}$  mass.

An  $\bar{H}$  kinetic energy of 200 meV is a good fit to our measurements (2400 K in temperature units). This conclusion is rather insensitive to our assumptions. For example, if we had assumed that all the  $\bar{H}$  was produced on the central axis, then we would have concluded that the  $\bar{H}$  velocity was about 100 meV. If we had instead assumed that all the  $\bar{H}$  was produced 4 mm off axis, then we would have concluded that the  $\bar{H}$  velocity was 300 meV. A 200 meV  $\bar{H}$  velocity is much higher than the 0.3 meV average energy for a 4.2 K thermal distribution—the lowest possible average  $\bar{p}$  and  $\bar{H}$  energy. Even the 1 meV curve in Fig. 3 is far from consistent with our data.

An electric field gradient  $\partial F_z/\partial z$  exerts a force on a highly polarizable  $\bar{H}$  [12]

$$f_z = \frac{e^2 \rho^3}{2r_e m_e c^2} \frac{\partial [F_z(z)^2]}{\partial z}. \quad (5)$$

Here  $e$  is the proton charge,  $\rho$  is the radial size of the  $\bar{H}$  atom,  $r_e$  is the classical electron radius, and  $m_e c^2$  is the electron rest energy. For fields nearly strong enough to ionize the atom the force increases beyond this value. We use the overestimates  $F_z = 100$  V/cm and a gradient  $\partial F_z/\partial z = 100$  V/cm<sup>2</sup> applied over 1 cm, together with the size  $\rho = 0.3 \mu\text{m}$  of the largest atom that survives  $F_{dc} = 40$  V/cm. The resulting force would change the velocity of a 200 meV  $\bar{H}$  by less than a percent, justifying the neglect of the gradient force on a polarized  $\bar{H}$  in this work. For lower  $\bar{H}$  speeds more care must be taken.

For a  $\bar{p}$  traveling in the  $\hat{z}$  direction through the  $e^+$  plasma, one  $\bar{p}$  speed that seems important is the one that equals the average axial speed of the  $e^+$  that are going in the same direction as the  $\bar{p}$ . For 4.2 K  $e^+$  this corresponds to a  $\bar{p}$  energy of 210 meV. This is close to what we measure, likely by coincidence given the approximate character of the estimate. One might expect increased  $\bar{H}$  production at this  $\bar{p}$  energy, but this depends in a complicated way upon how quickly the  $\bar{p}$  are being cooled by the  $e^+$ . A recombination rate that depends upon the relative velocity of the  $\bar{p}$  and  $e^+$  will become insensitive to  $\bar{p}$  energies below this value, since the relative velocity will be determined by the  $e^+$  velocity.

Another important speed is

$$v_p = n_e(\pi b^2)v_e L. \quad (6)$$

This  $\bar{p}$  speed would allow just enough time in the  $L \approx 1$  mm thick  $e^+$  plasma for there to be a deexcitation collision [15] between the  $e^+$  initially picked up by the  $\bar{p}$  and another  $e^+$  in the plasma on average. The expected  $e^+e^+$  collision rate should be of order  $n_e(\pi b^2)v_e$  where  $n_e = 1.6 \times 10^7/\text{cm}^3$  is the  $e^+$  density and  $v_e$  is the average thermal speed for a  $e^+$  at  $T_e = 4.2$  K. The distance of closest approach  $b$  comes from equating the potential energy  $(4\pi\epsilon_0)^{-1}e^2/b$  and the thermal energy  $kT_e$ . The corresponding  $\bar{p}$  energy, and hence the  $\bar{H}$  energy, is 460 meV—larger than we observe. The cross section used is only an estimate, of course, and the  $e^+$  may be heated some by the  $\bar{p}$ . Notice that  $v_p \propto n_e L T_e^{-3/2}$ , suggesting that a  $e^+$  plasma with a lower density, a shorter length and a higher temperature will produce  $\bar{H}$  with lower velocities.

The relatively high velocities that we observe may also be related to the fact that this first demonstration experiment measures only the speed of the most weakly bound  $\bar{H}$  states, which may have had less cooling time. Because the number of  $\bar{H}$  atoms detected goes down steeply as the strength of the ionization field  $F$  is increased, as  $F^{-3}$  [14], the  $\bar{H}$  atoms that we detect are essentially all atoms which will ionize just above the maximum static electric field [ $F_1(\rho)$ ] in the region before the detection well.

More deeply bound  $\bar{H}$  states may well have much lower velocities if these arise because of more collisions of the  $\bar{H}$  with  $e^+$  in the plasma. It should be possible to use this new technique to measure the velocity of more deeply bound states. The experiment is simple in principle. The deeply bound states can be selected by raising the maximum value  $F_1(\rho)$  of the static electric field  $F_{dc}(\rho, z)$ . The challenge in practice is that the number of deeply bound states observed goes down inversely as the cube of this field value, greatly increasing the time required to accumulate data.

In conclusion, a new method makes it possible to measure the speed of slow  $\bar{H}$  atoms for the first time. For the most weakly bound states, our measurements fit well to a 200 meV  $\bar{H}$  energy. This is close to the estimated 210 meV  $\bar{H}$  energy below which the  $\bar{H}$  formation rate no longer increases. It is lower than the 460 meV energy that is estimated to allow a deexcitation collision between the  $e^+$  in an  $\bar{H}$  and a  $e^+$  in the surrounding plasma on average. It is higher than the lowest possible energy, the 0.3 meV average energy of a 4.2 K thermal distribution of  $H$ .

The new method should reveal how the  $\bar{H}$  velocity depends upon the strength of the driving force, the number and density of the  $e^+$  and  $\bar{p}$ , and upon the binding energy or size of the  $\bar{H}$  atoms. Slowly lowering the depth of the center well in the nested Penning trap may produce

slower  $\bar{H}$ , as may interchanging the position of the  $e^+$  and  $\bar{p}$  in this trap. The first step towards devising ways to get the coldest possible  $\bar{H}$  atoms, of course, is a method to measure the  $\bar{H}$  speed, which is now available.

We are grateful to CERN, its PS Division and the AD team for delivering antiprotons. This work was supported by the NSF and AFOSR of the U.S., the BMBF, MPG, and FZ-J of Germany, and the NSERC, CRC, CFI, and OIT of Canada.

\*Corresponding author.

Electronic address: gabrielse@physics.harvard.edu

- [1] G. Gabrielse, in *Fundamental Symmetries*, edited by P. Bloch, P. Paulopoulos, and R. Klapisch (Plenum, New York, 1987), pp. 59–75.
- [2] G. Gabrielse, J. Estrada, J. N. Tan, P. Yesley, N. S. Bowden, P. Oxley, T. Roach, C. H. Storry, M. Wessels, J. Tan, D. Grzonka, W. Oelert, G. Schepers, T. Sefzick, W. Breunlich, M. Carnegelli, H. Fuhrmann, R. King, R. Ursin, H. Zmeskal, H. Kalinowsky, C. Wesdorp, J. Walz, K. S. E. Eikema, and T. Haensch, Phys. Lett. B **507**, 1 (2001).
- [3] G. Gabrielse, S. L. Rolston, L. Haarsma, and W. Kells, Phys. Lett. A **129**, 38 (1988).
- [4] M. Amoretti *et al.*, Nature (London) **419**, 456 (2002).
- [5] G. Gabrielse, N. S. Bowden, P. Oxley, A. Speck, C. H. Storry, J. N. Tan, M. Wessels, D. Grzonka, W. Oelert, G. Schepers, T. Sefzick, J. Walz, H. Pittner, T. W. Hänsch, and E. A. Hessels, Phys. Rev. Lett. **89**, 213401 (2002).
- [6] G. Gabrielse, N. S. Bowden, P. Oxley, A. Speck, C. H. Storry, J. N. Tan, M. Wessels, D. Grzonka, W. Oelert, G. Schepers, T. Sefzick, J. Walz, H. Pittner, T. W. Hänsch, and E. A. Hessels, Phys. Rev. Lett. **89**, 233401 (2002).
- [7] G. Baur, G. Boero, S. Brauksiepe, A. Buzzo, W. Eyrich, R. Geyer, D. Grzonka, J. Hauffe, K. Kilian, M. L. Vetere, M. Macri, M. Moosburger, R. Nellen, W. Oelert, S. Passagio, A. Pozzo, K. Rohrich, K. Sachs, G. Schepers, T. Sefzick, R. Simon, R. Stratmann, F. Stinzing, and M. Wolke, Phys. Lett. B **368**, 251 (1996).
- [8] G. Blanford, D. C. Christian, K. Gollwitzer, M. Mandelkern, C. T. Munger, J. Schultz, and G. Zioulas, Phys. Rev. Lett. **80**, 3037 (1998).
- [9] G. Gabrielse, Adv. At. Mol. Opt. Phys. **45**, 1 (2001).
- [10] G. Gabrielse, N. S. Bowden, P. Oxley, A. Speck, C. H. Storry, J. N. Tan, M. Wessels, D. Grzonka, W. Oelert, G. Schepers, T. Sefzick, J. Walz, H. Pittner, and E. A. Hessels, Phys. Lett. B **548**, 140 (2002).
- [11] J. Estrada, T. Roach, J. N. Tan, P. Yesley, and G. Gabrielse, Phys. Rev. Lett. **84**, 859 (2000).
- [12] D. Vrinceanu, B. E. Granger, R. Parrott, H. R. Sadeghpour, L. Cederbaum, A. Mody, J. Tan, and G. Gabrielse, Phys. Rev. Lett. **92**, 133402 (2004).
- [13] P. Oxley *et al.* Phys. Lett. B **595**, 60 (2004).
- [14] G. Gabrielse *et al.* (to be published).
- [15] M. Glinsky and T. O’Neil, Phys. Fluids B **3**, 1279 (1991).

## First Laser-Controlled Antihydrogen Production

C. H. Storry,<sup>1</sup> A. Speck,<sup>1</sup> D. Le Sage,<sup>1</sup> N. Guise,<sup>1</sup> G. Gabrielse,<sup>1,\*</sup> D. Grzonka,<sup>2</sup> W. Oelert,<sup>2</sup> G. Schepers,<sup>2</sup> T. Sefzick,<sup>2</sup> H. Pittner,<sup>3</sup> M. Herrmann,<sup>3</sup> J. Walz,<sup>3</sup> T. W. Hänsch,<sup>3,4</sup> D. Comeau,<sup>5</sup> and E. A. Hessels<sup>5</sup>

(ATRAP Collaboration)

<sup>1</sup>Department of Physics, Harvard University, Cambridge, Massachusetts 02138, USA

<sup>2</sup>IKP, Forschungszentrum Jülich GmbH, 52425 Jülich, Germany

<sup>3</sup>Max-Planck-Institut für Quantenoptik, Hans-Kopfermann-Strasse 1, 85748 Garching, Germany

<sup>4</sup>Ludwig-Maximilians-Universität München, Schellingstrasse 4/III, 80799 München, Germany

<sup>5</sup>York University, Department of Physics and Astronomy, Toronto, Ontario M3J 1P3, Canada

(Received 17 August 2004; published 21 December 2004)

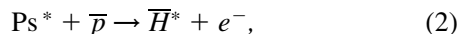
Lasers are used for the first time to control the production of antihydrogen ( $\bar{H}$ ). Sequential, resonant charge exchange collisions are involved in a method that is very different than the only other method used so far—producing slow  $\bar{H}$  during positron cooling of antiprotons in a nested Penning trap. Two attractive features are that the laser frequencies determine the  $\bar{H}$  binding energy, and that the production of extremely cold  $\bar{H}$  should be possible in principle—likely close to what is needed for confinement in a trap, as needed for precise laser spectroscopy.

DOI: 10.1103/PhysRevLett.93.263401

PACS numbers: 36.10.-k

All slow antihydrogen ( $\bar{H}$ ) atoms to date have been produced in the same way—during positron cooling of antiprotons [1] in a nested Penning trap [2], with the  $\bar{H}$  detected using two techniques [3–5]. The high production rate and the observation of highly excited states suggests that the  $\bar{H}$  is produced by a three body mechanism involving two  $e^+$  and one  $\bar{p}$ —the expected high-rate formation process at low temperature [2,6,7]. The coldest possible  $\bar{H}$  are required for the intriguing goal of achieving  $\bar{H}$  that is cold enough to be trapped for precise spectroscopic comparisons with hydrogen [8], building upon highly accurate hydrogen spectroscopy [9,10]. Hopes for three-body formation of  $\bar{H}$  that is colder than the 200 meV observed in the only  $\bar{H}$  velocity measurement so far [11] remain to be realized.

This Letter reports a very different way to produce  $\bar{H}$ . Lasers determine the binding energy of  $\bar{H}$  atoms that are most likely as cold as the  $\bar{p}$  from which they form. The lasers directly excite Cs atoms to high Rydberg states,  $Cs^*$ . Two resonant charge exchange collisions [12],



transfer the laser-selected  $Cs^*$  binding energy to an excited positronium atom ( $Ps^*$ ) [13] and then to an excited  $\bar{H}^*$ . Both processes have large cross sections because of the large size of the  $Cs^*$  and  $Ps^*$  [14], whereas  $\bar{H}$  formation using ground state  $Ps$  [15] has a rate too small to be observed. Very slow  $\bar{H}$  are expected because a  $Ps^*$  transfers little kinetic energy to a  $\bar{p}$  as  $\bar{H}$  forms. The  $\bar{p}$  can be no colder than 4 K here, but the  $\bar{p}$  could be made much

colder in principle—using techniques that cooled a trapped electron to 300 mK [16], for example.

The schematic in Fig. 1 shows three coaxial Penning traps (yellow regions)—for  $e^+$  (left), for  $\bar{p}$  (center), along with an initially empty trap for  $\bar{H}$  detection (right). Cs from an oven is excited with two lasers. The  $Cs^*$  collide with trapped  $e^+$  to form  $Ps^*$  atoms [Eq. (1)]. A small fraction of the  $Ps^*$  collides with trapped  $\bar{p}$  to produce  $\bar{H}^*$  [Eq. (2)]. A small fraction of the  $\bar{H}^*$  enters the detection trap, is ionized by the electric field in this trap, and deposits  $\bar{p}$  in the trap to be counted later. Three close traps are realized with potentials [Fig. 3(b)] applied to cylindrical ring electrodes that are 6 mm long and 12 mm diameter [Figs. 2 and 3(a)]. The close traps maximize the solid angles which nonetheless remain small enough that many more  $\bar{H}$  will be produced than can be detected.

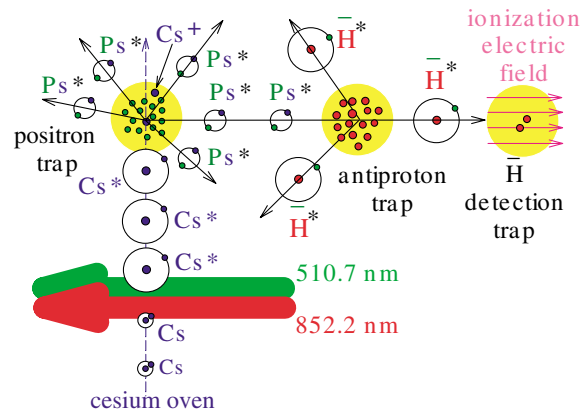


FIG. 1 (color). Schematic of laser-controlled  $\bar{H}$  production.

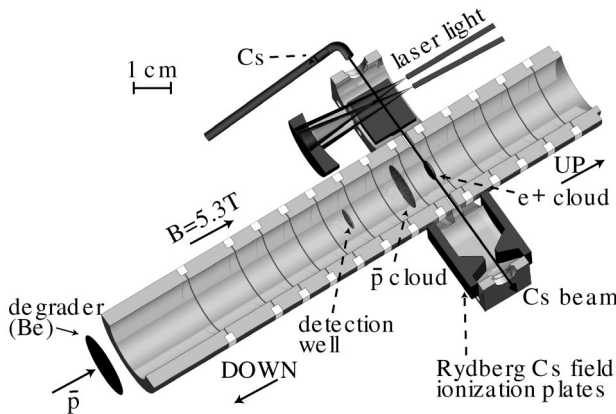


FIG. 2. Cutaway view of the Cs beam and the three traps for  $e^+$ ,  $\bar{p}$ , and for  $\bar{H}$  detection. The trap is surrounded scintillators that detect  $\bar{p}$  annihilation at high efficiency [19].

Positrons for  $\bar{H}$  formation are transferred into the location shown in Figs. 2 and 3 from an upper accumulation region of the trap apparatus (not shown). In a well-documented accumulation method [18],  $e^+$  from a 41 mCi  $^{22}\text{Na}$  source slow in tungsten crystals and produce a  $\text{Ps}^*$  that field ionize within a  $e^+$  trap. The trapped  $e^+$  radiate synchrotron radiation to come into thermal equilibrium with their 4 K environment. Their number,  $1.4 \times 10^6$  on average for these trials, is deduced from the measured width of the dip that they cause in the noise-driven resonance of an attached LCR circuit [18].

Our trials use  $2.4 \times 10^5 \bar{p}$  on average, accumulated typically in a half hour [19], and then located as shown in Figs. 2 and 3. They originate in CERN's unique anti-proton decelerator (AD). We accumulate  $\bar{p}$  at 4 K after reducing their energy by a factor of more than  $10^{10}$ . The slowing, trapping, cooling, and accumulation techniques which make this possible for all experiments attempting to make and study slow  $\bar{H}$  are well documented [19,20]. The number of  $\bar{p}$  is measured by releasing them from the trap, and counting the annihilation pions with calibrated scintillators that have near unit efficiencies.

Cs atoms are sent towards the trapped  $e^+$  [Figs. 2 and 3(a)] by heating to 350 K a thermally isolated,  $5 \text{ mm}^3$  Cs oven within the cryogenic vacuum enclosure for the trap. One of 16 Cs  $6S_{1/2}$  states is excited to  $6P_{3/2}$  ( $M_J = +1/2$  to  $M_J = +3/2$ , with  $M_J = -5/2$ ). The transition is saturated with infrared (852.2 nm) light from a diode laser. About 10 mW is sent into the 4 K vacuum enclosure of the trap through a 1 mm diameter optical fiber. It illuminates the Cs beam, reflects from a spherical mirror, again illuminates the Cs, and about 55% exits the system through a second fiber. Pulses of green 510.7 nm light from a copper vapor laser (20 ns duration every 50  $\mu\text{s}$ , 1250 W peak, 0.025 mJ) go through the same fiber and optics, and excite the Cs from  $6P_{3/2}$  to a state that would be  $37D$  (binding energy  $\sim 10$  meV) with no magnetic field. The approximately 45% of the light that does not exit the trap through the second fiber heats the trap

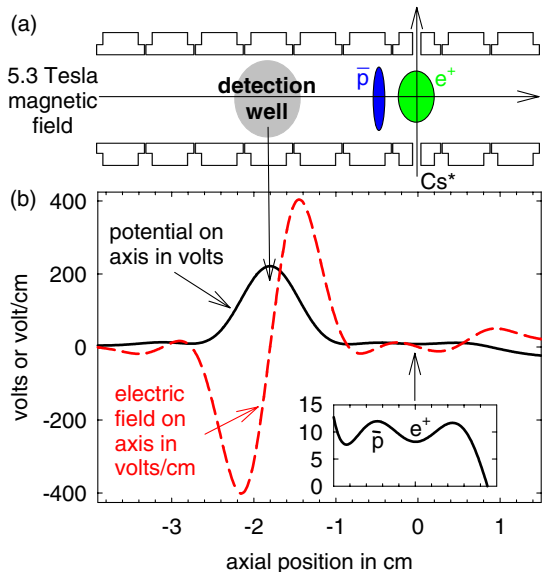


FIG. 3 (color online). (a) Trap electrode cross section with particle locations. (b) On-axis potential and electric field used to confine the  $e^+$  and  $\bar{p}$ , and to ionize and detect  $\bar{H}^*$ .

electrode by a couple of degrees during a typical experiment. A small electric field can tune the atoms into resonance with the fixed-frequency laser.

The  $\text{Cs}^*$  beam enters the trap through a 0.3 mm aperture at the entrance of a 1 mm hole in a trap electrode, passes through the  $e^+$  plasma, and leaves through a second 1 mm hole. The  $\text{Cs}^*$  flux is measured by field ionizing these atoms and measuring the ionization current [13]. The current is proportional to and calibrates the  $6P_{3/2}$  to  $6S_{1/2}$  fluorescence, measured with a photodiode, whose signal then determines smaller Cs fluxes. Of order  $10^{-3}$  of the Cs atoms are in large Rydberg orbits [13] with enormous charge exchange cross sections for producing  $\text{Ps}^*$ . Typically  $8 \times 10^5 \text{ Cs}^*/\text{s}$  pass though the trapped  $e^+$  location for 100 s.

Excited  $\text{Ps}^*$  form when  $e^+$  capture  $e^-$  from  $\text{Cs}^*$  [Eq. (1)]. The  $\text{Ps}^*$  formed in such resonant charge exchange collisions have approximately the  $\sim 10$  meV binding energy of the  $\text{Cs}^*$ , as initially determined by the laser frequencies. An initial study [13] revealed an enormous cross section estimated to be  $8 \times 10^{-10} \text{ cm}^2$ —the area of a disc with a radius of nearly  $0.2 \mu\text{m}$ —and approximately one in four of the trapped  $e^+$  formed  $\text{Ps}^*$  [13] assuming that the  $\text{Ps}^*$  distribution was isotropic. The  $\text{Ps}^*$  production also saturated when  $\text{Cs}^*$  passed through the  $e^+$  plasma for about 35 s, a time that should be much shorter here because of a much higher  $\text{Cs}^*$  flux.

To minimize possible  $\bar{p}$  heating the potential wells (Fig. 3) ensure that any  $\text{Cs}^+$  ion with enough energy to escape the  $e^+$  well will make no more than one pass back and forth through the  $\bar{p}$  before escaping to the right in Fig. 3. This precaution halves the number of  $\bar{H}$  we detect. We must forgo a second detection trap to the right of the  $e^+$  well in Fig. 3(b) since  $\text{Cs}^+$  could be confined between

the potentials of two detection traps and make many passes through the  $\bar{p}$ .

$\text{Ps}^*$  that enter the small solid angle presented by the trapped  $\bar{p}$  can collide with the  $\bar{p}$  to form  $\bar{\text{H}}^*$  with essentially the  $\sim 10$  meV binding energy of the  $\text{Cs}^*$ , via the second resonant charge exchange [Eq. (2)]. The large size of the  $\text{Ps}^*$  ensures a large (though yet unknown for a strong  $B$ ) cross section, but a large fraction of  $\text{Ps}^*$  still go through the  $e^+$  plasma without forming  $\bar{\text{H}}^*$ .

The effective solid angle for  $\bar{\text{H}}^*$  to be detected in the detection trap is also very small. The axial electric field exceeds 400 V/cm for all radii in the detection trap, more than enough to ionize the  $\bar{\text{H}}^*$  which should ionize by about 200 V/cm. The ionized  $\bar{\text{H}}$  deposit their  $\bar{p}$  in this trap to be counted later. This electric field is also more than enough to ionize  $\text{Ps}^*$  which arrive at the detection trap, and we can observe electrons that ionized  $\text{Ps}^*$  deposit in this same trap. These electrons cool  $\bar{p}$  captured from  $\bar{\text{H}}^*$  ionization to the bottom of the detection trap well. The electric field is so strong off the axis in the detection trap region that it can ionize  $\bar{\text{H}}^*$  before they enter the potential well of the detection trap. There is also a large radial component of the electric field off axis, whose effect upon  $\bar{\text{H}}$  ionization is not well understood. These two effects prevent the detection of  $\bar{\text{H}}$  that are more than some 3 to 5 mm away from the trap axis, but this radius and hence the effective detection solid angle is not precisely known.

To calibrate the detection time window we place  $\bar{p}$  in the detection trap, then reduce the well depth through zero [solid curve in Fig. 4(b)] while counting  $\bar{p}$  annihilations in scintillation detectors that surround the trap. The right edge of the peak in the histogram in Fig. 4(b) is used to select a  $700 \mu\text{s}$  time window that contains annihilation signals from  $\bar{p}$  released from the very bottom of the detection trap.

The  $\bar{p}$  captured from  $\bar{\text{H}}$  are released in the same way. A count in Fig. 4(a) indicates a coincidence of signals from at least two scintillating fibers, from different layers of a three layer fiber hodoscope, located just outside the trap's vacuum enclosure. When we sum 6 trials, 13 counts in the expected channel form a peak. This corresponds to 14  $\bar{\text{H}}$  ionized in the detection trap when the  $94 \pm 6\%$  detection

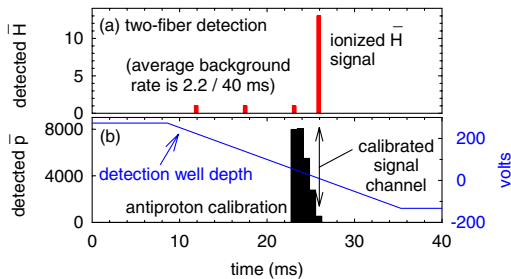


FIG. 4 (color online). (a) Antihydrogen detected (peak) as the potential well containing the ionized  $\bar{\text{H}}$  is ramped down. (b)  $\bar{p}$  annihilation signals (histogram and left axis) as the axial well depth is reduced through zero (solid curve and right axis).

efficiency is factored in. The detection efficiency is measured *in situ* by slowly ejecting  $\bar{p}$  from the trap and comparing the number of annihilations detected in coincidences between fibers in the hodoscope and a double layer of scintillators that surrounds the trap, outside of the superconducting solenoid and its Dewar.

On average 2.2 background counts are expected in the 40 ms width of Fig. 4(a), and we see 3 counts outside of the peak. Statistically there is about a 4% chance that a background count is in the peak. The 3 counts outside the peak are not present in a coincidence of the described signals and the signals from large plastic scintillators that surrounds the superconducting solenoid around our trap. About half the counts in the peak survive this background free detection, as expected.

Owing to small solid angles and few trials, only  $14 \pm 4$   $\bar{\text{H}}$  are detected in this proof-of-principle experiment. However, these correspond to between 100 to 200  $\bar{\text{H}}$  produced if the production is isotropic (with uncertainty coming from the mentioned uncertainty in the effective detection solid angle). Moreover, more atoms are expected for larger numbers of  $\bar{p}$  and  $e^+$ . This demonstration came in several hours at the end of the 2003  $\bar{p}$  run at the CERN AD so the method has yet to be optimized.

The most convincing evidence that the counts in Fig. 4(a) are from  $\bar{\text{H}}$  atoms is that the potential wells [Fig. 3(b)] are carefully arranged so that the only way to get a  $\bar{p}$  in the detection trap is by ionizing an  $\bar{\text{H}}$  within it, as discussed [4]. If a  $\bar{p}$  does manage to escape its trap and pass through the detection trap, it cannot be captured unless a collision within this well lowers the  $\bar{p}$  energy by more than an eV. This is the amount that the left side of the detection well is kept lower than the right in Fig. 3(b) (though the offset is too small to see in the figure). No counts are observed in the signal channel for two trials with the red laser detuned (so that only ground state  $\text{Cs}$  and no  $\text{Cs}^*$  pass through the trapped  $e^+$ ), nor for two trials without trapped  $e^+$ .

The lowest possible  $\bar{\text{H}}$  velocities and temperatures are required if  $\bar{\text{H}}$  atoms are to be confined in 0.5 K deep magnetic traps. A very important feature of this new  $\bar{\text{H}}$  production mechanism is that it seems likely to produce  $\bar{\text{H}}^*$  with the velocity distribution of the trapped  $\bar{p}$  from which they form. Measuring the  $\bar{\text{H}}^*$  velocity distribution (using the demonstrated oscillating field method [11], or perhaps by correlating pulsed laser and  $\bar{\text{H}}$  detection timing) requires more atoms than detected so far. The current  $\bar{p}$  velocity distribution is determined initially by the 4 K electrons that cool the  $\bar{p}$ , which are then moved into the desired location. Subsequent  $\bar{p}$  collisions with the much lower mass  $\text{Ps}^*$  should not substantially change the velocity of the  $\bar{p}$  when these collide to form  $\bar{\text{H}}^*$ . Dilution refrigerator and feedback cooling methods to cool a trapped electron below several hundred mK [16] could likely be adapted to trapped  $\bar{p}$ .

The strong 5.3 T magnetic field is an essential part of the three traps, but it also complicates this experiment

and its theoretical interpretation. First, exciting the Cs atoms from the  $6P_{3/2}$  state to the Rydberg state requires empirically varying an electric field to tune the atoms into resonance with the fixed-frequency copper vapor laser since the states have not been calculated. Second, internal orbits of both the  $\text{Cs}^*$  and  $\bar{\text{H}}^*$  atoms formed are significantly modified by  $B$  since the magnetic force is comparable to the Coulomb force. Third, the binding energies of Rydberg atoms moving across a strong magnetic field are not even conserved, but are instead coupled to the center of mass energy of the atoms [21]. A calculation of this double charge exchange process which neglects the magnetic field [12] gives a guide about what to expect, but a formation calculation that includes the crucial role of the magnetic field is needed.

Which of the two  $\bar{\text{H}}$  production methods is more useful in producing extremely cold, ground state  $\bar{\text{H}}$  that can be trapped for precise spectroscopic comparisons with hydrogen and for gravitational studies? Laser-controlled charge exchange has the advantages of naturally producing both colder atoms and a much narrower, laser-selected distribution of excited states. However, a method to deexcite them to the ground state has yet to be demonstrated.  $\bar{\text{H}}$  produced during  $e^+$  cooling of  $\bar{p}$  in a nested Penning trap produces atoms more easily and at a much higher rate, and it may be possible to collisionally deexcite them. However, now that the velocity of these  $\bar{\text{H}}^*$  can be measured [11], it remains to be seen if ATRAP's method for driving  $\bar{\text{H}}$  production [5] or some variant can produce very cold atoms as hoped. Other production methods, such as using a CO<sub>2</sub> laser to stimulate  $\bar{\text{H}}$  formation in a trap [2], are yet to be tried. The best method for producing useful  $\bar{\text{H}}$  is not yet clear.

In conclusion, this proof-of-principle experiment demonstrates the first laser-controlled  $\bar{\text{H}}$  production. The atoms revealed by essentially back-ground-free detection are a small fraction of what is produced because the detection solid angle and the number of trials are small. Many more  $\bar{\text{H}}$  are expected when more  $e^+$  and  $\bar{p}$  are used, and when the method is optimized. The produced  $\bar{\text{H}}$  are expected to have the velocity distribution of the  $\bar{p}$  from which they form, which can be made extremely low in principle. If measurements confirm a low  $\bar{\text{H}}$  energy, and if the highly excited states can be deexcited, this laser-controlled charge exchange method could become the method of choice for producing cold  $\bar{\text{H}}$  to be trapped for precise spectroscopic comparisons with hydrogen to test fundamental symmetries.

We are grateful to CERN, its PS Division, and the AD team for delivering the high energy antiprotons. This work was supported by the NSF and AFOSR of the U.S., the German BMBF, and the NSERC, CRC, CFI, and OIT of Canada.

\*ATRAP Spokesperson.

Email address: gabrielse@physics.harvard.edu

- [1] G. Gabrielse, J. Estrada, J. N. Tan, P. Yesley, N. S. Bowden, P. Oxley, T. Roach, C. H. Storry, M. Wessels, J. Tan, D. Grzonka, W. Oelert, G. Schepers, T. Sefzick, W. Breunlich, M. Carnegelli, H. Fuhrmann, R. King, R. Ursin, H. Zmeskal, H. Kalinowsky, C. Wesdorp, J. Walz, K. S. E. Eikema, and T. Haensch, Phys. Lett. B **507**, 1 (2001).
- [2] G. Gabrielse, S. L. Rolston, L. Haarsma, and W. Kells, Phys. Lett. A **129**, 38 (1988).
- [3] M. Amoretti *et al.*, Nature (London) **419**, 456 (2002).
- [4] G. Gabrielse, N. S. Bowden, P. Oxley, A. Speck, C. H. Storry, J. N. Tan, M. Wessels, D. Grzonka, W. Oelert, G. Schepers, T. Sefzick, J. Walz, H. Pittner, T. W. Hänsch, and E. A. Hessels, Phys. Rev. Lett. **89**, 213401 (2002).
- [5] G. Gabrielse, N. S. Bowden, P. Oxley, A. Speck, C. H. Storry, J. N. Tan, M. Wessels, D. Grzonka, W. Oelert, G. Schepers, T. Sefzick, J. Walz, H. Pittner, T. W. Hänsch, and E. A. Hessels, Phys. Rev. Lett. **89**, 233401 (2002).
- [6] M. Glinsky and T. O'Neil, Phys. Fluids B **3**, 1279 (1991).
- [7] P. O. Fedichev, Phys. Lett. A **226**, 289 (1997).
- [8] G. Gabrielse, in *Fundamental Symmetries*, edited by P. Bloch, P. Paulopoulos, and R. Klapisch (Plenum, New York, 1987), pp. 59–75.
- [9] M. Niering, R. Holzwarth, J. Reichert, P. Pokasov, T. Udem, M. Weitz, T. W. Hänsch, P. Lemonde, G. Santarelli, M. Abgrall, P. Laurent, C. Salomon, and A. Clairon, Phys. Rev. Lett. **84**, 5496 (2000).
- [10] C. L. Cesar, D. G. Fried, T. C. Killian, A. D. Polcyn, J. C. Sandberg, I. A. Yu, T. J. Greytak, D. Kleppner, and J. M. Doyle, Phys. Rev. Lett. **77**, 255 (1996).
- [11] G. Gabrielse, A. Speck, C. H. Storry, D. L. Sage, N. Guise, D. Grzonka, W. Oelert, G. Schepers, T. Sefzick, H. Pittner, J. Walz, T. W. Hänsch, D. Comeau, and E. A. Hessels, Phys. Rev. Lett. **93**, 73401 (2004).
- [12] E. A. Hessels, D. M. Homan, and M. J. Cavagnero, Phys. Rev. A **57**, 1668 (1998).
- [13] A. Speck, C. H. Storry, E. Hessels, and G. Gabrielse, Phys. Lett. B **597**, 257 (2004).
- [14] M. Charlton, Phys. Lett. A **143**, 143 (1990).
- [15] J. W. Humberston, M. Charlton, F. J. Jacobsen, and B. I. Deutch, J. Phys. B **20**, L25 (1987).
- [16] B. D'Urso, B. Odom, and G. Gabrielse, Phys. Rev. Lett. **90**, 43001 (2003).
- [17] J. Estrada, T. Roach, J. N. Tan, P. Yesley, and G. Gabrielse, Phys. Rev. Lett. **84**, 859 (2000).
- [18] L. S. Brown, and G. Gabrielse, Rev. Mod. Phys. **58**, 233 (1986).
- [19] G. Gabrielse, N. S. Bowden, P. Oxley, A. Speck, C. H. Storry, J. N. Tan, M. Wessels, D. Grzonka, W. Oelert, G. Schepers, T. Sefzick, J. Walz, H. Pittner, and E. Hessels, Phys. Lett. B **548**, 140 (2002).
- [20] G. Gabrielse, Adv. At. Mol. Opt. Phys. **45**, 1 (2001).
- [21] D. Vrinceanu, B. E. Granger, R. Parrott, H. R. Sadeghpour, L. Cederbaum, A. Mody, J. Tan, and G. Gabrielse, Phys. Rev. Lett. **92**, 133402 (2004).

# Acknowledgments

Finally, I would like to take the opportunity to thank everybody who helped to make this work a success.

Firstly, I want to express my gratitude to Prof. Dr. Theodor W. Hänsch for offering me the possibility of pursuing a PhD thesis in his group and for making it possible to carry out this work within the ATRAP Collaboration at CERN.

I am grateful to Prof. Dr. Walter Oelert for writing the co-certificate.

I would like to thank Dr. Jochen Walz for inviting me to work on this interesting project, for his support, and for proofreading this thesis.

I thank Prof. Dr. Gerald Gabrielse for his support and effort.

I am grateful to Dr. Cody Storry for letting me work without reservation on the hbar2 Penning trap apparatus and on the two-stage charge-exchange experiment. I learned a lot about how experimental physics is done from Cody and his never give up attitude made it possible to overcome many problems concerning the two-stage charge-exchange experiment.

I am greatly indebted to Dr. Paul Oxley for introducing me to the ATRAP experiment and for all his support during my first year at ATRAP.

I would like to thank Dr. Dieter Grzonka for explaining me the details of the ATRAP detector system, for making invaluable suggestions how to improve my Monte Carlo simulations, and for the careful proofreading of this thesis.

Thanks to Dr. Georg Schepers for his support during my  $3\frac{1}{2}$  years at CERN. He has always been there when I needed him.

I am also very grateful for the support of Dr. Nathaniel Bowden with whom I had the pleasure to work with during my first year at CERN and for the support and hard work of Andrew Speck with whom I had the pleasure to work with during the two last years.

I am also grateful to Prof. Dr. Eric Hessels for many discussions about charge-exchange reactions.

Thanks to Daniel Comeau for all his hard work during his time at CERN.

I also thank the part of the collaboration from Jülich, Prof. Dr. Walter Oelert, Dr. Frank Goldenbaum, Dr. Dieter Grzonka, Dr. Georg Schepers, and Dr. Thomas Sefzick for constructing and running this great detector system. Moreover, I would like to thank Walter and Brigitte Oelert for the many invitations to restaurants in Geneva and nearby France.

I am also deeply indebted to Peter Fendel for the many discussions about lasers and (anti)hydrogen on the phone, in Garching, and at Ringberg castle. I also thank him for his willingness to place all the orders of optical materials at the MPQ's purchasing office as well as sending all the goods to CERN.

I thank Maximilian Herrmann for the diode laser system that I have inherited in order to successfully carry out the two-stage charge-exchange experiment. I also thank him for his company at CERN.

I am also grateful to Birgit Henrich for all the explanations about the Lyman- $\alpha$  laser system and about EIT.

I am deeply indebted to Wolfgang Simon and Karl Linner for their support. Whenever I needed a workpiece, they took care that I got what I wanted.

I would also like to thank Dr. Kjeld Eikema and his PhD students S. Witte and R. T. Zinkstok for their help with the Titanium:Sapphire laser and for borrowing the Coherent Corona laser.

I would also thank David Le Sage for his hard work during the last year at CERN and Dr. John Estrada and his wife Sandra who helped me settle down when arriving in Geneva.

Thanks to Jean-Pierre Bertuzzi and coworkers from the CERN vacuum group for the help in adapting an ion pump to the CERN high voltage standard.

I would also like to thank Rosemarie Lechner and Gabi Gschwendtner who helped to solve many organizational problems, and the rest of the Garching group for many fruitful discussions about lasers and about hydrogen and for the good times at Ringberg castle.

On the personal side my parents have, as always, been entirely supportive during my PhD. Many thanks for all!

Last but not least, I want to thank my beloved Murielle for all her patience, support, and love during the last years.

# Lebenslauf

## Persönliche Daten

Heiko Pittner

Geboren am 18. Juli. 1974 in Mutlangen, Ostalbkreis  
Ledig, deutsche Staatsbürgerschaft

## Schulbildung

1981–1985	Scheuelbergschule in Schwäbisch Gmünd–Bargau
1985–1994	Scheffold–Gymnasium in Schwäbisch Gmünd
06/1994	Allgemeine Hochschulreife

## Wehrdienst

10/1994–09/1995 Wehrdienst in Mengen und Memmingen

## Studium

10/1995–08/1998	Studium an der Universität Stuttgart
10/1997	Vordiplom in Physik
09/1998–07/1999	Auslandsstudium am Georgia Institute of Technology, Atlanta, GA, USA
06/1999	Master of Science in Physics
09/1999–07/2001	Studium an der Universität Stuttgart
07/2000–07/2001	Diplomarbeit in der Arbeitsgruppe von PD Dr. O. Hess am Institut für Technische Physik der DLR in Stuttgart mit dem Thema: Numerische Analyse von Defekt-Strukturen in quasi-2D Photonischen Kristallen
07/2001	Diplom in Physik
Seit 09/2001	Doktorarbeit in der Arbeitgruppe von Prof. Dr. T. W. Hänsch Durchführung der Arbeit innerhalb der ATRAP Kollaboration am CERN in Genf